Investigating and Developing Fatigue-Healing Characterization of Asphalt Materials

by

Roberto Aurilio

A thesis

presented to the University of Waterloo

in fulfillment of the

thesis requirement for the degree of

Doctor of Philosophy

in

Civil Engineering

Waterloo, Ontario, Canada, 2023

Examining Committee Membership

The following served on the Examining Committee for this thesis. The decision of the Examining Committee is by majority vote.

External Examiner	**Dr. Eshan Dave** Civil and Environmental Engineering, University of New Hampshire
Supervisor	**Dr. Hassan Baaj** Civil and Environmental Engineering, University of Waterloo
Internal Member	**Dr. Pejoohan Tavassoti** Civil and Environmental Engineering, University of Waterloo
Internal Member	**Dr. Giovanni Cascante** Civil and Environmental Engineering, University of Waterloo
Internal Member	**Dr. Kaan Inal** Mechanical and Mechatronics Engineering, University of Waterloo

Author's Declaration

This thesis consists of material all of which I authored or co-authored: see Statement of Contributions included in the thesis. This is a true copy of the thesis, including any required final revisions, as accepted by my examiners.

I understand that my thesis may be made electronically available to the public.

Statement of Contributions

This thesis is partially the product of co-authored publications as follows. “The Effect of a Chemical Warm Mix Additive on the Self-Healing Capability of Bitumen” and “High-Performance Pavements: A focus on self-healing asphalt technologies” are co-authored by myself, my colleague (Mike Aurilio) and our supervisor, Professor Hassan Baaj. The first publication was prepared for the 2020 RILEM International Symposium on Bituminous Materials (ISBM) and was selected by the Scientific Committee for publication as a full journal paper in the ASTM Journal of Testing and Evaluation. In this paper, sample preparation, Superpave performance grading, experimental planning, data analysis, and discussion were completed by the author of this thesis, while Mike Aurilio primarily contributed by performing healing tests and edits of the final manuscript. The second publication is a literature review prepared for the 2020 Canadian Technical Asphalt Association Annual Conference. Some sections of the literature review pertaining to self-healing technologies and characterization techniques were adapted and updated for this manuscript.

Peer-reviewed publication(s):

1. Aurilio, R., Aurilio, M., Baaj, H. "The Effect of a Chemical Warm Mix Additive on the Self-Healing Capability of Bitumen" Prepared for the ISBM Lyon 2020 Conference in Lyon, France, hosted by RILEM. Accepted: February 6, 2020
2. Aurilio, R., Aurilio, M., Baaj, H. “The effect of a chemical warm mix additive on the self-healing capability of bitumen.” *Journal of Testing and Evaluation*, 50 (2). Published: July 2021. https://doi.org/10.1520/JTE20210207.

Conference publication(s) with abstract selection:

1. Aurilio, R., Aurilio, M., Baaj, H. “High-Performance Pavements: A focus on self-healing asphalt technologies”, Canadian Technical Asphalt Association Conference (2020). Presented: November 2020

Abstract

Canada's aging highway network, consisting of over 1.1 million kilometres of roads, is a vital component in ensuring the safe and reliable day-to-day movement of people and goods. Flexible asphalt pavements experience deterioration due to repeated traffic and environmental loading, and as a consequence, may require costly maintenance and rehabilitation treatments to remain functional over their service life. An alternative strategy to these reactive treatments can be found in the form of self-healing asphalt pavements.

The innovative strategies employed in self-healing materials are rooted in natural and biological processes. In the simplest sense, as these materials become damaged, a natural healing response allows them to restore their integrity or functional properties. Bitumen and asphalt materials have a very similar intrinsic healing ability which has been recognized since it was first observed in the 1960s. Asphalt material self-healing arises from the asphalt cement and its ability to fill microcracks caused by repeated small strain amplitude loading (i.e., fatigue). Intrinsic healing is influenced by internal factors (e.g., asphalt cement chemistry, aging level, and modification type) and external factors (e.g., moisture, UV exposure, rest period duration and temperature, etc.). To overcome the limitations of intrinsic healing, several extrinsic healing technologies have been used in literature including molecular interdiffusion techniques, structures containing healing agents and secondary self-healing polymer phases. In recent studies, healing is primarily characterized using destructive accelerated fatigue and fracture-based tests with rest periods, but the lack of industry-standard tests and terminology for both asphalt cement and mixtures leads to an often-ambiguous understanding of healing itself. This lack of standardization limits the capability of researchers to effectively characterize the intrinsic healing ability, but also develop new extrinsic healing technologies. The principal goal of this thesis is then to investigate current self-healing characterization techniques and develop new testing protocols for asphalt materials.

The work presented in this thesis uses a multiscale approach to the healing characterization of asphalt materials in collaboration with RILEM Technical Committee CHA-278 (Crack Healing of Asphalt Materials). Based on the initial healing study of unaged and aged asphalt cement containing a chemical warm mix additive using the linear amplitude sweep healing (LASH) test, it was evident that current generation DSR-based fatigue and healing characterization techniques experience measurement artifacts caused by geometry changes/ specimen flow under loading. As a result, a comprehensive

evaluation of the linear amplitude (LAS) test and different failure criteria found in literature was conducted. These failure criteria were then supplemented with the complementary parameters: the electric torque inflection point, the peak normal force, and the flow strain amplitude (FSA) as determined from the novel DSR Visual Analysis workflow. From the analysis of the LAS test, it was shown that failure criteria strain amplitudes could be categorized as either peak or post-peak behaviour; the traditional peak shear strain amplitude was concluded to be the most conservative failure criteria for all aging levels. From the FSA analysis, it was demonstrated that the shear stress-strain peak correlated with the onset of specimen flow, thus, the peak value was selected as the maximum strain amplitude for the first phase end condition for subsequent healing tests. In cooperation with the RILEM CHA-278 Task Group (TG) 2a, a second version of the LASH test protocol was proposed and evaluated based on the recommendations of the LAS visual analysis. From various works in literature, the Pure-LASH or P-LASH peak-based analysis method was derived using fracture mechanics to model the restoration ability of several binders at different aging levels using the LASH V2 protocol. Test parameters such as rest period duration and aging level were found to not be statistically significant factors, but further analysis determined that "damage" was only observed when the first loading phase end condition was the peak shear stress strain amplitude (γ_{peak}) as flow had already irreparably change the geometry of the DSR specimen. The general conclusion of these works was that geometric changes of the DSR sample during loading produce increasingly inaccurate measurements of post-peak data in amplitude sweep tests, thus, future work should take a greater emphasis on the characterization of pre-peak behaviour.

As a contribution to RILEM CHA-278 TG 2b, intermediate temperature fatigue tests with rest periods were conducted on a single asphalt mix at two strain levels. From the fatigue tests, a new fatigue model called the Intrinsic-VECD or iVECD linearization model was derived from the DGCB intrinsic damage model and simplified viscoelastic continuum damage model (VECD). The iVECD model was then extended to healing tests to separate "true" fatigue damage from common bias prevalent in accelerated fatigue testing of asphalt materials. From the iVECD model, several restoration/healing and damage indices were proposed: %Heal, %Recovery, %Restoration and Permanent Damage (%PD). Results of the iVECD healing indices indicated that the majority of recovery and healing occurs within the first 4 to 6 hours of the rest period. However, it was observed that increasing the strain level produces more permanent damage for the same loading duration. Finally, non-invasive ultrasonic measurements were coupled to these destructive fatigue tests and coda wave interferometry (CWI) was

used to analyze the effects of multiple scattering due to damage and healing. Two windowing selection methods were proposed (i.e., a simplistic statistical method and an adaptive analytical method). Using both window selection techniques, it was demonstrated that CWI could capture the effect of both loading/unloading and was sensitive enough to clearly distinguish between different strain levels.

Acknowledgements

This research project would not be achievable without the excellent guidance and support from my supervisor, Prof. Hassan Baaj. I am extremely grateful for your invaluable patience and expertise these past few years. I would also like to express my deepest gratitude to my thesis committee members, Professor Eshan Dave, Professor Kaan Inal, Professor Giovanni Cascante, and Professor Pejoohan Tavassoti. Additionally, this project would not have been successful without funding from the Natural Sciences and Engineering Research Council of Canada (NSERC); this project and many others were funded under the NSERC Discovery Grant program (RGPIN 2016-04859).

My gratitude also goes to the following supporting partners of this research:

- The Centre for Pavement and Transportation Technology (CPATT), Norman W. McLeod Chair, University of Waterloo.
- My colleagues in RILEM Technical Committee CHA-278 whom I had the pleasure of working with: Frank Williams, Dr. Fabrizio Miglietta, Dr. Orazio Baglieri, Dr. Lucia Tsantilis and Dr. Salvatore Mangiafico.
- The Civil and Environmental Engineering Department's technical staff: Rob Kaptein, Richard Morrison, and Peter Volcic.
- Yellowline Asphalt Products Limited.

Finally, I would like to extend my thanks to all my family and friends; getting through this work required more than just academic support and I wouldn't be where I am without your love and encouragement.

Table of Contents

List of Figures

List of Tables

List of Abbreviations

AAPT	Association of Asphalt Paving Technologists
AASHTO	American Association of State Highway and Transportation Officials
AMPT	Asphalt Material Performance Tester
ANOVA	Analysis of Variance
API	Application Programming Interface
ASTM	American Society for Testing and Materials
BBR	Bending Beam Rheometer
BFE	Binder Fracture Energy
BYET	Binder Yield Energy Test
CC	Concentric-Cylinder (Chapter 6)
CC	Correlation Coefficient (Chapter 10)
CHA	Crack-Healing of Asphalt Pavement Materials
CII	Colloidal Stability Index
COS	On-Specimen Strain Control Mode
COV	Coefficient of Variation
CP	Cone-Plate
CPATT	Centre for Pavement and Transportation Technologies
CS	Force/ Stress Control Mode
CTAA	Canadian Technical Asphalt Association
CWI	Coda Wave Interferometry
CX	Actuator Displacement Control Mode
DAQ	Data Acquisition
DECL	Dissipated Energy per Cycle
DER	Dissipated Energy Ratio
DF	Degrees of Freedom
DGCB	Département Génie Civil et Bâtiment
DIN	Deutsche Institut für Normung/ German Institute for Standardization
DMR	Dynamic Modulus Ratio
DPSE	Dissipated Pseudostrain Energy
DSLR	Digital Single Lens Reflex (Camera)
DSO	Direct Strain Oscillation
DSR	Dynamic Shear Rheometer
DTT	Direct Tension Test
DTW	Dynamic Time Warping
EC	Electronically Commutated
ENTPE	École nationale des travaux publics de l'État
ER	Elastic Recovery
FBD	Functional Block Diagram
FC	Friction Course

FED	Fracture Energy Density
FFT	Fast Fourier Transform
FHWA	Federal Highway Administration
FI	Fracture Index
FREI	Fatigue Resistance Energy Index
FSA	Flow Strain Amplitude
HI	Healing Index
HMA	Hot Mix Asphalt
HSD	Honest Significant Difference (Tukey)
IH	Initial Healing
iVECD	Intrinsic Viscoelastic Continuum Damage Model
J	Fracture Energy
LAOS	Large Amplitude Oscillatory Shear
LAS	Linear Amplitude Sweep
LASH	Linear Amplitude Sweep Healing Test
LP	Loading Phase
LSD	Least Significant Difference (LSD)
LTOA	Long-Term Oven Aging
LVE	Linear Viscoelastic
MANOVA	Multivariate Analysis of Variance
MARC	Modified Asphalt Research Center
MSCR	Multiple Stress Creep Recovery
MTS	Material Testing System
NCHRP	National Cooperative Highway Research Program
NDT	Non-Destructive Testing
NMAS	Nominal Maximum Aggregate Size
NSERC	National Science and Engineering Research Council
OAC	Optimum Asphalt Content
OPSS	Ontario Provincial Standards
PAV	Pressure Aging Vessel
PD	Permanent Damage
PGAC	Performance Graded (Asphalt Cement)
PLAS	Pure Linear Amplitude Sweep
PP	Parallel-Plate
PSE	Pseudostrain Energy
RDEC	Ratio of Dissipated Energy Change
RH	Residual Healing
RILEM	Réunion Internationale des Laboratoires et Experts des Matériaux, systèmes de construction et ouvrages
ROI	Region of Interest
RP	Rest Period

RTFO	Rolling Thin Film Oven
SAOS	Small Amplitude Oscillatory Shear
SARA	Saturates Aromatics Resins Asphaltenes
SBS	Styrene Butadiene Styrene (Polymer)
SED	Spectral Energy Density
S_F	Failure Strain
SGC	Superpave Gyratory Compactor
SHRP	Strategic Highway Research Program
SLASH	Simplified Linear Amplitude Sweep Healing Test
STOA	Short-Term Oven Aging
S-VECD	Simplified Viscoelastic Continuum Damage Model
TH	Total Healing
TOF	Time of Flight
TSRP	Temperature Sensitivity of Rheological Parameters
TTSP	Time-Temperature Superposition Principle
UA	Unaged
UPV	Ultrasonic Pulse Velocity
VECD	Viscoelastic Continuum Damage Model
WLF	Williams-Landel-Ferry
WMA	Warm Mix Asphalt

Chapter 1
Introduction

1.1 Background

Canada's transportation infrastructure (including road, rail, air and marine) enables the continual day-to-day movement of goods and people throughout the country. Canada's road network, which consists of over 1.1 million lane-kilometres of publicly owned roads, is a valuable asset and contributes more than 50% of the value of merchandise exports annually (Federation of Canadian Municipalities 2020; Transport Canada 2019). According to the 2019 Canadian Infrastructure Report Card, currently, 40% of all highways in Canada have been assessed as having only Fair to Very Poor condition rating, and almost 80% of these highways were constructed before the year 2000 (Federation of Canadian Municipalities 2020). A typical road or pavement is a layered structure designed to minimize vehicle loading transferred from the surface material to the soil beneath. However, pavements are not designed to withstand only a single static load; they must endure millions of repeated loads from vehicle traffic of different weights travelling at various speeds and in different environmental conditions throughout their20 to 30-year design life. Out of Canada's 1.1 million km of roads approximately 40% are paved and 90% of all paved roads are surfaced with flexible asphalt materials (Liu et al. 2017). The asphalt "concrete" or "mixture/ mix" is a combination of a bituminous asphalt "binder/ cement" and aggregates; when constructed as the top layer of this structure it provides a durable water-proof riding surface that bears a higher load compared to the lower pavement layers.

Due to its viscoelastic nature, asphalt pavements experience several types of distresses induced by both mechanical and environmental loading. The dominant North American asphalt mix design method established in the 1990s (i.e., Superpave) can readily produce mixes with adequate permanent deformation (rutting) resistance. However, several agencies across North America report an overwhelming tendency for these pavements to develop premature cracks (Aurilio and Newcomb 2018). Cracks commonly appear longitudinally (in the vehicle wheel path), transversally (caused by thermal changes in the pavement) or potentially as combination "block" or "alligator" cracks (Mneina and Smith 2022) Several simple strategies can improve cracking resistance by "softening" the asphalt cement in the mixture. Nevertheless, these solutions may come at the cost of rutting resistance. Furthermore, the susceptibility and severity of these distresses only increase as the pavement ages, and current maintenance and rehabilitation (M&R) practices cannot reliably counteract degradation from increasingly demanding conditions (Barman 2019).

Over the ten years from 2006 to 2016, Canada's National Highway System (NHS) experienced an 8% increase in truck traffic generating considerable strain on an already aging pavement infrastructure (Transport Canada 2019). Even as the transportation of goods increases to keep pace with the economy's demands, comparatively little has been done to address Canada's aging roads. To meet future economic and environmental challenges, pavement engineers must look to innovative high-performance solutions to develop degradation-resistant asphalt mixes while improving: (1) safety, (2) sustainability, (3) affordability, and (4) resilience.

Since the 1960s, it has been known that asphalt materials have an inherent ability to heal damage when loading is removed (Xu et al. 2018b). The healing ability is attributed to the asphalt cement; under certain conditions, the asphalt cement can "fill" microscale crack damage allowing for recovery of a portion of the prior mechanical properties. Consequently, the degree of healing is highly dependent on the chemistry of the asphalt cement, but it is possible to use additives to enhance the crack-healing ability of the mixture. As such, ongoing research into self-healing characterization and the development of self-healing asphalt mixture technologies has the potential to significantly increase long-term fatigue performance and decrease M&R costs as well as emissions over the lifespan of a pavement (Partl 2019).

1.2 Research Motivations

Due to increasing traffic and environmental loading, existing asphalt pavements experience higher deterioration rates (i.e., fatigue cracking, rutting, thermal cracking, etc.) putting progressively more significant strain on Canada's highway system. As these pavements age, more frequent maintenance and rehabilitation treatments are required to maintain an acceptable level of performance leading to a considerable increase in the economic, environmental, and social cost over the pavement's lifetime.

One solution for the next generation of high-performance flexible pavements is self-healing asphalt materials. These self-healing pavements can potentially maintain higher levels of fatigue performance leading to longer service lives, increased safety and decreased costs due to recurrent M&R treatments. Currently, there are no standardized healing tests for fatigue-damaged asphalt cements or mixtures, and while fatigue has been studied extensively, many difficulties arise separating reversible (i.e., thixotropy, non-linearity, internal heating) and non-reversible (i.e., microcrack damage) phenomena during loading and unloading in accelerated fatigue experiments.

The work presented in this thesis was completed under the supervision of Professor Hassan Baaj at the Centre for Pavement and Transportation Technology (CPATT) at the University of Waterloo. This

project has been funded by the Natural Sciences and Engineering Research Council of Canada (NSERC) under NSERC Discovery Grant: RGPIN-2016-04859. The work presented herein follows a multiscale approach to healing characterization through the author's involvement with RILEM Technical Committee (TC) CHA-278 (Crack Healing of Asphalt Materials).

As a graduate student member of RILEM TC CHA-278, the authour completed interlaboratory testing for Task Group (TG) 2a and 2b relating to the self-healing characterization of asphalt cements and mixtures, respectively. As a contributor to the interlaboratory testing, three asphalt cements (two unmodified and one elastomer modified) as well as a mix design were provided to the authour. Aside from the development of self-healing test protocols, the authour also contributed to TG 3 relating to self-healing characterization analysis and modelling. When necessary, the authour will detail when and how test protocols were influenced by working with the Task Group. However, the studies and results presented in this work were completed using local materials (e.g., asphalt cements and aggregates were kindly donated by Yellowline Asphalt Ltd.) and all analysis was conducted solely by the authour of this thesis.

1.3 Problem Statement and Research Objectives

The characterization of self-healing is a natural progression of the study of the fatigue phenomenon and damage caused by accelerated loading. Whether characterizing the restoration of physical properties directly through fatigue testing or indirectly by way of cracking resistance evaluation methods, a greater understanding of the intrinsic healing ability of asphalt materials is necessary to estimate the fatigue life of pavement materials more accurately.

As asphalt pavements experience time-related chemical changes as a result of aging. The aging phenomenon occurs at different time scales, due to environmental and climatic conditions, causing primarily irreversible chemical changes in the asphalt cement component of the mixture. Generally, asphalt mixes become stiffer and more brittle with increased aging causing a decrease in fatigue resistance. These chemical changes can also affect the intrinsic healing ability of asphalt materials. Current industry standard aging procedures only use high temperature or a combination of high temperature and pressure to simulate oxidative aging on asphalt samples. The initial intention of this research was to evaluate the following hypotheses about asphalt cement self-healing or crack healing and the effects of:

- Increased aging, which represents an irreversible change to the chemical structure of the asphalt cement due to oxidative processes, leads to a decrease in the fatigue resistance and healing ability of the asphalt cement.
- Modification of asphalt cement with additives (e.g., warm mix additives, secondary polymer phases, etc.) to increase healing ability by decreasing oxidation effects and increasing molecular mobility.

Both topics will still be featured in this thesis, albeit in a limited capacity. Especially as, early in the course of this work, it became apparent that fatigue characterization using the industry standard dynamic shear rheometer (DSR) test equipment for asphalt cements failed to capture the effects of both aging and modification meaningfully. As will be introduced in Chapter 4, measurement artifacts caused by changes in geometry/ instability flow led to misleading fatigue and healing characterization. This thesis then operates under the over-arching hypothesis that changes in sample geometry rather than "true" fatigue damage are responsible for the perceived fatigue and healing characteristics of asphalt cements observed using the DSR. As a result, this study has the following research goals (as related to asphalt cements):

1. To evaluate several accelerated fatigue testing failure criteria and analysis methods found in literature (specifically for the linear amplitude sweep test, also known as the LAS test).
2. To evaluate flow phenomena and specimen geometry changes using complementary/ non-invasive methods, thus, supplementing knowledge of DSR-based testing and asphalt cement rheology.
3. To propose modifications of existing test and new testing protocols as well as analysis frameworks for the next generation of fatigue-healing characterization tests for asphalt cements using the DSR.

In the second phase of this work, this thesis aims to investigate another major obstacle in typical asphalt mixture fatigue research: the separation of "true" fatigue damage from bias effects in accelerated fatigue studies. Methods to isolate fatigue damage from these bias effects have been proposed using both damage mechanics (e.g., the DGCB "Intrinsic" damage model (Baaj 2002)) as well as continuum mechanics (e.g., the AASHTO standardized viscoelastic continuum damage model or VECD technique (Underwood et al. 2012)) with varying degrees of success. And despite many attempts to adapt these methods to healing, self-healing characterization of asphalt mixtures is still

absent of a standardized or widely accepted methodology. Non-destructive techniques such as Ultrasonic Pulse Velocity (UPV) testing have been used for in-situ pavement evaluation. Still, they are not commonly used in a laboratory setting for fatigue (Grosso and Luca 2011). Adapting high sensitivity "non-invasive" testing techniques during destructive tests may enable researchers to overcome the limitations of traditional fatigue characterization. In the same fashion, this portion of research on asphalt mixtures has the following objectives:

1. To develop asphalt fatigue modelling methods to isolate bias effects from "true" fatigue. These methods can be extended to healing characterization in fatigue tests with rest periods (loading interruptions).
2. To develop and verify the viability of using alternate time-domain analysis methods (such as coda wave interferometry) to evaluate asphalt mixture fatigue and self-healing during typical destructive fatigue tests with rest periods.

1.4 Thesis Organization and Contributions

This thesis consists of eleven chapters; the list below highlights their contents and general contributions achieved during this study:

- *Chapter 1: Introduction*
    - This chapter briefly introduces the topic of interest to the reader. The research's main hypotheses, objectives and goals are also presented to provide the reader with the primary rationale for the subsequent works.
- *Chapter 2: Literature Review*
    - This chapter introduces asphalt pavements and a state-of-the-art review of self-healing definitions, mechanisms, technologies, and characterization methods. Note: sections of this chapter were adapted from the author's publication at the Canadian Technical Asphalt Association Conference in 2020, '*High-Performance Pavements: A Focus on Self-healing Asphalt Technologies*'.
- *Chapter 3: Research Methodology*

- This chapter provides an overview of the materials and methodology used in this research. The works presented in this thesis focus on the fatigue and healing characterization of (1) asphalt cements and (2) asphalt mixtures. More detailed explanations concerning the theoretical background, phenomenological modelling and statistical analysis are contained in their specific chapters.

- *Chapter 4: The Effect of a Chemical Warm Mix Additive on the Self-Healing Capability of Bitumen*

    - This chapter presents the first works in the characterization of asphalt cement self-healing behaviour using a DSR-based linear amplitude (LAS) based healing test. The research in Chapter 4 used the proposed simplified linear amplitude sweep healing (SLASH) test to evaluate the restoration ability of asphalt cements at different aging levels containing a chemical warm mix additive. The SLASH procedure used a pre-determined first loading phase termination amplitude compared to the pseudostrain energy (PSE) failure criteria found in the literature. Initial results of the SLASH restoration index demonstrated that more aged binders exhibit greater restoration, contradicting the conventional understanding of asphalt self-healing. However, when paired with the DSR Visual Analysis, a drastic decrease in the sample stiffness was accompanied by a significant change in the specimen geometry for unaged and short-term aged asphalt cements exposing a potential explanation for the contradictory restoration results. Note: this chapter was also adapted from the author's publication in the Journal of Testing and Evaluation, '*The Effect of a Chemical Warm Mix Additive on the Self-Healing Capability of Bitumen,'* Volume 50, Issue 2 (2021).

- *Chapter 5: Asphalt cement Fatigue Resistance using the Linear Amplitude Sweep (LAS): A Focus on Failure Criteria*

    - Based on the findings of Chapter 4, the work in Chapter 5 shifts away from asphalt cement modification and instead concentrates solely on the evaluation of the linear amplitude sweep test itself. Fatigue characterization methods and several failure criteria found in the literature, were evaluated. This includes the viscoelastic continuum damage (VECD) model, pseudostrain energy (PSE) analysis, crack length analysis/fracture index (FI), and other variations (i.e., CN and $C^2N(1-C)$), as well as rank-based methods such as fracture energy/ P-LAS analysis (using the FREI parameter) and ΔG. Strain amplitudes obtained

from different criteria could be categorized as either peak or post stress-strain peak phenomena. Due to the "peak broadening" effect observed due to binder aging, it was shown that the lag between peak strain amplitude and post-peak failure criteria was increased with aging. As a result, post-peak criteria methods often estimated greater fatigue resistance for more aged materials than peak-related criteria. When comparing the two ranking methods, P-LAS and ΔG, it was confirmed that both methods were able to capture the effects of aging due to their reliance on the peak shear strain amplitude. At every aging level, however, the peak shear strain amplitude was observed to be the most conservative failure criterion; due to its simplicity, this failure criterion was recommended for future asphalt cement fatigue characterization methods.

- Chapter 6: Linear Amplitude Sweep (LAS) Failure Criteria using Complementary Characterization Parameters

    - In Chapter 6, the LAS test is further analyzed using several 'complementary' metrics. The DSR electric torque (M_{el}) inflection point, and the peak normal force are used in conjunction with the DSR Visual Analysis (now formalized to include the flow strain amplitude or FSA), providing greater insight into the geometry change phenomenon initially observed in Chapter 4. A comprehensive statistical analysis determined that the amplitudes of peak shear-strain amplitude failure criteria and the first observable flow/ resultant geometry change of the DSR sample had a statistically significant relation. Notably, post-peak failure criteria shared a statistically significant relationship with the peak normal force and the electric torque inflection strain amplitudes. When investigating the effects of test temperature, it was demonstrated that flow-based changes in geometry were still observable even at temperatures below the recommended "intermediate PG temperature minus 4°C." Ultimately, the flow phenomena and all associated failure strain amplitudes were shifted to higher strain amplitudes with increasing temperature in contrast to what was speculated in literature.

- *Chapter 7: Asphalt Cement Healing Characterization: Concepts for Next-Generation Test Protocols*

- Using the information gained in Chapter 5 and Chapter 6, RILEM CHA-278 (Cracking Healing in Asphalt) selected desirable test parameters to propose version 2 of the LASH protocol. Based on the geometric flow phenomena, two first loading phase terminal strain amplitudes were selected for the LASH V2 protocol: the peak strain amplitude (γ_{peak}) and half the peak strain amplitude ($0.5\gamma_{peak}$). Restoration characterization was then adapted using several methods from the literature, including VECD-based and crack-length healing indices. As a contribution to RILEM CHA-278 Task Group 3 (Self-Healing Modelling), the P-LASH analysis method was proposed based on the P-LAS method evaluated in Chapter 5. From all five analysis methods, "full" restoration was observed when loading to the $0.5\gamma_{peak}$ end condition. When loading to the peak-end state, only unaged and short-term aged asphalt cements experienced losses due to "damage." This damage can be attributed to geometric changes and not "true" fatigue damage, which demonstrates that healing in DSR-based tests can easily be misleading based on the failure criteria chosen to determine the first phase termination strain amplitude. Consequently, the current generation of DSR-based fatigue and healing tests appear unsuitable for their intended purposes.

- *Chapter 8: Asphalt Mixture Testing Experimental Test Setup*

    - Starting with Chapter 8, the focus shifts from asphalt cement testing to the characterization of asphalt mixes using a uniaxial tension-compression setup. In this chapter, the preparation of CPATT's Material Testing Systems (MTS) multipurpose testing frame and a custom conditioning chamber/ control scheme is discussed in detail. Following both North American and European standards (e.g., DIN 12697-26-2012, AASHTO T 342, AASHTO TP 107-18), the MTS testing frame was equipped with specialized platen extensions to characterize cylindrical asphalt specimens using the complex modulus and fatigue tests. The use of loading interruptions/ rest periods is programmed into the MTS MPElite software to allow for the characterization of healing, recovery and restoration (Chapter 9). The specialized platen extensions also allow for the use of ultrasonic pulse-receiver equipment to couple non-destructive/invasive measurements during loading (Chapter 10). It is the intention that this chapter provides valuable guidance to those who would work towards a test set-up and workflow for similar test procedures.

- *Chapter 9: Preliminary Evaluation of Fatigue and Healing of Asphalt Mixtures using the "Intrinsic" VECD Method*

    - The preliminary work presented in this chapter proposes the use of the Intrinsic-VECD or iVECD model. Based upon the S-VECD and "DGCB"-style linearization method, the iVECD model is used to isolate bias effects in the fatigue test that may still be present despite the conversion of the material properties to their pseudo-variable counterparts. Based on the DGCB-interval style analysis, the iVECD damage rate is derived with distinct damage rates obtained using the provided intervals. When compared to the traditional S-VECD power law fatigue life estimation, fatigue life estimates using Interval 2 (150,000 to 300,000 cycles) show good agreement. In contrast, Interval 1 (50,000 to 150,000 cycles) tend to underestimate the fatigue life due to a greater damage rate.
    - Furthermore, the healing ability of a single asphalt mix was characterized by incorporating rest periods (4-, 8-, and 16-hour rest periods). Using the RILEM CHA-278 healing definitions, the permanent damage (%PD) and restoration (%Rest) were derived from the fatigue-healing test results. The restoration was further divided into two parts, recovery (%Rec) and healing (%Heal). The results of the fatigue-healing tests demonstrated that the rest period duration was not a significant factor when testing at the lower strain level. However, it was demonstrated that the strain level is a significant factor in the observed permanent damage. Specimens tested at higher strain showed more significant permanent damage and lower overall restoration.

- *Chapter 10: Viability of Coda Wave Interferometry for Fatigue Monitoring of Asphalt Mixtures*

    - Ultrasonic measurements were coupled with the asphalt mixture testing conducted in Chapter 9 using a dedicated pulse-receiver data acquisition system. Time signals were acquired periodically (i.e., 10-minute intervals) throughout the fatigue and healing test and then analyzed in the time-domain using the coda wave interferometry (CWI) technique. Two windowing procedures were proposed, including Method (1), which incorporated a simple statistical approach and Method (2), which was derived from the diffusive energy envelope (Epple, 2018, Planes and Larose, 2013) paired with an adaptive window length stretching technique. The CWI procedure was completed using a dynamic time-warping

(DTW) algorithm. CWI measurements using both windowing selection methods were demonstrated to be capable of distinguishing loading and rest periods during healing tests. The CWI technique was also sensitive enough to accurately differentiate loading at the lower and higher strain levels, used in this study. Notably, Method 2 CWI results were able to maintain lower signal-signal variability and capture the non-linearity or curvature observed in traditional fatigue tests typically attributed to bias effects.

- *Chapter 11: Conclusions and Recommendations*

    - Finally, this chapter presents a summary of the findings from the previous chapters, as well as a summary of the novelty and contributions of the work. The recommendations presented in Chapter 11 will pertain to next-generation fatigue-healing tests for both asphalt cement and mixtures.

Chapter 2
Literature Review

2.1 Asphalt Pavements

Pavements, in their simplest form, are layered structures designed to distribute loading from heavy multi-axle traffic to the soil below. There are two primary types of pavements: rigid and flexible pavements. Flexible pavements differ from rigid pavements because the entire pavement structure distributes the traffic loading to the subgrade whereas a concrete slab is the primary load carrier in rigid pavements. A traditional flexible pavement consists of a top layer of asphalt over a base layer and a subbase layer of compacted mineral aggregates above the existing subgrade material. The asphalt wearing layer is composed of a bituminous mixture called asphalt concrete or asphalt mixture. Asphalt mixtures are composed of approximately 4 to 6% asphalt cement and 94 to 96% mineral aggregates by weight. In contrast, the asphalt cement content is relatively low compared to its important contribution to the mixture's strength and cost (Canadian Technical Asphalt Association 2018).

Asphalt cement, a by-product of the crude oil distillation process, is composed of two primary groups of macromolecules: asphaltenes and maltenes. The asphaltenes act as springs and give the asphalt cement its strength and elastic behaviour, while the maltenes are characterized by viscous behaviour. The polar asphaltenes in the asphalt cement are suspended in the non-polar maltene matrix. Together, these molecules form a waterproof viscoelastic binder sensitive to temperature changes and the loading rate. The asphalt cement in the mixture is stiff at cold temperatures, making it susceptible to thermal cracking. At high temperatures, it is flowable, which can lead to permanent deformation in the wheel track (i.e., rutting) under slow or heavy loads. Asphalt pavements are also prone to cracking when undergoing a significant number of repetitive loads at intermediate temperatures in a process called fatigue.

2.1.1 Asphalt Material Design

Asphalt pavement design is divided between the pavement structural design (i.e., the thickness of individual layers) and the design of the material in the asphalt layer itself. In the early 1990s, a new Superpave system was proposed in North America as an alternative to the earlier Marshall and Hveem mix design methods. The Superpave method had several advantages, such as the ability to design larger stone mixes, more realistic compaction simulation, and environmental/ climatic considerations through

an asphalt cement grading system. The Superpave Performance Grading (PG) System for asphalt cement was proposed to replace older needle penetration grading methods. The PG System is a two-number classification system relating to the reliability of asphalt cement at both high and low temperatures; grades are demarcated in 6°C increments, and asphalt cements are denoted as a PG XX-YY. In the PG system, the XX-YY nomenclature denotes two temperatures, one above freezing (> 0°C) and one below freezing (< 0°C), and not two positive numbers separated by a hyphen. The first number (XX) in the grade corresponds to the 7-day average maximum pavement design temperature at a depth of 20 mm. It is intended as an indicator for reliability against rutting during periods of warmer temperatures and in areas with heavy, slow-moving traffic. The high PG temperature is determined by testing unaged asphalt cement samples at high temperatures on a dynamic shear rheometer (DSR) and compared against a threshold $G^*/\sin\delta$ value. $G^*/\sin\delta$ is sometimes referred to as the "rutting parameter" where G^* is the complex shear modulus, and δ is the phase angle. Larger rutting parameters obtained at the PG high temperature indicate greater potential for rutting resistance as the asphalt cement is stiffer (larger G^*) and more elastic (i.e., smaller δ). The failure threshold is 1.0 kPa and 2.2 kPa for unaged and short-term aged materials, respectively. The second grading number (-YY) is related to the stiffness and relaxation ability of an aged asphalt cement at the minimum pavement design temperature. The low PG temperature is determined from pressure aging vessel (PAV) long-term aged samples using the bending beam rheometer (BBR). Typical performance grades include PG 46-34, PG 58-28, PG 64-28, and PG 70-22. In Ontario, asphalt mixes with a specific PG grade are assumed to have 98% reliability in their designated temperature range (Ontario Hot Mix Producers Association 1999).

Beyond asphalt cement, there are requirements for aggregates and mixtures based on the traffic level. In the Superpave design method, aggregates are tested for consensus properties (such as coarse and fine aggregate angularity, flat and elongated particles, clay content, etc.) and source properties (such as specific gravity, abrasion toughness, soundness, etc.) (Ontario Hot Mix Producers Association 1999). The aggregate skeleton and its gradation can significantly contribute to permanent deformation resistance near the high PG temperature. Superpave mixture properties are based on the volumetric properties of compacted asphalt mixture samples. As previously stated, one of the main advantages of the Superpave method was improved compaction simulation using the Superpave Gyratory Compactor (SGC). The SGC gyratory motion kneads the hot mix simulating modern compaction equipment and densification due to early traffic. For Superpave mix designs, the Optimum Asphalt Content (OAC) is estimated when the target densification level is 96% of the theoretical maximum density or when the

sample has 4% air voids. The percentage of air voids (V_a) represents the volume of the compacted sample filled with air (i.e., not filled with aggregates or asphalt cement in a compacted specimen). The VMA, or Voids in Mineral Aggregate, is the theoretical volume of a compacted granular sample that can be filled with air or asphalt cement. The final volumetric property is the Voids Filled with Asphalt (VFA). It represents the volume of the compacted sample filled with asphalt cement and is expressed as a percentage of the VMA (Canadian Technical Asphalt Association 2018).

When Superpave guidelines were initially proposed by the Strategic Highway Research Program (SHRP) in 1991, they were originally designed to target the severe deformation problems caused by over-sanded mixes and changing American truck specifications in the 1980s (Canadian Technical Asphalt Association 2018). The early success of the Superpave method led to its widespread adoption across North America. However, pavements currently designed using the Superpave method are observed increases in intermediate temperature fatigue cracking due to repeated heavy loading. Relying on mixture volumetric parameters, Superpave can only be classified as a performance-related mix design method. Originally, there were plans to include performance testing, but this was never implemented meaningfully. The Tensile Strength Ratio (TSR) test evaluates mixes for moisture susceptibility. This test accounts for the primary asphalt material failure, such as cracking, rutting, or thermal cracking performance. Currently, there is motivation to design Superpave mixes with a balance between rutting and fatigue resistance using performance testing; this approach is called "Balanced Mix design" (Aurilio and Newcomb 2018).

In contrast to North America, where there is a heavier emphasis on asphalt cement properties, the French mix design method, commonly used in Europe, focuses on performance and mechanical properties of the asphalt mix itself with remarkable success. Using the French method, asphalt mixes are evaluated in four primary stages for moisture resistance, resistance to permanent deformation and fatigue cracking. In addition, the stiffness of the asphalt mix, which is an important parameter in pavement design, is evaluated using the complex modulus test. If the mix fails at one of these stages, it can be redesigned until it passes all the performance tests for its intended traffic level (Perraton et al. 2010b). While moving towards Balance Mix Design specifications in North America is a positive albeit potentially more expensive venture. Current and proposed performance-based design methods do not adequately consider the effects of asphalt cement chemistry and aging on long-term performance.

2.1.2 Asphalt Chemistry

During the refinement of petroleum products, the hydrocarbon-based crude oils are distilled into four classes: light, medium, heavy and residuum. Asphalt cement is one of the heaviest product residues obtained from this process; the "straight-run" or "neat" asphalt cement is relatively soft and chemically inhomogeneous. While neat asphalt cement can be used directly for engineering applications (i.e., road paving, roofing, etc.), the asphalt cement will typically be further blended and processed using air-blowing or production plant oxidization methods. This process is intended to improve the homogeneity and modify the asphalt cement grade (Azimi Alamdary 2019; Lesueur 2009). Asphalt cement is a mix of various macromolecules with different structures, molecular weights (MW) and polarities. Typically, molecules in asphalt cement contain 91 to 99% hydrogen and carbon, with the remaining 1 to 9% being heteroatoms such as sulphur, oxygen or nitrogen (Azimi Alamdary 2019). The major fractions can be classified as either asphaltenes or maltenes based on their solubility in *n*-heptane, as shown in Figure 2-1. Asphaltenes, the *n*-heptane insoluble fraction, are composed of the larger macromolecule and carbenes or carboids, which are a minor fraction of the asphaltenes and are often omitted from conventional chemical analyses. Maltenes, the *n*-heptane soluble fraction of asphalt cement, are composed of saturates, aromatics and resins (Lesueur 2009). These four fractions are commonly denoted through the acronym "SARA" (Saturates-Aromatics-Resins-Asphaltenes). Understanding the contribution of the different SARA fractions is critical to understanding the effect of loading, temperature, and aging on the asphalt cement itself.

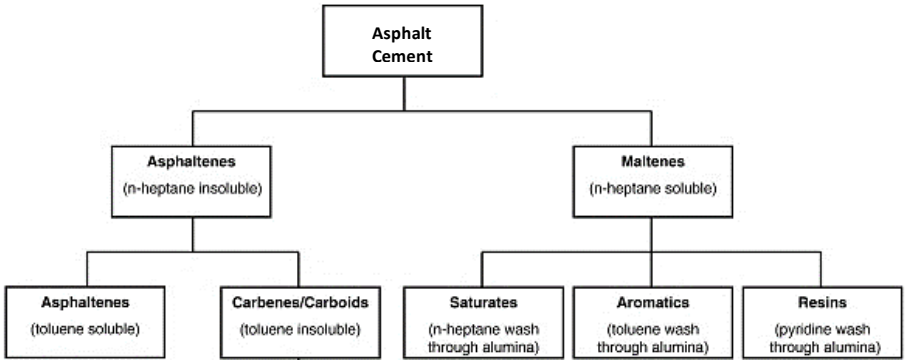

Figure 2-1 The separation of asphalt cement into its constituent fractions based on n-heptane solubility; adapted from (Lesueur 2009).

2.1.3 Asphalt Aging

Aging is the time-associated changes to asphalt cement's chemical structure and composition. The asphalt mixture aging susceptibility and degree of aging depend on the asphalt cement changes, which

can occur at all stages of the pavement life, including during the manufacturing (i.e., the refining and mixing processes), paving/construction and in service (Azimi Alamdary 2019). The high-temperature air-blowing process, as already discussed, is used by asphalt cement suppliers to control premature aging. Soft, non-homogenous asphalt cements can be oxidized to a desired grade by purposefully evaporating some of the lighter aromatics and saturates. After attaining the desired PG grade, the asphalt cement may be stored for long periods in specially designed storage containers that restrict additional age hardening by limiting the environmental oxygen (Lesueur 2009).

The stored asphalt cement is then mixed with aggregates to create the hot asphalt mix. For a typical hot mix asphalt (HMA), the asphalt cement is mixed with the hot aggregates at relatively high temperatures, ranging from 150 to 175°C, in an asphalt plant before being transported to the construction site. The manufacturing process of hot mix asphalt causes significant age hardening as the thin film of asphalt cement coating the aggregates is vastly more reactive oxidative species. The combination of a larger surface area and high processing temperatures leads to the volatilization of low MW components. During placement, the hot mix is still quite susceptible to high-temperature oxidative aging until it cools to ambient temperatures. In service, the asphalt pavement layer is susceptible to aging from environmental and climatic conditions, which have a long-term effect on the physical and mechanical properties of the asphalt cement (Azimi Alamdary 2019; van den Bergh 2011).

2.1.3.1 Asphalt Aging Mechanisms

Asphalt aging is caused by the change in the chemical structure or composition of the asphalt cement through mechanisms such as oxidation, volatilization, physical hardening and syneresis. Oxidation pertains to the oxygen reactivity of the hydrocarbon components in the asphalt cement and the transformation of cyclic structures (i.e., aromatics) into polar aromatics (i.e., resins) and polar aromatics into asphaltenes. The reactivity of methylene (─CH_2) bonds and unsaturated carbon bonds in the aromatic structures generate dicarboxylic anhydrides, carboxylic acids, sulfoxides and ketone groups (through the creation of carbonyl bonds). The polarized groups increase the tendency towards the formation of micellar structures, increasing the viscosity and stiffness of the asphalt cement. Volatilization reduces the relative maltene fraction of the asphalt cement as low molecular weight components evaporate. The volatilization rate is especially high during mixing and placing the hot mix. Steric or physical hardening occurs during the cooling of the HMA, referring to the restructuring of molecules in the asphalt cement and is often characterized by the slow crystallization of waxy

molecules. Syneresis or exudation evaporation occurs when the aggregates absorb oily components, decreasing the fluidity of the asphalt film. Overall, aging causes asphalt cement to become stiffer and more brittle as lighter components are lost over time (Azimi Alamdary 2019; van den Bergh 2011).

2.1.3.2 External Factors Affecting Aging

While the chemical composition and the asphalt source are important internal factors, external factors from the environment and climate also play a role in the aging process. In some climates, the asphalt pavement temperature can be over 20°C higher than the ambient air temperature. At these elevated service temperatures, the oxidative reactivity of hydrocarbon molecules is increased, and low molecular weight molecules have greater mobility leading to a change in the mechanical properties. Due to the exposure to solar radiation, asphalt cements are sensitive to photo-oxidation effects. Photo-oxidation occurs on the surface of the pavement in a small 50 μm region of the asphalt film referred to as the Ultraviolet (UV) penetration zone. Within the UV penetration zone, the UV rays increase the energy of the organic materials leading to unstable molecular structures with a greater affinity to bond with free oxygens and degrade polymer modifiers in the asphalt cement. Moisture and water can increase the deterioration of the asphalt film as the oxidation products are water-soluble. The breakdown of water-soluble products removes the "protective" aged layer leading to further oxidation (Azimi Alamdary 2019). Additional aging factors and mechanisms are listed in Table 2-1.

Table 2-1 Factors that affect asphalt cement aging mechanisms from Azimi Alamdary (2019).

Effect	**Influence by**					**Occurs**	
	Time	Heat	Oxygen	Sunlight	B & γ rays	At Surface	In Mass
Oxidation (in the dark)	X	X	X	-	-	X	-
Photo-oxidation (direct light)	X	X	X	X	-	X	-
Volatilization	X	X	-	-	-	X	X
Photo-oxidation (reflected light)	X	X	X	X	-	X	-
Photochemical (direct light)	X	X	-	X	-	X	-
Photochemical (reflected light)	X	X	-	X	-	X	X
Polymerization	X	X	-	-	-	X	X
Development of the internal structure (i.e., Thixotropy)	X	-	-	-	-	X	X
Exudation of oils (syneresis)	X	X	-	-	-	X	-
Changes caused by nuclear energy	X	X	-	-	X	X	X
Action of water	X	X	X	X	-	X	-
Absorption by solid	X	X	-	-	-	X	X
Adsorption of components at the solid surface	X	X	-	-	-	X	-
Chemical reactions or catalytic effects at the interface	X	X	-	-	-	X	X
Microbiological deterioration	X	X	X	-	-	X	X

2.1.3.3 Laboratory Aging Simulation

Standard aging simulation techniques in the asphalt industry use a combination of high pressure and temperature to simulate the short-term (i.e., considering mixing and placement) and the long-term (i.e.,

occurring during the pavement's service life) aging for both asphalt cements and mixtures. In Superpave mix design, asphalt cements are short-term aged using the Rolling Thin Film Oven Test (RTFOT); this test simulates aging by blowing air on asphalt films at 163°C for 85 minutes. The rheological properties of the RTFO-aged samples are then evaluated on the DSR at high and intermediate temperatures. The Pressure Aging Vessel (PAV) simulates 7 to 10 years of in-service aging by applying high pressure and temperature to RTFO-aged asphalt cement for 20 hours. The temperature of the PAV is set to simulate the climatic conditions of the intended pavement (90°C for colder climates, 100°C for moderate climates, and 110°C for hot climates). PAV-aged material is assessed at low temperatures using the bending beam rheometer (BBR) and direct tension tester (DTT) to assess low-temperature susceptibility to cracking and at intermediate temperatures to assess fatigue performance. Recent research has demonstrated that RTFO and PAV aging do not provide an adequate simulation of age hardening observed in the field; excessively high temperatures and pressures can induce oxidation and polymerization reactions that may not otherwise naturally occur (Azimi Alamdary 2019).

In the early 1990s, the SHRP A-003A development program proposed several basic procedures for simulating low-pressure oxidative mixture aging. Mixture's short-term oven aging (STOA) and long-term oven aging (LTOA), developed through the Strategic Highway Research Program (SHRP) program, became the basis for the current AASHTO (American Association of State Highway Transportation Officials) R30 aging standard. AASHTO R30 STOA requires the loose, uncompacted hot mix to be oxidized in a forced-draft oven at 135°C for two hours, simulating the short-term oxidative hardening during production. AASHTO R30 LTOA requires the continuous heating of a compacted sample in a forced-draft oven at 85°C for 120 hours to simulate approximately five years of aging. As discussed in the previous subsection, factors such as moisture, reactive oxidative species, and solar radiation can have a meaningful impact on the aging process. New long-term aging techniques for compacted mixtures include: the Viennese Aging Procedure (VAPro) which uses different gas reactive mixtures (i.e., pressurized air, ozone, and nitrogen oxides), and the Bespoke Weather Chamber developed at the University of Waterloo, which uses moisture and UV exposure. Both techniques are completed at lower temperatures than the AASHTO R30 test but represent a more realistic aging simulation by replicating atmospheric and climatic conditions (Azimi Alamdary 2019; Mirwald et al. 2020).

2.1.4 Asphalt Modification

As stated in the previous section, the “air blowing” process is one of the most common modification methods, as the controlled oxidation produces a stiffer and more chemically homogenous product. However, asphalt modification encompasses a much broader range of manufacturing techniques and additives that can significantly improve asphalt cement's chemical and mechanical properties.

2.1.4.1 Polymer modification

With the oil crisis of the 1970s, North Americans faced gasoline shortages and by extension, asphalt shortages. This socio-political crisis became the main driving force for asphalt cement modification research in North America with the hope that additives and substitutes would help to reduce the thickness of the asphalt layers thus reducing the cost of the pavement structure. In the 1980s, the first true polymer-modified asphalt (PMA) was used commercially. By the end of the 1980s, due to their increasing use, SHRP began developing the first standards and specifications for PMAs in North America (Zhu et al. 2014).

Polymers can be incorporated into asphalt mixture through “wet” methods (i.e., modifying the asphalt cement itself) using mechanical or chemical/ solvent mixing methods and “dry” methods (i.e. adding the polymer during the mixing stage”). Some polymers will provide low to moderate performance improvements at low concentrations. At ideal polymer concentrations, the asphalt and polymer separate into two interlocking discrete phases: one phase rich in asphalt cement and the other rich in the polymer. These interlocking phases create strong physical connections between asphalt and polymer molecules, improving the mechanical properties of the asphalt. As the concentration of the polymer increases past the ideal, a phase inversion may occur, causing the asphalt to behave more polymer-like, which can impact the workability of the asphalt mixture (Zhu et al. 2014).

Polymer modifiers can be either plastomeric or elastomeric. Plastomers do not provide elasticity but improve early-life strength, which may decrease premature cracking or permanent deformation. Elastomeric modifiers enhance the elasticity and elastic recovery of the mixture after loading but are sensitive to temperature changes (Zhu et al. 2014). Some crystalline polymers like polyethylene (PE) and polypropylene (PP) have poor adhesion in the asphalt cement, presenting both short-term and long-term issues for the mix. In the short-term, the crystallization can create instability in storage or transportation. In the long-term unfavourable phase separation may occur, creating a poorer-performing mixture with lower resistance to permanent deformation (Yildirim 2007; Zhu et al. 2014). Elastomers

are network-forming or cross-linked block polymers like SBS, styrene-butadiene rubber (SBR) and styrene-isoprene-styrene (SIS). Elastomers provide more flexibility to the mixture at lower temperatures while improving stiffness at higher operating temperatures. SBS is one of the most widely used modifiers for asphalt mixtures; the glassy polystyrene blocks account for stiffness increases, while rubbery polybutadiene chains increase asphalt cement elasticity. SBS and other elastomers are generally sensitive to environmental factors such as heat, oxidation and UV radiation due to the presence of weak double and hydrogen bonds in the networks (Zhu et al. 2014). Elastomeric crumb rubber modifiers (CRM) are recycled rubber particles that have been pelletized and added to the asphalt mixture. CRM asphalts can have improved durability and good reflective cracking control when placed as overlays on existing pavements, but properties depend highly on the rubber source (Yildirim 2007). PMAs give pavement engineers a more extensive inventory of materials to choose from when designing roads. However, high cost, aging resistance, storage compatibility and asphalt cement-polymer stability are a concern for short-term and long-term performance (Yildirim 2007; Zhu et al. 2014).

2.1.4.2 Warm Mix Asphalt

The elevated temperatures and greenhouse gas emissions associated with hot mix asphalt production have driven research toward more environmentally sustainable solutions such as Warm Mix Asphalt (WMA). Warm mix additives lower the viscosity of the asphalt cement, facilitating mixing and compaction at temperatures 20 to 55°C lower than traditional HMA production temperatures without inducing significant adverse long-term effects on the pavement performance (Ferrotti et al. 2019). WMA technologies are classified as either chemical, organic or foaming, but production plant foaming technologies and chemical additives are dominant in North America. Aside from lowering the production temperature, WMA technologies also offer a wide range of benefits, such as improved compaction and workability, reduced emissions, longer transport times, improved anti-stripping and decreased short-term associated oxidative age hardening. In 2018, it was estimated that almost 160 million long tons of WMA were produced in the United States alone (Ferrotti et al. 2019; Ragni et al. 2019; Williams et al. 2019).

2.1.4.3 Reclaimed Asphalt and Rejuvenation

Several standard rehabilitation methods generate aged pavement by-products that can be reclaimed and reused as a replacement for virgin material. Reclamation processes remove a portion of the asphalt layer using milling equipment or the entire depth of the asphalt mixture producing the valuable material

referred to as Reclaimed Asphalt Pavement (RAP). RAP can be stockpiled for future use and recycled into new pavements. Due to the aging mechanisms described in Section 2.1.3, the asphalt cement in RAP is very brittle and stiff due to the loss of the lighter oily components. Adding RAP to an asphalt mixture can improve high-temperature rutting performance, reduce raw/virgin material usage, and improve sustainability, but with a trade-off in reduced thermal cracking and fatigue resistance.

For this reason, many agencies place a limit on the use of RAP in certain situations (Mneina and Smith 2019; Ontario Hot Mix Producers Association 1999). Rejuvenators can be added to reconstitute the RAP and improve blending with the virgin asphalt in high RAP mixes. Rejuvenators are commonly produced from refinery base oils (e.g., paraffinic oils, aromatic extracts, etc.), bio-based products (e.g., plat oils and animal fats), waste-derived oils and cationic emulsions containing maltenes. In general, rejuvenators are used to lower the RAP asphalt cement's viscosity and reduce the mix's low-temperature susceptibility. However, determining the optimum dosage of these products is still a significant challenge (Gonzalez-Torre and Norambuena-Contreras 2020; Liao 2023).

2.1.5 Asphalt Mechanical Behaviour and Fatigue

Over the typical 20-year design life of a pavement, a pavement structure will deteriorate due to recurring mechanical stresses caused by vehicle loading and thermal stresses caused by changes in temperature or environment. The asphalt pavement may soften in warm periods, and heavy loading may lead to rutting. When faced with cold temperatures, the pavement may experience intense thermal stresses leading to transverse low temperature/ thermal cracking. However, these failure modes principally occur at the temperature extremes of the asphalt cement. Many pavements will spend a significant percentage of their design life in the intermediate temperature range, where there is a far greater certainty that they will experience failure by fatigue.

Due to the viscoelastic properties of the asphalt mixture, it is temperature and loading rate sensitive. The defining characteristic of viscoelastic material is the phase angle (δ) between the complex stress and the complex strain response of the material in a quasistatic repeated loading. The phase angle ranges from 0 to 90°; at 0°, the asphalt mixture has a purely elastic response, and at 90°, the asphalt mixture is purely viscous. There is a cross-over when the phase lag is 45°, as neither the elastic nor viscous behaviour is dominant. At phase angles greater than 45°, corresponding to higher temperatures and lower loading frequencies, the material behaves as a viscoelastic liquid as the apparent stiffness is low. Contrastingly, the apparent stiffness is high at phase angles below 45°, corresponding to lower

temperatures and higher frequencies. In this state, the material behaves as a viscoelastic solid. The mixture stiffness is characterized through the mechanical parameter, E^*, known as the complex Young's modulus, which is the ratio of the peak stress amplitude to the peak strain amplitude in a single cycle. The norm of the complex modulus, $|E^*|$, is the magnitude of the modulus at a given frequency/temperature pair and is determined as:

$$|E^*| = \sqrt{E'^2 + E''^2} \quad \text{Eqn. 2-1}$$

where E' is the Storage modulus relating to the elastic contribution of stiffness and E'' is the Loss modulus which relates to the viscous portion. The angle between the Loss and Storage modulus vectors is the phase angle and is denoted as δ (Larcher et al. 2015). Through the viscous component, the asphalt experiences an energy loss upon loading. The energy loss is due to the formation of cracks, visco-plastic flow and heat, which are internally generated in the sample and dissipated to the surrounding environment. The dissipated energy (W) in the i^{th} cycle is calculated as:

$$W_i = \pi \tau_{0,i} \gamma_{0,i} sin\delta_i \quad \text{Eqn. 2-2}$$

where $\tau_{0,i}$ and $\gamma_{0,i}$ are the shear stress and strain amplitudes, respectively (Baaj 2002; Santagata et al. 2017).

As depicted in Figure 2-2, fatigue becomes the dominant failure mode in the asphalt layer when the pavement experiences small strain amplitudes for many loading cycles (Baaj 2002). Fatigue cracking is primarily caused by repetitive traffic loading by heavy or multiple axle vehicles such as trucks and buses at intermediate temperatures. Repeated loading conditions introduce compressive stress at the top of the asphalt layer and tensile stresses at the bottom at the interface with the base layer material. When the tensile strain at the bottom of the asphalt layer exceeds the theoretical "critical" tensile strain, cracks may begin to form; as these cracks occur from the bottom of the asphalt layer, they are commonly referred to as "bottom-up" cracks. Additionally, as fatigue cracks begin to propagate towards the surface of the pavement, fine materials (such as sand or silt), moisture or other incompressible materials can infiltrate the crack increasing the rate of deterioration and leading to further weakening of the pavement structure (Canadian Technical Asphalt Association 2018).

In the Superpave mix design system, only the long-term PAV-aged asphalt cement is typically tested for fatigue resistance using an intermediate temperature DSR test. Using the DSR, asphalt cement is tested using a short time sweep at several temperatures (3°C increments) at 1.59 Hz to determine when the fatigue parameter, $G^* \cdot sin\delta$, is less than or equal to 5,000 kPa. The PAV aged critical temperature is extrapolated at the 5,000 kPa value. The fatigue parameter is linked to the viscous dissipated energy

per cycle. A lower fatigue parameter indicates that the asphalt cement is more ductile and elastic, which should allow for greater deformation recovery while dissipating less energy. This parameter has widespread use but does not correlate well with fatigue resistance performance data observed from the field (Canadian Technical Asphalt Association 2018; Hajj and Bhasin 2017).

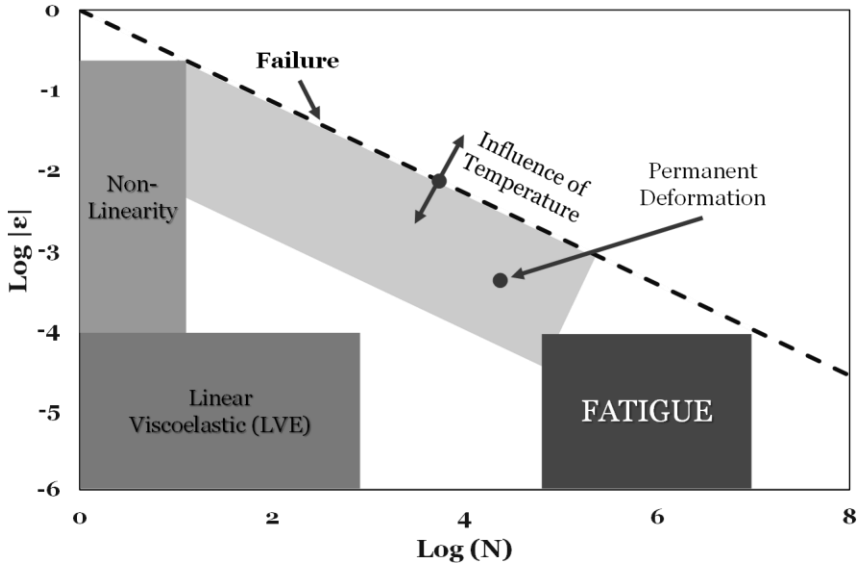

Figure 2-2 Domains of asphalt behaviour recreated from Baaj (2002).

2.2 Introduction to Self-Healing

For much of the 21st century, the prevailing design philosophy has been to develop more robust materials and structures with a greater ability to resist critical failure under the increasingly demanding conditions of modern engineering applications. In recent years, however, researchers have been focusing their efforts on novel materials that can prolong the useful lifespan and delay failure through self-healing (Mauldin and Kessler 2010).

Self-healing materials (SHM) can heal at the microscopic level (i.e., microcracks) or macroscopic level (i.e., healing of large-scale fractures or cracks) using a variety of mechanisms to delay catastrophic failure. Typically, SHMs are classified as employing autonomic and non-autonomic self-healing mechanisms. Autonomic self-healing materials do not require external stimuli to initiate a self-healing event. In contrast, non-autonomic materials will require external intervention to trigger a healing event, typically human or environmental intervention. Non-autonomic self-healing materials are generally less expensive and easier to manufacture compared to autonomic self-healing materials. However, autonomic self-healing mechanisms are more adequately suited for applications where failure

prevention is a priority (i.e., reducing microcrack formation and propagation). Non-autonomic SHMs are more suited for use in material management systems as specific maintenance routines can be devised to target both micro and macro-level cracking (Grabowski and Tasan 2015; Mauldin and Kessler 2010). Table 2-2 below features a collection of autonomic and non-autonomic self-healing mechanisms in the literature categorized by material class. The study of self-healing mechanisms in asphalt and the development of self-healing technologies for pavements presents an environmental and economical solution for the current challenges of the aging road infrastructure.

Table 2-2 Self-healing mechanisms: autonomic vs non-autonomic (*note: SMA in this context refers to shape memory alloy) (Aurilio et al. 2020b).

Material Class	Autonomic Healing	Non-autonomic Healing
Polymer	Microencapsulation Dangling chain diffusion Metal-ligand dissociation/ association Viscoelastic healing Supramolecular assembly	Phase separation Thermally reversible reactions UV initiated
Metal	High T precipitation Low T precipitation NanoSMA*-dispersoids	SMA*-Clamp&melt Solder tubes/capsules Coating agents Electrohealing
Ceramic	Microencapsulation High T oxidation reactions	

2.2.1 Introduction to Asphalt Self-Healing

While in-depth research into self-healing pavements is relatively new, the discovery of healing in asphalt materials can be traced back to almost 60 years ago when several studies observed that the addition of a rest period (i.e., periods of unloading) could improve fatigue life in laboratory tests (Sun et al. 2017; Xu et al. 2018b). In the asphalt mixture, the self-healing properties are solely attributed to the asphalt cement component and its ability to flow to repair microcracks when given sufficient rest periods (Lv et al. 2017). With the invention of new healing technologies for asphalt pavements, it is necessary to properly define "healing", as well as the concept and extent of "healable" fatigue damage. The following terminology for future self-healing studies was proposed by the RILEM Technical Committee on Crack-Healing of Asphalt Pavement Materials (TC 278-CHA) (Leegwater et al. 2020). The definitions are summarized below with a few additional details. These definitions are depicted in Figure 2-3 in the context of an accelerated fatigue test.

- *Damage*: the loss of mechanical properties due to the initiation and propagation of meso- and micro-scale cracks within the asphalt mixture during loading (Leegwater et al. 2020). However,

pavements experience several types of damage and distress (i.e., thermal cracking, rutting, wearing) over their lifetime, healable damage will only be considered through intermediate temperature repeated loading leading to fatigue microcracking. Fracture and ductility testing can be used to evaluate the healing potential of the material. Still, these methods rely on the generation of macroscale discontinuities which are not representative of microcracking occurring during fatigue.

- *Restoration*: the total impairment of mechanical properties that are returned during a rest period; restoration is a combination of two components: recovery and healing (Leegwater et al. 2020).
- *Recovery*: the component of restoration attributed to reversible phenomena in the asphalt caused by cyclic loading observed during laboratory testing (Leegwater et al. 2020); these reversible effects, such as non-linearity, thixotropy and local heating, are temporary bias effects caused by the accelerated testing methods used to study fatigue (Boussabnia et al. 2019).
- *Healing*: the component of the restoration attributed to the closure of non-reversible meso- and microcrack damage; healing reflects a true return of the mechanical properties of the asphalt. Intrinsic healing is the inherent self-healing ability of asphalt cement. In contrast, extrinsic healing is identified as repair attributed to additional phases (i.e., additives) or crack repair technologies (Leegwater et al. 2020).
- *Rest period*: a period of unloading; during this period, it is assumed that the applied stresses are effectively zero. The rest period must be long enough to allow for restoration to occur, as only recovery through reversible effects will be observed during short rest periods (Kim 1999).

2.2.2 Self-Healing Theories and Mechanisms

Wool and O'Connor detailed the first theory for self-healing thermoplastic polymers (Wool and O'Connor 1981). In the original theory, molecules at the crack surface rearrange, and the surfaces approach until contact occurs. After contact, the molecule chains can diffuse across the crack boundary, and healing occurs when there is full integration and randomization in the undamaged polymer matrix. This approach was soon adopted to provide insight into the healing mechanisms in asphalt materials. In literature, three competing mechanisms facilitate the healing of the non-reversible effects of fatigue, including wetting, diffusion and molecular randomization.

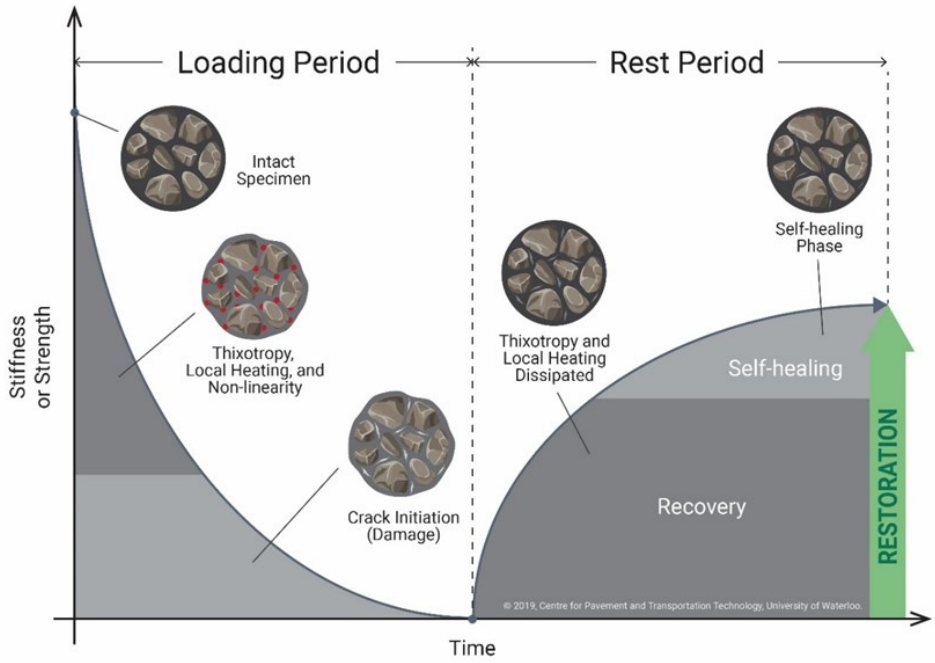

Figure 2-3 The damage and healing process for asphalt materials from Leegwater et al. (2020).

From these mechanisms, several other theories have formed to describe crack healing, including (1) surface energy theory, (2) capillary flow theory, (3) molecular diffusion theory, and (4) the phase field theory. Each theory details the redistribution of material from an area of high concentration (i.e., the asphalt matrix) to an area of low concentration (i.e., a crack or void). Surface energy theory is characterized by the flow of asphalt cement to decrease the high surface energy at the free crack surface. Capillary flow theory describes a flowable asphalt cement transported through capillary action to reduce the pressure at a crack tip. Molecular diffusion theory simply relates healing as the diffusion of asphalt cement from the asphalt matrix to the crack due to Einsteinian diffusion; the subsequent return of mechanical properties is attributed to molecular randomization after longer periods. Finally, the phase field theory postulates that interfaces between different phases within the asphalt material are likely to be zones of microcrack formation; with the addition of thermal or mechanical energy, the phases can rearrange themselves to a new configuration, thus, reducing the distribution of microcracks and recover material integrity (Bhasin et al. 2008; Sun et al. 2017; Xu et al. 2018b; Varma et al. 2021).

2.2.3 Factors affecting Intrinsic Self-Healing

The following subsection details factors that affect the intrinsic healing ability of the asphalt cement itself, including rest period duration, rest period temperature, asphalt cement chemistry, aging, moisture, and the presence of conventional additives.

2.2.3.1 Rest Period Duration and Temperature

It is widely accepted that longer rest periods and higher temperatures significantly improve the intrinsic self-healing ability of asphalt cement (Baaj et al. 2018; Leegwater et al. 2018; Tabaković and Schlangen 2015). The viscoelastic nature of the asphalt itself influences the kinetics of the intrinsic healing process. At intermediate temperatures, evidence shows that longer rest periods improve healing compared to short rest periods, as the mechanisms required to ensure complete repair are very slow. At elevated temperatures, asphalt cement self-healing can be instantaneous, and at lower temperatures, self-healing is hindered by low rates of molecular diffusion; rest periods below 10°C show a significant decrease in the recovery potential of asphalt mixtures tested in tension-compression tests (Baaj et al. 2018; Sun et al. 2016). In accelerated healing tests in the laboratory, rest periods can be implemented as "intermittent rest periods" or "prolonged rest intervals." When using intermittent rest periods, specimens are loaded for short periods (approximately 0.1 seconds) followed by 1-, 5- or 10-second periods of unloading. This type of rest period is typically only used in fatigue-healing tests. This loading-unloading scheme is theorized to accurately reflect the in-situ fatigue-healing phenomenon (Witczak et al. 2013). Rest interval healing tests are composed of uninterrupted loading tests followed by longer periods of unloading ranging from several minutes to several days; unlike the intermittent rest periods, longer rest intervals have been employed in both fatigue and fracture-based healing tests (Baaj 2003; Baaj et al. 2018; Varma et al. 2021).

2.2.3.2 Asphalt Chemistry

While asphalt cement chemistry is essential to the mechanical properties and aging, understanding differences in chemistry is also fundamental to understanding healing. The ratio of asphaltenes and maltenes in asphalt cement can affect healing. The colloidal instability index (CII) relates the ratio of asphaltenes and saturates to resins and aromatics; it is calculated as follows,

$$CII = \frac{As + S}{R + Ar} \quad \text{Eqn. 2-3}$$

where *As* is the weight percent of asphaltenes, *S* is the weight percent of saturates, *R* is the weight percent of resins, and *Ar* is the weight percent of aromatics. The CII of the cement can give insight into the peptizing ability. Increased small molecule (i.e., R and Ar) content gives rise to smaller CII values, indicating that the colloidal structure is more stable and flowable, corresponding to higher rates of self-healing as an asphalt cement with a less branched, linear molecular structure has better molecular mobility. Asphalt cements with a smaller CII value are softer which led to the conclusion that softer asphalt cements have superior healing potential (Kim et al. 1990; Sun et al. 2017).

2.2.3.3 Aging and Moisture

As discussed previously in Subsection 2.1.3.2, oxidative aging, exposure to ultraviolet (UV) light, and moisture can lead to changes in the asphalt chemistry, ultimately impacting long-term performance. The changes in chemistry over time lead to a stiffening of the asphalt cement, which creates a more brittle material at intermediate temperatures, negatively impacting the long-term fatigue resistance of the HMA layer and the intrinsic healing ability (Azimi Alamdary 2019; Baaj et al. 2005). Using the Binder Bond Strength (BBS) test, Lv et al. (Lv et al. 2017) observed that Rolling Thin Film Oven (RTFO) and Pressure Aging Vessel (PAV) samples show lower self-healing due to age hardening and oxidation. Still, the reduced healing potential was not reported to be significant. Wu et al. (Wu et al. 2019) irradiated loose asphalt mix under UV lamps in a temperature-controlled chamber for 7, 14 and 28 days. The asphalt cement was extracted using 99% purity trichloroethylene, and the residue obtained was analyzed using Fourier Transform Infrared (FTIR) spectroscopy. It was observed that with increasing durations of UV irradiation, carbonyl and sulfoxide content as well as the proportion of oxygen-containing functional groups; irradiated samples demonstrated poorer fatigue resistance and healing ability. Moisture-induced damage can also hinder the intrinsic healing ability significantly for unaged asphalt cements. In the short-term, the aggregates in the asphalt mixture are highly attracted to water molecules causing saturation at crack surfaces disrupting molecular motion. In the long-term moisture damage can lower the cement fracture bond energy required to initiate cracking leading to decreased susceptibility to fracture, however, crack healing of water-saturated asphalt mixtures is significantly reduced due to similar decreases in the mobility of molecules in the asphalt cement.

2.2.3.4 Effect of Conventional Additives

Stiffer cements are used in warmer climates where rutting is a concern or in locations where the pavement is likely to experience heavy or slow-moving traffic. While more appropriate in these conditions, stiffness modified (i.e., SBS, reclaimed asphalt pavement or air-refined) cements have been reported to have lower rates of self-healing (Lv et al. 2017). Often there is conflicting information about the healing ability of SBS-modified asphalt cements. Little et al. evaluated the healing ability of five different asphalt cement sources with SBS modification. It was observed that SBS reduced the healing index in only two of the five samples. Molecular dynamics simulations performed by Sun et al. (Sun et al. 2016) found that SBS-modified asphalt cement has a greater ability to heal instantaneously but the process requires more energy (i.e., higher temperature). While the true healing ability of SBS-modified asphalt cements is not well defined, it has been shown that fatigue resistance and recovery ability can be improved with the addition of SBS when tested at higher microstrain values (Baaj et al. 2018; Kim 1999; Sun et al. 2016).

In the works by Shirzad et al. (Shirzad et al. 2019b; a), the addition of reclaimed asphalt pavement (RAP) and reclaimed asphalt shingles (RAS) both lead to substantial increases in the stiffness of the extracted cement. The addition of recycled materials into the mix resulted in significantly lower recovery when allowed to rest at room temperature. More significantly, the recycled materials decrease the ability of the asphalt cement to recover even when the rest period was conducted at higher temperatures (e.g., 50°C) as the introduction of larger, oxidized asphalt molecules reduces the overall molecular mobility of the blended asphalt cements. Kie Badroodi et al. (2020) in high RAP content warm mixes (up to 100% RAP) with 2% Sasobit and 7% nanosilica. Badroodi et al. tested the warm mixes using the 4-point bending beam fatigue test with a 24-hour rest period between loading phases. Based on their study, warm mixes containing higher RAP contents exhibited greater flexural stiffness but an overall lower ability to recover flexural stiffness after rest (Kie Badroodi et al. 2020). Alternatively, Pan et al. (Pan et al. 2018) investigated the softening effect of two rejuvenating oils (e.g., sunflower-based cooking oil and an aromatic oil), two emulsions made using those same oils as well as a resin-rich maltene-based emulsion on laboratory-aged asphalt. The additives were employed to enhance the healing through softening, thus increasing the molecular mobility of the aged asphalt cement. It was observed that oils as healing agents had better performance compared to the emulsions created from the same oil. It was also observed that strength recovery was initially lower partly due to the softening effect, but long-term healing was much improved. Liu et al. (2022) investigated the use

of both waste engine oil (WEO) and polyphosphoric acid (PPA) in asphalt cement. In loading-rest-loading time sweep tests, the addition of 6% WEO/PPA was shown to extend the healing time of the modified binders (Liu et al. 2022).

2.3 Self-healing Technologies for Asphalt

Qiu et al. (2009) posed several requirements of the ideal self-healing technology, including (1) compatibility with asphalt cement, (2) stability at mixing temperatures for conventional HMAs, (3) durability during construction, (4) healing in a reasonable temperature range (i.e., from -30 to 70°C), and (5) be able to heal multiple times through the pavement lifespan (Qiu et al. 2009). These requirements can be used as an initial framework to evaluate existing self-healing technologies; however, manufacturability, cost, and potential health risks should also be considered for new technologies. This section will detail several extrinsic technologies, including capsule-based healing, hollow fibre and vascular network healing, secondary self-healing polymer phases, molecular interdiffusion (e.g., microwave and induction heating methods), and nanoparticle modification (Leegwater et al. 2020; Qiu et al. 2009). Figure 2-4 below demonstrates four examples of these technologies and their crack-healing mechanisms.

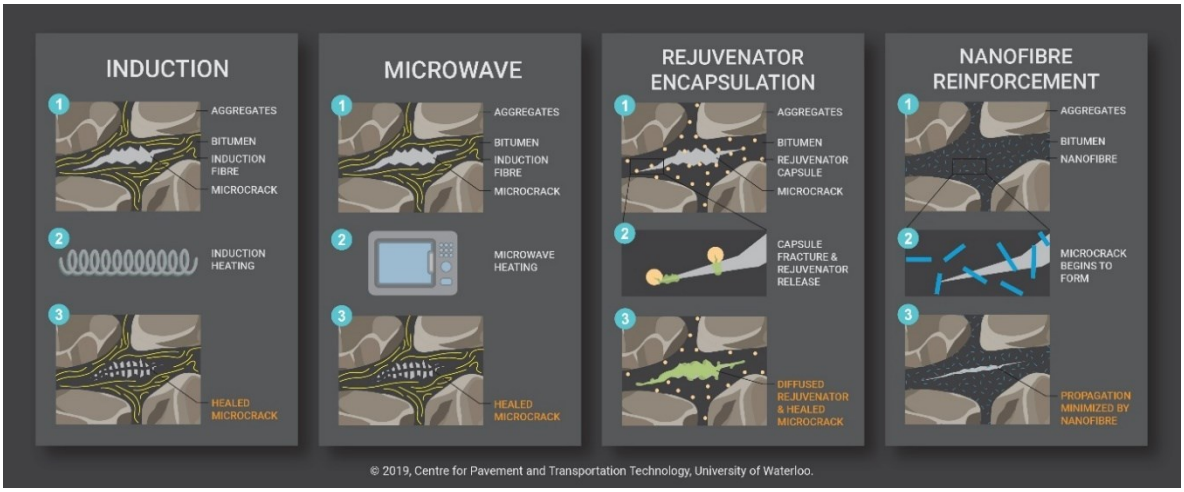

Figure 2-4 Existing extrinsic self-healing technologies for asphalt materials from Leegwater et al. (2020).

2.3.1 Molecular Interdiffusion

Molecular interdiffusion methods require external stimuli in the form of microwaves or an induced current to heat conductive components (e.g., metal fibres, conductive particles, etc.) in the asphalt mixture. In the induction heating method, magnetic fields generated above the pavement induce eddy

currents in the electromagnetically conductive particles; the resistance to the eddy current generates heat which is dissipated to the asphalt matrix (Jahanbakhsh et al. 2018; Tabaković and Schlangen 2015). Microwave heating, unlike induction heating, can have a dual effect on the asphalt mixture; microwaves can induce healing by (1) increasing the mobility of highly polar molecules in the asphalt cement and (2) reflecting and radiating heat via metallic particles in the mix. In both methods, the excitation of these particles softens the asphalt cement and increases its volume, allowing it to fill cracks. After filling, the molecules can diffuse across crack wall surfaces into the surrounding asphalt matrix, improving cohesion. After the pavement cools, the healed asphalt exhibits an improvement in mechanical properties. The primary benefit of these techniques is the repeatability over the life of the pavement. However, the effectiveness of molecular interdiffusion techniques is limited based on crack size. Molecular interdiffusion techniques can also prematurely age the asphalt cement leading to increased stiffness and poorer late-life healing ability (Liu et al. 2012; Xu et al. 2018a).

In previous studies, asphalt mixes were modified with metallic waste products, including Hot Pour steel slag (HPSS), Hot braised steel slag (HBSS) and iron slag (IS). A study by Lyu et al. (2020) demonstrated that asphalt mixtures containing up to 60% aggregate replacement could attain uniform heating (up to 90°C) with as little as 30 seconds of irradiation. From crack healing tests, the 60% HBSS asphalt mixtures had 40% greater healing ability after seven fracture-healing cycles compared to the unmodified mix (Lyu et al. 2021). Fakhri et al. (2020) added scrap metal additives (i.e., steel shavings and recycled tire steel fibres) to warm asphalt mixes with a copper slag filler. Mixes were fractured using the semi-circular bend (SCB) test at -20°C and allowed to return to room temperature. Once at room temperature, the mixes were heated in a microwave for 20 to 40 seconds. Results showed that the mixes containing only copper slag could be an effective solution to improve healing as mixes containing steel fibres and shavings required higher optimum asphalt cement content and had poorer heat distribution (Fakhri et al. 2020). Concha and Norambuena-Contreras (2020) extended this technology beyond simple healing to determine if self-healing asphalt mixtures containing steel-wool fibres could be used as “solar collectors” (Concha and Norambuena-Contreras 2020).

2.3.2 Healing Structures Containing Healing Agents

There are three types of healing structures: microcapsules, hollow fibres, and vascular networks. Structures containing healing agents are a single-use healing technology; they can be beneficial to the matrix material as they can fill cracks and delay crack propagation, but their effectiveness is limited to

early-life healing. In pavements, the liquid healing agent may take the form of polymer resins or rejuvenators.

Microcapsules are composed of hollow-sphere shells ranging in size from hundreds of nanometres to a few millimetres containing a liquid core. When cracks propagate through the matrix material, the microcapsules rupture, releasing a liquid healing agent. After release, the healing agent is drawn into microcracks through capillary pressure. As such, the hollow, brittle shell structure must be sufficiently thick to shield the core when processing the material but sufficiently thin to release the healing agent when the material fractures under loading. Capsules used for self-healing asphalt mixtures can rupture during production (i.e., mixing and compaction), and the empty shell becomes a void that can weaken the mixture. The premature release of rejuvenator healing agents may also result in premature softening of the pavement (Mauldin and Kessler 2010; Qiu 2012; Qiu et al. 2009; Xu et al. 2018a). It has been found that microcapsules with a mean size below 10 μm tend to coalesce due to electrostatic attraction (Tabaković and Schlangen 2015).

Garcia et al. (2015) used porous sand with an average size greater than 1 mm to absorb a rejuvenator; the capsules were then covered in an epoxy-cement shell to contain the liquid core. Upon the fracturing of the epoxy-cement shell, the rejuvenator is released, allowing for the aged binder to recover some of its mechanical properties. Su et al. created microcapsules from in situ polymerized methanol-melamine-formaldehyde (MMF) containing a rejuvenator. It was determined that MMF microcapsules had an ideal size range of 20 – 50 μm, and capsules above 100 μm tended to fracture prematurely due to squeezing rupture. Similarly, MMF microcapsules were found to withstand the mixing and heating process up to 200 ºC without rupturing prematurely but pose a potential environmental hazard through leaching (Garcia et al. 2015). Yang et al. (2021) investigated the use of urea formaldehyde-epoxy (UFE) resin microcapsules in SBS-modified asphalt binders. Healing was evaluated by cutting ductility test specimens with a razor blade and loading the specimen after 4 hours of healing. Yang et al. observed that approximately 28% of the ductility was recoverable using a dosage of 0.4% UFE microcapsules by weight of the asphalt cement (compared to only 9.3% recovery in the SBS modified binder without the UFE microcapsules) (Yang et al. 2021). Alpizar-Reyes et al. (2022) generated microcapsules from the biobased spores using defatting. The empty sporopollenin capsules were then filled using cold-pressed sunflower oil. Healing was observed in fractured PAV-aged specimens using inverted fluorescence microscopy; healing efficiency was quantified by the visual observation of microcrack closure over time (Alpizar-Reyes et al. 2022).

Calcium alginate is a biopolymer stored in brown algae, making it an environmentally friendly and widespread alternative microcapsule material (Xu et al. 2018b, 2019). Inozemtcev and Korolev produced calcium-alginate microcapsules derived from the sodium salt of alginic acid. The calcium-alginate microcapsules were created by the drying and breaking of an alginate emulsion to produce microspheres containing sunflower oil as a reducing agent (Inozemtcev and Korolev 2018). Xu et al. (2019) optimized calcium alginate capsules and found that a ratio of 30% alginate to 70% rejuvenator was very effective. The capsules are porous with a honeycomb structure, allowing for increased mechanical and thermal resistance and improved absorption of the rejuvenating agent. Asphalt mixtures containing the calcium-alginate capsules saw a 40% restoration in bending strength, while the unmodified mixture experience only 4% restoration (Xu et al. 2018b, 2019).

Hollow fibres themselves can be made from glasses or alginates. There are several methods to produce these structures, but they can be challenging to manufacture and are easily damaged during the mixing or construction process, decreasing the overall effectiveness of healing. Shu et al. (2018) created continuous alginate-silica fibres using a co-axial extrusion technique and containing a rejuvenating agent. After cross-linking the continuous fibre using a calcium chloride solution, the self-healing fibre was cut into shorter fibres with a length of approximately 1 cm. The rejuvenating fibres were added after the asphalt cement was mixed with the aggregates and fillers to ensure adequate dispersion. Asphalt mixes with and without the fibres were monotonically loaded until failure using a 3-point bending set up at -10 °C, allowed to heal at room temperature for 48 hours and then subsequently loaded to failure. Using this technique, the crack healing of the modified asphalt mix improved by approximately 19% compared to the unmodified reference mix (Shu et al. 2018). In a follow-up study by Shu et al (2020), calcium alginate/SiO_2 composite fibres containing sunflower oil were synthesized using a similar manufacturing process. After undergoing fracture under the same 3-point bending setup, specimens were allowed to be subjected to 24 hours of dry conditioning or submerged/wet conditioning using different media (i.e., deionized water, an acidic solution, an alkali solution and a salt solution) to evaluate the effect of harsh environmental conditions of the integrity of the healing fibres. After treatment, both the mixes with and without the healing fibres were allowed to heal for up to 5 days at temperatures ranging from 20 to 40°C before retesting. It was observed that the single day immersion treatment did not significantly affect the healing ability of the asphalt mixture, and healing was improved by the presence of the healing fibres. It was also demonstrated that the healing effect was

increased in solutions containing sodium ions (Na^+) as the ions promoted a de-cross-linking effect allowing more oil to diffuse into the mix (Shu et al. 2020).

In general, the relative ease of manufacturing microcapsules and hollow fibres has made them the dominant technology in producing self-healing asphalt mixtures containing healing structures. Vascular self-healing materials, composed of large-scale microchannel networks throughout the matrix material, have been used in other self-healing materials but are significantly more challenging to implement in an asphalt mix. Ensuring the integrity of this network during the construction process is a significant hurdle; as a result, very little research has been focused on this method for asphalt materials (Bekas et al. 2016; Shu et al. 2018; Tabaković and Schlangen 2015).

2.3.3 Secondary Self-Healing Polymer Phases

Secondary healing polymer phases are an exciting concept for self-healing asphalt research because they can potentially have multiple autonomic healing events at ambient temperatures. Mixes containing secondary healing polymer phases in the binder are typically easier to manufacture compared to encapsulated healing structures, as they can be blended directly into the asphalt cement. Qiu (2012) evaluated the self-healing of asphalt cements modified with ionomers and supramolecular rubbers (SMR). Ionomers are resins capable of healing through reversible ionic bonds while supramolecular rubbers utilize reversible hydrogen bonding to heal cracks (Qiu 2012). In the work by Qiu, it was observed that ionomer-modified asphalt materials exhibited similar healing compared to the unmodified asphalt, but SMR-modified asphalt experienced lower healing due to poor compatibility with the asphalt cement (Bekas et al. 2016; Khan et al. 2018). Shirzad et al. (Shirzad et al. 2019b; a) blended a UV-activated self-healing polymer, oxetane-substituted chitosan-polyurethane (OXE-CHI-PUR), into the asphalt cement. Irradiating the OXE-CHI-PUR modified samples for 48 hours under UV lighting after fracture tests demonstrated improved healing compared to the neat asphalt, but healing decreased when co-blended into an SBS-modified asphalt cement possibly due to unfavourable interactions between the two polymers.

Lyu et al. (2021) modified asphalt binders using diselenide-crosslinked polyurethane elastomer (DCP); DCP is produced from the two-step polymerization of polypropylene glycol and isophorone diisocyanate. Within the diselenide bonds are reversibly formed, dynamic covalent bonds that can metathesize after cleavage or fracture. Lyu et al. demonstrated that the DCP-modified binder had improved fracture and fatigue healing ability compared to the unmodified asphalt cement; this effect

was even more significant at elevated healing temperatures (Lyu et al. 2021). Similarly, in Aurilio (2020) work, polydimethylsiloxane (PDMS) was blended into PG 58-28 asphalt cement. The PDMS used in this study contained reversible covalent and non-covalent bonds that enabled potential improvements in intrinsic self-healing ability and elastomeric behaviour (Aurilio 2020).

2.3.4 Nanoparticle Modification

Nanoparticles are any material that ranges from 1 to 100 nm in size; due to their inherently high specific surface area, they exhibit exceptional chemical (i.e., corrosion resistance, electrical conductivity, etc.) and mechanical properties. When used as an asphalt cement modifier, nanoparticles increase the stiffness, which can improve rutting resistance, and nanofibers can act as nano-reinforcement impeding crack propagation. Nanosilica, nanocarbon allotropes (i.e., carbon nanotubes, graphene nanoplatelets, graphite nanofibers, etc.), nanoclays, and rubber nanopowders are commonly used in asphalt modification. When adequately dispersed into the asphalt cement, Amin and Esmail (Amin and Esmail 2017) observed that asphalt mixtures containing nanosilica had improved healing compared to unmodified mixtures. The nanosilica particles could "fasten" the microcrack allowing more time for diffusion across crack surfaces in the asphalt cement. It was also observed that 3% was the optimal nanosilica concentration for healing; at concentrations greater than 3%, healing is negatively affected as the nanoparticle behaves as a nanofiller limiting molecular mobility (Amin and Esmail 2017; Qiu 2012). Nanosilica particles were also used by Kie Badroodi et al. (2020) in high RAP content warm mixes (up to 100% RAP) with 2% Sasobit. Kie Badroodi et al. tested mixes containing up to 7% nanosilica in the 4-point bending beam test (400 and 800 microstrains) with 24-hour rest periods between loading phases. Based on their study, warm mixes containing 5% nanosilica were found to promote the highest recovery of flexural stiffness after rest for both strain levels (Kie Badroodi et al. 2020). Khavandi Khiavi and Asadi (2022) tested the healing ability of mixes containing nano-graphite powders irradiated with microwaves. Using the indirect tensile (IDT) strength test, mixes were loaded to failure before irradiating specimens for up to 160 seconds and resting for up to 24 hours. With the proposed optimum dosages of nano-graphite, specimens were able to recover approximately 51 to 61% of their original maximum tensile strength under reloading (Khavandi Khiavi and Asadi 2022).

2.4 Self-Healing Characterization

A healing index can be easily defined as the ratio of the material's mechanical properties before damage and after the damage has been healed. Using the before-damage to after-damage ratio, several factors

such as extrinsic mechanisms, additives, asphalt cement aging, rest period duration and temperature have been compared, but there is currently no universal healing index. Several properties have been used to assess the before and after testing properties of neat and modified asphalt cements, including ductility, shear modulus, complex modulus, and strength, to varying degrees of success. However, it should be noted that not all tests create the appropriate "healable" damage, nor do all analysis methods properly isolate the healing phenomenon (Baglieri et al. 2020; Qiu et al. 2009).

2.4.1 Asphalt Cement Healing Tests

Accelerated fatigue tests using the dynamic shear rheometer (DSR) have been the most common tests to characterize asphalt cement self-healing characteristics. DSR-based accelerated fatigue tests appear most in the form of time sweeps or amplitude sweep tests with single or multiple rest periods. Extension/ tensile and adhesion tests are less common but will be discussed briefly in Section 2.4.1.3.

2.4.1.1 Time Sweep tests

Time sweep tests were the first DSR-based tests designed for fatigue characterization of asphalt cement at intermediate temperatures. Time sweeps are typically conducted at a single frequency, temperature and strain level for a desired number of cycles; the desired strain level can be pre-selected or determined from simple linearity tests (Anderson et al. 2001; Bahia et al. 2001). The PoliTO protocol, developed by researchers at the Politecnico di Torino, is a time-sweep healing test with a single rest period (TS-SRP) preformed in strain control mode. The test is conducted at 3% strain at 10 Hz and 20 °C. The test is completed in four stages: (1) a 30-minute conditioning period at low strain to observe steric hardening, (2) a loading phase until a designated decrease in the dissipated energy is observed (i.e., 15, 35, or 50% dissipated energy loss), (3) a 2-hour rest period is conducted at low strain, and (4) a final loading phase until failure. For this test, the failure condition was chosen as 20% of the initial value denoted at the end of the first loading phase. The value, N_{rest}, is determined as the number of loading cycles in the second loading phase (stage 4) required to reach the dissipated energy value at the end of the first loading phase (stage 2). The number of cycles to failure, N_f, is determined as the subtraction of N_{rest} from the total number of loading cycles, $N_{total,}$ in stage 4. The healing index (HI) is then calculated as the ratio between N_{rest} and N_f. This loading diagram can be seen in the plot of the complex shear modulus versus the number of cycles in Figure 2-5 below (Aurilio 2020; Santagata et al. 2013).

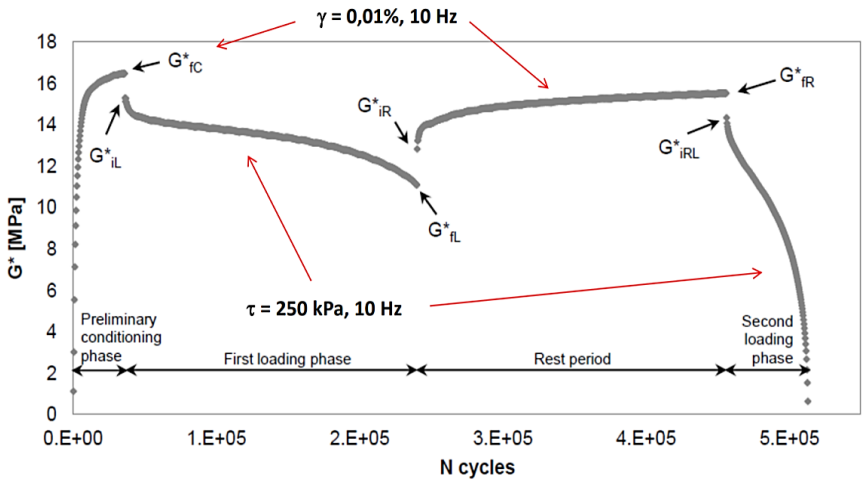

Figure 2-5 PoliTO TS-SRP loading diagram from Santagata et al. (2013).

Li et al. (2020) applied a similar TS-SRP approach but applied the crack length analysis approach proposed in the original work of Hintz (2012). Initially, Li. et al. performed an amplitude sweep from 0.01 to 100% strain to determine a strain amplitude at which a "zero" damage state was maintained. Time sweeps (20 minutes) were then interrupted at 5, 7 and 10% strain amplitude before unloading for various rest periods (Li et al. 2020). Qiu et al. (2020) performed similar TS-SRP tests at 25°C using a single strain amplitude of 8%. The TS-SRP procedure was paired with 'heated' rest periods at the binder's softening point plus 5°C (Qiu et al. 2020). Similar time-sweep type tests were carried out by Gaudenzi et al. on unmodified and modified asphalt cements containing 10% wood pulp extract. In the study by Gaudenzi et al. (Gaudenzi et al. 2020), a time sweep test with multiple 30-minute rest periods (TS-MRP) was employed to characterize self-healing using $|G^*|\sin\delta$ evaluate damage evolution over time. Multiple rest periods aim to simulate in-service pavements' loading and unloading process.

2.4.1.2 Amplitude Sweep Tests

The LASH (Linear Amplitude Sweep with a Healing rest period) test uses the same basic framework and S-VECD analysis procedure outlined in AASHTO TP 101. A continuous LAS (cLAS) test is initially evaluated to calibrate the cohesive failure strain value (S_f). For new undamaged samples, the sample is loaded continuously using a linear amplitude sweep until the strain corresponding to a percentage of the S_f value and a single rest period is applied; Xie et al. (2017) originally proposed using 25, 50, 75 and 125% S_f to assess healing. After the rest period, the test resumes at the same strain amplitude from the first loading phase, and the sample is loaded up to the original 30% of the LAS test

(Xie et al. 2017). The healing index, $\%H_S$, is calculated using the change in damage parameter from the first and second loading phases. The $\%H_S$ is calculated as follows,

$$\%H_s = \frac{(S_1 - S_2)}{S_1} \cdot 100 \qquad \text{Eqn. 2-4}$$

where S_1 is the first loading period damage parameter, and S_2 is the second loading phase damage, as depicted in Figure 2-6 (Aurilio 2020; Xie et al. 2017). In more recent adaptations of the LASH test (Asadi and Tabatabaee 2020; Aurilio 2020; Aurilio et al. 2020c; Baglieri et al. 2018; Chen and Wang 2020; Wang et al. 2018), the selection of the failure strain amplitude produced conflicting results and trends, thus, demonstrating the need to standardize the methodology of LAS-based healing tests.

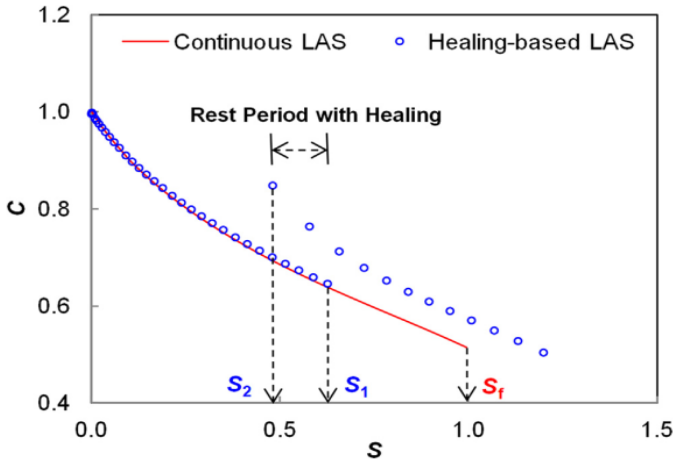

Figure 2-6 Pseudo-stiffness (C) vs damage parameter (S) for the original LASH Test incorporating the cohesive failure damage level, S_f, from Xie et al. (2017).

2.4.1.3 Tension-Based/ Adhesion Tests

Like DSR-based healing tests, binder bond strength (BBS) test specimens are prepared by pouring liquid asphalt into a silicon mould, and a metal stub is placed on top; as the asphalt cools, it adheres to the stub. According to AASHTO TP 91, the BBS specimen is loaded in tension until the stub is removed due to adhesive failure and the pull-off tensile strength (POTS) is measured. Traditionally, this test has been used to quantify the adhesion between binders and different substrates, but several studies have adopted this technique for adhesive healing tests (Huang et al. 2016; Lv et al. 2017). Lv et al. (2017) tested the healing ability of unmodified and SBS-modified asphalt cements in this setup. In the initial study, specimens were cured at room temperature before being submerged in water at elevated temperatures (i.e., 40°C) to stimulate potential adhesive failure. After the initial loading to failure, the

stubs were replaced without applying pressure on the sample and allowed to rest for an additional 24 hours submerged in water before retesting. Healing was evaluated by measuring the ratio of the initial and after-rest POTS (Huang et al. 2016; Lv et al. 2017).

Leegwater et al. (2018) produced a DSR-based extension healing test to evaluate the effect of different boundary conditions/crack geometries on the self-healing behaviour of asphalt cements. Figure 2-7 below shows that two asphalt cement cylinders were assembled with a silicon paper ring placed along the outer diameter. The silicon ring limits the contact at the asphalt specimens' outer edges, simulating a discontinuity or macrocrack within the asphalt cement. Healing could then be stimulated in two ways: (1) by increasing the rest/ contact time of the two cylindrical sections and (2) by applying different levels of normal force using the actuation of the upper DSR plate. After the appropriate contact time (e.g. 1 hour), direct tensile loading was conducted by increasing the gap height between the two plates using a controlled loading scheme and measuring the tensile strength of the healed specimens. Leegwater et al. observed that progressively increasing the normal force increased the maximum measured tensile strength of the specimens for the same contact time. This demonstrated that the compressive load was a significant factor in the cohesive healing of asphalt cement (Leegwater et al. 2018).

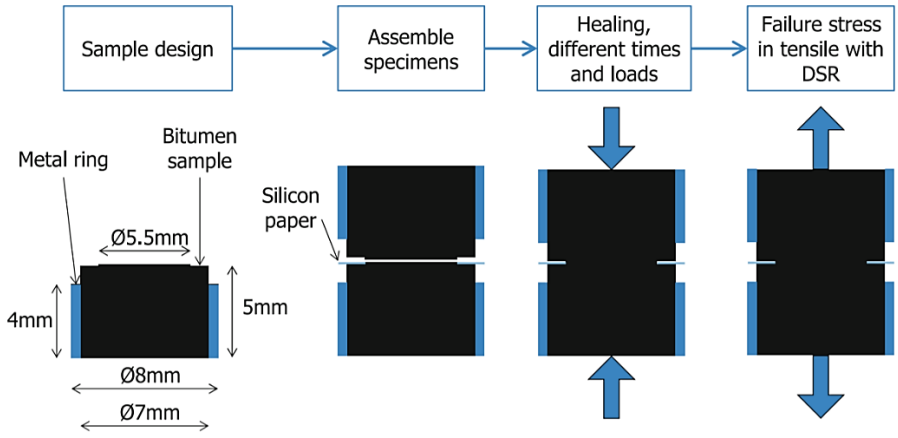

Figure 2-7 Direct-tension healing test schematic from (Leegwater et al. 2018).

Pérez-Jiménez et al. (2012) applied a cyclic uniaxial tension-compression test on cylindrical unaged and RTFO-aged asphalt cement samples. A sinusoidal displacement was applied at 10 Hz in the strain-controlled mode in the form of time sweep tests, increasing amplitude sweeps as well as “up & down” amplitude sweeps at 10°C. In this work, a 30-minute rest period was only applied to the up & down

test specimens after one up-down cycle. In the up & down amplitude sweeps, an increase in the strain semi-amplitude resulted in a significant and sudden increase in the dissipated energy, but that dissipated energy eventually stabilized at a value near that seen in time sweep tests performed at the same strain amplitude. The researchers observed that binders completely recovered during the rest periods and that this recovery rate is much faster when a mechanical load is applied to the specimen (Pérez-Jiménez et al. 2012).

2.4.2 Asphalt Mixture Healing Tests

A wide variety of accelerated fatigue tests such as flexural bending (3-Point, 4-Point, etc.), tension-compression, and the indirect tensile test (IDT) have been used for evaluating self-healing of microcrack damage in asphalt mixtures. Flexural fracture tests such as the semi-circular bend (SCB) test and the Beam-on-elastic-foundation (BEOF) test have also been used to characterize the macroscale crack healing potential of asphalt mixes.

2.4.2.1 Accelerated fatigue tests

In NCHRP Report 762, Witczak et al. (2013) explored the relationship between the theoretical fatigue limit of HMA and its ability to heal using the 4-Point Bending set-up. Fatigue beams were loaded sinusoidally for 0.1 seconds, followed by 1-, 5- or 10-second rest periods. For tests with rest periods, samples were only loaded up to 20,000 cycles, and the fatigue life was extrapolated to 200,000 cycles to compare to samples tested without a rest period. It was concluded that any "theoretical fatigue limit" is unique for each mixture depending on the grade of the asphalt cement, level of compaction, testing temperature, the presence of rest periods and even the test method employed (i.e., flexural versus uniaxial fatigue tests); in general, endurance limits were higher for softer binder grades, higher asphalt cement content and mixes with lower air voids. It was also reported that complete healing could occur in 5 to 10 seconds in flexural tests. However, to simulate traffic using very short loading periods, testing was not severe enough to cause lasting fatigue damage, and as a result, only short-term recovery was most likely observed (Witczak et al. 2013). Liu et al. (2012) also used the 4-Point Bending fatigue test to compare the intrinsic healing ability and the enhanced induction healing of porous asphalt mixtures containing reinforcing steel wool fibres. Healing tests were employed at several microstrain levels and rest period temperatures (Liu et al. 2012). Healing (or, more accurately, the restoration) was characterized by the extension of fatigue life after the rest period. The fatigue life extension ratio (FLER) using the 50% reduction in modulus (*Nf50%*) as the failure criteria is calculated as follows,

$$FLER = \frac{\Delta f_i}{f} \quad \text{Eqn. 2-5}$$

where Δf_i is the increase in fatigue life due to a rest period at temperature, T_i, and f is the original fatigue life considered before the rest period (Figure 2-8). The rest period temperature was varied at intermediate temperatures (5 and 20 °C) for all mixes; however, induction-heated samples were quickly heated to a surface temperature of 70, 85 or 100 °C and then cooled to the control temperature before the 18-hour rest period began. When using this method, it was observed that induction heating successfully restores stiffness to the fatigue-damaged beams, and the magnitude and rate of healing for induction-heated samples are greater than the non-heated fatigue beams (Liu et al. 2012).

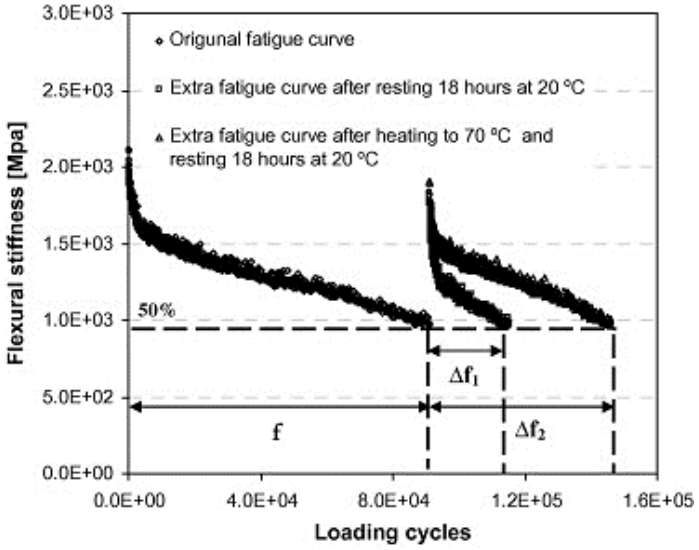

Figure 2-8 Flexural stiffness vs loading cycles from (Liu et al. 2012).

Uniaxial tension-compression (T/C) testing provides more homogenous stress conditions than flexural beam tests and calculating the stresses and strains in the sample do not require external behavioural laws (Boussabnia et al. 2019). In previous research, T/C tests with multiple rest periods were performed by Baaj et al. (2018) to evaluate the restoration potential of several unmodified and modified mixes. Using a 10 Hz sinusoidal excitation at 10°C, samples were loaded to a specific number of cycles and allowed to rest for 24 hours. The temperature was held constant during loading but varied between higher and lower temperatures during the rest periods. From the study, it was noted that the fatigue life increased significantly through the addition of the rest periods when the temperature was 10°C or higher as a minimum temperature is required to allow molecular mobility and rearrangement

of the molecular structure (Aurilio 2020; Baaj et al. 2018). Regardless of the testing method, the main limitation of interrupted fatigue tests such as those completed by Baaj et al. (2018), Witczak et al. (2013) and Liu et al. (2012) is that recovery and healing are not adequately isolated from restoration during rest periods (Liu et al. 2012 Witczak et al. 2013),.

Sun et al. (2019) characterized stone mastic asphalt (SMA), and two Marshall mixes in fatigue-healing tests using an indirect tensile testing (IDT) test setup. Using an intermittent loading scheme akin to the resilient modulus test (AASHTO TP9-94) at -5 and 5°C, short loading pulses were followed by a short rest period (up to 3 seconds). Sun et al. observed that the SMA had a higher resistance to loading, presumably due to improved stone-to-stone contact and a larger film thickness compared to the two Marshal mixes. After fatiguing the specimens, computed tomography (CT) scanning was done to monitor healing in several specimens (Figure 2-9). Both 2D and 3D scans of the asphalt mix samples demonstrated that the overall length of microcracks decreased with increased rest time (Sun et al. 2019). As a note: IDT-style fatigue tests may not be the most appropriate to evaluate fatigue properties as the IDT test set-up induces permanent deformation during the test. Thus, IDT may be considered a cyclic compression test, not a "true" fatigue test (Baaj et al. 2004).

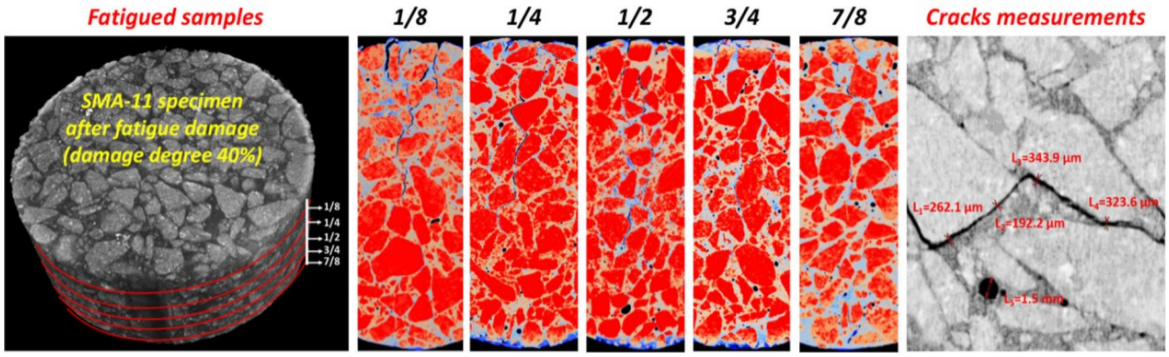

Figure 2-9 Fatigued 3D core section (left) and 2D CT scans at different depths (right) after allowing for healing from (Sun et al. 2019).

2.4.2.2 Fracture-based Healing Tests

Riara et al. (2017) loaded samples to failure at a rate of 0.5 mm/min at -10 °C using the semi-circular bend test set up (Figure 2-10a). After fracture, samples were left to warm to room temperature over approximately 2 hours. After reaching room temperature, the crack surface was brushed with crack healing agents and stored for 1, 2, 4, 8 or 30 days (Riara et al. 2017). Pan et al. (2018) followed a similar procedure to investigate bio-based rejuvenators (i.e., sunflower and aromatic). Using the SCB set-up,

three healing indices were proposed: (1) the strength healing index, (2) the stiffness index, and (3) the fracture energy index. The strength index is the ratio between the original and healed peak strength value, while the stiffness index is the ratio of original and healed stiffness from the pre-peak behaviour of the load-displacement curve. The fracture energy index is the ratio between the original and healed fracture energy derived from the area under the load-displacement curve (Pan et al. 2018; Riara et al. 2017).

The Beam-on-elastic-foundation (BEOF) test was developed at Delft University to evaluate macrocrack healing under a dynamic load. As seen in Figure 2-10b, a notched asphalt beam is glued to a neoprene-covered steel plate and loaded in its centre. In the first phase of the test, monotonic loading is applied at a low rate until the crack opening reaches a target value. After the monotonic loading phase, a dynamic load is applied, and a rest period (e.g., 1, 3 or 24 hours) is allowed after the load is removed. Macrocrack healing was then measured in terms of the before and after rest period apparent stiffness of the beam (Qiu et al. 2012). Fracture-based healing tests can be beneficial to compare a "bulk healing potential", but do not accurately simulate the in-situ damage process. This may lead to a misleading understanding of micro-level mechanisms of healing affected by macrocrack propagation and the fracture of large aggregates.

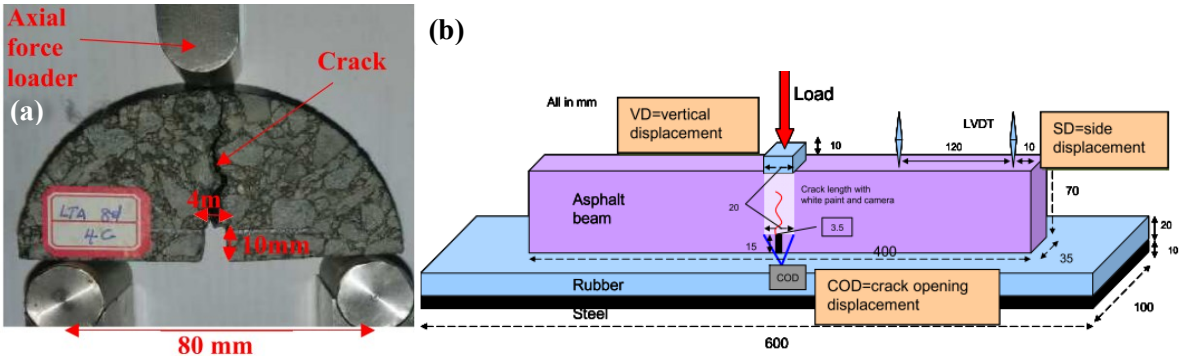

Figure 2-10 (a) SCB test set-up and (b) BEOF test set-up (Qiu et al. 2012; Riara et al. 2017).

2.4.2.3 Non-Destructive Testing for Healing Characterization

In an early study by Daniel and Kim (2001), impact resonance (IR) testing was employed on 3-Point Bending fatigue samples. Initially, the resonant frequencies of undamaged samples were determined at 20°C using the set-up found in Figure 2-11a following ASTM C 215 (2000). Initially, undamaged samples were tested from -15 to 50°C to investigate the effect of temperature on the detection of the

transmitted wave (Daniel and Kim 2001). Afterwards, samples were loaded for 3000 cycles in the 3PB setup and allowed to rest for 4 hours at 20°C or 60°C. Following the rest period, the longitudinal impact resonance was measured before a subsequent 10,000 cycles were applied. Rest periods and loading cycles were alternated until a 50% reduction of the dynamic modulus was measured. Impact resonance testing on undamaged samples demonstrated that the dynamic modulus decreased as temperature increased, indicating that wave attenuation increases as the viscosity of the asphalt cement increases. From fatigue tests, Daniel and Kim observed that the wave velocity of damaged samples was lower than undamaged samples and that there was a noticeable increase in wave velocity following rest periods. From both 3PB and IR, fatigue recovery was more significant for rest periods at higher temperatures but decreased as more rest periods were employed (Daniel and Kim 2001).

Abo-Qudais and Suleiman (2005) employed UPV measurements after testing samples using the Indirect Tensile test (IDT). Before and after applying rest periods, the velocity of a transmitted P-wave was measured, as shown in Figure 2-11b (Abo-Qudais and Suleiman 2005). It was determined that the P-wave velocity decreases due to the presence of microcracks in the sample and that healing is observable from UPV measurements, although there was more significant variation in healing for longer rest periods (i.e., 7 to 14 days). However, it should be noted that the IDT test setup induces permanent deformation during the test. Thus, IDT should be considered a cyclic compression test, not a fatigue test (Abo-Qudais and Suleiman 2005; Baaj et al. 2004; Daniel and Kim 2001; Hofko and Blab 2014).

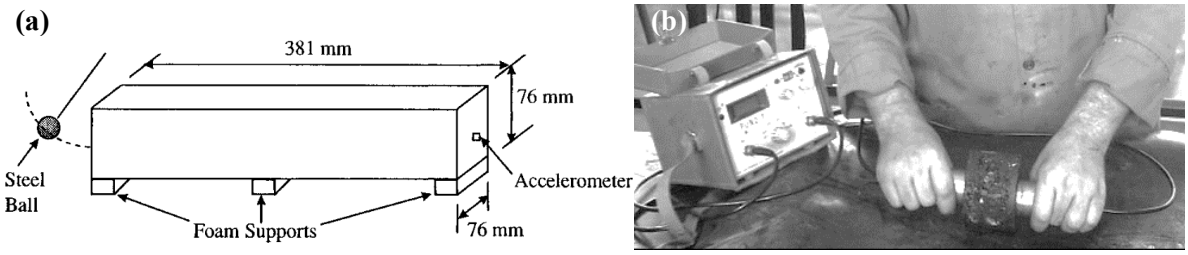

Figure 2-11 (a) Impact resonance method and (b) UPV set up for asphalt healing tests (Abo-Qudais and Suleiman 2005; Daniel and Kim 2001).

2.5 Summary of Research Gaps

From the literature review, the following research gaps can be summarized:

- The asphalt cement component is the major contributing factor to the intrinsic healing ability of asphalt materials. Asphalt cement's mechanical and rheological properties depend highly on

the chemical composition/ crude oil source, asphalt cement aging (oxidation, photo-oxidation, volatilization, etc.) and other factors such as temperature, moisture, and the use of additives/ modifiers. As such, the healing process in asphalt mixtures can be altered by changing factors such as rest period duration, rest period temperature, aging level, moisture, UV exposure, additives, and asphalt cement chemistry.

- The "true" effect on healing by these factors is not well characterized as different studies use different metrics to describe the different phenomena in self-healing tests. The lack of standard tests and analysis for asphalt healing causes discrepancies between healing studies and often leads to misleading conclusions about the effect of healing technologies, additives, and test conditions. The proposed definitions for damage, recovery, healing, and restoration provided by RILEM TC CHA-278 are a good foundation to ensure that future healing investigations can adequately describe the outcomes of next-generation healing tests.
- Accelerated asphalt cement (i.e., time sweeps, amplitude sweeps, etc.) and mixture tests (T/C, 4-point Bending, etc.) adapted for fatigue-healing research often attribute the observable "repair" of damage during rest periods to healing. In many previous studies on healing, it can be said that most research has focused on restoration and not true healing (according to the definitions of RILEM CHA-278). Current fatigue-healing tests primarily evaluate the before and after rest period properties without isolating recovery and healing from the observed restoration. Fracture-based healing tests may not experience "bias" effects typically observed in fatigue tests, but other challenges exist due to the scale and geometry of cracks during testing.
- Non-invasive, non-destructive techniques, which have not been completely explored in asphalt materials testing, may be used to appropriately detect damage and healing through changes in the asphalt dynamic properties during fatigue-healing tests. Measurement of dynamic properties of asphalt presents new challenges in equipment selection (i.e., transducers, data acquisition front ends, etc.) and data analysis (e.g., time-domain vs frequency-domain) as asphalt is a highly attenuative temperature-sensitive composite material. The successful adoption of non-destructive analysis techniques coupled with fatigue-healing testing may provide additional insight into the repair process during rest periods that is unavailable using conventional mechanical testing equipment.

Chapter 3
Research Methodology

3.1 Scope

This chapter describes the scope of work for this thesis; Figure 3-1 below presents a basic flow chart of the three primary phases of the proposed research. Figure 3-1 also details the authour's involvement and contribution to RILEM TC CHA-278 Task Group 2a and 2b (asphalt material self-healing characterization) and Task Group 3 (self-healing modelling). The thesis is separated into two main sections:

- Asphalt cement fatigue and healing characterization (Chapter 4 to Chapter 7) and
- Asphalt mixture fatigue and healing characterization (Chapter 8 to Chapter 10).

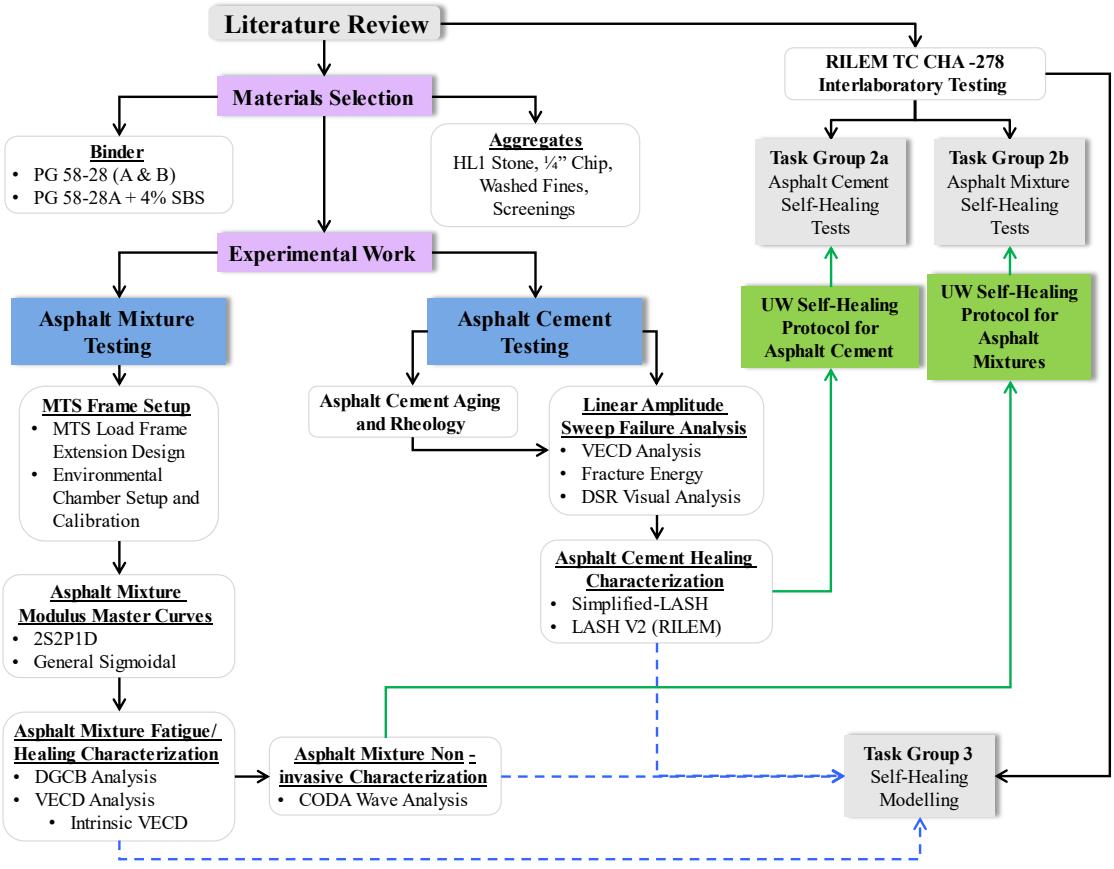

Figure 3-1 A summary of the three proposed stages of research.

3.2 Materials and Methodology

Separate from the authour's involvement in the RILEM technical committee, the results presented in this work were completed using local materials including asphalt cements and aggregates provided through a partnership with Yellowline Asphalt Ltd.

3.2.1 Asphalt Cement and Aggregates

For this research, a locally supplied PG 58-28 asphalt cement is the primary focus for the following investigation and was supplied by Yellowline Asphalt Products Limited. This binder will be investigated in Chapter 4 to Chapter 6 to thoroughly evaluate fatigue and healing tests conducted using the DSR. Starting in Chapter 7, the healing tests will be evaluated using the original PG 58-28 and then accompanied by a PG 58-28 binder from a second source as well as the same PG 58-28 binder modified with 4% SBS. Performance grading results for the two unmodified asphalt cements are provided in Table 3-1 below.

Table 3-1 Performance grading results for the unmodified asphalt cements (PG 58-28 A and B).

Parameter	PG 58-28A			PG 58-28B			AASHTO M320 Spec
	Temp. (°C)	Result	Cont. PG (°C)	Temp. (°C)	Result	Cont. PG (°C)	
Viscosity [Pa·s]	135 165	0.386 0.117	-	135 165	0.267 0.083	-	< 3 Pa·s
$G^*/\sin\delta$ (Unaged) [kPa]	58 64	1.62 0.78	62.0	58 64	1.43 0.66	60.8	≥ 1.0 kPa
$G^*/\sin\delta$ (RTFO-aged) [kPa]	58 64	4.24 1.99	63.2	58 64	3.46 1.54	61.4	≥ 2.2 kPa
$G^*\cdot\sin\delta$ (PAV-aged) [kPa]	16 19	6056 5481	17.4	16 19	7324 4961	19.0	≤ 5000 kPa
BBR Stiffness [MPa]	-18 -24	205 384	-31.6	-18 -24	230 476	-31.8	≤ 300 MPa
BBR m-value	-18 -24	0.341 0.282	-32.2	-18 -24	0.320 0.266	-31.9	≥ 0.3
Continuous Grade	62.0-31.6 (17.4)			60.8-31.8 (19.0)			-

Chapter 9 and Chapter 10 will use the original PG 58-28 binder for fatigue and healing mixture tests. Aggregates sourced from quarries located in Bruce Mines and Marmora, Ontario are used. The locally

sourced aggregates include an HL1 stone, ¼" chip, washed fines (WF) and screenings (Sc); the aggregates are graded following Ontario Provincial Standard Specification (OPSS) provision 1003. The gradation for each aggregate is featured in Table 3-2 and Figure 3-2 below.

Table 3-2 Aggregate gradation by sieve size.

	Percent Passing (%)									
Sieve (mm)	**16**	**12.5**	**9.5**	**4.75**	**2.36**	**1.18**	**0.6**	**0.3**	**0.15**	**0.075**
HL1	100.0	90.5	62.0	4.0	1.0	1.0	0.9	0.9	0.8	0.8
Chip	100.0	100.0	100.0	80.6	20.0	8.6	5.4	4.0	3.3	2.7
WF	100.0	100.0	100.0	99.8	92.0	56.5	34	18.5	9.5	5.0
Sc	100.0	100.0	100.0	96.5	66.5	44.0	31.5	22	16.3	11.5

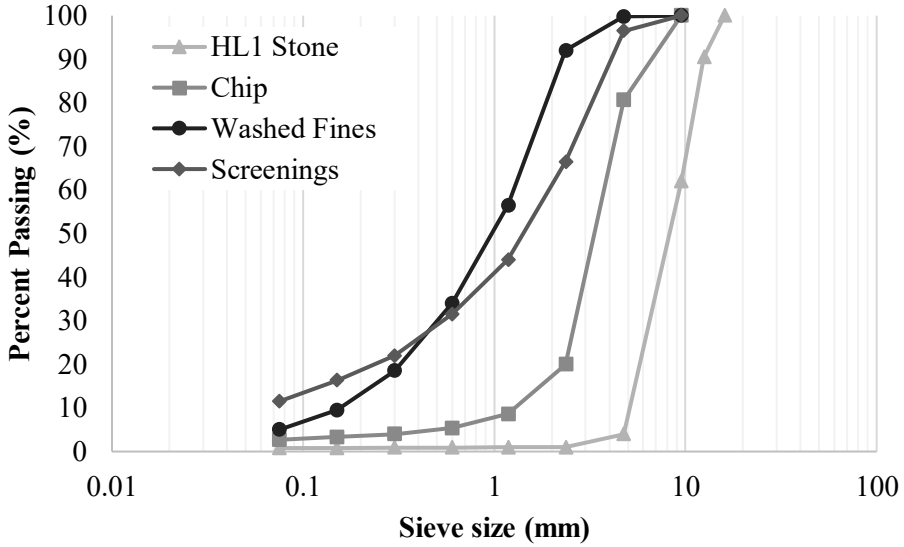

Figure 3-2 Aggregate gradation by source.

3.2.2 Asphalt Mix Design

For this project, a single Superpave SP 12.5 Friction Course (FC) 2 mix design as originally tested in the work of Qabur (2018) and provided through the partnership with Yellowline Asphalt Ltd. Using the aggregate sources described in Section 3.2.1, Table 3-3 contains the job mix formula proportion for this mix. Consequently, the target gradation and Ontario Provincial Standard Specification (OPSS) limits for the SP 12.5 FC2 asphalt mix can be found in Table 3-4 and Figure 3-3 SP12.5 FC2 mix final gradation below. The materials used in this research are representative of the locally available materials which are commonly used for the construction of roads and highways, and they satisfy the Provincial standards for reliability based on the climatic conditions of Ontario, Canada. All mixes studied are

prepared using the same PG 58-28 provided by Yellowline. As per the Superpave volumetric design report, the mix has an optimal asphalt content of 5.2%; specimens are manufactured/ mixed at a temperature of 149°C and then compacted at a temperature of 137°C following the appropriate short-term oven aging specimen conditioning time.

Table 3-3 SP12.5 FC2 aggregate proportions according to the project job mix formula.

Testing Temperature (°C)	Job Mix Formula Proportion	G_{sb}
HL1 Stone	0.43	2.883
¼" Chip	0.13	2.945
Washed Fines	0.27	2.926
Screenings	0.17	2.918
Combined	1.00	2.905

Table 3-4 Aggregate gradations by sieve size for the project SP12.5 FC2 mix.

	Percent Passing (%)									
Sieve (mm)	**16**	**12.5**	**9.5**	**4.75**	**2.36**	**1.18**	**0.6**	**0.3**	**0.15**	**0.075**
OPSS SP12.5 FC2 Specification	-	90.0 - 100.0	45.0 - 90.0	50.0 - 65.0	58.0 - 39.0	-	-	-	-	2.0 - 10.0
Final SP12.5 FC Mix	100.0	96.0	84.0	56.4	40.4	25.8	17.3	11.4	7.8	5.5

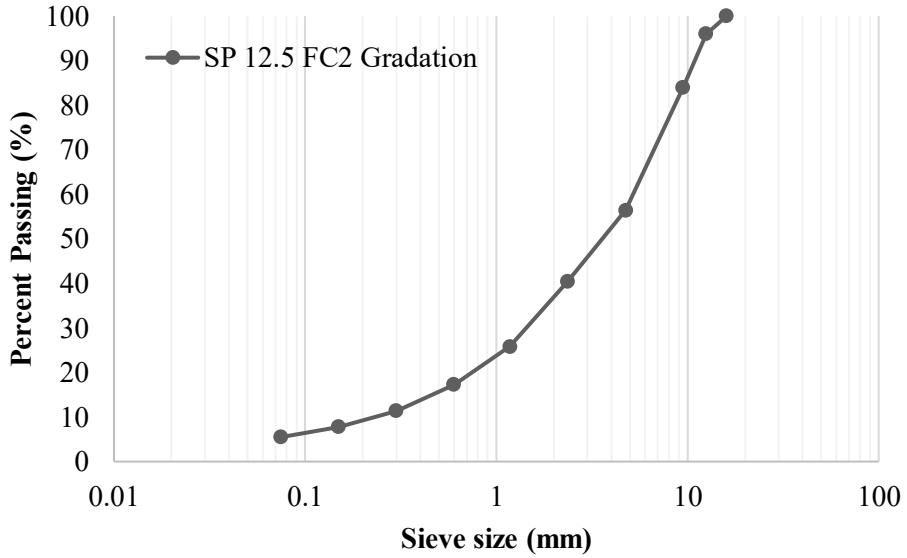

Figure 3-3 SP12.5 FC2 mix final gradation.

3.2.3 Asphalt Cement Fatigue and Healing Testing

This section provides a brief overview of the asphalt cement testing and analysis methods used in Chapter 4 to Chapter 7. For greater detail, the reader is encouraged to view the appropriate Materials and Methodology section in each chapter.

3.2.3.1 The Effect of a Chemical Warm Mix Additive on the Self-Healing Capability of Bitumen (Chapter 4)

A locally sourced PG 58-28 was selected and modified with a commonly used chemical warm mix additive (cWMA) derived from pine tree waste. The cWMA was then added at three concentrations (0.25, 0.5 and 0.75%) by weight to the binder and the binder was RTFO aged at 135 and 163°C to simulate conventional short-term aging and warm mix production temperatures; short-term aged specimens were subsequently aged using the PAV at 100°C for 20 hours.

- *Rheological and Aging Characterization*: All specimens were tested using the standard Superpave tests required to grade the material at low, intermediate and high temperatures according to AASHTO M320. Subsequent analysis of aging and thermorheological analysis was conducted using the 2S2P1D master curve model to determine the specimen cross-over temperature and the temperature sensitivity of rheological parameters (TSRP) as derived by Azimi-Alamdary (2019).
- *Healing characterization*: Asphalt cement self-healing was characterized using the Simplified-LASH Test proposed by CPATT; the SLASH test is a modification of the original LASH test proposed by Xie et al. (2017) whereby the first loading phase terminal strain amplitude is fixed for each binder.
- *DSR Visual Analysis*: Based on the initial observations of instability flow during loading, a procedure was devised to film DSR specimens during the amplitude sweep tests. This visual analysis work flow was automated using a custom MATLAB application to examine DSR specimen geometric changes under loading.

3.2.3.2 Asphalt Cement Fatigue Resistance using the Linear Amplitude Sweep (LAS): A Focus on Failure Criteria (Chapter 5)

Using the same PG 58-28 binder as in Chapter 4, the fatigue resistance at different aging levels (unaged, RTFO and PAV-aged) is once again tested using the LAS test at 19 °C according to AASHTO TP101-

14. The focus of this chapter was to improve the understanding of different failure criteria to determine an appropriate end condition for future healing tests.

- *Fatigue Life Prediction*: Using different analysis templates, available from the Modified Asphalt Research Center (MARC) from the University of Madison-Wisconsin, a rudimentary sensitivity analysis is conducted to demonstrate the effect of different VECD modelling parameters (C_0, α, amplitude sweep failure criteria).
- *Failure Criteria Found in Literature*: Different amplitude sweep failure criteria from literature were evaluated and compared including peak Shear Stress, CN (Safaei et al. 2014), $C^2N(1\text{-}C)$ (Cao and Wang 2018), stored pseudostrain energy (Wang et al. 2015), and crack length/ fracture index (Hintz and Bahia 2013).
- *Fatigue Resistance Ranking*: Two fatigue resistance ranking metrics from literature were evaluated and compared including the Pure LAS (PLAS) and FREI parameter (Zhou et al. 2017) as well as the ΔG parameter (Mainieri et al. 2021).

3.2.3.3 Linear Amplitude Sweep (LAS) Failure Criteria using Complementary Characterization Parameters (Chapter 6)

As a continuation of the study in Chapter 5, Chapter 6 evaluates the same PG 58-28 asphalt cement at different aging levels (unaged, RTFO and PAV-aged) undergoing the linear amplitude sweep with the addition of three complementary failure strain amplitudes. The original analysis in Chapter 5 was extended to a larger temperature range: 13 to 25°C.

- *Supplementary DSR Parameters*: Based on the instability flow/ edge fracture phenomenon found in literature, the DSR normal force is evaluated (Anderson 2001). From the DSR torque balance, the DSR electric torque is also used to supplement the understanding of flow and specimen geometric changes (Läuger et al. 2002; Franck 2005).
- *DSR Visual Analysis*: Following the observations from Chapter 4, the visual analysis procedure is formalized to obtain the DSR specimen *flow strain amplitude* (FSA). The flow strain amplitude was devised to determine the strain amplitude at which the first observable flow is detected.
- *Statistical Analysis*: A comprehensive statistical analysis was used to determine relationships between the complementary failure strain values (normal force, electric torque and flow strain amplitude) with the failure strain amplitudes obtained in Chapter 5 Section 5.3.3.

3.2.3.4 Asphalt Cement Healing Characterization: Concepts for Next-Generation Test Protocols (Chapter 7)

Based on the knowledge gained in Chapter 5 and 6, Chapter 7 details the LASH Version 2 test protocol proposed by RILEM TC CHA-278 Task Group 2a. In this chapter, three asphalt cements (PG 58-28A, PG 58-28B and PG 58-28A + 4% SBS) at three aging levels were evaluated for their restoration ability using the new modified LASH procedure. The procedure features two first loading period terminal strain amplitudes, $0.5\gamma_{peak}$ and γ_{peak}, and two preliminary rest period durations, 5 and 30 minutes. A single testing temperature, 20°C, was selected by the Task Group.

- *Healing Analysis Found in Literature*: Several healing analysis methods from literature were adapted and assessed including VECD-based (Asadi and Tabatabaee 2020) and crack length-based (Hintz and Bahia 2013; Li et al. 2020).
- *Proposed Healing Analysis*: Based on the work of Zhou et al. (2017), the P-LASH analysis method was proposed with two variations. Method 1 was proposed using the ratio of the first and second loading phase FREI parameters while Method 2 simply evaluates the ratio of the pre- and post-rest period released fracture energy, *J*.
- *Statistical Analysis*: Paired MANOVA significance studies were finally completed to assess the significant test parameters (e.g., binder type, aging level, rest period duration and first loading phase end condition).

3.2.4 Asphalt Mixture Fatigue and Healing Testing

This section provides a brief overview of the asphalt mixture testing and analysis methods used in Chapter 8 to Chapter 10. For greater detail, the reader is encouraged to view the appropriate Materials and Methodology section in each chapter when applicable.

3.2.4.1 Asphalt Mixture Testing Experimental Setup (Chapter 8)

This chapter details the apparatus used, the data collection scheme, as well as the test procedures designed from both North American and European standards (e.g., DIN 12697-26-2012, AASHTO T 342, AASHTO TP 107-18) using a uniaxial tension-compression setup. The preparation of CPATT's Material Testing Systems (MTS) multipurpose testing frame, mixture test procedures, custom conditioning chamber/ control scheme, and coupled non-destructive/invasive testing work flow is described.

3.2.4.2 Preliminary Evaluation of Fatigue and Healing of Asphalt Mixtures using the "Intrinsic" VECD Method (Chapter 9)

The preliminary work for the proposed Intrinsic-VECD or "iVECD" fatigue modelling is conducted using a single Superpave 12.5 mix containing 5.2% PG 58-28 asphalt cement. Samples were compacted and cored to their final dimensions: height = 120 (+/- 2.5) mm and diameter = 75 mm. After cutting and coring, the average air voids of the samples were measured to be 4.8%. Fatigue and healing tests were conducted using on-specimen strain control mode at 10 Hz and 10°C.

- *Fatigue Life Estimation*: The fatigue life of the project mix was tested at two strain levels 100 and 125 μm/m. The fatigue life of the mix was evaluated using three methods: the "DGCB" Intrinsic damage rate model (Baaj 2002), the Simplified VECD model using the Power Law formulation (Underwood et al. 2012), and the newly proposed iVECD model.
- *Healing Analysis*: Using the same strain levels (100 and 125 μm/m), fatigue-healing tests are conducted with 4-, 8- and 16-hour rest periods. Several healing indices found in literature are evaluated and compared to new healing indices proposed based on the iVECD model. The iVECD heal parameters are rooted in the healing definitions defined by RILEM CHA-278 (Leegwater et al. 2020).

3.2.4.3 Viability of Coda Wave Interferometry for Fatigue Monitoring of Asphalt Mixtures (Chapter 10)

Combined with the T/C fatigue and healing testing conducted in Chapter 9, ultrasonic measurements were coupled with the asphalt mixture testing. A dedicated pulse-receiver front end was triggered using the test frame controller and used to acquire ultrasonic measurements using P-wave transducers; time signals were acquired at 10-minute intervals over the duration of the T/C test. The acquired signals were then analyzed in the time-domain using the coda wave interferometry (CWI) technique.

- *Windowing Procedure*: Two methods are proposed to pre-process time signals before applying the CWI algorithm. Method 1 incorporates a simple statistical approach using the MATLAB function "findchangepts" from the Signal Processing Toolbox (MathWorks 2022). Method 2 is derived from the diffusive energy envelope (Epple, 2018, Planes and Larose, 2013) paired with an adaptive window length stretching technique.
- *CWI Procedure*: The CWI procedure was completed using a dynamic time warping (DTW) algorithm as opposed to the conventional cross-correlation or trace stretching algorithms used in

other studies. DTW uses an alignment-based dynamic computing algorithm to determine the shortest distance between two time traces (Zhang et al. 2017).

- *CWI and Asphalt T/C Testing*: The CWI procedure was then applied to fatigue and healing tests to validate the use of the diffusive coda waves for asphalt materials.

Chapter 4
The Effect of a Chemical Warm Mix Additive on the Self-Healing Capability of Bitumen

4.1 Introduction

The high temperatures associated with hot mix asphalt (HMA) production have driven research toward more environmentally sustainable solutions. Warm Mix Asphalts (WMA) are an increasingly common industry solution to improve sustainability (Williams et al. 2019). Warm mix additives can reduce mixing and compaction temperatures by 20 to 55°C compared to HMA production temperatures without inducing negative long-term effects on the pavement (Ferrotti et al. 2019). WMA technologies also offer a wide range of benefits such as improved compaction and workability, reduced emissions, longer transport times, improved anti-stripping, and decreased oxidative age hardening. WMA technologies can be broadly classified as chemical, organic, and foaming technologies, but production plant foaming technologies and chemical additives are dominant in North America. In 2018, it was estimated that almost 160 million long tons of WMA were produced in the United States alone (Ferrotti et al. 2019; Ragni et al. 2019; Williams et al. 2019).

While in-depth research into self-healing pavements is relatively new, the first observations of "healing" in bituminous materials can be traced back almost 60 years ago. It was observed that the addition of a rest period (i.e., periods of unloading) could improve the fatigue life of bituminous mixtures in laboratory tests (Sun et al. 2017; Xu et al. 2018b). Under cyclic loading in accelerated fatigue testing, bituminous materials experience a decrease in mechanical properties that can be attributed to the occurrence of both reversible and non-reversible phenomena. Initially, the rapid decrease in properties is due to the dominance of reversible bias effects (non-linearity, thixotropy, local heating, etc.). After continued loading, non-reversible microcrack initiation and propagation become dominant until failure or the sample is unloaded. During a rest period, the total impairment of mechanical properties that are returned is referred to as restoration; restoration is a combination of two components, recovery, and healing (Baaj et al. 2018). When given a sufficient rest period, the "true" self-healing ability and the degree of self-healing are primarily attributed to the bitumen component and its ability to flow and repair microcrack damage (Baaj et al. 2018; Lv et al. 2017).

At higher service temperatures, bitumen self-healing can be instantaneous; at lower temperatures, self-healing is hindered by low rates of molecular diffusion (Lv et al. 2017). Thus, asphalt material self-

healing is affected by internal and external factors including rest period duration, rest period temperature, asphalt cement chemistry and source, aging, moisture, and the presence of additives. Warm mix additives, when used to decrease the production temperature of the asphalt mixture, have the potential to improve the healing ability of the asphalt mixture by decreasing short-term oxidation effects. It is also possible the chemical changes afforded by certain warm mix additives could alter the molecular mobility of the asphalt cement.

In literature, healing is often characterized using accelerated fatigue tests using the dynamic shear rheometer (DSR) in the form of time sweeps or amplitude sweep tests with single or multiple rest periods (Aurilio et al. 2020b). During these mechanical tests, healing is quantified using a "healing index" (i.e., the ratio of the material's mechanical properties before damage and after the damage has been healed). The characterization of bitumen healing is an evolving area of research and, currently, there exists no standardized healing index just as there is no standard healing test (Baglieri et al. 2020; Qiu et al. 2009). The current work uses the Simplified-LASH (SLASH) test, developed at the University of Waterloo, to evaluate the intrinsic self-healing behaviour of bitumen modified with a chemical warm mix additive (cWMA) at different aging levels. Following the initial phase of work with the SLASH test it was determined to introduce visual analysis to develop a greater understanding of bitumen behaviour during the test. This analysis was introduced to complement the observations made during the initial testing.

4.2 Materials and Methodology

4.2.1 Sample Preparation

For this study, a locally sourced PG 58-28 was selected and modified with a commonly used chemical warm mix additive (cWMA). The chosen cWMA is a surfactant that is chemically derived from pine tree waste in the production of paper products and is generally used as a waterless compaction aid or an anti-stripping agent. The cWMA was then added at three concentrations (0.25, 0.5 and 0.75%) by weight to the base binder using a mechanical mixer for 15 minutes at 135°C ± 5°C. Samples were then aged according to standard AASHTO procedures for the Rolling Thin Film Oven (RTFO) test at 163°C and using Pressure Aging Vessel (PAV). Bitumen samples containing 0.5 wt.% cWMA were also RTFO aged at 130°C to simulate lower processing temperatures that may be used to produce a warm mix asphalt. The nomenclature R163 and R130 are used specifically to denote RTFO aging completed

at 163 and 130°C respectively; samples subsequently aged using the PAV are referred to as R163+PAV or R130+PAV.

4.2.2 Rheological Characterization

All bitumen samples were tested for their continuous grade critical temperature values according to AASHTO M320 using a dynamic shear rheometer (DSR); unaged and RTFO aged samples were tested at high temperatures using the 25 mm plate while RTFO+PAV aged samples were tested at intermediate temperatures using the 8 mm plate. Short-term aged bitumen was characterized using the Multiple Stress Creep Recovery (MSCR) test per AASHTO T350 to produce the $J_{nr\,3.2}$, percent recovery, and $J_{nr\,Diff}$ at 58°C based on the climate of Southwestern Ontario, Canada. The $J_{nr\,3.2}$ is the compliance of the sample and has shown an excellent correlation with rutting (Aurilio et al. 2018). Bending Beam Rheometer (BBR) testing was completed on all RTFO+PAV aged material at -18°C.

The Linear Amplitude Sweep (LAS) test, as described in AASHTO TP101, is used to evaluate the intermediate temperature fatigue behaviour of either RTFO or RTFO+PAV aged bitumen; currently, the intermediate testing temperature is determined as 4°C greater than the average of high and low PG temperatures. The LAS test consists of a frequency sweep and an amplitude sweep. Results for RTFO+PAV aged material at 0.0 and 0.5 wt.% cWMA tested at 19°C were analyzed using an Excel spreadsheet developed by researchers at the Modified Asphalt Research Center (MARC) at the University of Wisconsin-Madison; the number of cycles to failure (N_f) values are reported using 50% damage at the 5% strain level (Safaei and Castorena 2016).

4.2.3 Cross-Over Temperature and Temperature Sensitivity of Rheological Parameters (TSRP)

The cross-over frequency (ω_{cross}), the frequency at which the phase angle is 45°, is estimated when the storage and loss moduli are equal (i.e., G' = G'') using shifted isothermal frequency sweeps (i.e. the complex modulus master curve). As the contribution of both the elastic and viscous components of the complex modulus are equal at this frequency, loading at frequencies below the ω_{cross} causes the bitumen to behave as a viscoelastic liquid, and contrastingly, as a viscoelastic solid at frequencies above ω_{cross}. Most commonly, the Williams-Landel-Ferry (WLF) shift parameters are used to shift data from a higher frequency to a lower frequency or vice versa with a reference temperature T_{ref}. The WLF shift factors for each dataset are calculated as follows:

$$\log a(T) = -\frac{C_1(T - T_{ref})}{(C_2 + T - T_{ref})} \quad \text{Eqn. 4-1}$$

where log a(T) is the natural logarithm of the shift factor, T is the isothermal test temperature for a given dataset, in °C, C_1 and C_2 are the empirical shift factors parameters; the isothermal frequency, ω, obtained in the sweep can be then shifted to the reduced frequency, $\omega_{red} = \omega \cdot 10^{\log a(T)}$. Using the shift factor fitting parameters, the cross-over frequency can then be converted to a cross-over temperature (T_{cross}) by substitution of ω_{cross}. As the two are inversely proportional, a higher cross-over frequency produces a lower cross-over temperature. In literature, the effect of aging has been shown to increase the cross-over temperature as more energy is required to induce motion in the age-hardened binders (Garcia Cucalon et al. 2019). However, the cross-over temperature provides insight into a single temperature and does not give any information on the rheological behaviour at low and high temperatures or the aging history of the material (Azimi Alamdary 2019; Ragni et al. 2019).

The Temperature Sensitivity of Rheological Parameters (TSRP), developed by Azimi Alamdary (2019), using the master curve shift factors, evaluates the temperature sensitivity over the entire experimental temperature range. The TSRP has the advantage that it can be applied to pre-calculated master curve shift factors for both bituminous binders and mixtures. The TSRP is derived as the tangent slope of the generated shift factor curve (Azimi Alamdary 2019; Azimi Alamdary and Baaj 2020). Using the WLF shift factors, the TSRP is calculated as:

$$\tan(\alpha) = \frac{d(\log \alpha(T))}{dT} = -\frac{C_1 C_2}{(C_2 + T - T_{ref})^2} \quad \text{Eqn. 4-2}$$

where tan(α) is the temperature sensitivity of the α factor, 1/°C. As the tan(α) represents the tangent slope of the shift factor curve, it should be noted that when comparing the resultant tan(α) curves over the temperature range, lower values (i.e., negative values with a greater magnitude) indicate an increased temperature sensitivity. Using this parameter, aged bituminous materials typically have lower tan(α) values as they are more temperature-sensitive compared to less aged materials at intermediate and high temperatures. As a generalization, binders will also appear to be more sensitive at lower temperatures and less sensitive at higher temperatures regardless of aging level. While the TSRP provides information over the whole testing temperature range compared to the single value cross-over temperature, the TSRP is derived from an empirical/mathematical fitting procedure as the equation is not based on any material behavioural mechanisms (Azimi Alamdary 2019). For this study, master

curves were developed using temperatures ranging from 10 to 70°C on RTFO and RTFO+PAV aged samples containing 0.0 and 0.5 wt.% cWMA using the 2S2P1D model. The cross-over temperatures and TSRP tan(α) values were then obtained using the shifted master curve data.

4.2.4 LAS-Based Healing Characterization

The Linear Amplitude Sweep Healing (LASH) test uses the LAS test as a basis and incorporates a rest period to characterize the self-healing ability of the binder. During the LASH test, unaged samples are loaded at 20°C to a strain amplitude corresponding to a percentage of the cohesive failure damage level (%S_f); for example, 50%S_f, 100%S_f, and 150%S_f. Upon loading to %S_f, the sample is unloaded for a single rest period ranging from 1 to 30 minutes. The rest period is followed by a second loading phase resuming at the strain value at the end of the first loading phase. Percent healing (%H_S) is calculated as follows:

$$\%H_S = \frac{S_1 - S_2}{S_1} \quad \text{Eqn. 4-3}$$

where S_1 is the damage parameter at the end of the first loading phase, and S_2 is the damage parameter corresponding to the beginning of the second loading phase (Xie et al. 2017). It should be noted that current LAS-based healing tests quantify restoration which encompasses both self-healing ability and the recovery of reversible phenomena such as internal heating and thixotropy. For this reason, the authors of this paper suggest relabelling the left-hand side of equation (3) to use the percent restoration (%R_S) to denote the restoration potential hereafter; %R_S is then calculated using equation (3) without any modification of the damage parameters.

4.2.5 Determining the Cohesive Failure Damage Level

In the original LASH test, rest period strain levels are derived from the strain amplitude at the cohesive failure damage level (S_f) obtained from a pseudostrain energy (PSE) analysis of an uninterrupted or continuous LAS (cLAS) test (Xie et al. 2017). PSE-based methods have been proposed to develop fatigue failure criteria in the LAS test as the PSE analysis is independent of the loading mode and is applicable over a wide range of temperatures (Wang et al. 2015). During the amplitude sweep, the total cumulative pseudostrain energy, W^R_{Total}, is approximated as:

$$W^R_{Total} = 0.5\left(\gamma^R_p\right)^2 \quad \text{Eqn. 4-4}$$

where γ_p^R is the peak pseudostrain amplitude obtained during the test. The W^R_{Total} relates to the stress response of a theoretical "undamaged" linear viscoelastic material as the pseudostrain amplitude increases. However, as the material becomes damaged during the test, the observable change in pseudostrain energy is composed of the stored pseudostrain energy, W_S^R, and the released stored pseudostrain energy, W_R^R. At the desired cycle in the LAS test, the stored pseudostrain energy density, W_S^R, is calculated as:

$$W_S^R = 0.5 \cdot C(S) \cdot \left(\gamma_p^R\right)^2 \quad \text{Eqn. 4-5}$$

where C is the pseudostiffness, S is the damage level (Safaei and Castorena 2016; Wang et al. 2015). The released PSE, W_R^R, caused by the formation and propagation of microcracks in the binder sample, is calculated as the difference between the total and stored PSE:

$$W_R^R = W_{Total}^R - W_S^R = 0.5 \cdot (1 - C) \cdot \left(\gamma_p^R\right)^2 \quad \text{Eqn. 4-6}$$

From Figure 4-1, it can be observed that the stored pseudostrain reaches a maximum during the test and this point was chosen as the failure point for the LAS test as the material loses the ability to store PSE. Using this rationale, the strain amplitude at the maximum W_S^R value was chosen for the LASH test to represent the amplitude of the cohesive failure strain, S_f (Wang et al. 2015; Xie et al. 2017).

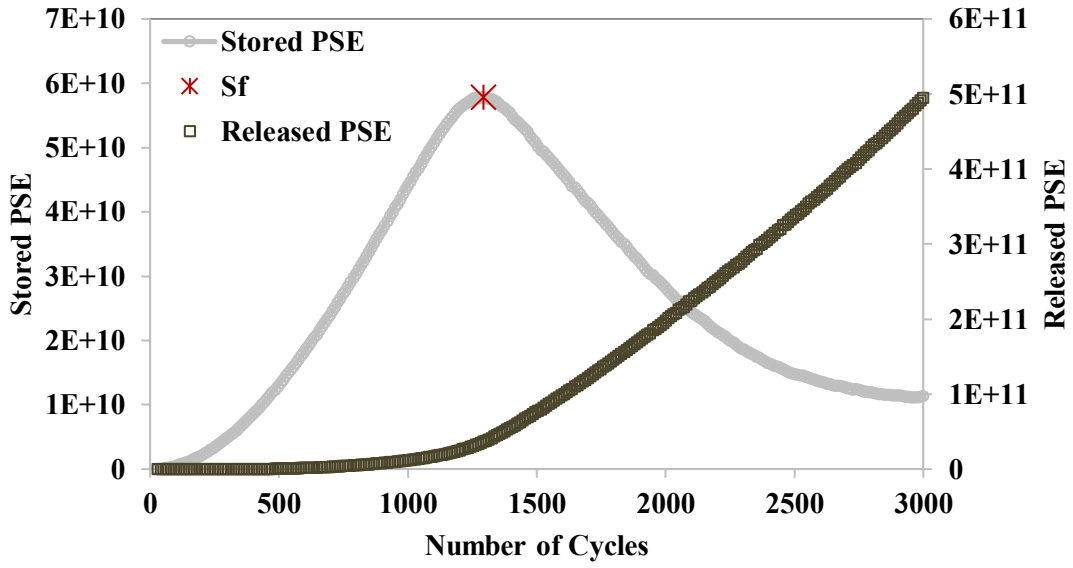

Figure 4-1 Observed evolution of stored and released pseudostrain energy during an amplitude sweep test.

4.2.6 Simplified-LASH Test

As depicted in Figure 4-2, the proposed Simplified-LASH or SLASH test uses the same procedure as the LASH test with the S_f calibration omitted. The rationale being that the strain amplitude at S_f can vary greatly between different binders with different treatments and aging levels thus preventing a true comparison of the restoration ability. For this study, SLASH test samples were initially loaded to 10% strain at 19°C and a 15-minute rest period was applied before completing the second loading phase. It should be noted that a different DSR was used to perform the cLAS and SLASH tests than was used to perform the preceding rheological characterization.

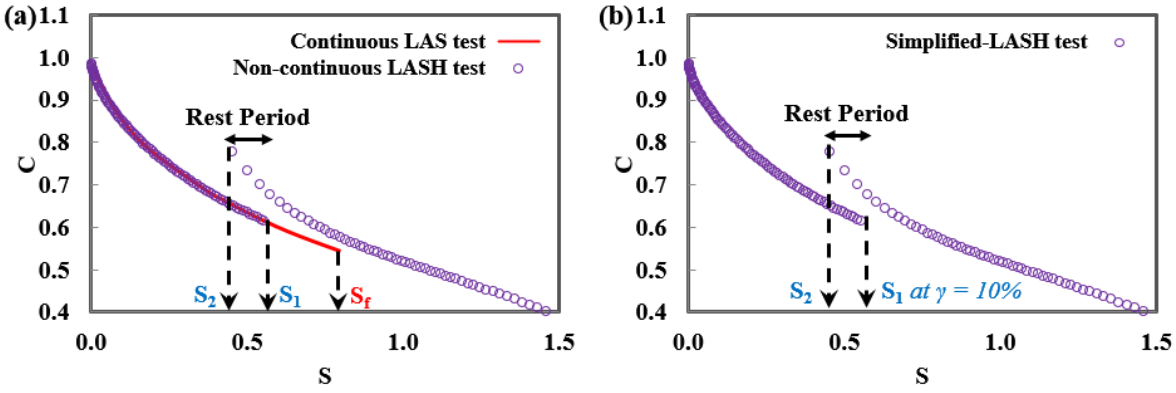

Figure 4-2 Exemplary schemes for: (a) the original LASH test procedure, and (b) the SLASH test procedure without the peak stored PSE S_f calibration.

4.2.7 DSR Visual Analysis

To further investigate the LAS-based healing tests, the unmodified binder samples at the different aging levels were filmed during a cLAS test. The videos were processed using commercial video editing software to improve brightness and contrast before still frames were extracted at a rate of 1 frame per second (fps). The still frames were then binarized for analysis using MATLAB. For each still frame, the region of interest (ROI) was selected manually to include the theoretical area occupied by an "undamaged" sample as shown in Figure 4-3. Using the user-selected ROI as a foundation, four regions were defined for the image analysis; Regions 1 and 4 (R1/R4) are used to measure any changes in the geometry outside the sample area while Regions 2 and 3 (R2/R3) are used quantify the changes in the geometry inside the sample area. In each region, the area of white pixels is recorded and then the two regions are correspondingly averaged and normalized for the test. The visual analysis was used after the healing tests to verify whether the neat binder samples may have changed in geometry during the

continuous linear amplitude sweep rendering the previous LAS and PSE analysis invalid. A MATLAB app created by the authors is also available by contacting the corresponding author. The MATLAB app, compatible with MATLAB 2020a and later versions, allows the operator to upload an image set extracted from a video, apply the binarization process, manually select the ROI and analyze the geometry change through the method described above using an accessible graphical user-interface.

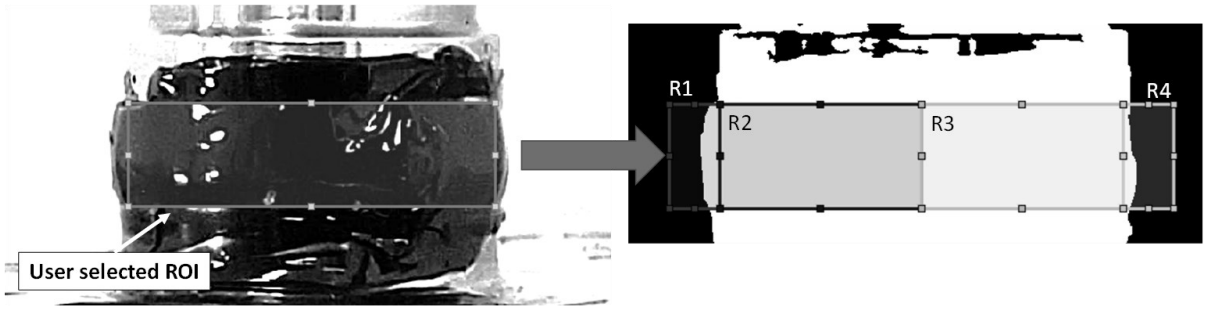

Figure 4-3 Example of DSR video frame analysis on an RTFO+PAV aged sample.

4.3 Results

4.3.1 The Effects of Aging

The results of conventional binder tests on unaged and RTFO-aged specimens are shown in Table 4-1. From the binder grading results on unaged material, a slight increase in the critical temperature is observed. Using the standard short-term aging temperature (R163), it was observed that the critical temperature of samples decreases with increasing %cWMA. Correspondingly, there is a more significant decrease in the critical temperature for specimens containing 0.5 wt.% cWMA aged at R130. RTFO samples with decreased aging also exhibit slightly higher J_{nr} values which are consistent with results found in literature (Ragni et al. 2019). According to AASHTO M332 J_{nr} requirements, all cWMA modified RTFO aged binders maintain the “Standard” or “S” grade excluding the binder aged at R130 as it is above the maximum J_{nr} limit of 4.0 kPa^{-1} but would be deemed acceptable as per the current local Ontario Provincial Standard Specifications 1101 (OPSS.MUNI 1101).

Table 4-1 Rheological analysis for unaged and RTFO-aged samples.

	Unaged	RTFO Aged				
%cWMA (wt.%)	**T_{crit}, °C**	**T_{crit}, °C**	**$J_{nr-3.2}$, kPa^{-1}**	**%Rec, %**	**$J_{nr\ Diff}$, %**	**T_{cross}, °C**
0.0	62.0	63.2	2.12	3.7	20.5	-21.1
0.25	62.5	63.0	2.25	1.9	23.0	-
0.5 (R163)	62.6	62.6	2.35	2.8	21.8	-21.6
0.5 (R130)		58.3	4.42	0.4	15.9	-27.1
0.75	62.4	62.4	2.43	1.5	21.5	-

Binder grading results from RTFO+PAV-aged specimens are shown in Table 4-2. For RTFO+PAV-aged materials, the bitumen is only slightly affected by decreasing the short-term aging conditions to 130°C demonstrating that the intermediate temperature critical temperature is less sensitive to the initial conditions after PAV aging. BBR results demonstrate that the binder samples containing 0.5 wt.% cWMA have higher m-values indicating improved stress relaxation ability which is also related to the reduction in oxidative aging. For RTFO+PAV-aged samples, the neat binder had the highest N_f. Overall, it appears that the less aged bitumen samples have lower N_f values possibly indicating poorer resistance to fatigue.

Table 4-2 Rheological analysis for RTFO+PAV aged samples.

%cWMA (wt.%)	Intermediate T_{crit}, °C	T_{cross}, °C	m-value at -18°C	Stiffness at -18°C, MPa	N_f at 5% strain
0.0	17.5	16.6	0.341	205	5420
0.5 (R163)	16.8	15.4	0.344	186	4990
0.5 (R130)	16.7	14.2	0.351	197	4130

This result is reflected in the master curves as seen in Figure 4-4. For both RTFO and RTFO+PAV aged material, it appears that the presence of the cWMA does not have a significant effect on the stiffness of the binder aged using the R163 aging condition. The addition of cWMA in conjunction with the R130 aging condition demonstrates a much greater observable decrease in stiffness at reduced frequencies corresponding to higher temperatures and lower frequencies. At intermediate and low temperatures, all three bitumen specimens converge to similar stiffness values at both aging levels. From the Black Space diagrams in Figure 4-5, we observe a flattening of the curve for more aged specimens as the binder becomes more elastic in the intermediate to high-temperature range (Aurilio et al. 2020a).

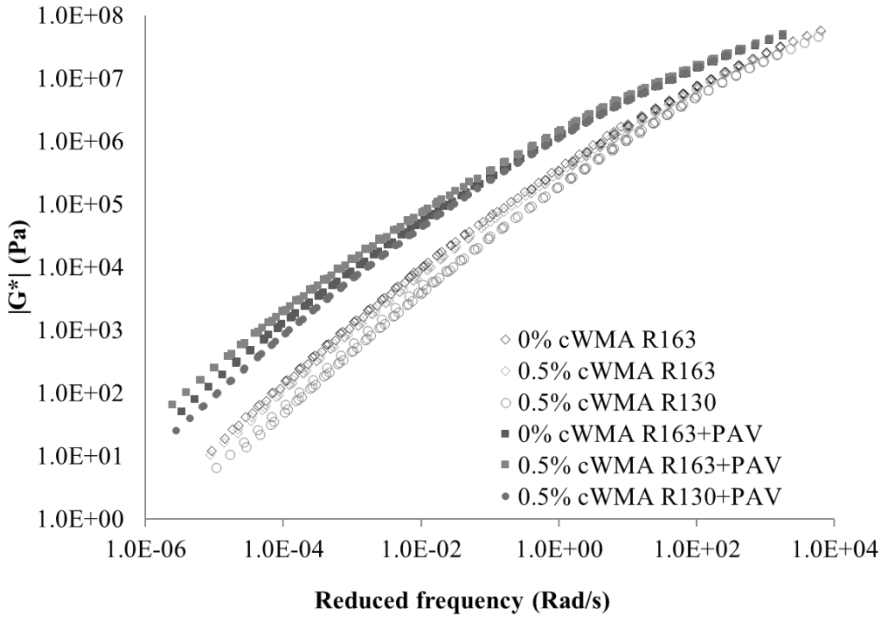

Figure 4-4 Modulus master curves for RTFO and RTFO+PAV aged samples (T_{ref} = 20°C).

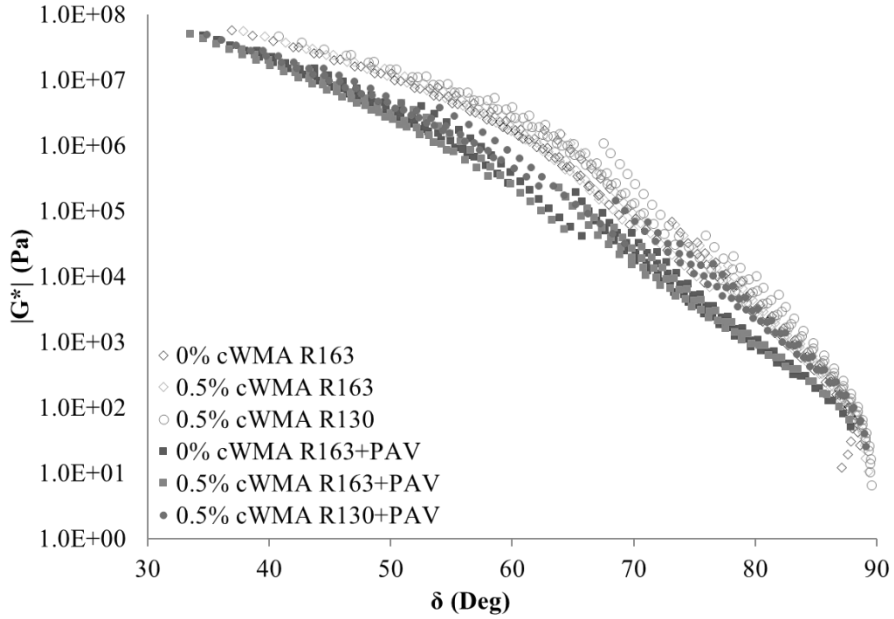

Figure 4-5 Black space diagrams for RTFO and RTFO+PAV aged samples (T_{ref} = 20°C).

The cross-over temperature was also calculated for each bitumen using their respective master curve data as shown in Tables 4-1 and 4-2. It was observed that the neat bitumen has the highest T_{cross} while

0.5 wt.% cWMA has a lower T_{cross} when aged. The 0.5 wt.% cWMA samples aged at R130 and R130+PAV have the lowest T_{cross} of all the studied bitumen samples at both the RTFO and RTFO+PAV-aging levels. From the TSRP analysis in Figure 4-6, it was observed that the tan(α) curves for the 0 wt.% and 0.5 wt.% cWMA binder aged using the R163 condition are very similar indicating a similar temperature sensitivity over the range; the 0.5 wt.% cWMA binder aged at the R130 condition has a much lower temperature sensitivity compared to the samples aged at R163 as indicated by the smaller negative values over the whole temperature range. In contrast to the RTFO-aged materials, the 0.5 wt.% cWMA R130+PAV appears to be the most temperature-sensitive in the intermediate temperatures in the range (i.e., 10 to 30°C), while the 0 wt.% cWMA R163+PAV binder becomes most sensitive at higher temperatures.

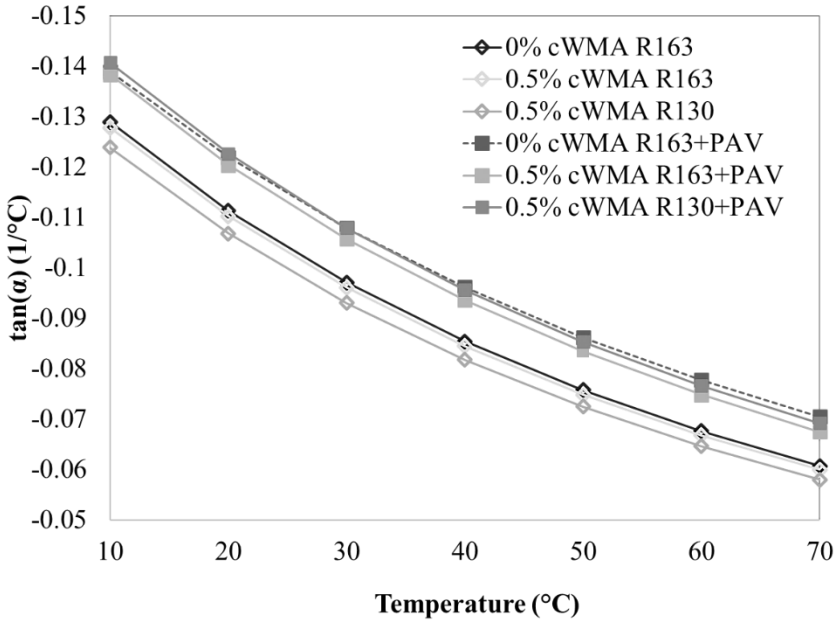

Figure 4-6 TSRP analysis on RTFO and RTFO+PAV aged samples (T_{ref} = 20°C).

4.3.2 Healing Characterization

Percent Restoration SLASH test results for unaged and RTFO (R163) aged containing from 0.25 to 0.75 wt.% cWMA can be found in Figure 4-7. Similarly, SLASH test results for unaged, RTFO (R130 and R163) and RTFO+PAV aged samples containing either 0.0 or 0.5 wt.% cWMA are found in Figure 4-8. From Figure 4-7, it was observed that increasing the concentration of cWMA does not significantly affect the unaged $\%R_S$. With the addition of cWMA, there is an increased percent restoration for R163 aged material compared to the neat binder. However, only a slight improvement is observed when

cWMA concentration increases from 0.25 wt.% to 0.75 wt.% cWMA. After RTFO aging at R163 and R130 as depicted in Figure 4-8, it was observed that both binders containing cWMA have improved restoration ability. After RTFO+PAV aging, the neat binder demonstrates superior restoration compared to samples containing cWMA. The results of SLASH testing demonstrate that increased aging increases $\%R_S$, however, the DSR visual analysis in the next section demonstrates that there are inherent flaws in conducting LAS-based healing tests for unaged and short-term aged materials.

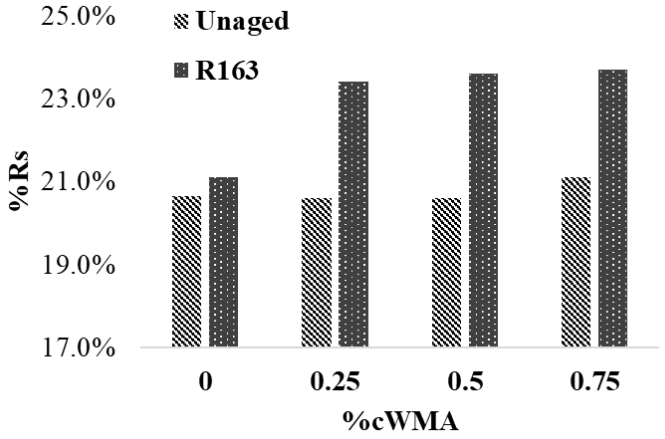

Figure 4-7 Percent restoration for unaged and R163 aged samples from 0.0 to 0.75 wt.% cWMA.

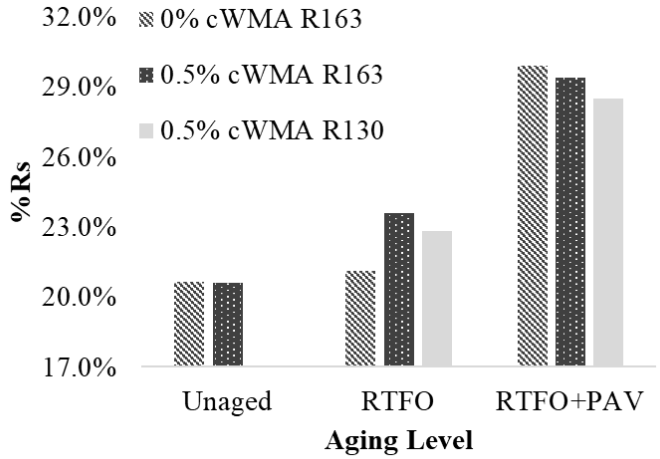

Figure 4-8 Percent restoration for unaged, RTFO and RTFO+PAV aged samples at 0.0 and 0.5 wt.% cWMA.

4.3.3 Assessment of LAS Tests Using DSR Visual Analysis

As shown in Table 4-3, the cohesive failure damage level ranges from approximately 12.9 to 16.5% strain for the supplied binder. The general trend observed from the data suggests that as the aging

condition becomes tougher that S_f values are shifted toward higher strain amplitudes. When using the 10% pre-selected strain value in the SLASH test, this roughly corresponds to 60-80%S_f calculated using the original LASH procedure.

Table 4-3 Cohesive failure strain amplitude values for unaged, RTFO and RTFO+PAV aged samples obtained from cLAS testing.

%cWMA (wt.%)	Unaged (%)	RTFO Aged (%)	PAV Aged (%)
0.0	12.9	13.9	16.7
0.25	13.7	13.9	-
0.5 (R163)	13.1	14.4	16.4
0.5 (R130)		13.5	15.1
0.75	13.0	13.7	-

Still frames from a single cLAS run are depicted in Figure 4-9 for the neat binder at the unaged, RTFO and RTFO+PAV aging condition over the 300 seconds. The still frames from Figure 4-9 combined with the automated visual analysis results found in Figure 4-10 demonstrate that the softer unaged and RTFO-aged bitumen can fail prematurely during strain sweeps as the geometry changes.

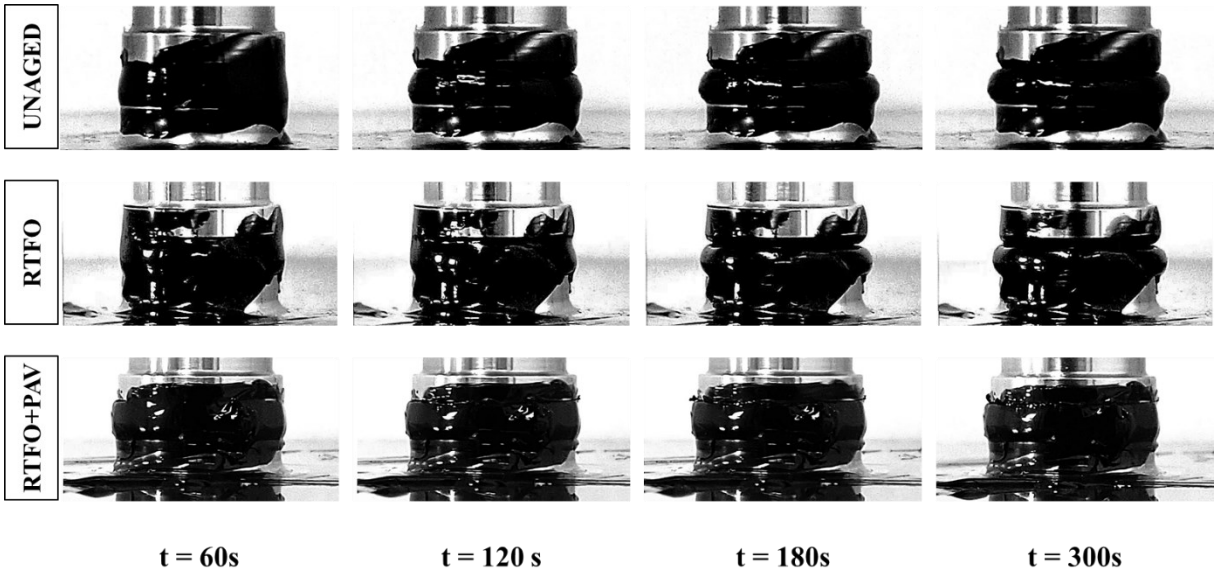

Figure 4-9 Video frames at t = 60, 120, 180, and 300 seconds for unmodified bitumen samples for unaged, RTFO and RTFO+PAV aged conditions.

Although the RTFO+PAV-aged material appears to maintain its geometry during the test, some moderate flow is observable in the outer ROIs possibly rendering the LAS results of the RTFO+PAV-aged material invalid (Safaei and Castorena 2016). It should be noted that due to the challenges of creating a reproducible sample filming procedure the degree or magnitude of flow is not currently

within the scope of the project. The presence of any amount of observable flow in and of itself may be sufficient evidence to invalidate the current RTFO+PAV LAS analysis results reported for this binder(Safaei and Castorena 2016). This aspect of LAS testing requires further analysis.

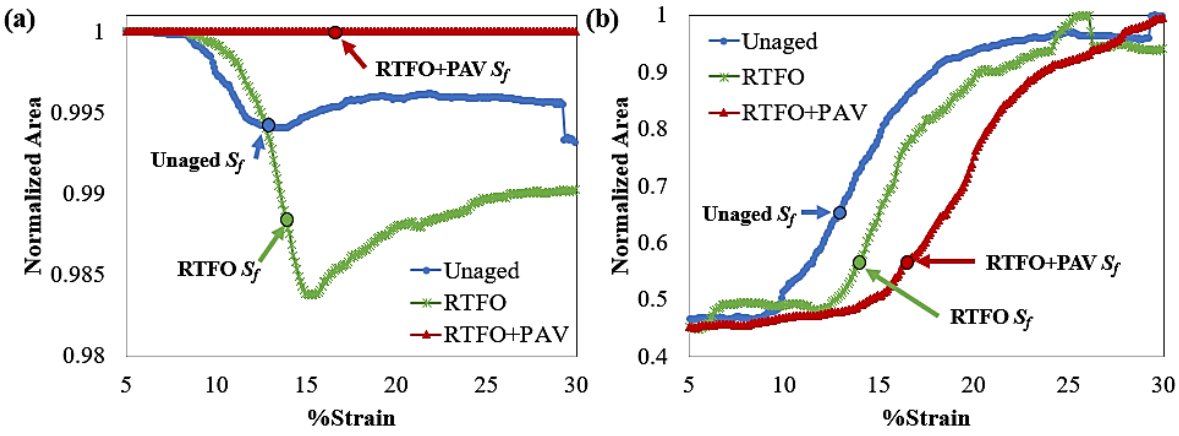

Figure 4-10 Video frame visual analysis results: (a) inner region normalized area and (b) outer region normalized area.

4.4 Discussion

4.4.1 Rheological Characterization and the Effect on Aging

The rheological analysis of the neat and cWMA-modified binders at different aging levels shows evidence that the aging temperature (R130 vs R163) plays a large role in reducing the degree of oxidative aging. Although the presence of the cWMA itself appears to play some role in the degree of aging, the role of temperature seems to be greater. From the MSCR analysis of RTFO-aged material found in Table 1, samples containing 0.5 wt.% cWMA aged at R130 exhibit the highest J_{nr} demonstrating that the J_{nr} may be more sensitive to aging temperature than %cWMA. Higher J_{nr} values can be a concern for rutting resistance but increasing %cWMA does not have a significant effect when the bitumen is short-term aged at the R163 aging temperature. The rutting resistance of the binder aged at the R130 aging temperature appears to decrease significantly as the J_{nr} value is almost doubled compared to the R163 aging temperature (Aurilio et al. 2018). The percent recovery and $J_{nr\ Diff}$ have no significant relationship with the increasing concentration of cWMA at the normal R163 temperature although the values for the 0.5 wt.% cWMA R130 samples are considerably lower, but still within regular test variability.

From the analysis of the master curves, the cross-over temperatures are lower for samples aged at lower temperatures further demonstrating that lower production temperatures, as well as the presence of the cWMA, can decrease the oxidative aging of bitumen (Garcia Cucalon et al. 2019). Applying the TSRP analysis to the master curve shift factors in Figure 6, the tan(α) curves for the 0 wt.% and 0.5 wt.% cWMA binder aged using the R163 condition demonstrate similar temperature sensitivity while the 0.5 wt.% cWMA binder aged at the R130 condition has a much lower temperature sensitivity. When observing the RTFO+PAV-aged samples, the tan(α) curves are less steep compared to the RTFO-aged materials indicating that there is less sensitivity to temperature due to the long-term aging, but there is less distinction between the three PAV-aged binders. However, the 0.5 wt.% cWMA R163+PAV appears to be consistently less sensitive to temperature over the whole temperature range potentially reflecting the moderate m-value but the lowest stiffness value obtained from the BBR testing at -18°C.

4.4.2 Restoration Characterization

Using the SLASH test procedure, it was observed that increasing the concentration of cWMA does not significantly affect the unaged $\%R_S$. With the addition of cWMA, there is a noticeable increase in the percent restoration for R163 aged material. However, only a slight improvement is observed when cWMA concentration increases from 0.25 wt.% to 0.75 wt.% cWMA. After RTFO aging at R163 and R130, it was observed that both binders containing cWMA have improved restoration ability. After RTFO+PAV aging, it was observed that the neat binder has superior restoration compared to samples containing cWMA. The results of SLASH testing demonstrate that increased aging increases $\%R_S$. Additionally, SLASH testing performed on SBS-modified binders at different aging levels similarly revealed that RTFO+PAV-aged materials had a higher $\%R_S$ than unaged and RTFO-aged materials (Aurilio 2020). However, in a different study by Chen and Wang (2020) using the original LASH procedure on aged and unaged binders, the $\%R_S$ of bitumen decreased with increased aging (Chen and Wang 2020). Other previous research has demonstrated that the LAS test does not correlate well with aging level and, in some cases, aging can improve LAS performance as the test is sensitive to factors such as the original binder source, strain level and modification type (Aurilio et al. 2020a; Hintz et al. 2011; Zhou et al. 2017). In previous work by (Baaj et al. 2003), it was similarly demonstrated that stiffer binders have a lower damage accumulation rate which may explain the improved restoration behaviour of aged bitumen.

4.4.3 DSR Visual Analysis

The visual analysis results from this study indicate that the softer, less aged binders can fail prematurely during strain sweeps due to geometric changes to the sample through flow. In previous works by other researchers, the change in geometry is attributed to instability flow which is expected to occur when the testing temperature is too high (Safaei and Castorena 2016). From Figure 4-10, both the unaged and RTFO aged binders exhibit some flow before the selected 10% strain in the SLASH test and significant flow occurs by the time the strain reaches the S_f strain amplitude. Therefore, the original S_f values obtained from cLAS tests could not be used to calibrate the original LASH test for this specific binder. As the culmination of the work by Safaei and Castorena (2016), it was suggested that the testing temperature for LAS testing be set 4°C below the average PG temperature to ensure that the linear viscoelastic complex modulus remains in the range of 12 to 60 MPa at 10 Hz thus facilitating cohesive cracking without inducing even moderate flow (Safaei and Castorena 2016). However, this temperature guideline is only extended to RTFO+PAV-aged binders meaning that for unaged and RTFO-aged material, the testing temperature would need to be significantly lower to reach the 12 MPa modulus threshold. testing at sufficiently low temperatures to mitigate instability flow may severely hinder the healing potential of the binder requiring excessively long rest periods and rendering testing impractical. Furthermore, the challenge of minimizing instability flow may not be solved by simply reducing the test temperature. At lower temperatures, instability flow in bitumen samples may still occur if the actual shear rate at the edge of the DSR plates is sufficiently greater than the applied shear rate (Motamed and Bahia 2011).

For future studies, it may be possible to simply screen for binders that will experience excessive flow during the cLAS by comparing the deviation of the calculated pseudostiffness data with the S-VECD model fit. Figure 4-11 depicts the pseudostiffness data with the S-VECD model fit for an unaged and an RTFO+PAV-aged sample. As observed in Figure 4-11, the unaged binder will begin to have a significant deviation from the model fit at strains greater than the S_f strain amplitude. In contrast, the RTFO+PAV aged material deviates slightly from the model at the beginning and end of the amplitude sweep but has a greater agreement with the model at strain levels approaching the S_f strain amplitude. This screening measure was retroactively applied to all cLAS data for all bitumen samples in this study (Table 4-4). Upon review of the cLAS test, it was determined that only long-term RTFO+PAV-aged samples did not deviate from the model fit. From this knowledge, unaged and RTFO-aged samples may experience significant flow during both the cLAS tests which provides evidence that S_f value calibration

and the PSE analysis required to complete the original LASH test may not be applicable for unaged and short-term aged binders. Moreover, the $\%R_S$ values listed from this earlier study may only be valid for the RTFO+PAV aged binders.

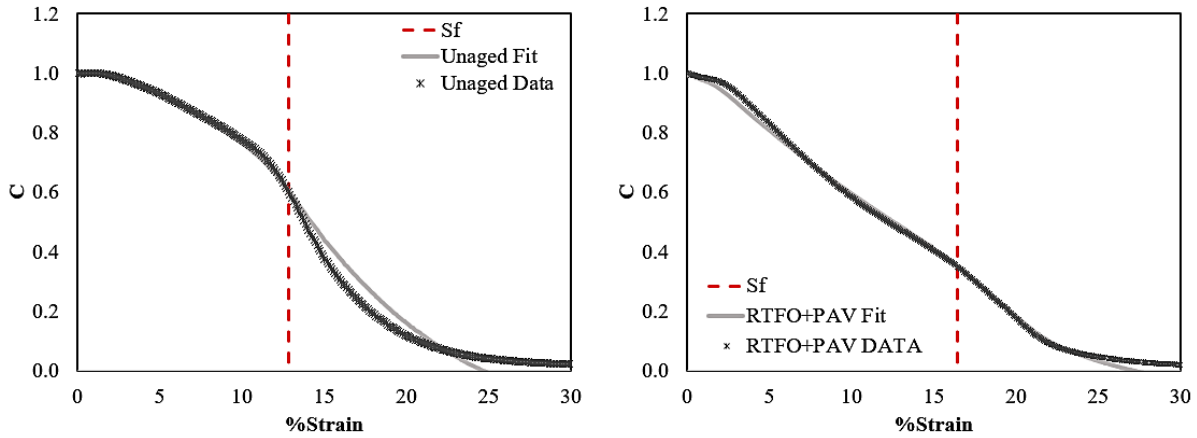

Figure 4-11 Example S-VECD Model vs LAS data for: (a) unaged material and (b) RTFO+PAV aged material.

Table 4-4 Observable deviation from S-VECD fit for unaged, RTFO and RTFO+PAV aged samples obtained from the previously tested continuous linear amplitude sweeps.

%cWMA (wt.%)	Unaged	RTFO Aged	PAV Aged
0.0	Yes	Yes	No
0.25	Yes	Yes	-
0.5 (R163)	Yes	Yes	No
0.5 (R130)	Yes	Yes	No
0.75	Yes	Yes	-

4.4.4 Limitations of Visual Analysis

Currently, the image analysis only provides insight into the flow behaviour of the bitumen sample at the surface for a limited set of samples. Considering the findings from the visual analysis component of this study, the current procedure has several limitations which should be addressed for future studies. When initially filming the sample, different lighting sources in the room can produce specular highlights and reflections on the surface of the bitumen; most highlights are removed through the subsequent binarization process but cause fluctuations in the reported area values in MATLAB. Also eliminating the hood/ thermal system to film the sample makes it susceptible to variations in room temperature throughout the day potentially increasing the variability on a sample-to-sample basis.

Furthermore, the quality of the analysis is reliant on the operator's judgment when processing the video and selecting the ROI. The use of a dedicated, semi-permanent enclosed hood system with a

built-in camera could be used in the future to address some of these concerns. This system would ensure that the ROI would be located at the same location during each test and diminish variation due to temperature. Also applying stronger, more uniform backlighting, like that found in commercial tensiometers, would allow for the sample to be silhouetted against the background reducing variation due to reflections on the sample surface. The addition of these controls would allow for the determination of sample flow reproducibility in future studies.

4.5 Conclusions

In conclusion, the Simplified-LASH or SLASH test was used to characterize the restoration potential of bitumen containing a chemical warm mix additive aged at standard HMA and WMA production temperatures. After evaluating the results from SLASH testing, it was evident that the selected terminal strain amplitude for the first loading phase favoured more aged materials. Thus, the DSR visual analysis was used to supplement the observations from the amplitude sweep healing tests. From these works, the following conclusions are presented:

- LAS-based healing tests in their current form measure restoration and not "true" healing. The LASH and SLASH tests only compare properties before the rest period and after the rest period without isolating the true healing from the observed restoration.
- The addition of cWMA reduces the degree of oxidative aging, but aging temperature appears to play a larger role in the degree of aging.
- For less-aged samples, the addition of cWMA appears to have no significant effect on the bitumen's restoration ability. Neat RTFO+PAV aged bitumen has a higher $\%R_S$ compared to cWMA-modified RTFO+PAV specimens as stiffer binders may have lower damage accumulation rates during testing.
- The DSR visual analysis demonstrated that the cohesive failure damage strain amplitude may not be an appropriate failure point due to changes in sample geometry for less-aged binders. For these reasons, the percent restoration data presented in this paper for this binder may only be valid at the RTFO+PAV aging condition. However, the visual analysis presented was only applied to a small set of samples and is limited by sample filming conditions as well as the skill of the operator during processing.

- Future studies on the LAS test and LAS-based healing tests would require much more emphasis on unaged and short-term aged binders to mitigate premature geometric failures thus ensuring that DSR measurements are accurate.

Chapter 5
Asphalt Cement Fatigue Resistance using the Linear Amplitude Sweep (LAS): A Focus on Failure Criteria

5.1 Introduction

Since its development in the 1990s, the Superpave Performance Grade (PG) system has been widely adopted throughout North America. Divided between the asphalt cement grading and the asphalt mixture volumetrics, this system provided a straightforward method to design asphalt materials for a specific traffic load or climatic condition. The initial PG system was developed using the unmodified asphalt cements of its time. The basic PG system fails to adequately predict new modifiers and additives' influence on rutting and fatigue resistance (Hajj and Bhasin 2017; Zhou et al. 2013a).

Although the simple fatigue resistance criteria initially developed by SHRP (i.e., the dissipated energy-based $G^*\sin\delta$ parameter) fails to provide adequate predictions of fatigue resistance of pressure aging vessel (PAV) binders at intermediate temperatures, it is still widely used today. The intermediate dynamic shear rheometer (DSR) grading of PAV-aged binders is quick and easy to interpret for operators, producers, and engineers. However, the lack of rigour and poor correlation to mixture testing results has relegated it to mainly quality control purposes (Hajj and Bhasin 2017).

Early research using the DSR proposed that DSR-based time sweep tests could be used to characterize binder fatigue (Bahia et al. 2001). The time sweep tests were conducted at a single frequency and strain amplitude. Time-sweep test failure definitions could be derived from the number of cycles at which the modulus or phase angle was reduced to a predetermined value or the change in dissipated energy ratio per cycle. Failure determined from dissipated energy (W) analysis seemed to be the most promising, as a reduction in the stiffness or phase angle was not always equated to the presence of damage. The dissipated energy ratio (DER) at the cycle of interest could be calculated simply as the ratio of the cumulative dissipated (W_{cumul}) to the per cycle change in energy dissipation (W_n) and was a logical parameter to monitor changes in the binder integrity. Failure was typically defined as the onset of the non-linearity appearing in the second stage of the DER-number of cycles curve. Early studies using first-generation DSRs often experienced challenges requiring impractical amounts of compliance corrections to solve the torque overshoot issues during time sweeps (Anderson et al. 2001).

Later studies used a different variation on the failure criteria, such as the time sweeps were even conducted using sand asphalt mortars (SAMs) by Martono et al. 2007. Stress-controlled time sweeps on SAM torsional cylinder specimens were analyzed using a dissipated energy analysis method using the typical number of cycles corresponding to a 20% deviation from linearity of the DER curve (e.g., N_{p20}) was used as failure criteria. The stress and strain control time sweeps conducted by Tan et al. (2012) used a simpler 20%, 40% and 60% reduction of the initial modulus to determine the end of the first loading phase for healing tests. Alternatively, the study by Zhang and Gao (2019) demonstrated a crack length analysis method to treat time sweep data. Steineder et al. (2022) focused on predicting the fatigue behaviour of asphalt mastics using both time-sweep and amplitude-sweep tests with two different sample geometries (cylindrical and hyperbolic specimens). Results for all tests were analyzed using a dissipated energy approach which was extended to a ratio of dissipated energy change (RDEC) and the dissipated energy per cycle (DECL) parameters. In the study conducted by Seif and Molayem (2022), time sweeps were performed over a range of strain amplitudes (1 to 6%), and data were analyzed using the ratio of dissipated energy change (RDEC) combined with the plateau value (PV) approach. The PV approach was used to rank the fatigue resistance of several binders and mixtures (tested using 4-Point bending fatigue) concurrently; the ranking between the two was compared to determine a relationship between binder and mixture fatigue resistance. Seif and Molayem (2022) concluded that there was a good correlation between the RDEC fatigue life for both binders and mixtures. Although binder fracture studies are typically in the domain of low-temperature tests, (Shi et al. 2021) investigated the cracking fracture properties of binders using both time sweeps and stress sweep tests at intermediate temperatures. Shi et al. (2021) explored the use of both the dissipated pseudostrain energy (DPSE) and the fatigue crack density parameters to evaluate the fatigue resistance of asphalt cements. Using the Griffith crack initiation/ propagation theories, a Modified Paris law was developed to model the crack growth of asphalt cements under shear loading.

Although time sweeps are still commonly used in research, conducting time sweep tests for fatigue resistance estimation is a habitually lengthy endeavour. Eventually, the development of several “PG-plus” binder tests, such as the linear amplitude sweep (LAS) test, DSR elastic recovery (DSR-ER), and the binder yield energy test (BYET) test been proposed as a relatively quicker alternative and to supplement the fatigue characterization shortcomings of the original PG system (Lyngdal 2015). The LAS test proposed from the original works of Johnson (2010) and (Hintz 2012), a simple test was proposed that ramped the strain from 0.1 to 30%. In stark contrast to the time sweeps it replaced, the

LAS takes approximately 5 minutes to complete. Hintz (2012) proposed a crack growth rate (da/dN) analysis of the amplitude sweep data, as it was observed that the binder specimen experienced significant cracking due to loading. It was observed that the crack growth rate exhibited two behaviours attributed to a "shallow" vs "deep" cracking phenomenon. In the "shallow" crack regime of the test (pre-peak conditions), the crack growth rate increases with increasing time due to the geometries dependence of crack initiation. The "deep" crack/ post-peak behaviour demonstrates a decreasing crack growth rate as it is more associated with crack propagation. This eventually led to the development of the critical crack length parameter, a_{CL}, which corresponds to a local minimum observed before the deep crack regime begins; this point corresponds to a peak in fracture energy release rate and the decrease in specimen torque from the peak torque (Hintz, 2012).

Eventually, the original crack length analysis was superseded by the simplified viscoelastic continuum damage (VECD) modelling as was found in the first version of the provisional standard, AASHTO TP 101. The VECD modelling required the "fingerprint" frequency sweep test at the testing temperature to calibrate the material parameter α. The approach then allows for fitting the pseudo-stiffness (C) vs damage (S) curve. The model parameters can be calculated from the C-S curve fitting to predict the binder fatigue life at several "applied" strain amplitudes analogous to different traffic loading levels. Since its acknowledgment as a provisional standard, numerous studies have adapted LAS test approaches to evaluate the effects of aging, modifiers, and other additives (Abed et al. 2020a; Cuciniello et al. 2020; Wang et al. 2020; Zhou et al. 2017). As of 2020, the LAS test has been revised to a full standard test, AASHTO T 391.

In later studies used to evaluate the temperature dependence of the LAS test, several researchers (Chen and Bahia 2021; Safaei and Castorena 2016) noted that the LAS data could be interchangeably shifted to different temperatures using the time-temperature superposition principle (TTSP) using the associated shift factors. Chen and Bahia (2021), for example, then proposed a simplified procedure to shift pseudo-stiffness damage (i.e., C-S) curves to the desired temperature. It was also concluded that failure criteria corresponding to the peak shear stress-strain amplitude were unsuitable for the time-temperature shifting procedure (Chen and Bahia 2021). Yan et al. 2021) compared the LAS test using several failure criteria (35% reduction in $G^*\sin\delta$, peak shear stress and peak released pseudostrain energy) to develop an intermediate ductility test referred to as the binder fracture energy (BFE) test. In the BFE test, the sample is loaded at a constant displacement rate to produce the true stress-true strain curve. As typical in other ductile materials, the curve can be described as having two "peaks." The first

peak occurs at the stress corresponding to the Yield Stress. What may be described as "strain hardening" occurs until the Ultimate Tensile Stress (UTS) is achieved; the fracture energy density (FED) is then calculated as the area under the curve up to the UTS. Yan et al. (2021) reported that using the reduction in $G^*\sin\delta$ and peak shear stress failure criteria was unsuccessful in demonstrating the predicted performance improvement of polymer modification. However, the PSE failure criteria demonstrated similar trends to the BFE test, which were both more successful at distinguishing between the unmodified and polymer-modified binders. Alternate methods of fatigue resistance ranking were proposed by Zhou et al. (2017) through the fatigue resistance energy index (FREI) and the ΔG parameter proposed by (Mainieri et al. 2021).

Two relatively less common DSR-based tests in provisional standard AASHTO TP 123 are the Binder Energy Yield Test (BYET) and the Elastic Recovery (ER-DSR) Test. These tests were first formalized as a provisional standard in 2016 as an alternative to the binder ductility (AASHTO T 51), and the elastic recovery (ASTM D6084) tests completed using a ductilometer. The BYET and ER-DSR tests are conducted on the DSR using the typical 8 mm parallel plate configuration with a gap height of 2 mm; unaged, RTFO, or PAV-aged materials can be used. BYET temperatures are selected as either 4 or 25°C to match the typical ductility test temperatures. The BYET uses a constant strain rate of 2.315%/s corresponding to an approximate extension rate of 5cm/min using a ductilometer; the test is completed at 2778% strain. The BYET requires the determination of the peak shear stress value (τ_{max}) as well as the strain amplitude corresponding to the maximum shear stress ($\gamma_{\tau,max}$). The binder yield energy is then calculated as the cumulative area under the stress-strain curve (AASHTO TP 123). The ER-DSR test is conducted at 25°C using the same shear rate as the BYET. However, the loading is terminated at a strain amplitude of 277.8%, and the sample is held in a resting state (zero-shear stress) for 30 minutes to monitor the recovery of the sample (AASHTO TP 123).

In a study by (O'Connell et al. 2017), the BYET (both 2009 and 2013 versions) was compared to four-point bending fatigue results for asphalt mixes containing the same six binders. O'Connell et al. (2017) ranked the yield energy and the $\gamma_{\tau,max}$ of samples tested at 5, 10, 20 and 28°C and demonstrated that the BYET test was unreliable at the temperature range extrema. Excessively low temperatures were said to create slippage between the binder and the DSR plate, producing very sudden decreases in yield energy. In contrast, the higher testing temperature produced stress-strain curves that did not peak before the termination strain level. From the available ranking scenarios, a significant change in the rankings was observed at 10 and 20°C, and in some cases, the yield energy from the unmodified binders was

higher than the polymer-modified binders due to a defined "double peak" behaviour. In general, O'Connel et al. (2017) reported a very poor correlation between the four-point bending results and the results of the BYET. Tariq Morshed et al. (2020) performed a similar study on polymer/ SBS-modified binders from 10 sources to compare the MSCR and the ER-DSR test with a ductilometer-based elastic recovery test. Tariq Morshed et al. (2020) then compared the same binders using the LAS test with the BYET. The study demonstrated that binders with a greater observed fatigue life (as determined by the estimated fatigue life, N_f, at 2.5% strain) typically exhibited higher binder yield energy.

5.2 Objectives

Based on the results of Chapter 4, the main goal of this study is to supplement the observations based on the simplified linear amplitude sweep healing (S-LASH) test and the flow observed during the amplitude sweep test. Thus, a review of the LAS test and several analysis methods found in the literature is to be conducted to determine which failure criteria are most suitable for LAS-based asphalt cement healing tests.

5.3 Materials and Methodology

The following experimental work was completed using an unmodified PG 58-28 asphalt cement. The 58-28 binder was aged using the rolling thin film oven to simulate short-term aging and then long-term aging using the pressure aging vessel for a single 20-hour period at 100°C. As laboratory testing was completed prior to the standardization of AASHTO T 351, the LAS procedure performed herein conforms to AASHTO TP 101-14.

5.3.1 Linear Amplitude Sweep Testing

Initially, the "fingerprint" frequency sweep was conducted from 0.2 to 30 Hz to assess the modulus of the undamaged sample and to calibrate the α-value for the subsequent Simplified-VECD analysis. During the amplitude sweep, the strain was ramped linearly from 0.1 to 30% over a period of 310 seconds with a frequency of 10 Hz; all testing was performed at 19°C. For each trial, a minimum of three replicates were used. S-VECD analysis was completed using an Excel spreadsheet initially developed by researchers at the Modified Asphalt Research Center (MARC) at the University of Wisconsin-Madison. The spreadsheet was then modified to determine the failure strain amplitude using several additional failure criteria found in the literature.

5.3.2 LAS Fatigue Analysis Methods Found in Literature

This section of the methodology will detail the failure criteria found in literature, including: VECD modelling (using MARC LAS templates 1.52, 1.55 and 1.56), pseudostrain energy (PSE) analysis, crack length analysis/ the fracture index, and other variations (i.e., CN and $C^2N(1\text{-}C)$). Rank-based methods such as fracture energy/ P-LAS analysis and ΔG will also be evaluated.

5.3.2.1 Viscoelastic Continuum Damage (VECD) Model

The VECD model, based on the extensive work of Schapery (Schapery 1975, 1984, 1990) as well as Park, Kim and Schapery (Park et al. 1996; Park and Schapery 1997), provides a framework for the fatigue behaviour of viscoelastic materials under minor strains. The VECD model adapts several critical theories on the elastic-viscoelastic correspondence principle and Schapery's work potential theory to model damage evolution during loading. Using the elasto-viscoelastic correspondence (E-VC) principle, it is possible to approximate a viscoelastic material over a very short time span. In conjunction with Schapery's work potential theory, the work potential of the viscoelastic material under loading is a function of the number of cycles applied during a cyclic test. The VECD had been successfully applied to model the fatigue behaviour of both neat and modified asphalt mixtures in several studies before it was applied to binders (Daniel and Kim 2002; Hintz et al. 2011; Kim et al. 1997; Kutay et al. 2008; Kutay and Lanotte 2018). The VECD model for asphalt mixtures requires the equivalence between the elastic and viscoelastic constitutive equations. To do so, the actual strain (ε) must be converted to the pseudostrain (ε^R) through the convolution integral:

$$\varepsilon^R(t) = \frac{1}{E^R}\int_0^t E(t-\tau)\frac{\partial \varepsilon}{\partial \tau}d\tau \qquad \text{Eqn. 5-1}$$

where E^R is a reference modulus, $E(t)$ is the relaxation modulus in the linear viscoelastic regime, t is time, and τ is the integration variable (sometimes referred to as the characteristic time). Creating these pseudo-parameters is necessary as the time-independent conversion viscoelastic stresses and strain are not physical quantities; thus, any hysteresis is eliminated when the sample is undamaged. Using E-VC, the pseudostrain is equivalent to the magnitude of the linear viscoelastic stress under cyclic loading conditions for small values of t. This allows the derivation of the pseudostiffness, C, which is defined as the ratio of stress, σ, to pseudostrain at a given time, *t*:

$$C(t) = \frac{\sigma(t)}{\varepsilon^R} \quad \text{Eqn. 5-2}$$

Moreover, for cyclic tests (performed at constant frequency and without the use of rest periods), the pseudostiffness can be calculated as the ratio of the peak complex modulus, $|E^*|$, at cycle, N, compared to the initial linear viscoelastic complex modulus for an undamaged sample:

$$C_N = \frac{|E_N^*|}{|E_{LVE}^*|} \quad \text{Eqn. 5-3}$$

The damage parameter concept, S, is then defined as:

$$S = \left(\int_0^t |\varepsilon^R|^p dt\right)^{1/p} \quad \text{Eqn. 5-4}$$

where *p* represents the damage growth rate determined indirectly from the slope of relaxation modulus of a single temperature frequency sweep through viscoelastic interconversion. The characteristic damage (C-S) curve can then be plotted to model the decrease in the material's pseudostiffness as damage increases over time (Hintz et al. 2011; Kutay and Lanotte 2018). The VECD modelling procedure is essentially unchanged for the asphalt cement formulation, but minor revisions to the calculation procedure have been made by MARC since it was initially standardized. The most obvious computational distinction is the simplification of the damage parameter, D(t):

$$D(t) = \sum [\pi I_D \gamma_i^2 (G_i^* sin\delta_i - G_{i-1}^* sin\delta_{i-1})^{\frac{\alpha}{1+\alpha}} (t_i - t_{i-1})^{\frac{1}{1+\alpha}}] \quad \text{Eqn. 5-5}$$

where I_D is the initial $|G^*|$ value at 1% strain amplitude, γ_i, G_i^*, δ_i and t_i are the strain amplitude, modulus, phase angle and time at the *i*th cycle, respectively. The relationship between $|G^*|\sin\delta$ and the damage parameter is fitted to a linearized power law in the form of:

$$\log(C_0 - |G^*|sin\delta) = \log(C_1) + C_2 \log(D) \quad \text{Eqn. 5-6}$$

where C_0 is the initial pseudostiffness corresponding to the $|G^*|\sin\delta$ at 0.1% strain amplitude, and C_1 and C_2 are curve fitting coefficients. Initially, the failure criterion was selected as a 35% reduction of the C_0 parameter calculated as:

$$D_{35} = 0.35\left(\frac{C_0}{C_1}\right)^{1/C_2} \quad \text{Eqn. 5-7}$$

From the D_{35}, the A_{35} and B parameters can be used to calculate the binder fatigue prediction parameter, $N_{f,}$ at the applied strain, γ_{app}. The fatigue life prediction parameter is then calculated as follows:

$$N_f = A_{35}(\gamma_{app})^{-B} \quad \text{Eqn. 5-8}$$

The applied strain (or maximum strain as is designated in the AASHTO T 315) is the theoretical maximum strain that a given pavement structure is expected to experience due to a certain level of traffic loading; commonly, γ_{app} = 2.5 and 5% values are used to simulate a low and high traffic scenario, respectively (AASHTO T 315). Consequently, Table 1 below contains a summary of the major changes from three different versions of the MARC LAS template concerning failure criteria, as well as the derivations of the alpha (α) parameter and C_0 (the initial pseudostiffness parameter). The changes from version 1.52 to 1.56 will be assessed in this study (Modified Asphalt Research Center 2022).

Table 5-1 Notable MARC LAS template changes (Modified Asphalt Research Center 2022).

Template Version	Last Updated	Failure Criteria	alpha (α)	C_0
1.52	April 2013	$0.65C_0$	$\frac{1}{m}$	1.0
1.55	September 2013	τ_{max}	$\frac{1}{m}$	1.0
1.56	March 2022	$0.65C_0$	$\frac{1}{m}+1$	$\lvert G^*_{init}\rvert \cdot \sin\delta_{init}$

5.3.3 Alternative LAS Failure Criteria and Analysis Methods

5.3.3.1 Phenomenological Failure Criteria: Shear Stress, CN and $C^2N(1-C)$

The peak shear stress-strain amplitude is a logical failure criterion as is related to the yield behaviour of a material; traditionally, deformation transitions from elastic to plastic at the yield point (Abdewi 2017). This criterion was adopted for time and amplitude sweep tests for asphalt cements. Due to the viscoelastic properties of asphalt cement, another logical failure criterion could be obtained from the peak in phase angle. Research on asphalt-sand mixtures demonstrated that the peak in phase angle always occurred after the peak shear stress and corresponded to a rapid decrease in the stress response of the mixtures (Wang et al. 2015). The CN failure definition was originally applied by (Safaei et al. 2014) for the LAS test; this failure criterion was primarily used in time sweep tests but was proposed

for the LAS as it was observed that the CN peak strain amplitude often corresponded to the peak shear stress-strain amplitude (Wang et al. 2015).

In 2018, Cao and Wang proposed the $C^2N(1-C)$ failure criteria when it was observed that other phenomenological failure criteria, such as CN and τN demonstrated unexpected trends when analyzing asphalt cement at different aging levels; this result could be attributed to peak "broadening" effect of aged binders and the whether the failure criteria corresponded to peak/post-peak shear stress conditions as shown in Figure 5-1. The proposed $C^2N(1-C)$ criteria were functionally quite similar to the original CN definition but with an added correction factor of $(C-C^2)$, which typically ranged from 0 to 0.25 (Cao and Wang 2018). For this study, the failure strain corresponding to the peak shear stress, CN, $C^2N(1-C)$ will be designated as $S_{PeakStress}$, S_{CN} and $S_{C2N(1-C)}$, respectively; the strain amplitude corresponding to the peak phase angle will not be used.

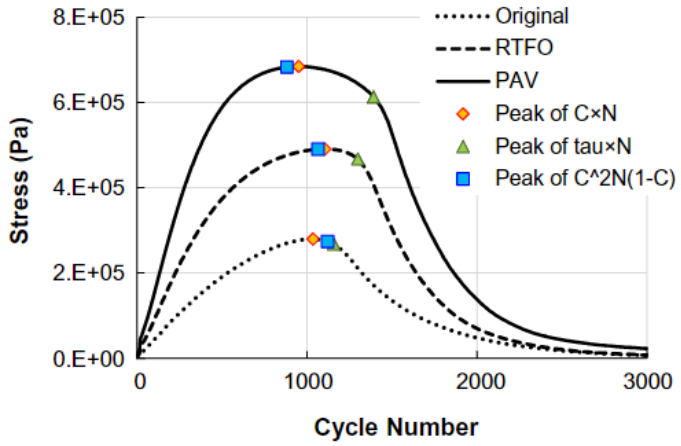

Figure 5-1 Failure points for CN, τN and $C^2N(1-C)$ for an unaged, RTFO and PAV-aged 58-28 binder (Cao and Wang 2018).

5.3.3.2 Pseudostrain Energy (PSE) Analysis

The pseudostrain energy (PSE) density analysis of a continuous LAS test was proposed as a unifying failure criterion by Wang et al. (2015). The PSE analysis was intended to compensate for the omission of the phase angle in the original VECD LAS modelling by providing a mechanistic-based parameter and the "true" assessment of damage effects. As shown in Figure 5-2a, a viscoelastic material should exhibit perfectly linear elastic behaviour. However, a deviation from linearity can be observed when the material has been "damaged". The resultant released and stored pseudostrain energy can be analyzed to evaluate the asphalt cement using the time-independent pseudo-strain domain. In Figure 5-

2a, the blue data point series represents the observed shear strain during an amplitude sweep experiment. The stored pseudostrain energy density, W_S^R, which is defined by the triangle bounded by the solid red line approximating these data points, is calculated as:

$$W_S^R = \frac{1}{2} C(S)\left(\gamma_p^R\right)^2 \quad \text{Eqn. 5-9}$$

where C is the pseudostiffness at the damage level S, and γ_p^R is the peak pseudostrain amplitude (Safaei and Castorena 2016; Wang et al. 2015). The total cumulative pseudostrain energy, W^R_{Total}, is approximated from the peak pseudostrain as:

$$W_{Total}^R = \frac{1}{2}\left(\gamma_p^R\right)^2 \quad \text{Eqn. 5-10}$$

At the desired cycle, the total PSE is bound by the green dotted line and the red vertical line. The released PSE, W_R^R, caused by the formation and propagation of cracks in the asphalt cement sample, is calculated as the difference between the total and stored PSE:

$$W_R^R = W_{Total}^R - W_S^R = \frac{1}{2}(1 - C) \cdot \left(\gamma_p^R\right)^2 \quad \text{Eqn. 5-11}$$

The depictions of the stored and released PSE, as shown in Figure 5-2b, demonstrate that the stored PSE reaches a maximum and then decreases as the material loses the ability to store additional energy. The released PSE, however, continues to increase in magnitude until the termination strain amplitude in the sweep as damage accumulates within the sample. Wang et al. (2015) determined that the peak stored PSE was a reliable, energy-based indicator of sample failure as it was not only dependent on the peak shear stress value but also the number of cycles in the test. As a simplification, the failure strain corresponding to the peak stored PSE will be designated S_{PSE} for this study. Functionally, it was observed that the peak stored PSE provides computationally similar results as the stress multiplied by the number of cycles, τN (Cao and Wang 2018); the strain amplitude corresponding to this peak τN (i.e., $S_{\tau N}$) will also be explored herein.

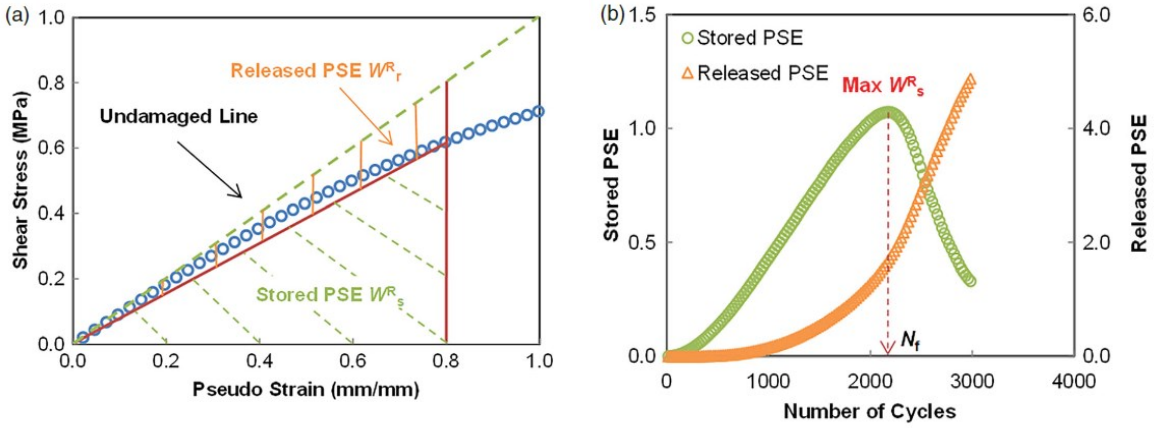

Figure 5-2 LAS-based PSE definition and evolution: (a) PSE distribution and (b) evolution of stored and cumulative released PSE from (Wang et al. 2015).

5.3.3.3 Crack Length Analysis (Fracture Index)

For asphalt materials tested in time sweep tests, a power law relationship between the energy release (J) and crack growth (ċ) rates was initially proposed in the original works of Hintz (2011) and again in Hintz and Bahia (2013). The relationship was developed directly for time sweep tests on asphalt cements on the DSR and is calculated as follows:

$$J = \frac{|G^*|\gamma^2 h}{2r^2(r-c)}\left(r - c + z\left(1 - e^{-\frac{c}{z}}\right)\right)^3 (1 - e^{-\frac{c}{z}}) \qquad \text{Eqn. 5-11}$$

where $|G^*|$ is defined as the complex shear modulus, γ is the shear strain amplitude, r is the sample radius (i.e., 4 mm when using the 8 mm DSR plate), h is the sample height (i.e., 2 mm when using the 8 mm DSR plate), c is the crack length, and z is a numerical factor. Based on crack propagation in concrete media, Eq. 6-13 was modified to include the fracture energy rate parameter J/J_f:

$$\frac{J}{J_f} = \frac{|G^*|\gamma^2 h}{2r^2(r-c)J_f}\left(r - c + z\left(1 - e^{-\frac{c}{z}}\right)\right)^3 (1 - e^{-\frac{c}{z}}) \qquad \text{Eqn. 5-12}$$

where J_f is the fracture energy obtained from a monotonic test. Based on this derivation for asphalt cements, the simple fracture index, $|G^*|\gamma^2/J_f$, was proposed, and it was hypothesized that smaller fracture index values indicate better fatigue resistance as the crack propagation occurs at a lower rate. This fracture index model was then applied to the LAS test in the same work by Hintz and Bahia (2013), as it was postulated that a fracture mechanics-based approach would be preferred due to the edge fracture observed during loading. The edge fracture phenomenon was correlated to a release in energy due to

the change in the cross-section surface area due to the effective sample radius. A simple correction was applied to the model as the fracture energy release rate, G_f could be rewritten with the effective sample radius = initial radius (r_{init}) – the crack length (a). The resultant crack length per cycle (da/dN) analysis (Hintz and Bahia 2013) resulted in the creation of the critical cracking length parameter (a_{CL}), denoting the point at which the cracking rate reaches a local minimum. The global maximum observed in the da/dN curve indicated an unsteady, rapid failure related to a rapid decrease in the applied torque. For this study, two failure criteria were used: the strain amplitude corresponding to the critical crack length parameter (designated as S_{FI_aCL}) as well as the strain amplitude corresponding to the global maximum value (designated as S_{FI_peak}).

5.3.3.4 Ranked Analysis: Pure-LAS (P-LAS) and ΔG

Several studies observed the inherently poor correlation between the fatigue life predictions of the original VECD modelling in the LAS standard and asphalt cement aging (Cao and Wang 2018; Mainieri et al. 2021; Zhou et al. 2017). Zhou et al. (2017) proposed a further adaptation of Hintz's fracture index, $|G^*|\gamma^2/J_f$, The Pure Linear Amplitude Sweep (P-LAS) test proposed had the same framework as the original LAS test without the "fingerprint" frequency sweep and with the added advantage that the analysis method could be completed on past LAS data. From the PLAS, the reciprocal index known as fatigue resistance energy index (FREI) was proposed:

$$FREI = \frac{J_{f-\tau_{max}}}{G_{0.5\tau_{max}}} \cdot \left(\gamma_{0.5\tau_{max}}\right)^2 \qquad \text{Eqn. 5-13}$$

where $J_{f\text{-}\tau max}$ is the shear fracture energy up to the maximum shear strain value, $G_{0.5\tau max}$ and $\gamma_{0.5\tau max}$ are the shear moduli and the strain amplitude is evaluated at half of the maximum shear stress, respectively. Smaller FREI values indicate worse fatigue resistance, as it was hypothesized that the reciprocal index (J_f/G) better captured the effect of aging as the binder became stiffer and more brittle (Zhou et al. 2017). Based on similar observations by Mainieri et al. (2021), the ratio of the initial G^* and the G^* observed at the strain amplitude corresponding to the peak shear stress (i.e., the $\Delta G_{\tau peak}$ parameter) was used and demonstrated similar success when factoring the age of the asphalt cement. Both the FREI and $\Delta G_{\tau peak}$ parameters are assessed and verified in this study.

5.4 Results and Discussion

5.4.1 VECD Analysis

Table 5-2 below contains the S-VECD Model parameter for each aging level and each LAS template. The N_f fatigue predictions for both 2.5 and 5% applied strain can be observed in Figure 5-3 below; it should be noted as well that the y-axis is presented using a log scale due to the dramatic increase in N_f values when switching to Template 1.56. When comparing N_f at 2.5% applied strain, it is observed that the change from Template 1.52 to 1.55 is accompanied by an increase in N_f, but more interestingly there is a change in the ranking from Unaged < RTFO < PAV (1.52) to Unaged > RTFO > PAV (1.55). This can be attributed to the change in damage level and its effect on the 'A' model parameter when all other factors are equal. Overall, the change to Templates 1.52 to 1.56 reflects an increase in N_f values due to the increase in the A model parameter because of increases in either C_0 and/or C_1 and a decrease in C_2.

Table 5-2 VECD model parameters for unaged, RTFO and PAV-aged material.

Age	Template	α	D_f (%)	C_0	C_1	C_2	A	B	Summed Error
Unaged	1.52	1.169	35.0	1.000	0.034	0.619	3.856E+04	2.339	1.146
RTFO	1.52	1.328	35.0	1.000	0.063	0.503	3.594E+04	2.657	0.549
PAV	1.52	1.772	35.0	1.000	0.107	0.410	6.094E+04	3.543	0.284
Unaged	1.55 (1/m)	1.169	36.9	1.000	0.038	0.602	3.893E+04	2.339	1.095
RTFO	1.55 (1/m)	1.328	52.0	1.000	0.077	0.471	1.046E+05	2.657	0.514
PAV	1.55 (1/m)	1.772	57.3	1.000	0.155	0.349	3.350E+05	3.543	0.410
Unaged	1.55 (1/m+1)	2.169	36.9	1.000	0.050	0.542	1.717E+06	4.339	0.546
RTFO	1.55 (1/m+1)	2.328	52.0	1.000	0.093	0.431	5.748E+06	4.657	0.292
PAV	1.55 (1/m+1)	2.772	57.3	1.000	0.171	0.330	1.450E+07	5.543	0.350
Unaged	1.56	2.169	35.0	2.552	0.065	0.530	1.323E+07	4.339	3.202
RTFO	1.56	2.328	35.0	4.994	0.125	0.465	8.228E+07	4.657	13.444
PAV	1.56	2.772	35.0	9.486	0.205	0.424	3.712E+09	5.543	53.444

The change from α = 1/m to α = 1/m + 1 produces an overall decrease in the template model fit summed error parameter but increases in N_f can be attributed to a similar effect on the resultant increase on the A parameter. The most recent change to the 1.56 template version exhibits the most severe

increase in N_f values primarily due to the change from $C_0 = 1$ to $C_0 = |G^*_{init}|\sin\delta_{init}$ leading to A parameter values. It should be noted that since each template was treated with the same datasets, the much larger increase in summed error in Template 1.56 results from the increased fitted values in the S-VECD model, reflecting a change in scale and not necessarily a "true" increase in error. When observing Template 1.55 N_f results at 5.0% strain, the observed ranking changes, and the RTFO-aged binder has the highest projected fatigue resistance compared to unaged and PAV-aged binders. This result can be explained by plotting each fatigue model, as shown in Figure 5-4. In Figure 5-4 (right), the fatigue parameter at each strain amplitude is derived from the A and B parameters calculated from the S-VECD model, where A represents the y-intercept and B represents the slope of a line. When plotting the three materials in the same graph, there is a cross-over at approximately 3.5% strain where the RTFO aged binder becomes the binder with the "better" fatigue resistance; if the maximum strain in the analysis increases beyond 6%, another cross-over would occur and the unaged binder would have a higher N_f value compared to the PAV aged binder. This method can also be used when comparing the three aging levels using the 1.52 template version; as the A parameter for all three binders is of relatively similar magnitude, the steepness of the slope is the most significant contributing factor as to what rank the three binders will have at 2.5 and 5.0% strain.

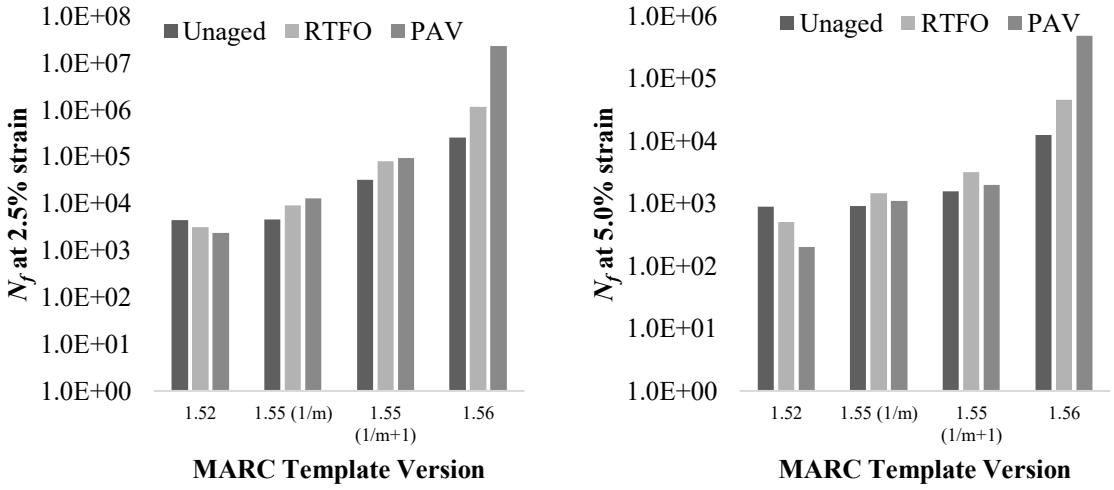

Figure 5-3 Projected N_f for each template (note: error bars have been omitted due to the use of a logarithmic scale).

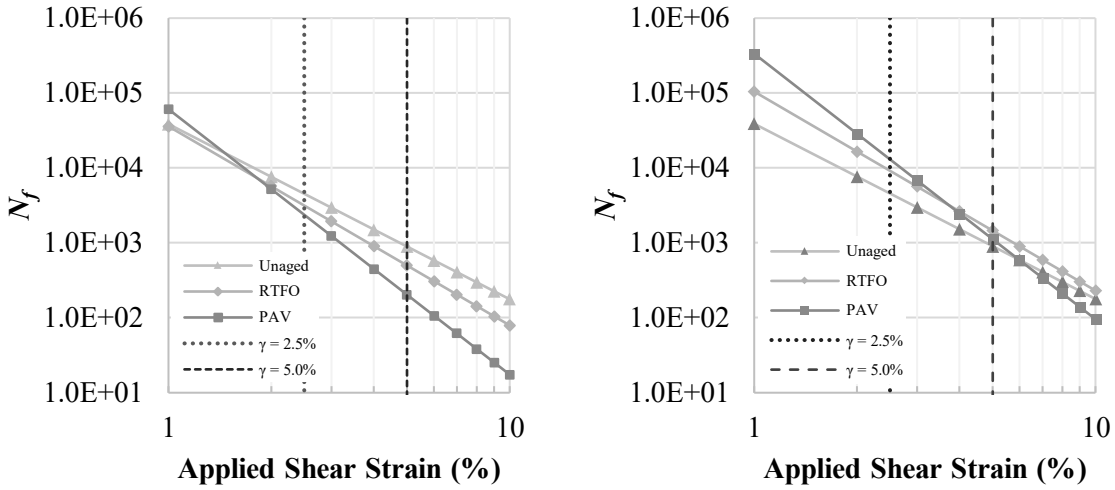

Figure 5-4 N_f fatigue model for unaged, RTFO and PAV aged binders: Template 1.52 (left) and Template 1.55 using $\alpha = 1/m$ (right).

5.4.2 LAS Failure Criteria Found in Literature

From the FI analysis results in Table 5-3, it is observed that the critical crack length increases with aging, indicating that the fracture "performance" increases with increased aging. In Table 5-3, the location and magnitude of the peak in the da/dN curves are also provided; a representative plot of the da/dN curves for all three aging levels is also provided in Figure 5-5. It should be noted that although the peak crack length/ strain increases with aging, the peak magnitude is quite similar. Critically, it can also be observed that there is increasing scatter in the DSR measurements at higher strain amplitudes and that the crack growth rate appears to converge to similar values at higher strain levels despite the noise.

The five remaining failure strain criteria, S_{PSE}, S_{CN}, $S_{\tau N}$, $S_{C2N(1-C)}$ and $S_{PeakStress}$, for the 58-28 binder can be found in Figure 5-6. Generally, the trends are expected based on the issues observed in literature when comparing different aging levels (Cao and Wang 2018; Zhou et al. 2017). The failure strain for the PSE/ τN analysis are almost identical and increase with increasing aging. The failure strain observed from the Peak Stress, CN and $C^2N(1-C)$ generally increases from the unaged to RTFO-aged binder, and then failure strain decreases at a lower strain amplitude PAV-aged binder. In the case of CN, the error bars indicate a significant overlap in the ranking of the unaged and PAV-aged binder, while a similar result can be observed for the $C^2N(1-C)$ criterion. At all aging levels, however, the strain amplitude corresponding to the peak shear stress value is the most conservative of all failure criteria.

Table 5-3 Fracture index analysis

Age	a_{CL} (mm)	a_{Peak} (mm)	S_{CL} (%)	S_{Peak} (%)	Peak Magnitude (mm/cycle)
Unaged	0.43	0.83	8.35	10.39	0.0026
RTFO	0.63	1.09	8.42	11.52	0.0025
PAV	1.06	1.62	9.87	13.59	0.0026

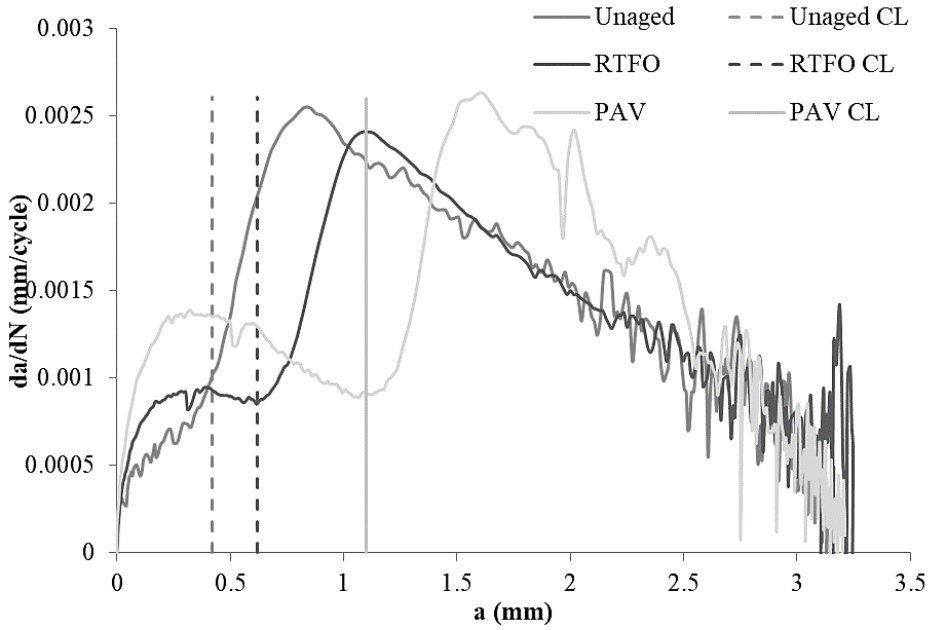

Figure 5-5 Representative da/dN curves for unaged, RTFO and PAV-aged binders.

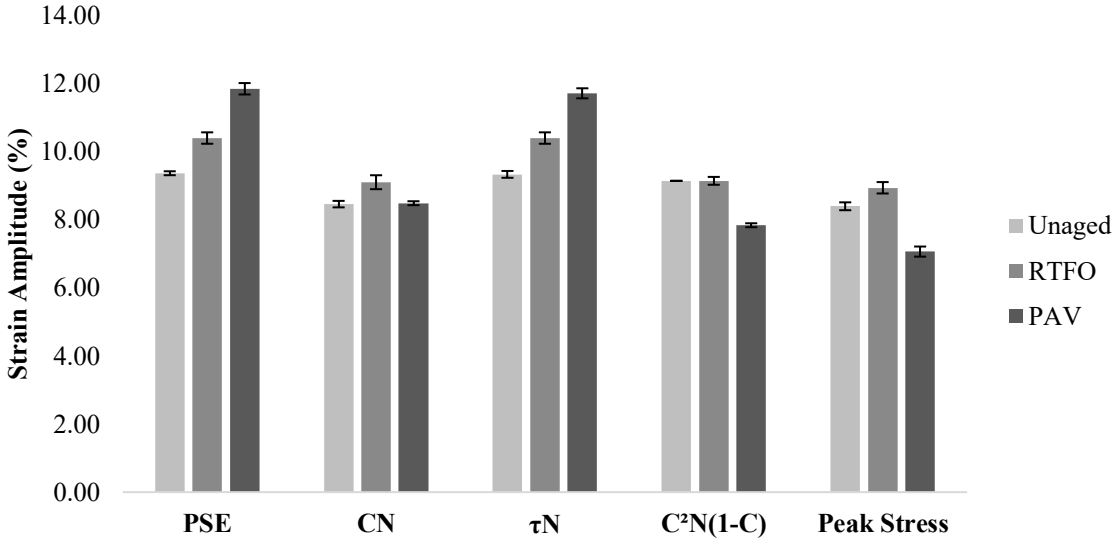

Figure 5-6 Failure strain values for stored PSE, CN, τN, $C^2N(1-C)$ and Peak Stress for unaged, RTFO and PAV aged binders.

5.4.3 PLAS and ΔG

From the PLAS analysis, it was observed that fatigue resistance (FREI) decreased with increased aging, as shown in Figure 5-7 (left). A similar trend was observed with decreasing ΔG values, as shown in Figure 5-7 (right). The similarity between the FREI and ΔG analysis methods is not entirely unexpected. Both methods rely upon the peak stress-strain amplitude values and, as such rely on essentially the same data range, thus, producing similar results. The demonstrated decrease in both the FREI and ΔG values with increased aging verifies the works of both Zhou et al. (2017) and Mainieri et al. (2021). However, the more complex index formulation of the FREI parameter appears to provide a better distinction compared to the simpler ΔG due to the addition of the shear modulus and strain at $0.5\tau_{max}$. As is evident by the PLAS analysis, the drastic decrease in the FREI value for the PAV-aged material indicates that the rate of change in the shear modulus (being proportional to both the rate of change in shear stress and applied torque) seems to be a significant factor in determining the "fatigue performance." In the opinion of the author, based on the findings of the FREI and ΔG analysis, the $S_{PeakStress}$ value becomes the most logical failure condition due to its traditional phenomenological importance in material science and the added benefit of being the simplest failure criterion to acquire. Therefore, the peak shear stress-strain amplitude is recommended for future healing studies as it can be obtained without significant post-processing of the LAS data, thus reducing the potential for any transpositional or computational errors.

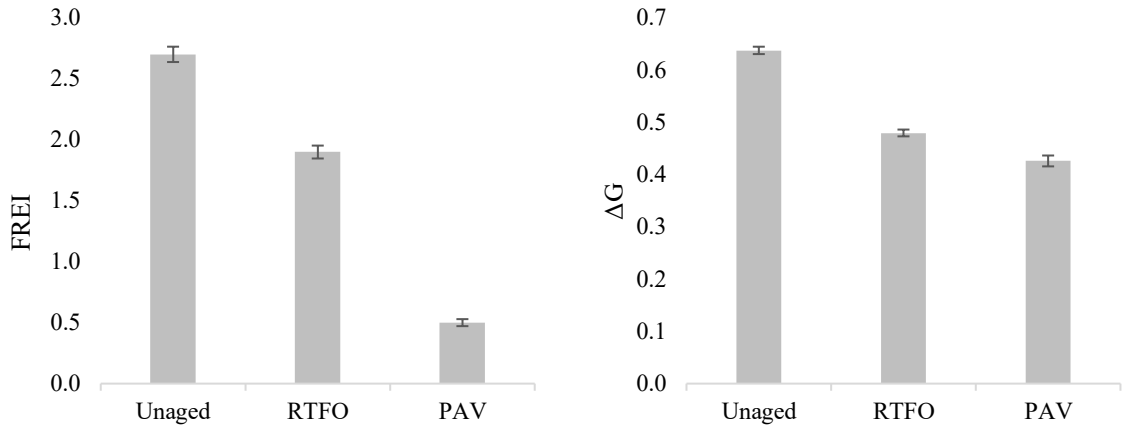

Figure 5-7 Fatigue resistance energy index (left) and ΔG (right) rankings for the unaged, RTFO and PAV aged binders.

5.5 Conclusions

The initial rationale of the study was centred around the common assumption that the fatigue life of asphalt materials decreases with increased aging. To verify that assumption, a single unmodified binder was tested at several aging levels using the linear amplitude sweep (LAS) test. A wide variety of failure analysis methods were used, including phenomenological variables/ indices (peak shear stress, τN, CN, $C^2N(1-C)$), fracture mechanics (a_{FI_CL} and a_{FI_peak}) and continuum-based/ mechanistic parameters (VECD and PSE). Based on the above, the following conclusions can be drawn:

- The VECD analysis demonstrated that the N_f-fatigue life predictions increased significantly with the change from the original (1.52) LAS template to the more recent (1.56) template due to the change in the C_0 parameter. The change of the $\alpha = 1/m$ to $\alpha = 1+(1/m)$ for template v 1.55 merely scales the fatigue life predictions but does not change the rankings at either 2.5 or 5% applied strain.
- Several LAS failure strain amplitudes, such as released S_{PSE}/ $S_{\tau N}$, and S_{FI_peak} correspond to post-peak stress-strain behaviour; these values typically lag the stress-strain peak by approximately 2 to 4% strain depending on the aging level.
- Failure criteria such as S_{FI_CL}, S_{CN}, and $S_{C2N(1-C)}$ correspond to the peak behaviour of the shear stress-strain curve. However, the peak shear stress failure criterion is the most conservative of all the proposed failure criteria at all aging levels.
- Both the FREI and ΔG parameters, which rely upon the shear stress peak strain amplitude, were verified to decrease with increased aging, as described in their respective studies. Although the ΔG parameter is a much simpler, straightforward parameter, the index formulation of the FREI parameter was better able to distinguish a difference in aging level.
- The peak shear stress value is recommended for future healing studies as it can be obtained without post-processing the LAS data, thus, reducing the potential for any transpositional or computational errors that may arise with the VECD or crack length analysis methods.

One potential criticism of this study could be the decision to use one single binder at several aging levels instead of several binders. However, in the author's opinion, standard laboratory aging was the optimal solution for providing a predictable, repeatable, and controllable method to tune the thermorheological behaviour of the different specimens for testing. By predictably oxidizing the control binder, the stiffness can be increased by changing the ratio of the SARA fractions without introducing potential confounding factors that may arise due to the binder source or other modifications.

Chapter 6
Linear Amplitude Sweep (LAS) Failure Criteria using Complementary Characterization Parameters

6.1 Introduction

The stress-strain response of a complex material can be evaluated using simple tests such as steady shear, stress relaxation, creep, oscillatory shear, and steady extension tests using rheometers (Deshpande 2010). In typical small amplitude oscillatory shear (SAOS) testing, a rheometer applies small strains to complex fluids, and the resultant strain response is linear. Oscillatory shear, used for viscoelastic materials, varies stress and strain cyclically; by increasing or decreasing the frequency of the test, the material response can be evaluated for different simulated timescales. In the linear regime, the shear stress, τ, is proportional to the shear strain, γ_0, through the simple Hookean relation:

$$\tau = |G^*|\gamma_0 \sin(\omega t) \qquad \text{Eqn. 6-1}$$

where G^* is the complex shear modulus, ω is the angular frequency, and t is time. The complex shear modulus is composed of the storage (G') and loss (G") moduli, and the phase lag or angle (δ) between the in-phase and out-of-phase components indicates whether the viscoelastic material behaves more as a solid or liquid. Different viscoelastic materials (e.g., polymer melts, gels, emulsions, etc.) have a unique response at different frequencies/ timescales. However, the small strain response is always complex, and relaxation at these frequencies can give insight into the microstructure or molecular organization of the material (Deshpande 2010). Depending on the geometry, whether it is the parallel-plate (PP), cone-plate (CP) or concentric cylinder (CC) geometry, the calculation of several rheological parameters (e.g., viscosity, complex shear modulus, etc.) can be difficult to assess due to potential measurement artifacts (or perturbations). Correctly identifying these artifacts remains one of the greatest challenges against accurate measurements in rheology.

Under ideal simple shear flow conditions, the accurate calculation of stresses and strains requires several basic assumptions: (1) the material remains homogeneous throughout the test, (2) the volume does not change within the boundaries of the testing geometry, (3) the geometry remains unchanged and occupies the volume assumed in theory, and (4) a uniform shear load is applied in the testing direction. For parallel-plate rheometers, some commonly observed perturbations include sample volume perturbations (i.e., reductions in sample volume), sample-plate wall slippage, particulate

migration, thixotropic shear banding, instability flow/ edge fracture, turbulence, and viscous dissipation (Coussot 2014).

Sample volume perturbations tend to occur due to the installation of the sample between the plates and often manifest due to under-filling between the plates due to improper trimming technique. As a result of the incorrect geometry, the boundary surface area between the specimen and air will experience more significant stress. As the shear rate at the edge of the sample increases, the sample can then flow at an increased rate, decreasing the effect radius of the sample. Shear banding occurs commonly in a homogenous material with thixotropic tendencies; shear bands form when the material is loaded at a shear rate below a material-specific critical shear rate, and a local unstable flow state is achieved as the material restructures itself. The resultant heterogeneous velocity profile within the sample creates bands with different apparent shear rates at different heights. As the shear banding effect will only be abated at a sufficiently high shear rate, the bottom portion of the cylindrical sample will remain unaffected by the shearing of the top plate, thus remaining stationary with an effective shear rate of zero (Coussot, 2014). Instability flow or edge fracture is often associated with shear banding as the thixotropic restructuring mechanism also plays a role in these edge effects. Instability flow occurs when the magnitude of these non-homogenous normal forces across the edge of the sample exceeds the material limits; the resultant geometry change appears as "necking," as shown in Figure 6-1 (Coussot 2014; Anderson 2001). As demonstrated in several studies (Anderson et al. 2001; Aurilio et al. 2021; Hintz and Bahia 2013; Safaei and Castorena 2016), asphalt cement is not immune to edge effects under loading although the phenomenon is poorly understood in the asphalt industry.

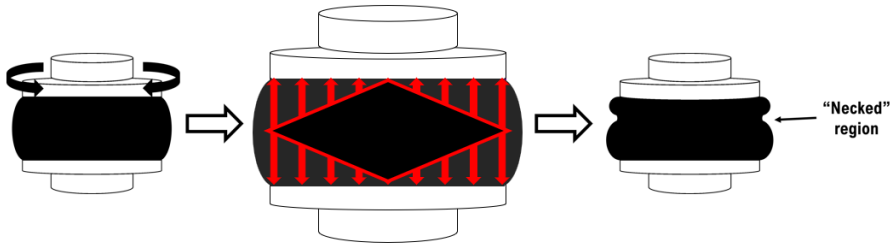

Figure 6-1 Representation of the normal force distribution in a DSR sample and the resultant "necking" phenomenon.

Anderson et al. (2001) prepared one of the first studies to evaluate binder instability flow during DSR testing. Anderson et al. prepared a comprehensive study on four RTFO-aged binders, including: an unmodified base binder, a 4% SBS modified binder, a 4% EVA modified binder and a chemically modified base binder. All binders were subjected to strain-controlled time sweeps in isostiffness

conditions ranging between 5 and 45 MPa requiring test temperatures from -4 to 12°C. A separate set of samples were similarly tested at different gap sizes (1, 2, and 3mm) as it was hypothesized that failure should be independent of gap size. Anderson et al. (2001) reported that when removing the DSR plates after observing distortion on the surface of the sample, "cracks" could be observed in the binder, as shown in Figure 6-2. It was concluded that any loss of modulus observed due to repeated shearing could lead to either one of two failure modes: (1) internal microcracking and (2) edge fracture. Based on that initial study, it was determined that fatigue cracking occurs when the initial modulus is above 15 MPa, and edge fracture occurs when the modulus is lower at around 5.0 MPa. At lower strains, fatigue life was dependent on gap height, and as a result, failure could not be attributed to fatigue microcracking for larger gap sizes (Anderson et al. 2001).

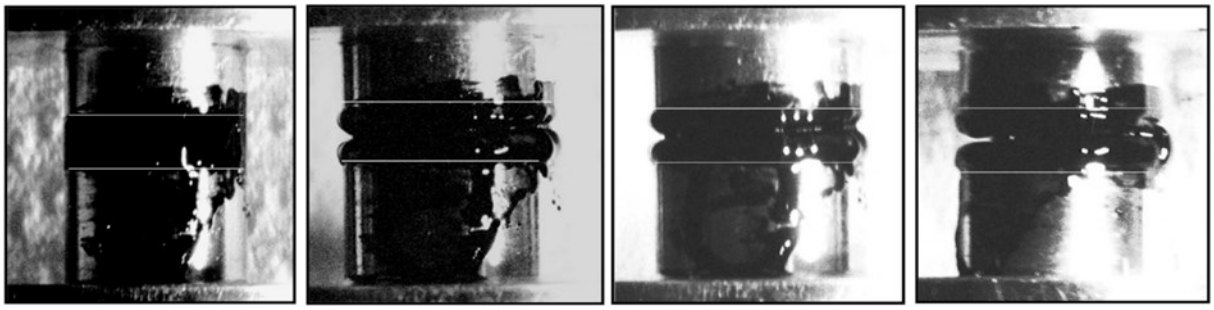

Figure 6-2 Specimen (a) before the test, (b) at beginning of the drop of modulus, (c) during the decrease of modulus, and (d) after a 90 percent decrease of modulus in a time sweep test from (Anderson et al. 2001).

In the development of the linear amplitude sweep (LAS) test by Hintz (2012), the surface of the DSR specimens was painted after loading to examine the reduction in sample radius due to cracking, as shown in Figures 6-3a. Using image analysis techniques, the ratio of paint to binder was evaluated at increasing time lengths, and it determined that a relationship existed between the effective radius of the binder connecting the two parallel plates and the DSR torque measured (Hintz 2012). Despite the reasonably good correlation between the observed crack length (a_{obs}) and crack length predicted (a_{pred}) through torque measurements, the torque measurements often overestimated the crack length, demonstrating the difficulty of correcting for a reduction in the sample radius (Coussot 2014; Hintz 2012). In a study by Tan et al. (2012), the crack surface of several RTFO-aged DSR samples was imaged using an optical microscope with up to 200x magnification using a digital zoom function. Tan et al. (2012) observed radial hairline cracks at the edge of the sample at approximately 20% of the initial modulus, while circular/ concentric "cracks" were observed closer to the inner section when the

observed modulus decreased past 10% of the initial value as shown in Figure 6-3b (Tan et al. 2012). Higher-resolution images of DSR sample cracking are found in Figure 6-3c (Qiu et al. 2020).

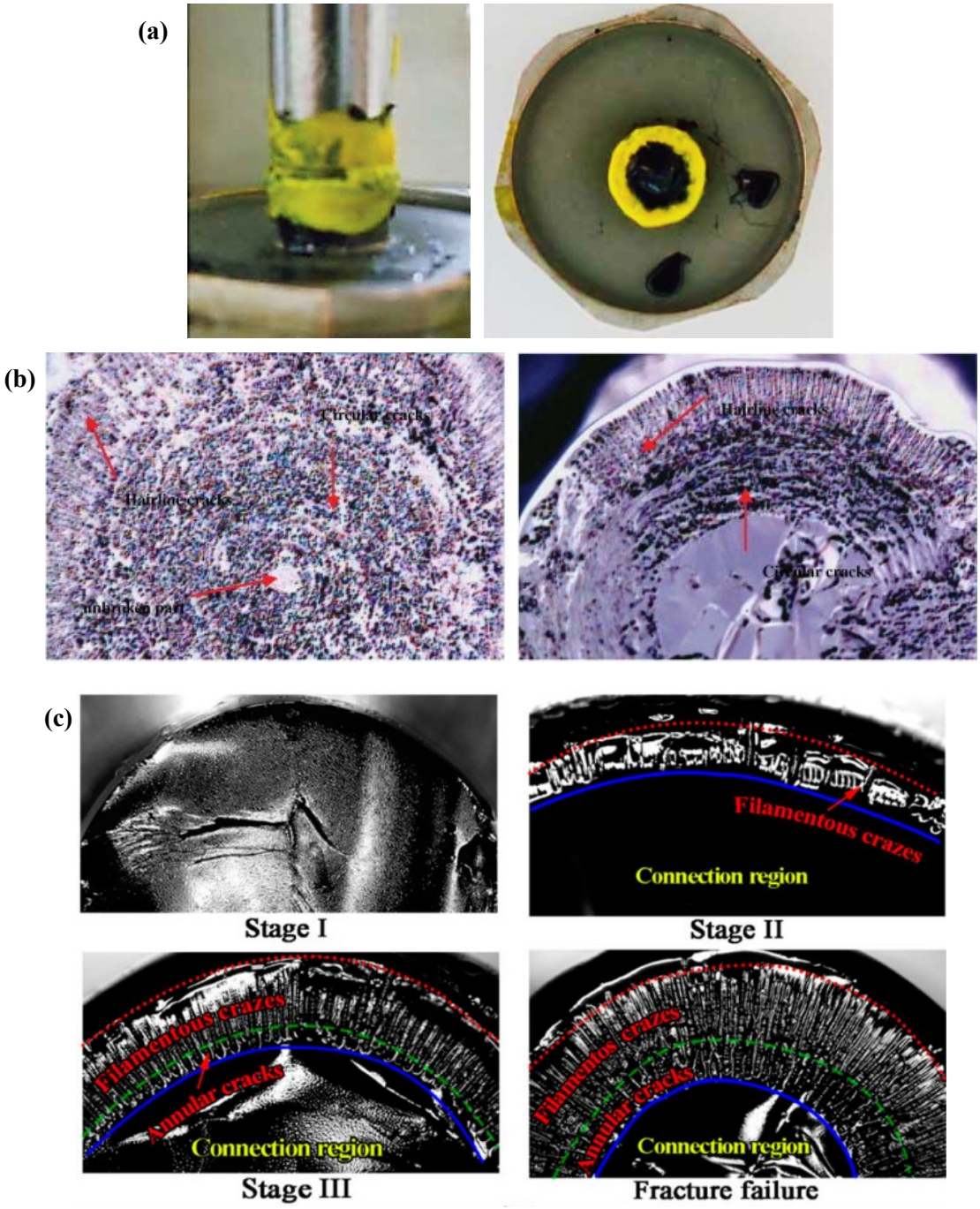

Figure 6-3 (a) Paint DSR sample before and after loading (Hintz and Bahia 2013), (b) hairline cracks and the circular crack region observed by (Tan et al. 2012), (c) DSR sample crazes observed by (Qiu et al. 2020).

In a different study by Safaei and Castorena (2016), the linear amplitude sweep was conducted on four pressure aging vessel (PAV) aged binders from 5 to 30°C to examine the LAS test at different climatic temperatures using the peak released pseudostrain energy failure criteria. Using the LTPPBind software, several geographical regions were identified in which each binder would be commonly used; the average morning springtime temperature (T_{AMS}) was then estimated at a depth of 25 mm in a typical pavement structure and compared against the standard climatic PG testing temperature. Through the comparison, it was determined that the intermediate PG minus 4°C would be the ideal temperature for subsequent LAS tests. Figure 6-4 shows that Safaei and Castorena (2016) observed three failure modes with increasing temperature: adhesive failure, cohesive cracking (with or without some observable flow), and instability flow. Fatigue testing results would be considered valid only for samples that experienced cohesive cracking, which occurred for binders with an initial modulus of approximately 12 to 60 MPa at 10 Hz. Using the time-temperature superposition principle (TTSP), Safaei and Castorena (2016) modified the standard VECD analysis damage parameter, S, at time, t, by incorporating the reduced time, ζ, parameter:

$$S(t) = \sum_{i=1}^{n}\left[\frac{DMR}{2}\left(\gamma_{p_i}^{R}\right)(C_{i-1} - C_i)\right]^{\alpha/(1+\alpha)} \cdot [\zeta_i - \zeta_{i-1}]^{1/(1+\alpha)} \qquad \text{Eqn. 6-2}$$

where DMR is the dynamic modulus ratio = $|G^*|_{fingerprint}/|G^*|_{LVE}$, α is a material dependant constant, and γ_{pi}^{R} and C_i are the peak pseudostrain and the pseudostiffness at *i*th cycle, respectively. By incorporating the reduced time into the damage equation, the study demonstrated that the C-S curves for valid samples could be shifted to a single reference temperature (i.e., 20°C), and ad hoc fatigue life predictions could be made.

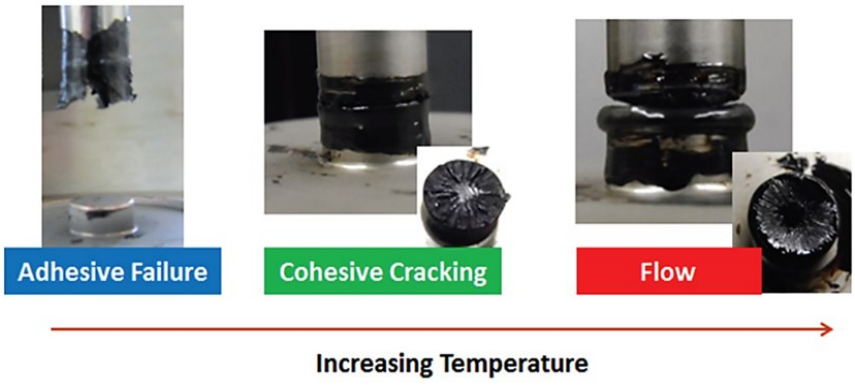

Figure 6-4 DSR sample failure modes as described and demonstrated by Safaei and Castorena (2016).

6.2 Materials and Methodology

The following experimental work was completed using an unmodified PG 58-28 asphalt cement. The 58-28 binder was tested in an unaged (UA) state and then aged using the rolling thin film oven (RTFO) to simulate short-term aging. The RTFO-aged material was subsequently aged using the pressure aging vessel (PAV) for a single 20-hour period at 100°C (the typical aging temperature used to simulate long-term aging in Southern Ontario). As an extension of the previous chapter, the LAS test is evaluated using three complementary parameters to further examine specimen failure/ geometry change during the amplitude sweep. Included in this chapter is the analysis of the normal force (F_n), the electric torque (M_{el}) and the DSR visual analysis flow strain amplitude (FSA). As with the previous chapter, the LAS test was conducted at the intermediate temperature (19°C), but tests were also conducted at 13 and 25°C to evaluate the effect of temperature. The supplementary temperature, 13°C, was selected to ensure that the temperature range exceeded the intermediate PG temperature minus 4°C recommendation by Safaei and Castorena (2016).

6.2.1 Normal Force

One of the key assumptions in the accurate rheological measurement of complex materials is that the geometry of the specimen remains constant during continuous shear loading. To be more precise, edge fracture and the associated phenomenon is theorized to occur when the second normal force difference reaches a critical magnitude. The normal stress difference within a parallel-plate sample is calculated as follows:

$$(\tau_{11} - \tau_{22}) - (\tau_{22} - \tau_{33}) = \frac{2F_N}{\pi R^2}\left(1 + \frac{1}{2}\frac{d \ln F_N}{d \ln \dot{\gamma}_a}\right) \quad \text{Eqn. 6-3}$$

where $\tau_{11} - \tau_{22}$ is the primary normal stress difference, $\tau_{22} - \tau_{33}$ is the secondary normal stress difference, R is the radius of the disk, F_N is the total normal force on the disk, and $\dot{\gamma}_a$ is the shear rate at the outer edge of the disk. Under shear loading, the normal stresses are distributed in the cross-section of the sample in the configuration depicted in Figure 6-1, with the maximum normal stresses occurring at the outer edge of the plate. This normal force distribution creates a "thrust" against the top and bottom plates. Once the critical magnitude is achieved, the vertical extensional flow occurs, which appears as necking. The critical magnitude is a function of both the geometry of the sample and the air-fluid surface tension (Γ) of the specimen, which is proportional to the modulus of the fluid and the length of the interface (Anderson et al. 2001; Hemingway and Fielding 2019).

Anderson et al. (2001) theorized that as microcracks develop to relieve stress, the viscosity of the binder will decrease, corresponding to a drop in the stiffness. It was also theorized that this stress relief softening mechanism competes with the force imbalance, ultimately leading to the observed decrease in modulus (Anderson et al. 2001). As the shear rate is unchanging during time sweep tests, the normal force remains relatively constant throughout the test. In amplitude sweeps tests, however, the shear rate at the edge of the plate is increasingly monotonically, thus leading to a theoretical increase in normal force under stable shear flow conditions.

Figure 6-5 below demonstrates the representative F_N-strain curves for an unmodified asphalt cement at three aging levels: unaged, RTFO and PAV aged. As is seen in the curves for each aging level, the normal force will exhibit a defined peak as the strain amplitude increases. The strain amplitude corresponding to the peak normal force will be denoted as S_{Fn} and used in the analysis of instability flow for asphalt cements in this study.

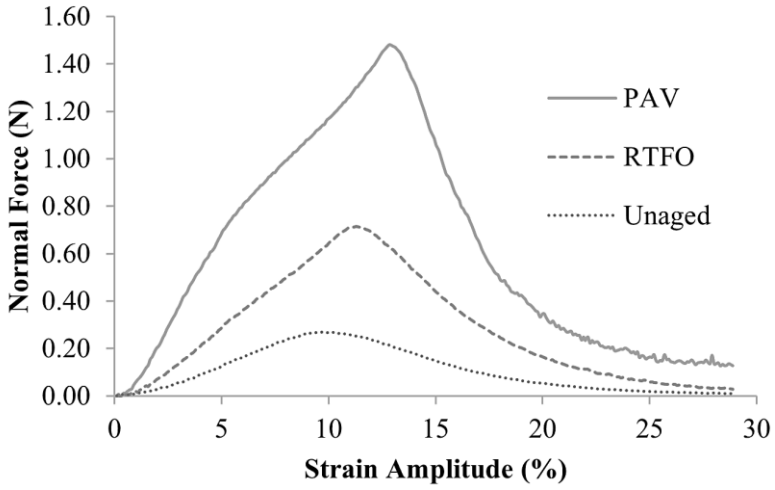

Figure 6-5 Normal force vs. strain amplitude plot for unaged, RTFO and PAV-aged binders at 19°C.

6.2.2 Electric Torque

In the broader field of rheology, there are two basic types of rotational rheometers: controlled rate/ strain and controlled stress. In the controlled rate rheometer, the displacement rate is applied, and the resultant torque is measured, while the controlled stress rheometer applies a force and then the resultant displace/ speed of the measuring system is measured. Controlled stress rheometers can be referred to as single head (SH), and controlled rate rheometers can also be referred to as dual head (DH) due to the number of elements acquiring the signal data (Franck 2005; Läuger et al. 2002). Modern rheometers,

such as research-grade DSRs, will use electronically commutated (EC) sync motors and can analyze materials in either mode. In EC motor rheometers, the EC-motor uses permanent magnets with a distinct rotor field that can be controlled with the appropriate controller to finely and instantaneously adjust the electromagnetic torque applied, thus reducing strain overshoot (Läuger et al. 2002).

As a result of the EC-motor and spindle assembly, the DSR measurements require corrections to reduce the inertia contributions of the spindle-rotor shaft. Thus, the total torque required to accelerate the spindle by a defined deflection angle or force is called the acceleration torque, M_a. The acceleration torque must be sufficiently large enough to overcome the inertia of the measuring system itself (i.e., the spindle-rotor shaft) as well as the inertia of the sample; these corrections are primarily necessary for low-viscosity materials (Franck 2005; Läuger et al. 2002). When neglecting friction of the bearing in use, the electric torque (M_{el}) is the total sum of the sample torque (M_s) and acceleration/inertia torque for both SH and DH rheometers. For SH rheometers, the sample torque is the product of the sample complex modulus, G^*_S, and the sample deflection angle, ϕ^*_S:

$$M_S = \frac{G_S^*}{k_g}\phi_S^* \qquad \text{Eqn. 6-4}$$

while the acceleration torque is the product of the moment of inertia, I, and the angular acceleration of the drive shaft:

$$M_a = -I(\omega^2 \phi_S^*) \qquad \text{Eqn. 6-5}$$

where k_g is constant dependant on the measuring system geometry and ω is the angular frequency of the drive shaft. In this system, the sample complex torque only requires inertia correction to the modulus's real/elastic portion. For DH rheometers, the "non-zero" transducer compliance (C_T) of the shaft remains constant, so the measure complex torque (M^*) is proportional to the sample deflection (ϕ^*_S). Thus, DH rheometers require inertial correction on both the real and imaginary components of the measured moduli. In both cases, the required inertial compensation increases with frequency to the power of two, ω^2 (Franck 2005). The three torques previously described are accompanied by two additional parameters to complete the torque balance: the viscous torque, M_v, and the elastic torque, M_e, as shown in Figure 6-6 below. The sample torque is the sum of the elastic and viscous torque vectors; the sample phase angle is the angle between M_s and M_e. Similarly, the acceleration torque is the sum of the electric and viscous torque with the raw phase angle, α, between them (Läuger and Stettin 2016).

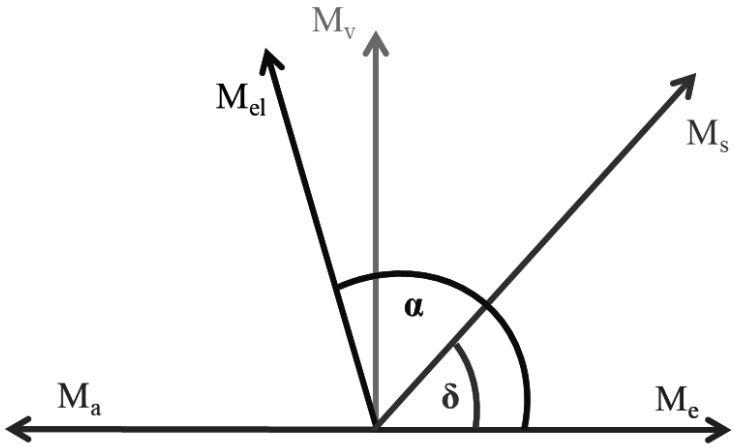

Figure 6-6 Rheometer torque balance as described by (Lauger and Stettin, 2016).

For SH rheometers, the torque ratio (TR) between the sample and the acceleration torque depends on both the sample's viscosity and the system moment of inertia. The TR for DH rheometers only depends on the parameters of the measuring system (C_T and I). Consequently, it is ideal for SH rheometers to use measuring systems with a low moment of inertia (i.e., low *I* spindle geometries) to reduce the correction factor (Franck 2005).

In modern DSRs, the experimentally observed sample stress is calculated from the torque balance; therefore, it is crucial to understand the torque balance and how it changes during either time sweeps or amplitude sweeps of asphalt cements. Figure 6-7 below shows the representative electric torque-strain curve for an unmodified asphalt cement at three aging levels: unaged, RTFO and PAV aged. The electric torque curve exhibits three primary phases focused around the electric torque inflection point: (1) this stage begins at the initiation of loading; as the strain amplitude increases, a 'local' torque peak may be observed, leading to the electric torque inflection point, (2) this stage begins at the electric torque inflection point and ends at the 'local' trough in the torque-strain curve, and (3) this stage is defined by a linear region and ends at the termination strain amplitude. Similarly, to the normal force, the strain amplitude corresponding to the electric torque inflection point will be recognized as the S_{Mel} failure parameter and evaluated in the analysis of instability flow for asphalt cements.

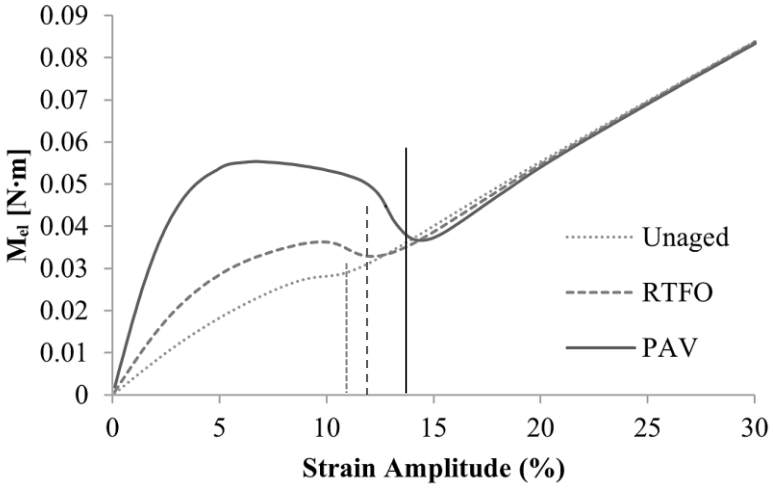

Figure 6-7 Electric torque vs. strain amplitude plot for unaged, RTFO and PAV-aged binders at 19°C.

6.2.3 DSR Video Analysis

Video analysis was initially conducted using a Canon DSLR with an 18-135 mm lens (providing approximately 0.3x magnification). The digital camera was aimed toward the sample requiring the DSR thermal hood to be raised during testing. A piece of white cardstock was placed behind the sample, and an LED ring light was used to illuminate the sample, as shown in Figure 8 below. As the camera was connected to a computer via a USB cable, the video was captured at 30 frames per second (fps) using the freely available Open Broadcast Studio (OBS) software. If necessary, minor edits were performed to improve image contrast, add sharpening, and straighten the image. Still, image files were then manually extracted approximately every 10 seconds, and the image stack could be analyzed using an ImageJ batch script.

Figure 6-8 shows that the resultant normalized area vs strain diagram was relatively low resolution. Each still image is binarized and processed to remove reflections and other specular highlights, which may affect the measurement of white pixels in each region. The area of white pixels is averaged between the regional pairs and then normalized. The flow strain amplitude (FSA) is determined as the deviation from the initial linear region of the curve where the flow has yet to occur. A MATLAB script was used to extract still images at a resolution of 1 fps, which improved the resolution and decreased the processing time for each video. The resultant image stack was then imported into a specially coded MATLAB app, as shown in Figure 6-9. The MATLAB app allows the user to define a region of interest (ROI); the ROI is selected to encompass the theoretical area occupied by an “undamaged” sample and

then partitioned into two inner regions (R2/R3) and two outer regions (R1/R4). Thus, an outer and inner FSA can be determined for each specimen.

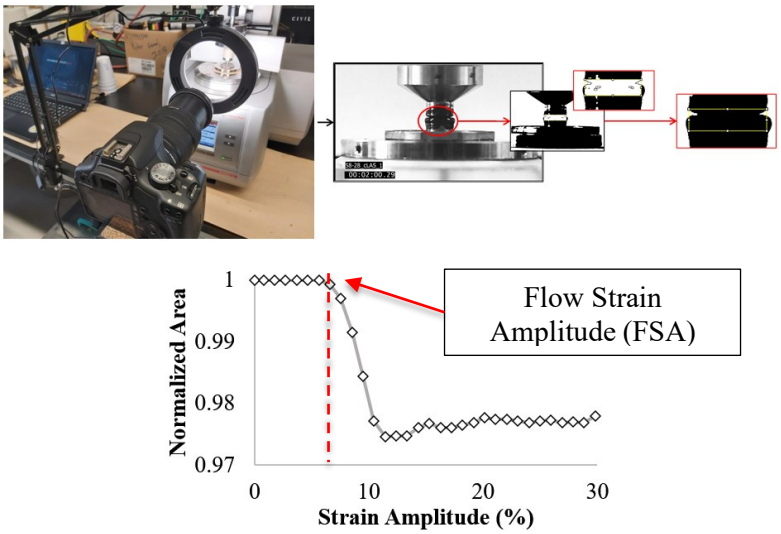

Figure 6-8 Initial DSR video analysis test setup demonstrating the image binarization and resultant low-resolution FSA plot.

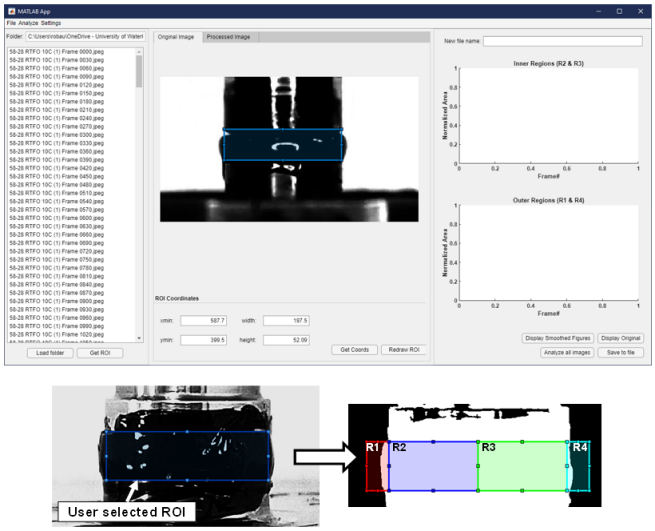

Figure 6-9 Improved MATLAB app used to increase the resolution of the FSA curves.

6.3 Results and Discussion

Figure 6-10 below demonstrates the failure strain values obtained for the peak normal force (left) and the electric torque inflection point (right). Both S_{F_n} and $S_{M_{el}}$ values increase with increased aging corresponding to the PSE/ τN values obtained in Chapter 5; this result mirrors the normal force

observations by Mainieri et. (2021). There is a positive correlation between the total torque applied by the DSR, the normal force required to keep the plates at a constant gap height, and the post-peak stress-strain behaviour of the asphalt cements.

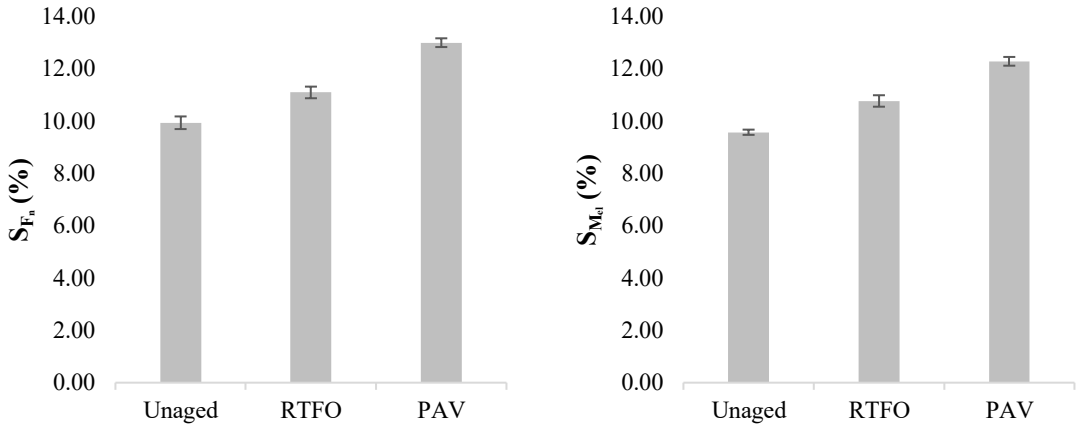

Figure 6-10 Failure strain values for peak normal force (left) and the electric torque inflection point (right) for unaged, RTFO and PAV-aged binders at 19°C.

As an attempt to explain this phenomenon, an updated torqued balance is visualized in Figure 6-11; Figure 6-11 (left) portrays the torque balance under stable homogenous simple shear conditions, while Figure 6-11 (right) portrays unstable simple shear conditions. Before unstable conditions occur, the sample and electric torque have comparable magnitudes, and the raw phase angle is equal. As the strain amplitude increases and the flow becomes unstable, the binder starts to flow and the observed raw phase angle and sample phase angle increase. As the raw phase angle is not constrained, it increases such that it passes 90° and the sample phase angle tends towards 0°. As this occurs, the viscous and elastic torque decreases, and the electric/ total applied torque is dominated by the torque required to overcome the inertia of the spindle and any binder residue that remains adhered to the top plate.

Sample geometric changes were observed at all aging levels using the video analysis, as demonstrated by results in Figures 6-12 and 6-13. Although the inner FSAs occur at lower strain amplitudes nearing the peak shear stress, it can be observed that inner FSA values reflect the trend observed by some other failure criteria, primarily PSE/ τN, F_n, and M_{el}. The Outer FSA exhibits a similar trend to the peak stress-strain amplitudes observed in Chapter 5 where the PAV-aged binder exhibits the earliest onset of failure by the geometric flow. However, it should also be stated that much

greater data variability is observed for Outer FSAs of the PAV-aged binder, indicating a weaker correlation.

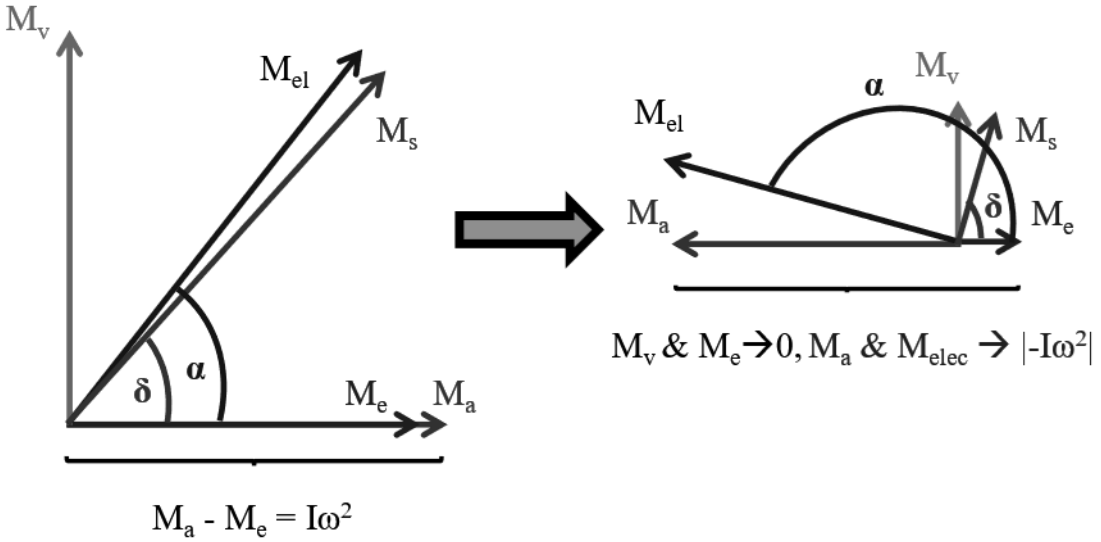

Figure 6-11 Torque balance under stable homogenous simple shear conditions (left) and while unstable simple shear conditions (right).

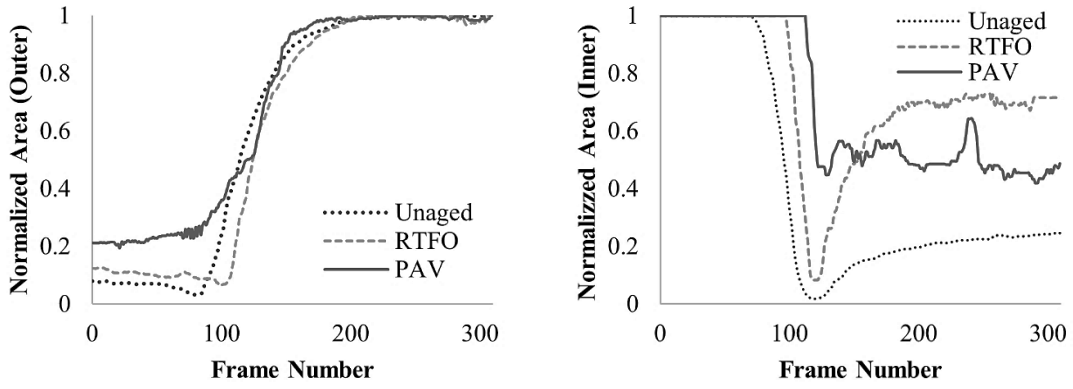

Figure 6-12 Outer and inner FSAs for unaged, RTFO and PAV-aged binders at 19°C.

Based on the combined results of electric torque, normal force, and FSA analysis, the three stages of the LAS test can be detailed as follows:

- *Stage 1* begins at the initiation of loading; as the strain amplitude increases, a 'local' torque peak as the binder begins to flow. After the peak, the torque gradually decreases following a decrease in the "effective" radius of the sample due to necking. Depending on the rate of change, this stage

ends at the strain amplitude corresponding to the "stationary turning point", as is seen in less-aged binders or the "falling inflection point", as observed in long-term aged binders.

- *Stage 2*: this stage begins at the electric torque inflection point; the decrease in torque results in the observation of a 'local' trough in the torque-strain curve exhibiting an upward concavity. During this stage, the effective sample radius reaches a minimum, and the observed torque values become dominated by the inertia of the DSR spindle. At the minimum effective sample radius, the amount of material connecting the top and bottom plates is insufficient to create thrust leading to a decrease in the force required to maintain the gap height.
- *Stage 3* is defined by a linear region and ends at the terminal strain amplitude (i.e., 30%). In this stage, the DSR measures only the inertia of the spindle as the sample no longer resists the movement of the measurement system. As a result, the experimentally observed modulus decreases dramatically due to a drastic decrease in measurement accuracy.

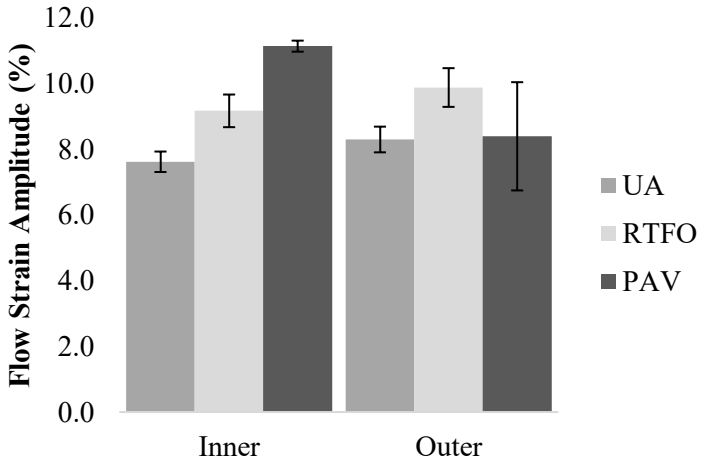

Figure 6-13 Sample flow strain amplitude for unaged, RTFO and PAV-aged binders at 19°C.

6.4 Statistical Analysis on Failure Strain Values at a Single Temperature

The following section provides a statistical analysis of the failure strain amplitude values obtained in this study and Section 5.4.2 of this manuscript. Sample data at 19°C was pooled together for all aging levels to perform analysis of variance (ANOVA) as well as Tukey's Honest Significant Difference (HSD) test and Fisher Least Significant Difference (LSD) test. For the ANOVA, the null hypothesis was selected such that all sample means are equal, and the alternative hypothesis was selected that all sample means are not equal; this analysis was performed with a significance level of $\alpha = 0.05$ and the

assumption of equal variances. The ANOVA table, shown in Table 6-1, demonstrates a statistically significant difference between the strain amplitude values obtained from the different failure criteria producing the resultant P-value, $P = 6.9 \times 10^{-13}$; therefore, it is possible to reject the null hypothesis. From the interval plot in Figure 6-14, it is observed that the variation between the different failure strain amplitudes are consistent, and it should be noted that the variability arises from the data spread between groups (i.e., the binder aging level).

Table 6-1 Combined unaged, RTFO and PAV aged material failure strain ANOVA table.

Source	DF	Adj SS	Adj MS	F-Value	P-Value
Factor	10	141.9	14.2	12.1	6.9e-13
Error	88	103.3	1.2		
Total	98	245.2			

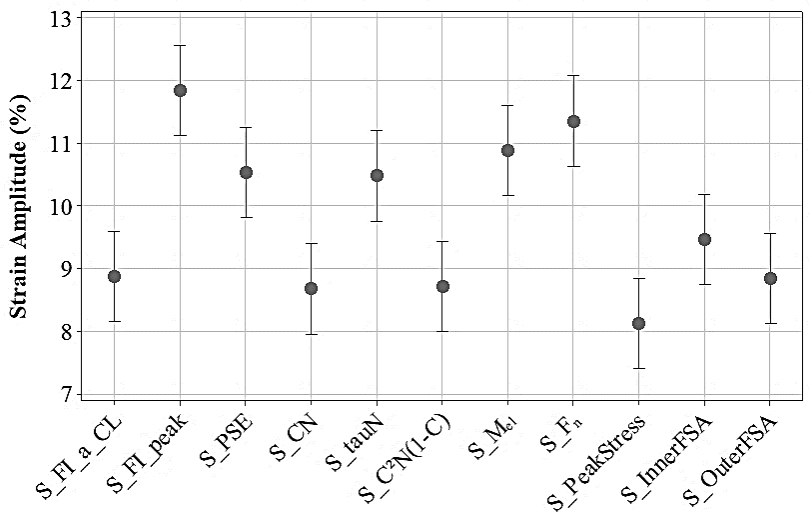

Figure 6-14 Failure strain interval plot for the combined unaged, RTFO and PAV datasets.

Figure 6-14 demonstrates a clear separation between peak Stress and post-peak failure criteria. When comparing the failure strain amplitude mean values using both Tukey's HSD and the Fisher LSD tests, a similar finding can be obtained, as shown in Table 6-2. Typically, Tukey's HSD test provides a more conservative result by controlling the experiment-wise error, while the Fisher LSD method only controls the paired error rate. However, clear groupings for peak stress and post-peak values are evident from the comparisons. From Tukey's HSD, post-peak failure criteria are found in Group A, and peak-related failure criteria are arranged in Group D. Similar groups can be found in the Fisher LSD test if Groups A and B are combined as well as Groups C and D. Regardless of the method used, it is observed

that the peak stress failure strain amplitude is consistently the most conservative criteria obtained from these datasets.

Table 6-2 Tukey test and Fisher LSD groupings using the combined unaged, RTFO and PAV datasets and a 95% confidence interval. Mean failure strain values are sorted from largest to smallest value; any values that do not share a different letter are considered statistically different.

Factor	Mean	Tukey HSD				Fisher LSD			
S_{FI_peak}	11.83	A				A			
S_{F_n}	11.35	A	B			A	B		
$S_{M_{el}}$	10.88	A	B			A	B		
S_{PSE}	10.53	A	B	C			B		
$S_{\tau N}$	10.48	A	B	C			B		
$S_{InnerFSA}$	9.46		B	C	D			C	
S_{FI_aCL}	8.88			C	D			C	D
$S_{OuterFSA}$	8.85			C	D			C	D
$S_{C^2N(1-C)}$	8.72				D			C	D
S_{CN}	8.68				D			C	D
$S_{PeakStress}$	8.13				D				D

Based on the statistical analysis, it may be concluded that groupings occur because of each failure criteria's specific interactions with the DSR torque balance. For both CN and $C^2N(1-C)$ criteria, the pseudostiffness parameter is proportional to the sample shear stress vector and the corresponding angle with the elastic torque; these parameters are then modified with the linearly increasing N values through the sweep. Similarly, in the Fracture Index critical crack length failure strain, the crack growth rate is dependent on the sample torque and the deflection angle. The post-peak failure strain criteria, mainly the τN/PSE and the Fracture Index peak strain amplitudes, correspond to changes in the normal force peak and the electric torque inflection point, indicating that these failure criteria are a consequence of the change in measurement artifacts and any succeeding measurements should be disregarded. For future analysis, the electric torque inflection point will be prioritized as it contains relevant information about the location of the peak shear and the peak normal force strain amplitudes.

6.5 Examining the Effect of Temperature

Figure 6-15 shows the maximum shear modulus observed during the LAS test for the PG 58-28 binder at all three aging levels at 13, 19 and 25°C. From Figure 6-15, the maximum shear strain value at the peak increases with both temperature and aging level, which is not unexpected. More importantly,

Figure 6-16 demonstrates that only the PAV-aged binder at 13 and 19°C meet Safaei and Castorena's (2016) minimum modulus criteria of 12 MPa to induce cohesive cracking (as indicated by the bolded line in Figure 6-15). Based on this criterion alone, it could be argued that only specimens at these two temperatures would provide valid VECD fatigue life predictions. Nevertheless, the results of the strain amplitude at the peak shear stress (Figure 16) and the strain amplitude of the electric torque inflection point (Figure 6-17) provide a different interpretation of the effect of temperature on the LAS results.

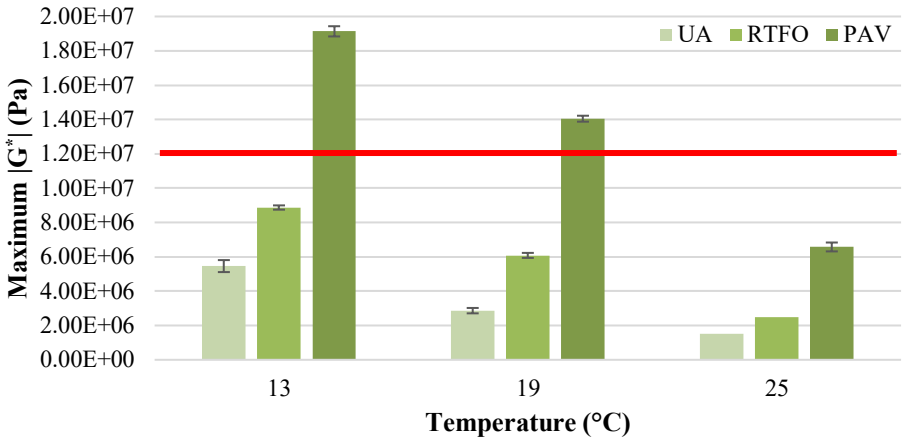

Figure 6-15 Minimum modulus criteria based on Safaei and Castorena's (2016) study and the maximum modulus for the unaged, RTFO and PAV-aged binders at different temperatures.

Figures 6-16 and 6-17 demonstrate that the strain amplitude of the peak shear stress and M_{el} inflection point increase with increasing temperature; both parameters display strong statistical linearity in the selected temperature range, as exhibited by the R^2 values. For all aging levels, the corresponding strain amplitude lag (difference between $S_{PeakStress}$ and S_{Mel}) increases with increased aging, which is consistent with the "peak broadening" phenomena observed for aged binders (Cao and Wang 2018; Hintz 2012). With these findings, it is fair to suggest that the data becomes increasingly inaccurate after the peak shear stress (reaching maximum unreliability at the M_{el} inflection point) at lower strain amplitudes when the temperature is decreased. Similarly, it is important to note that regardless of the test temperature or aging level used in this study, the M_{el} inflection point was observed in every sample. This observation suggests that the inertia of the measuring system dominated the post-peak stress-strain behaviour. However, this transition is slower when the sample is more aged.

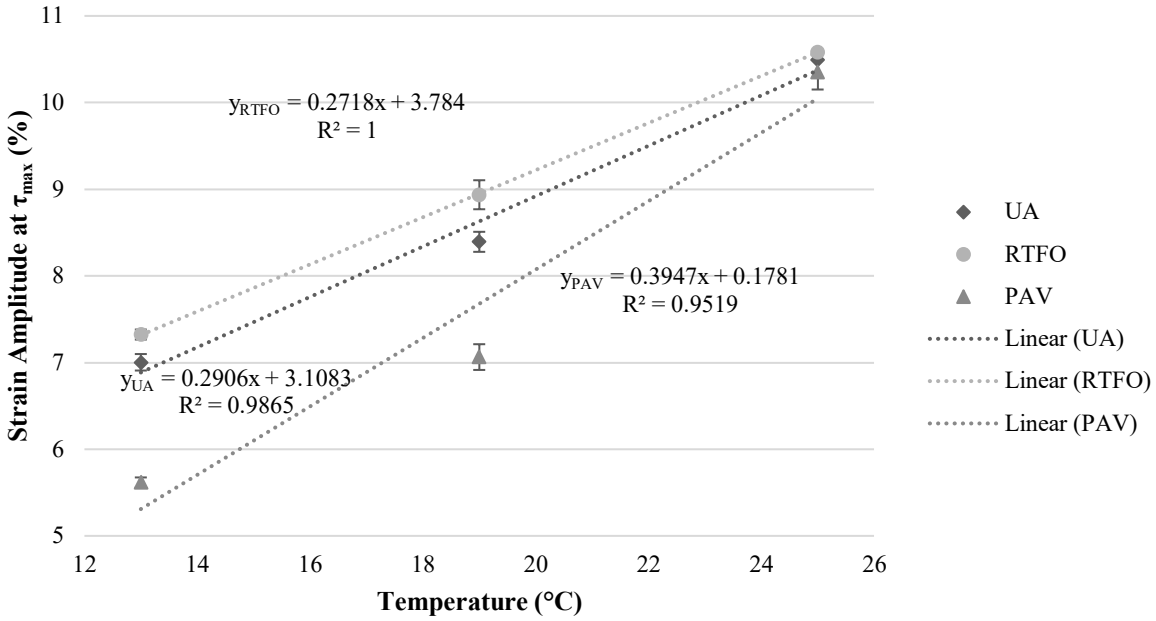

Figure 6-16 Strain amplitude at τ_{max} at 13, 19 and 25°C.

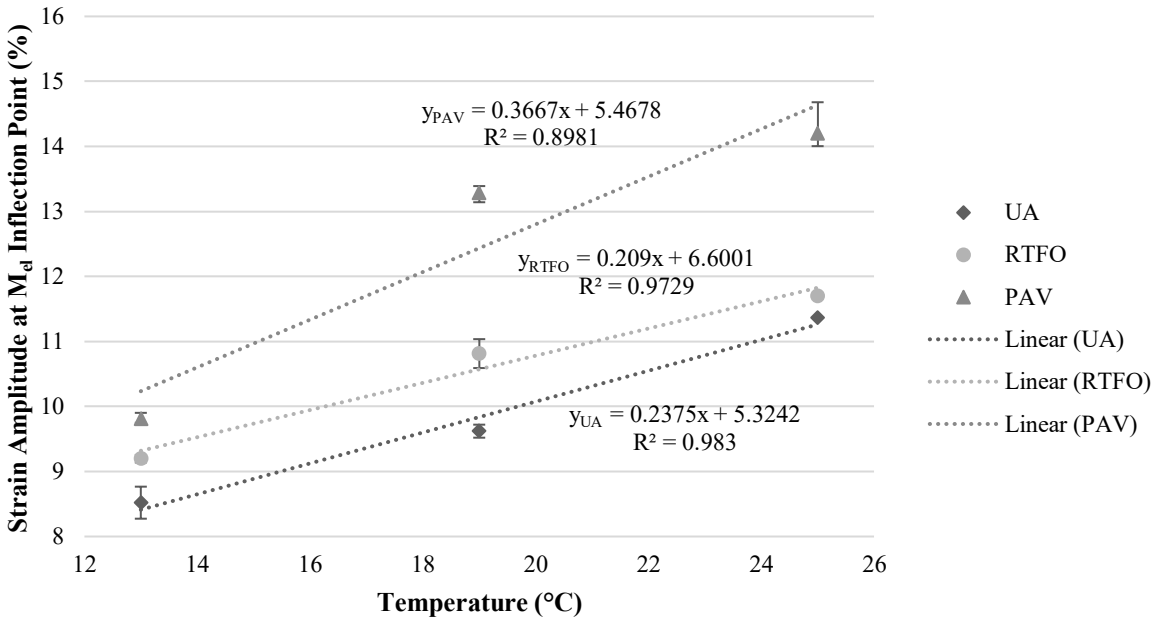

Figure 6-17 Strain amplitude at M_{el} inflection point at 13, 19 and 25°C.

6.6 Conclusions

The initial study evaluated the failure criteria of several complementary parameters, including the normal force, the electric torque and the flow strain amplitude obtained from the digital video analysis. A statistical analysis was conducted using the failure criteria strain amplitudes found in Chapter 5. The following conclusions can be drawn:

- The electric torque inflection point and the normal force peak strain amplitudes have a strong correlation and a weaker correlation to the inner flow strain amplitude.
- However, the inner flow strain amplitude correlates well with other failure criteria corresponding to the peak shear stress-strain amplitude.
- Both Tukey HSD and Fisher LSD determined that the 11 failure criteria can be segmented into two distinct groups. Failure criteria corresponding to the peak value include S_{FI_aCL}, $S_{OuterFSA}$, $S_{C^2N(1-C)}$, S_{CN}, $S_{PeakStress}$, and $S_{InnerFSA}$. Failure criteria corresponding to post-peak values include S_{FI_peak}, S_{F_n}, $S_{M_{el}}$, S_{PSE}, $S_{\tau N}$.
- The results of the statistical analysis strongly suggest that any amplitude sweep data after the peak shear stress decreases in measurement accuracy. Once the M_{el} inflection point strain amplitude is achieved, the test is dominated by the inertia of the measurement system, and the accuracy is almost zero.
- In contrast to the recommendations found in the literature, analysis of the peak shear stress and M_{el} suggests that increasing the test temperature shifts the failure strain amplitude to lower values, thus decreasing measurement accuracy at higher strain amplitudes in the sweep.
- Based on the above findings, it is recommended not to surpass the peak shear stress-strain amplitude concerning future healing tests due to the increasingly inaccurate measurement of the sample torque, modulus, and phase angle.

Chapter 7
Asphalt Cement Healing Characterization: Concepts for Next-Generation Test Protocols

7.1 Introduction

Fatigue microcrack damage, caused by repeated heavy or multi-axle vehicles loading on the pavement structure, initiates as the cumulative tensile strain at the bottom of the asphalt layer exceeds a theoretical endurance limit (Witczak et al. 2013). As loading persists over the life of the pavement, these microcracks coalesce into macrocracks which propagate to the surface; this degradation leads to a functional loss in the pavement lifespan (Di Benedetto et al. 2004). At the microscale, the asphalt cement component in the mixture experiences considerably larger local strains in comparison to the "global" strain experience by the pavement layer. The Superpave intermediate temperature fatigue criteria (i.e., the $G^*\sin\delta$ fatigue parameter) for aged binders poorly capture the effects of these larger strains, the effect of long-term repeated loading or the effect of different film thickness, which are impacted by the binder content or mixture gradation (Hajj and Bhasin 2017; Rezende et al. 2021).

The study of the intrinsic self-healing ability of asphalt cement during loading interruption or rest periods is, therefore, the natural progression from the characterization of asphalt fatigue. Asphalt cement intrinsic self-healing has been attributed to several mechanisms: molecular rearrangement and surface approach between crack surfaces, crack surface "wetting" and closure through the capillary flow and crack closure through molecular randomization produced by Einsteinian diffusion (Qiu 2012; Sun et al. 2017; Tabaković and Schlangen 2015; Xu et al. 2018b). While the underlying mechanism of healing in the binder is still not well understood, the successful characterization of healing would provide a more accurate prediction of a pavement's fatigue life leading to potential environmental and economic benefits.

7.1.1 Damage and Healing Terminology

In the framework of this project, it is essential to restate the definitions of damage and healing used herein as proposed by RILEM (Réunion Internationale des Laboratoires et Experts des Matériaux, systèmes de construction et ouvrages) Technical Committee on Crack-Healing of Asphalt Pavement Materials (TC 278-CHA). For this study, only fatigue damage will be considered (although other types of damage caused by different pavement distresses or laboratory tests may be "healable"). In that sense,

the damage will be characterized by the loss of mechanical properties (i.e., stiffness) due to the formation of microcracks and the period of interrupted loading, where the externally applied stress is assumed to be zero, is referred to as a rest period (Leegwater et al. 2020).

During the rest period, the observed restoration is the total reversal of the deterioration of mechanical properties due to damage and other non-damage-related effects. Restoration is composed of: (1) the recovery of both reversible and temporary bias effects and (2) true "healing," as is related to the reversal of mechanical property loss due to microcrack closure. Asphalt self-healing is further categorized as intrinsic (i.e., healing attributed to the inherent ability of the binder itself) or extrinsic (i.e., healing attributed to the use of additives or modifiers or other external stimuli) (Leegwater et al. 2020).

7.1.2 Asphalt Cement Healing Tests

As discussed previously, binder fatigue is typically evaluated on the dynamic shear rheometer (DSR) using time or amplitude sweeps, although methods such as ductility or strength/ cracking resistance tests have also been employed (Hajj and Bhasin 2018). Many of the same DSR-based tests have been expanded for healing characterization. DSR-based time sweep healings tests were some of the earliest attempts to characterize intrinsic binder healing. Time sweep tests are still dependent on amplitude sweeps/ linearity tests, and as a best practice, many researchers use amplitude sweeps to determine an appropriate strain amplitude for their time sweep test. Typically, the amplitude sweep is used to determine the strain amplitude at which a specified decrease from initial complex shear modulus (most commonly $90\%G^*_{init}$ as per the research of Anderson et al. (2001) and AASHTO T 315) is achieved. In most cases, time sweeps are then conducted using strain control mode at the determined strain amplitude or higher to accelerate the damage that occurs during the test (Canestrari et al. 2015; Gaudenzi et al. 2020; Li et al. 2020; Qiu et al. 2020; Santagata et al. 2015).

Healing tests performed at the Politecnico di Torino (PoliTO) incorporate time sweeps with a single rest period (also called TS-SRP). The PoliTO TS-SRP test is conducted at 3% strain at 10 Hz and 20°C. The TS-SRP test protocol has four primary phases. An initial low-strain amplitude (0.01%) conditioning period of 30 minutes is used to evaluate the change in modulus of an undamaged sample at rest. The first loading phase after the conditioning period runs at the testing strain level until the target failure condition is attained. This procedure uses a 15, 35 or 50% decrease in the observed dissipated energy. After reaching this failure condition, a rest period is applied at the same low strain amplitude as in the conditioning phase, and a second loading phase is conducted until the specimen

completely fails (Santagata et al. 2017). Li et al. (2020) applied a similar TS-SRP approach but applied a crack length analysis approach like the work of Hintz (2012). Initially, Li. et al. performed an amplitude sweep from 0.01 to 100% strain to determine a strain amplitude at which a "zero" damage state was maintained. Interrupted time sweeps were performed at 5, 7 and 10% after the calibration amplitude sweep at 20°C. The first loading phase in each test was conducted for approximately 20 minutes with rest periods of various durations. Qiu et al., (2020) performed TS-SRP tests at 25°C using a strain amplitude of 8%. The TS-SRP procedure was paired with 'heated' rest periods from 25 to 65°C; the maximum rest period temperature was set as the binder's softening point plus 5°C. A similar protocol was used by Gaudenzi et al. (2020) on unmodified and modified asphalt cements containing 10% wood pulp extract. In contrast to the TS-SRP previously performed, Gaudenzi et al. (Gaudenzi et al. 2020) performed a time-sweep test with multiple rest periods (TS-MRP). Self-healing characterization was assessed using $|G^*|\sin\delta$ evaluate damage evolution over time with the reasoning that the multiple rest periods would provide a more realistic simulation of real-life traffic conditions.

As the linear amplitude sweep (LAS) test gained more recognition in the asphalt industry, numerous studies have been conducted attempting to determine its ability to evaluate fatigue resistance at different temperatures and additives using the LAS test (Abed et al. 2020b; Chen and Bahia 2021, 2022; Sabouri et al. 2018; Safaei and Castorena 2016; Yan et al. 2021; Zhou et al. 2013). Not unlike the progression of time sweep fatigue tests to healing tests, amplitude sweeps with rest periods were introduced as the original LAS test was attractive compared to the time sweeps due to its short test duration. The original LASH (Linear Amplitude Sweep with a Healing rest period) procedure used the same basic framework as the LAS test but required a calibrating uninterrupted/continuous LAS (also known as cLAS) test to determine the failure strain amplitude (S_f); the Sf value was then used to determine the appropriate first phase termination strain level before applying a rest period. Xie et al. (2017) initially proposed using 25, 50, 75 and 125% S_f determined using the peak released pseudostrain energy (G^R) to assess healing (Xie et al. 2017). After the rest period, the test is resumed at the same strain amplitude from the first loading phase, and the sample is loaded up to the original 30% of the LAS test (Aurilio 2020; Xie et al. 2017). In more recent adaptations of the LASH test (Asadi and Tabatabaee 2020; Aurilio 2020; Aurilio et al. 2020c; Baglieri et al. 2018; Chen and Wang 2020; Wang et al. 2018), the selection of the failure strain amplitude offered conflicting results and trends, thus, demonstrating the need to standardize the methodology of LAS-based healing tests.

7.2 Objectives

The study presented herein aims to provide a greater understanding of the fatigue behaviour and healing characterization offered by LAS-based healing tests on the dynamic shear rheometer; this will be accomplished by providing recommendations for modifications to the original LASH test as well as the rationale behind those modifications. The study will also attempt to apply analysis methods using several modelling approaches ranging from continuum mechanics to classical fracture mechanics to determine which approaches can successfully distinguish between the effects of rest periods, failure strain amplitude and the effects of polymer modification.

7.3 Materials and Methodology

The following experimental work was completed using three binders: 2 PG 58-28s (i.e., 58-28A and 58-28B) and a PG 58-28 containing 4% SBS; the SBS-modified binder was initially modified from 58-28A. Each binder was aged using the rolling thin film oven (RTFO) to simulate short-term aging and then aged using the pressure aging vessel (PAV) for a single 20-hour period at 100°C (the typical aging temperature used to simulate long-term aging in Southern Ontario).

7.3.1 Healing Test Procedure

The work in this study was conducted using the methods agreed upon by RILEM CHA-278 (Cracking Healing of Asphalt Materials) Task Group 2a (Asphalt cement Healing Characterization) after the completion of the preliminary interlaboratory testing. Based on the results of the preliminary work, the task group agreed to continue additional interlaboratory studies on asphalt cements using a modified version of the LASH test.

7.3.1.1 Original LASH Concerns

The original LASH procedure featured two loading phases separated by a single rest period. The first loading phase ended at the strain amplitude corresponding to the peak release PSE and was then subjected to the same strain amplitude at the beginning of the second loading phase. Several participants in the task group observed that the ramp to the initial strain of the second loading phase was often inconsistent and inaccurate, which had not been previously reported in the literature. As the DSR ramped to the higher strain value from rest, the data points were often varyingly imprecise, and the DSR may take up to several seconds to return to the desired strain amplitude, as shown in Figure 7-1; this issue appeared to be dependent on the DSR manufacturer, model, and spindle design. This

inaccuracy may result from inertia-elastic or viscoelastic ringing, a common artifact of high-frequency oscillatory shear tests and stepped amplitude sweep tests (Ewoldt et al. 2015). The common solution among operators was to remove the "outliers" at the beginning of the second loading phase and commence the analysis once the DSR values had stabilized. This solution was inconsistent between operators, and it was decided that the second loading phase be reinitiated from 0.01% using a continuous ramp without any large steps in strain amplitude.

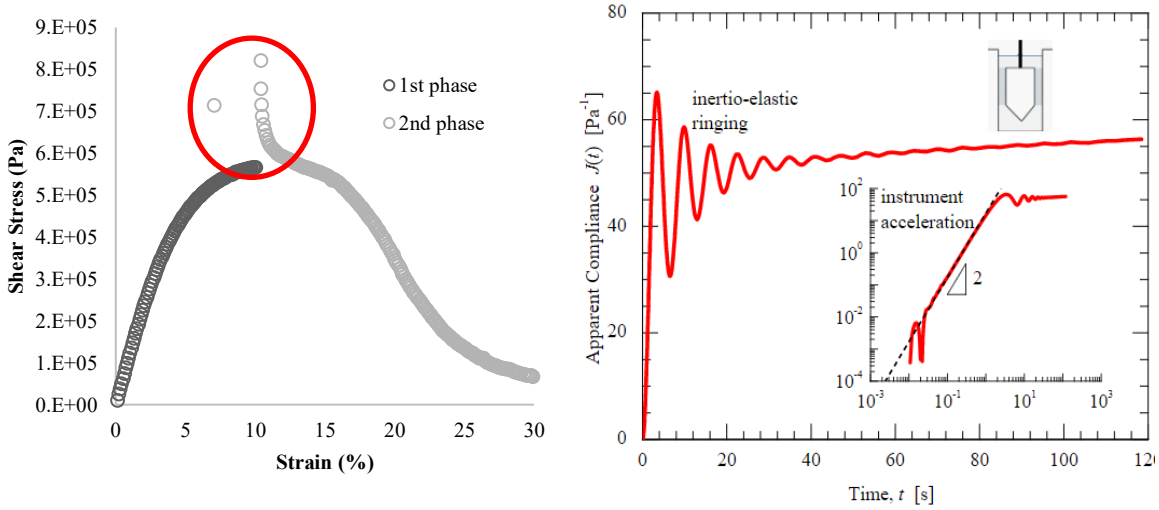

Figure 7-1 Original LASH test second loading phase outliers (left) and viscoelastic ringing phenomenon observed in stepped amplitude sweeps as discussed by Ewoldt et al. (2015).

The second modification of the LASH test was made based on the recommendations provided by the DSR video analysis in Chapter 4, Section 4.2.7 and Chapter 6, Section 6.2.3. As was discussed in these chapters, the onset of instability flow and a change in the sample geometry was observed near the strain amplitude corresponding to the peak shear stress (γ_{peak}) in the stress-strain curve. It was also determined that the measurement accuracy of the DSR decreases as the strain amplitude increases past γ_{peak} in part due to the change in geometry. In concurrent testing, it was determined that γ_{peak} provided the most conservative failure criteria (among those detailed in the literature), and it was decided that the first loading phase terminal strain amplitude would not exceed γ_{peak} for all binders.

7.3.2 Modified LASH Test Protocol

Binder samples were to be placed in a forced draft oven for approximately 10 minutes at the appropriate temperature (140°C for unmodified binders and 160°C for polymer-modified binders) in a silicon 8 mm DSR mould. After being removed from the oven, the liquid binder sample is mixed, allowed to

cool at room temperature for 10 minutes, and, finally, placed in a freezer at -20°C for 2 minutes before loading on the DSR plates. Once loaded on the plates and trimmed, all samples are initially conditioned at the test temperature for 30 minutes at 0.01% strain amplitude to assess any changes in the shear modulus caused by potential steric hardening during cooling. The newly proposed LASH test procedure is conducted in two steps:

1. A continuous linear amplitude sweep is conducted from 0.01 to 30% strain amplitude as described in the original provisional standard, AASHTO TP101. The strain amplitude of the Peak Shear Stress, γpeak, is recorded from at least two replicates and the average value is used in subsequent testing.
2. Healing is evaluated in three steps using new binder samples,: (1) a linear amplitude sweep is conducted by ramping the strain amplitude from 0.01% to 50% of the peak shear stress-strain amplitude (i.e., 0.5·γpeak) or 100% of the peak shear stress-strain amplitude (i.e., 1·γpeak), (2) a rest period is applied at very low strain amplitudes (γ = 0.01%) for 5 or 30 minutes, and (3) a second loading phase consisting of an uninterrupted amplitude sweep is performed from 0.01 to 30% strain amplitude. Similarly, it was agreed that two replicates were sufficient for each test scenario. For the RILEM Interlaboratory test, the testing temperature was set at 20°C for all binders. Therefore, all the tests in this study are also conducted at 20°C for consistency.

As the final contribution of the University of Waterloo to RILEM CHA-278 Task Group 3 (Self-Healing Modelling), the amplitude sweep healing test data were analyzed using methods adapted from several prior works; these reference works utilized VECD modelling approaches, as well as fracture energy and crack length analysis (Asadi and Tabatabaee 2020; Hintz and Bahia 2013; Zhang and Gao 2019; Zhou et al. 2017). As the test modifications were initially considered through the interlaboratory testing for RILEM CHA-278, it was agreed that all binder samples would undergo the sample preparation method and testing plan described above to reduce potential differences caused by specimen heating/ cooling and steric hardening.

7.3.2.1 VECD-Based Healing

In the healing study by Asadi and Tabatabaee (2020), two binders (a neat PG 64-22 and an SBS-modified binder graded to PG 70-22) were tested at three aging levels; the PG 64-22 binder was also blended with a rejuvenator after PAV aging and then re-aged for a 2nd 20-hour period. A VECD modelling approach was implemented as described previously, requiring the uninterrupted cLAS to

determine the failure strain (S_f) and determine an ending strain amplitude for the first loading phase. Asadi and Tabatabaee (2020) selected the $C^2N(1-C)$ failure proposed by Cao and Wang (2018), with the reasoning that peak τN and CN failure criteria failed to capture the effects of aging. The study ended the first loading phase at 0.2, 0.5 and $1S_f$ with single 1-, 15-, 30- and 90-minute rest periods at 25°C. From the results in Chapter 5, it was determined that the peak shear stress-strain amplitude, on its own, was the most conservative failure criteria due to the change in geometry associated with post-τ_{max} failure criteria; thus, the first deviation from Asadi and Tabatabaee's work will be the failure criteria.

The study also proposed two healing indices using both the change in material integrity/pseudo stiffness (C) and the failure damage intensity ratio (S/S_f); a schematic test is demonstrated in Figure 7-2 below. Asadi and Tabatabaee identified six points of interest in three pairs: (C_1, S_1), (C_2, S_2), and (C_3, S_3). These points are determined as follows:

- C_1 is the pseudostiffness value corresponding to the end of the first loading phase; S_1 corresponds to the damage intensity factor at C_1.
- C_2 is the pseudostiffness value measured at the beginning of the second loading phase after the rest period; S_2 corresponds to the damage intensity factor at C_2.
- $C_3 = C_1$, where C_3 represents the pseudostiffness when the damage level observed, S_3, attains the same decrease in pseudostiffness as determined from the first loading phase.

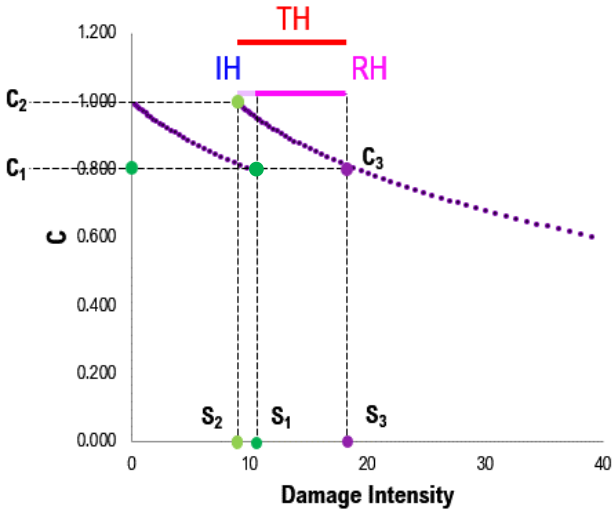

Figure 7-2 Total healing (TH), initial healing (IH) and residual healing (RH) recreated from Asadi and Tabatabaee (2020).

From these six points of interest, three indices were proposed to evaluate the healing potential of the binders: initial healing (IH), residual healing (RH), and total healing (TH). Each healing indicator is calculated as follows:

$$IH(C_1) = \frac{S_1 - S_2}{S_1} \quad \text{Eqn. 7-1}$$

$$RH(C_3 = C_1) = \frac{S_3 - S_1}{S_1} \quad \text{Eqn. 7-2}$$

$$TH(C_1) = IH(C_1) + RH(C_1) = \frac{S_3 - S_2}{S_1} \quad \text{Eqn. 7-3}$$

The IH parameter can be found commonly in other studies using the VECD modelling analysis for healing; this index simply compares the before and after rest period change in pseudostiffness and can be attributed to "wetting". The RH parameter is intended to represent healing corresponding to a lower damage accumulation rate in the amplitude sweep. The sum of RH and IH forms the complete picture of the healing potential of the binder (Asadi and Tabatabaee 2020). The second proposed change in the adaptation of this procedure is the elimination of the failure damage intensity ratio (S/S_f), and instead, this work only uses the damage intensity at the end or beginning of each phase. This change allows easier comparison between the $0.5\gamma_{peak}$ and γ_{peak} first phase termination criteria.

7.3.2.2 Crack Length Healing Analysis

When developing the LAS test procedure, Hintz and Bahia (2013) used the works of De and Gent (1998) and Gent and Yeoh (2003) to derive an equation from the energy required to change the surface area of a cylindrical sample under torsion. When undergoing edge fracture, a cylindrical sample releases energy proportional to the change in cross-sectional surface area (SA) caused by the fracture, which can be calculated as:

$$SA = \pi(r_{init}^2 - r_n^2) \quad \text{Eqn. 7-4}$$

where r_{init} is the initial radius of the sample and r_n is the sample radius at the time of observation. When combining the change in cross-section surface area with the fracture energy release rate, G_f, which is:

$$G_f = \frac{|G^*|\varphi^2(r_{init} - a)^2}{2h} \quad \text{Eqn. 7-5}$$

where $|G^*|$ is defined as the complex shear modulus, φ is the deflection angle, r_{init} is the initial sample radius, h is the sample, and *a* is the crack length. This crack length analysis (Hintz and Bahia 2013) resulted in the creation of the critical cracking length parameter (a_{CL}) denoting the point at which the cracking rate reaches a local minimum.

Crack length can be estimated by two methods: (1) using the pre-processed sample torque and deflection angle inputs or (2) using the processed complex shear modulus and phase angle outputs. Using the torque and deflection angle inputs, the crack length, "a" (mm), can be calculated as:

$$a = 4 - 4\left(\left[\frac{M_i/\varphi_i}{M_0/\varphi_0}\right]^{\frac{1}{4}}\right) \quad \text{Eqn. 7-6}$$

where M_x is the torque (mN·m) and φ_x is the deflection angle (degrees) at x = *i*, the value at the *i*th cycle or x = 0, the initial value. A similar derivation can be completed as crack length, c (mm):

$$c = \left\{1 - \left(\left[\frac{|G_i^*|/\sin(\delta_i)}{|G_0^*|/\sin(\delta_0)}\right]^{\frac{1}{4}}\right)\right\} \cdot r_0 \quad \text{Eqn. 7-7}$$

where $|G_x^*|$ and δ_x are the complex modulus and phase angle at x = *i*, the value at the *i*th cycle or x = 0, the initial value, and r_0 is the sample radius at the beginning of the test (assumed to be 4 mm) using the stress control mode. Furthermore, using either crack length derivation, the per cycle cracking rate (denoted as either $\dot{c}$ or *da/dN*) can be calculated using a numerical gradient approach for its analysis (Zhang and Gao 2019).

Building on the prior work of Zhang and Gao (2019) and their study on crack growth using the DSR, Li et al. (2020) applied crack length analysis approach to strain-controlled time sweep tests examining the healing ability of a single elastomer-modified binder. Li et al.'s test procedure requires an amplitude sweep from 0.01 to 100% strain amplitude at the testing temperature. This initial amplitude sweep was chosen to determine the amplitude at which zero damage had occurred in the sample; from the results, a maximum of 0.6% strain amplitude was imposed. Healing tests were then initiated with an amplitude from 0.01 to 0.6% to determine the initial sample via the shear modulus (Figure 7-3). After the amplitude sweep, the healing test continued with a 20-minute time-sweep at 5, 7 or 10% with a single rest period at 10 Hz at 20°C; rest periods ranged from 5 seconds to 40 minutes. After the rest period, the sample was reloaded to the selected strain amplitude until failure (Li et al. 2020).

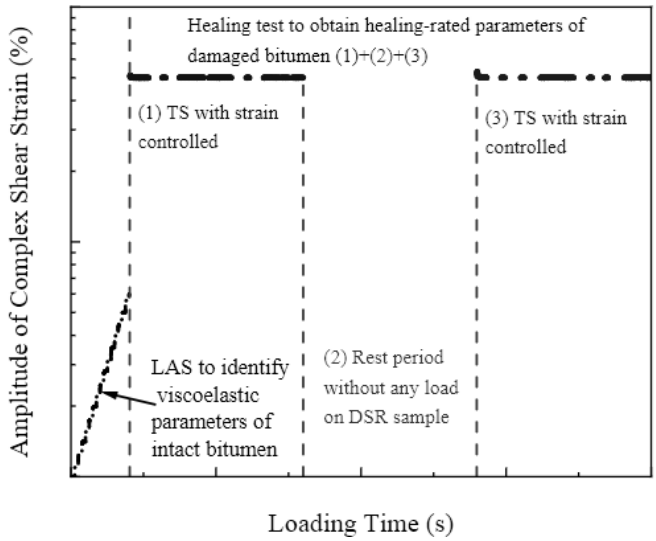

Figure 7-3 Time-sweep healing test procedure proposed by Li et al. (2020).

Li et al. (2020) then analyzed the result of healing tests using three methods: dissipated pseudostrain energy (DPSE), pseudostiffness (S) and crack length (CL) parameters. A healing index was devised for each parameter:

$$\%HI = \frac{M_H - M_D}{M_0 - M_D} \cdot 100\% \qquad \text{Eqn. 7-8}$$

where 'M' is the corresponding parameter (DPSE, S or CL) and the subscripts denote the time of the observation; 'H' denotes the value at the beginning of the 2nd loading phase/ end of the rest period, 'D' denotes the value at of the last cycle at the end of the first loading phase and '0' represents the initial value (Figure 7-4). The healing rate was then modelled over the rest period duration using a modified Ramberg-Osgood model. Li et al. concluded that the DPSE and pseudostiffness approaches underestimate the observed healing, especially at higher damage levels. The crack length approach was considered to improve high-damage healing characterization as the creation of a considerably larger crack surface would hinder the typical mechanism of healing (Li et al., 2020).

As Li et al. (2020) opted to use the previous formulation for c from Zhang and Gao (2019), it should be noted that the $|G^*|/\sin\delta$ parameter is more suited to stress control tests (Hajj and Bhasin, 2018). For this study, the crack length was calculated using the ratios of the initial $|G^*|\sin\delta$ to the $|G^*|\sin\delta$ at the *i*th cycle. Thus, the formula is simply changed to use the product of $|G^*|$ and $\sin\delta$ in strain control mode:

$$c = \left\{1 - \left(\left[\frac{|G_i^*|\sin(\delta_i)}{|G_0^*|\sin(\delta_0)}\right]^{\frac{1}{4}}\right)\right\} \cdot r_0 \qquad \text{Eqn. 7-9}$$

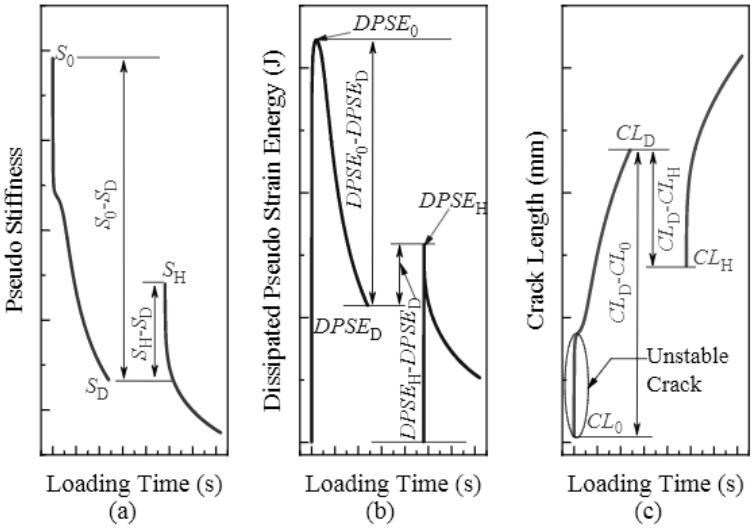

Figure 7-4 Representative pseudostiffness, dissipated pseudostrain energy and crack length vs time curves for time sweep healing tests (Li et al. 2020).

Fundamentally, this results in the "c" crack length parameter becoming a scaled version of the "a" crack length parameter as torque could be converted to stress, and deflection angle can be converted to strain amplitude. The usage of the phase angle does present a difference between the method of Li et al. and Bahia and Hintz. However, the crack length derivation using the $|G^*|\sin\delta$ is advantageous as this represents only the viscous component of the G^* vector. The viscous component, or the Loss modulus, G'', is relatively unaffected by the change in phase angle observed during testing due to the torque balance used by the DSR.

Finally, to adapt this crack length analysis to the new LASH test procedure, the healing indices were simplified to include only two points of interest for each crack derivation: (1) the crack length at the end of the first loading phase and (2) the crack length corresponding to the same strain in the second loading phase. These points were selected to emulate Asadi and Tabatabaee's (2020) approach in their VECD analysis. Thus, two new healing indices are described as follows:

$$\%IH_a = \frac{a_1}{a_2} \cdot 100\% \qquad \text{Eqn. 7-10}$$

$$\%IH_c = \frac{c_1}{c_2} \cdot 100\% \quad \text{Eqn. 7-11}$$

Note that the crack length analysis used herein assumes that the crack length again begins at 0 mm at the start of the second loading phase for simplification purposes. Also, these indices are proposed as reciprocal indices with the intention that healing would be indicated by an %IH greater than 100%, whereas permanent damage or a "lack of healing" would be indicated by values below 100%.

7.3.2.3 P-LASH Analysis

The P-LAS analysis was first proposed by Zhou et al. in 2017 as an extension to the crack growth analysis originally proposed by Hintz and Bahia in 2013. Zhou et al.'s work primarily aimed to overcome the apparent poor correlation between binder aging and the fatigue life prediction obtained from the standard VECD analysis (Zhou et al. 2017).

For asphalt materials tested in time sweep tests, a power law relationship between the energy release (J) and crack Hintz and Bahia initially proposed growth (ċ) rates in 2013. The relationship was developed directly for time sweep tests on asphalt cements on the DSR and is calculated as follows:

$$J = \frac{|G^*|\gamma^2 h}{2r^2(r-c)}\left(r - c + z\left(1 - e^{-\frac{c}{z}}\right)\right)^3 (1 - e^{-\frac{c}{z}}) \quad \text{Eqn. 7-12}$$

where $|G^*|$ is defined as the complex shear modulus, γ is the shear strain amplitude, r is the sample radius (i.e., r = 4 mm when using the 8 mm DSR plate), h is the sample height (i.e., h = 2 mm when using the 8 mm DSR plate), c is the crack length and z is a numerical factor (z = 0.1 for asphalt cements). Further extending the Paris' law-type crack growth equation used by Bazant and Prat (1988) for Portland cement concrete, the Hintz and Bahia crack growth rate equation was modified to include the fracture energy rate parameter, J/J_f:

$$\frac{J}{J_f} = \frac{|G^*|\gamma^2 h}{2r^2(r-c)J_f}\left(r - c + z\left(1 - e^{-\frac{c}{z}}\right)\right)^3 (1 - e^{-\frac{c}{z}} \quad \text{Eqn. 7-13}$$

where J_f is the fracture energy obtained from a monotonic test (this value functions similarly to the fracture energy rate, G_f, defined previously). Based on this derivation for asphalt cements, it is hypothesized that smaller $|G^*|\gamma^2/J_f$ values indicate better fatigue resistance as the crack propagation occurs at a lower rate in the time sweep test.

The $|G^*|\gamma^2/J_f$ value was further adapted to amplitude seep tests by Zhou et al. (2017) to develop the Pure Linear Amplitude Sweep (PLAS) test. The PLAS uses the same framework as the LAS test but

does not require the "fingerprint" frequency sweep at the beginning of the LAS test; thus, the analysis can even be completed on existing LAS data without any necessary modification. From the PLAS, the fatigue resistance energy index (FREI) is proposed:

$$FREI = \frac{J_{f-\tau_{max}}}{G_{0.5\tau_{max}}} \cdot \left(\gamma_{0.5\tau_{max}}\right)^2 \qquad \text{Eqn. 7-14}$$

where $J_{f\text{-}\tau max}$ is the shear fracture energy up to the maximum shear strain value, $G_{0.5\tau max}$ and $\gamma_{0.5\tau max}$ are the shear moduli, and the strain amplitude is evaluated at half of the maximum shear stress, respectively (Zhou et al. 2017). A schematic of the components of the FREI is found in Figure 7-5.

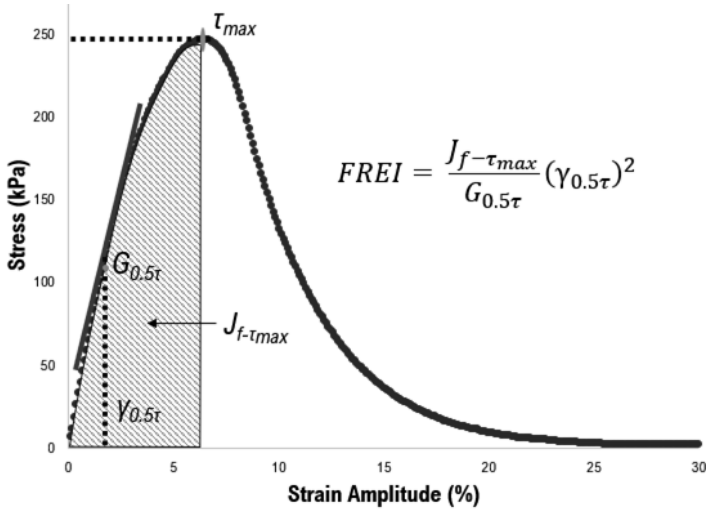

Figure 7-5 P-LAS schematic diagram recreated from Zhou et al. (2017) featuring the shear fracture energy calculated to the stress peak and the shear modulus and strain amplitude evaluated at half of the maximum shear stress.

The FREI index as shown in the equation above was selected as a reciprocal index as a larger FREI value would indicate a superior ability of the binder to resist fatigue. The rationale behind the index is as follows:

- $J_{f\text{-}\tau max}$: A higher fracture energy would indicate better resistance to fracture. The $J_{f\text{-}\tau max}$ is only calculated up to the peak shear stress value for two reasons: (1) in a realistic scenario, the asphalt cement would not experience the stress-strain behaviour experienced in the accelerated DSR testing, and (2) the post-peak data may be unreliable as the true radius of the DSR specimen is unknown with the occurrence of a macrocrack.
- $\gamma_{0.5\tau max}$: Larger $\gamma_{0.5\tau max}$ values would indicate higher flexibility and possibly relaxation capability for the binder. As such, the $\gamma_{0.5\tau max}$ term of the index was selected to remain in the numerator for the amplitude sweep derivation.

- $G_{0.5\tau max}$: It is postulated that a larger shear modulus is associated with a decrease in the binder's ability to resist cracking.

In their study, Zhou et al. (2017) tested two unmodified binders at up to 80 hours of PAV aging and four unaged binders containing up to 10% rejuvenator. Binder test results were also compared with past mixture cracking test data (the Texas Overlay Test, also known as the OT test, and the Illinois Flexibility Index test, also known as the I-FIT test) as well as full-scale accelerate pavement testing (also known as ALF) conducted by the Federal Highway Administration (FHWA) TPF-5(019) study. The results of the study demonstrated that the fracture mechanics-based index was significantly more successful at distinguishing between both aging level and rejuvenator dosage. PLAS results also correlated reasonably well with the results of both mixture cracking tests, while a poorer correlation was reported with the ALF fatigue results.

The new method, P-LASH, is based upon the work of the Pure LAS (P-LAS) test proposed by Zhou et al. In each of the four phases, the area of the curve is determined using a simple numerical integration procedure (i.e., using the trapezoidal rule) for the chosen time duration and end condition. As demonstrated in Figure 1, the area under the curve in each phase is represented by the released fracture energy, *J*, to remain consistent with the original P-LAS procedure. However, it should be noted that using the J parameter calculated during the conditioning and rest periods does not represent the released fracture energy at very low strain amplitudes and, once again, is used for consistency with the prior work by Zhou et al. (2017). Data obtained from the P-LASH procedure are analyzed using two methods:

- *Method 1*: Using the same analysis method as described in the original P-LAS work, the retention of the fatigue resistance, %Ret, is calculated as:

$$\%Ret = \frac{FREI_2}{FREI_1} \cdot 100 \qquad \text{Eqn. 7-15}$$

where the FREI parameter for both the pre- and post-rest period loading phases are denoted as $FREI_1$ and $FREI_2$, respectively. The fatigue resistance lost due to damage, %Loss, is then calculated as:

$$\%Loss = 100\% - \%Ret \qquad \text{Eqn. 7-16}$$

- *Method 2*: Using only the released energy calculated in each of the four phases of the test, the percentage of restoration, %Res, is similarly calculated as:

$$\%Res = \frac{J_2}{J_1} \cdot 100 \qquad \text{Eqn. 7-17}$$

where the energy release for both the pre- and post-rest period loading phases are denoted as J_1 and J_2, respectively. Restoration is used in this case to remain consistent with the definitions proposed by RILEM TC CHA-278. In other instances where the term 'healing index' is used, it is used simply to remain consistent with the reference literature that the analysis technique was adapted. A similar %Loss can also be calculated using the %Res as completed in Equation 7-17. Method 2 differs from Method 1 with the inclusion of the RP:SH ratio, which is calculated as:

$$RP{:}SH = \frac{J_{RP}}{J_{SH}} \cdot 100 \qquad \text{Eqn. 7-18}$$

where the area under the curve for the conditioning and rest periods are denoted as J_{SH} and J_{RP}, respectively. This parameter compares the total change in modulus observed for an "undamaged" and "damaged" sample. Schematic diagrams for both P-LASH analysis methods 1 and 2 can be found in Figures 7-6 and 7-7, respectively.

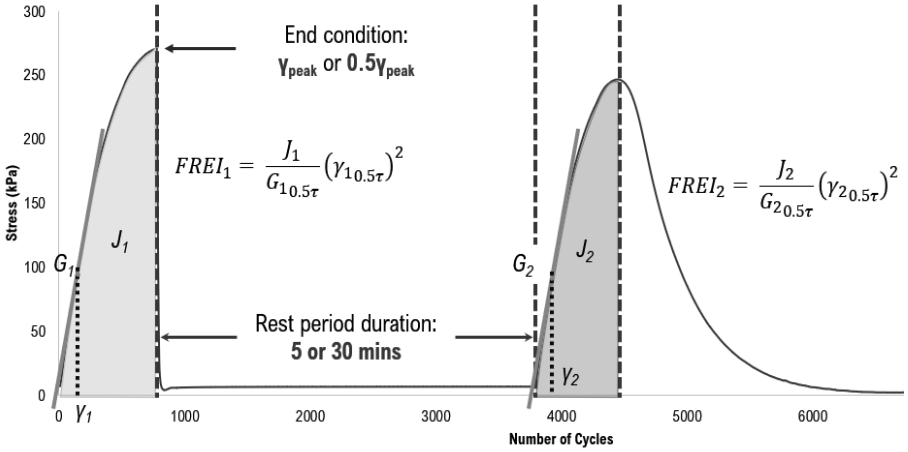

Figure 7-6 P-LASH procedure demonstrating the first and second loading periods interrupted with a single rest period using the FREI analysis procedure (Note: number of cycles is plotted on the x-axis in place of strain amplitude to demonstrate the time contribution of the rest period).

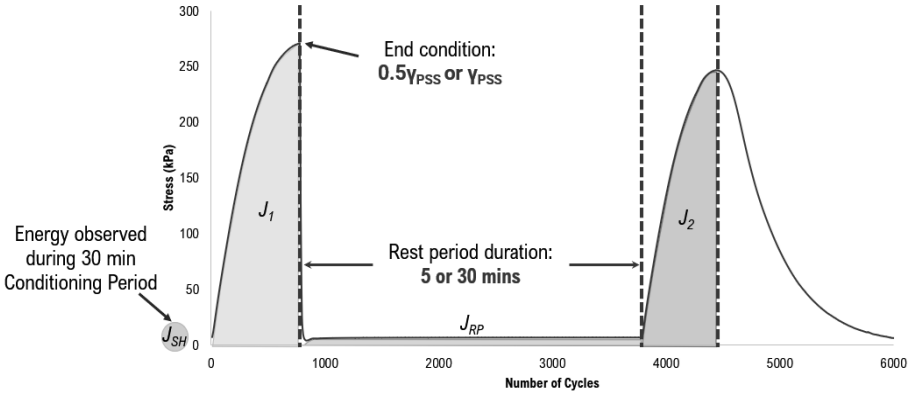

Figure 7-7 P-LASH procedure demonstrating the first and second loading periods interrupted with a single rest period using the pseudo-J-integral analysis procedure (Note: number of cycles is plotted on the x-axis in place of strain amplitude to demonstrate the time contribution of the rest period).

7.4 Results and Discussion

7.4.1 VECD Healing Analysis

Figures 7-8 and 7-9 depict the initial healing and total healing observed through the new LASH procedure for the $0.5\gamma_{peak}$ end condition, while Figures 7-10 and 7-11 depict the initial healing and total healing for the γ_{peak} end condition. The healing indices in each figure below show a noticeable difference in the IH observed at both the $0.5\gamma_{peak}$ and γ_{peak} end conditions. Logically, the IH values determined experimentally should be relatively similar (at least in groupings of the same binder). However, this is not the case based on the indices adapted from Asadi and Tabatabaee (2020).

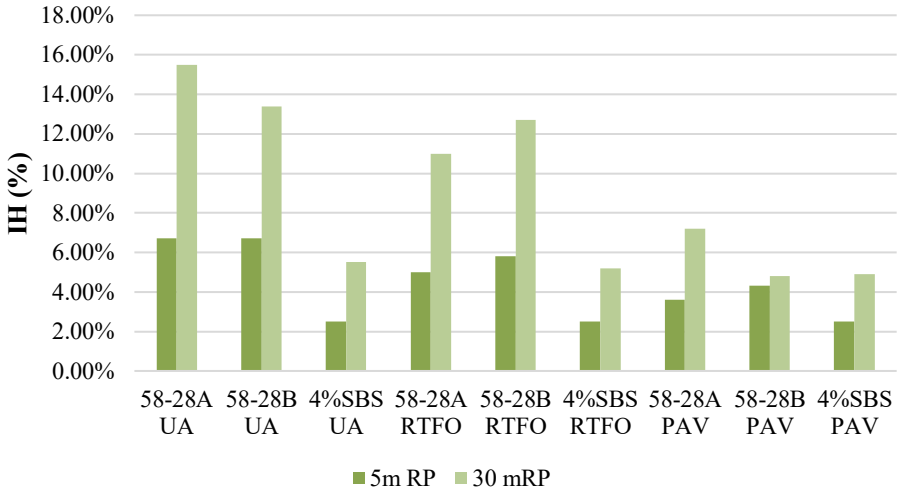

Figure 7-8 Initial healing for the $0.5\gamma_{peak}$ end conditions with 5 and 30 minutes of rest (20°C).

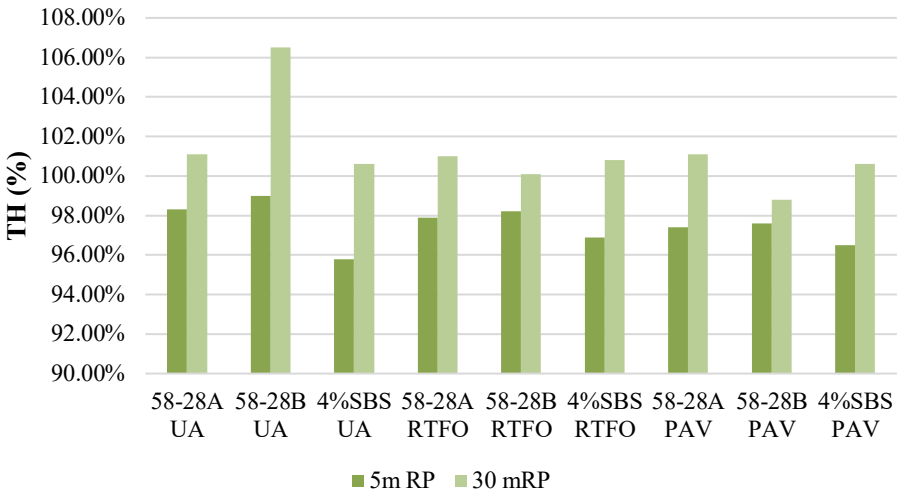

Figure 7-9 Total healing for the $0.5\gamma_{peak}$ end conditions with 5 and 30 minutes of rest (20°C).

To explain why this phenomenon occurs, two separate issues must be discussed. Firstly, Asadi and Tabatabaee (2020) do not detail the exact method used to incorporate the rest period duration into the VECD modelling. In a practical sense, there are two ways that the rest period can be incorporated: (1) the rest period time is not considered and there exists a continuous counting of time between the first and second loading phase (i.e. the time at the end of first loading phase is t_1 and the time at the beginning of the second loading phase is $t_2 = t_1 + 1$ second) or (2) the rest period duration was not removed from the time component of the analysis leading to a "time jump" (i.e. the time at the end of first loading phase is t_1 and the time at the beginning of the second loading phase is $t_2 = t_1 +$ rest period duration).

Based on Asadi and Tabatabaee's results, the latter appears to have been used and, thus, that procedure was used in this study as well. The considerably larger Δt resulting from a longer rest period decreases the S_2 parameter to proportionally smaller values even when S_1 and S_3 are in good agreement. This result can be seen in Tables A1, A3 and A5 in Appendix A.1 VECD Healing Analysis. Consequently, a second issue arises: the ratios between IH and RH in the observed total healing are skewed and tests with longer rest periods exhibit greater IH values. The result could be potentially misleading, and it is especially noticeable when comparing tests with very large differences in rest periods (e.g., 300 vs 1800 seconds, as is the case here).

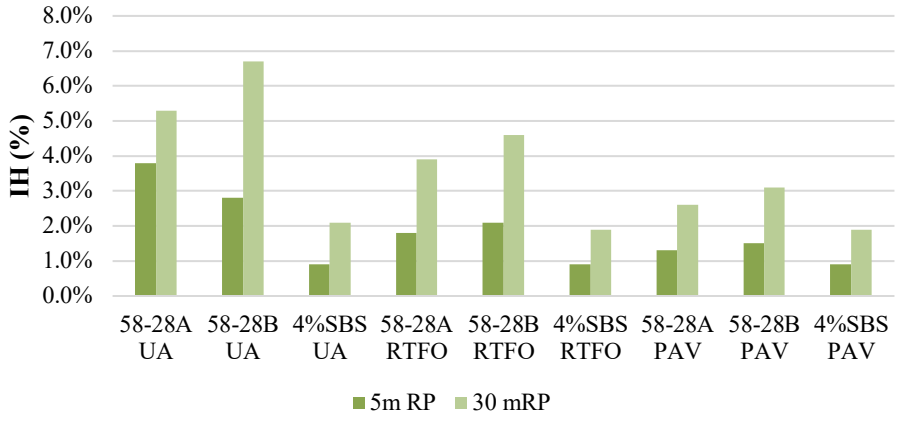

Figure 7-10 Initial healing for the γ_{peak} end conditions with 5 and 30 minutes of rest (20°C).

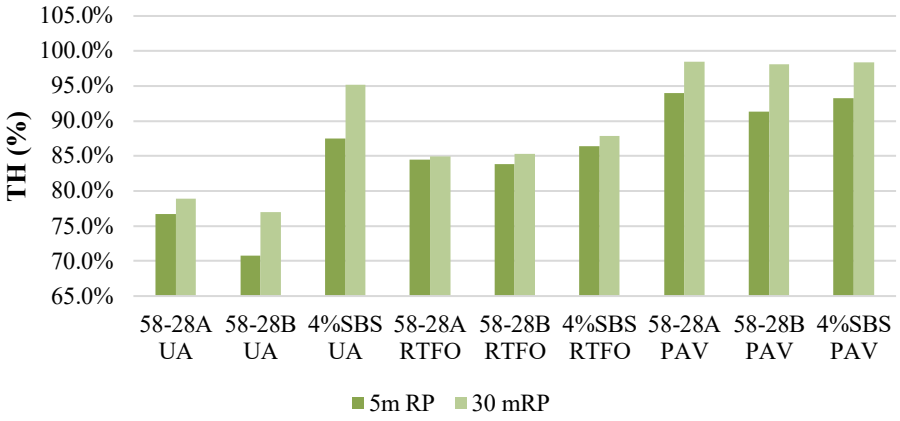

Figure 7-11 Total healing for the γ_{peak} end conditions with 5 and 30 minutes of rest (20°C).

It was observed that PG58-28A and PG 58-28B exhibit similar amounts of healing at each of the three aging levels. However, it is also observed that aging appears to decrease the amount of initial healing while also increasing the amount of total healing. This effect may be caused by the VECD material integrity parameter calculation, C. As observed in Chapter 6, more aged binders appear to have "broader" stress-strain curves compared to less aged binders. Consequently, a greater decrease in material integrity is calculated as can be seen in Tables A2, A4 and A6 in Appendix A.1 VECD Healing Analysis. A similar peak broadening effect resulted in lower C values calculated for the polymer-modified binder; the addition of 4% SBS to PG58-28A appears to significantly increase the total healing while decreasing the initial healing for the unaged and RTFO-aged binders. Once the binders are PAV aged, all three binders appear to have similar healing abilities based on the adapted VECD healing indices.

7.4.2 Crack Length Healing Analysis

Figures 7-12 and 7-13 depict a_1/a_2 indices of the $0.5\gamma_{peak}$ and γ_{peak} end condition, respectively, while Figures 7-14 and 7-15 depict c_1/c_2 indices of the $0.5\gamma_{peak}$ and γ_{peak} end condition, respectively. Raw data can be found in Tables A7 – A9 in Appendix A.2 Crack Length Healing Analysis. From the analysis of the DSR sample crack length, it can be observed that there is generally good agreement between the a_1/a_2, and c_1/c_2 indices. For both crack length indices, all binders appear to exhibit nearly 100% or greater healing ability at all aging levels when looking at the $0.5\gamma_{peak}$ end condition; although the RTFO aged 58-28A appears to exhibit an approximate 5 to 6% decrease in healing ability.

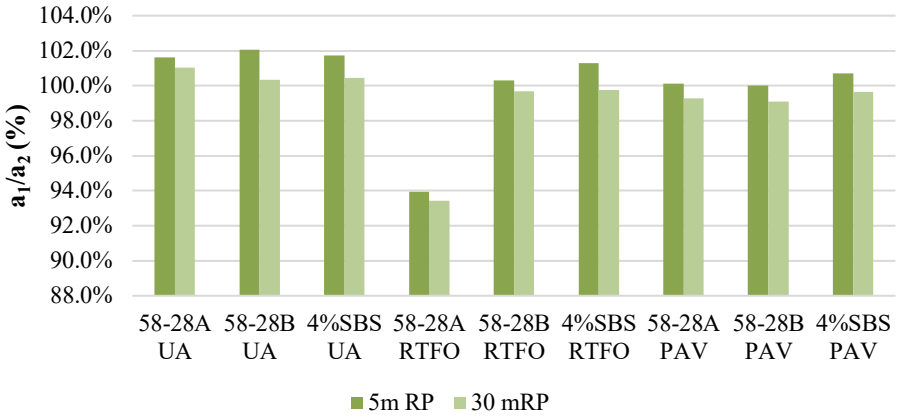

Figure 7-12 Crack length "a" ratio (a_1/a_2) for tests with the $0.5\gamma_{peak}$ end condition (20°C).

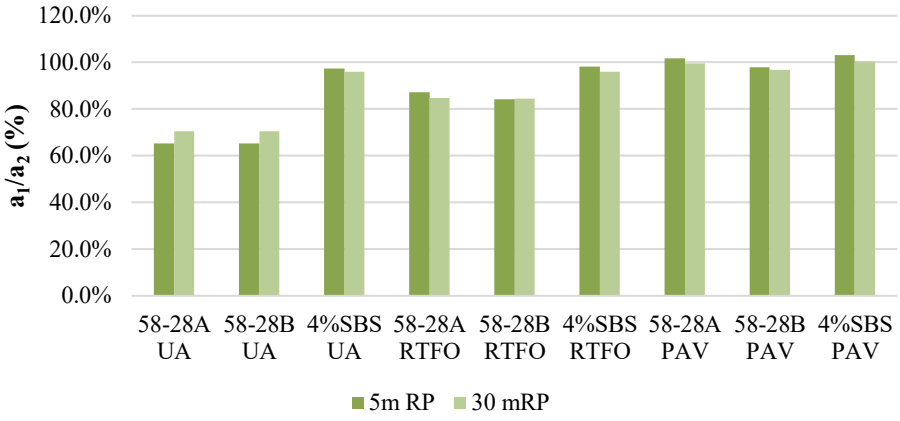

Figure 7-13 Crack length "a" ratio (a_1/a_2) for tests with the γ_{peak} end condition (20°C).

At the γ_{peak} end condition, "permanent damage" is observed for all three binders at the unaged and RTFO aging levels. Healing is only observed in the 58-28A and 58-28A+4%SBS PAV aged samples while the 58-28B PAV samples exhibit only minor damage. It is interesting to note that in most

scenarios more healing/ less damage is observed in the 5-minute rest period tests. Only the 58-28A and 58-28B unaged specimens exhibit less damage as a result of the increasing rest period duration. In literature, it is commonly accepted that SBS modification of asphalt cements is a successful strategy to improve cracking and fatigue resistance due to the ability of the polymer network to both extend and recover elastically (Zhu et al. 2014). Subsequently, the addition of the 4%SBS appears to serve as an improvement at the γ_{peak} end condition when the samples are unaged or short-term aged; at the PAV level, polymer modification appears to have a smaller effect.

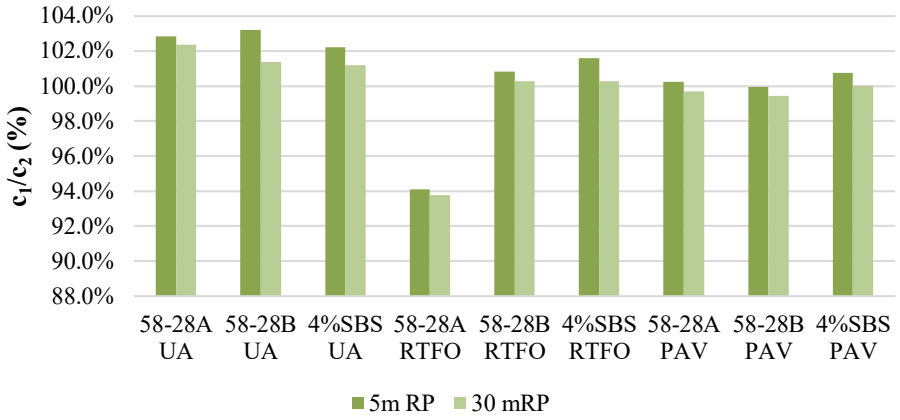

Figure 7-14 Crack length "c" ratio (c_1/c_2) for tests with the $0.5\gamma_{peak}$ end condition (20°C).

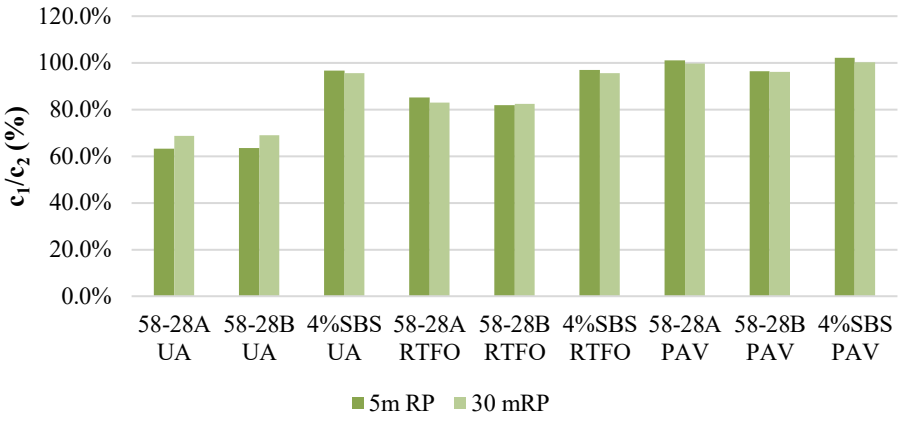

Figure 7-15 Crack length "c" ratio (c_1/c_2) for tests with the γ_{peak} end condition (20°C).

7.4.3 P-LASH Analysis

Figures 7-16 and 7-17 depict the %Ret indices of the $0.5\gamma_{peak}$ and γ_{peak} end conditions, respectively. Likewise, Figures 7-18 and 7-19 depict the $\%Res_J$ indices of the $0.5\gamma_{peak}$ and γ_{peak} end conditions, respectively. Raw data for the P-LASH Analysis Method 1 and 2 are found in Tables A10 – A15 in

Appendix A.3 P-LASH Healing Analysis. From the P-LASH analysis, both FREI and J-integral-based healing indices show good agreement as was the case for the crack length healing indices. For both %Ret and %Res, all binders appear to exhibit nearly 100% or greater healing ability at all aging levels when looking at the $0.5\gamma_{peak}$ end condition. Once again, the RTFO aged 58-28B appears to exhibit a 4% decrease in healing ability, and an additional irregular result can be seen in the %Ret for the PAV aged 58-28B samples.

The similarities between the VECD analysis and the two P-LASH analysis methods indicate that these three methods are sensitive to the same factors, especially as the relevant data ranges are quite similar. Similar to both the crack length and VECD healing analysis methods, the P-LASH methods demonstrate similar trends between strain amplitude end condition, aging and SBS modification. From the figures below, it appears that the %Ret method shows a similar or even a decrease in healing behaviour when increasing the rest period duration, similar to the cracking length healing analysis. Unlike the %Ret method, however, the $\%Res_J$ P-LASH demonstrates a benefit from the increased rest period duration, as was observed in the VECD method.

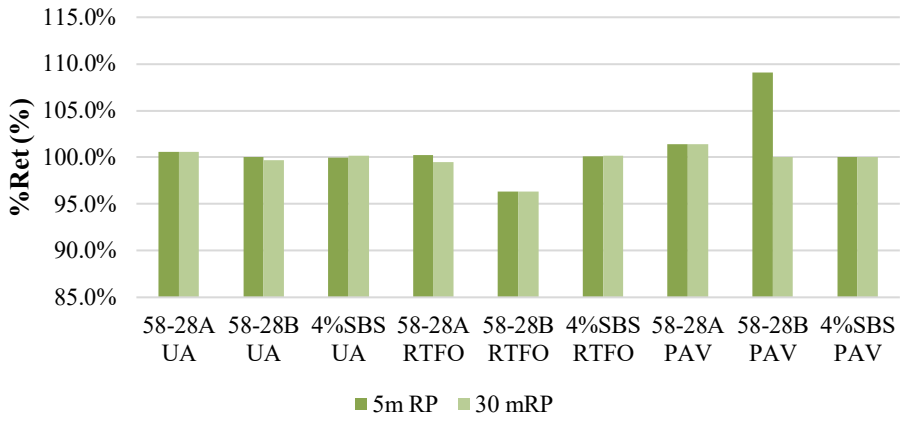

Figure 7-16 %Ret for tests with the $0.5\gamma_{peak}$ end condition with 5 and 30 minutes of rest (20°C).

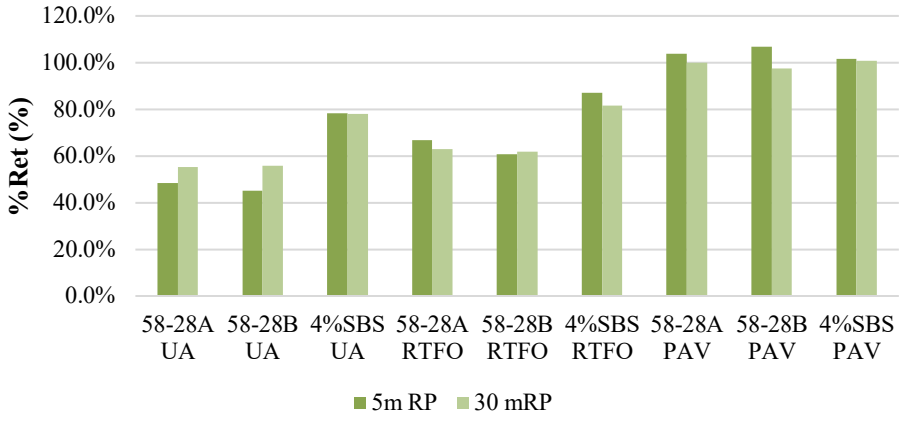

Figure 7-17 %Ret for tests with the γ_{peak} end condition with 5 and 30 minutes of rest (20°C).

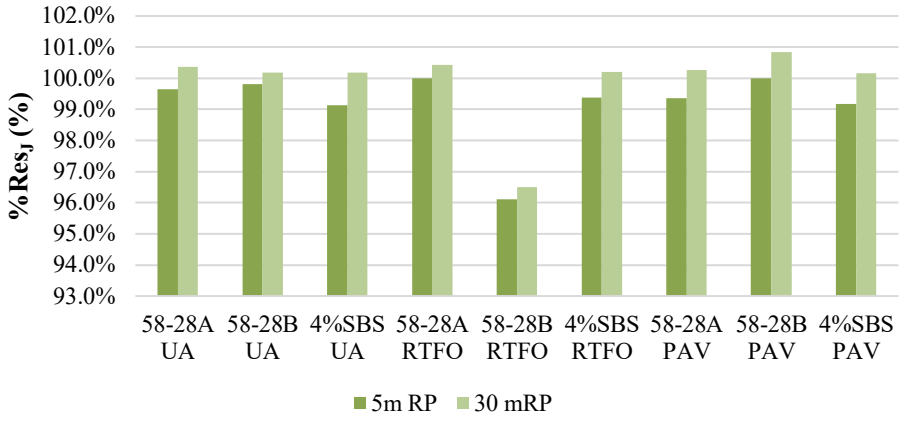

Figure 7-18 %Res$_J$ for tests with the 0.5γ_{peak} end condition with 5 and 30 minutes of rest (20°C).

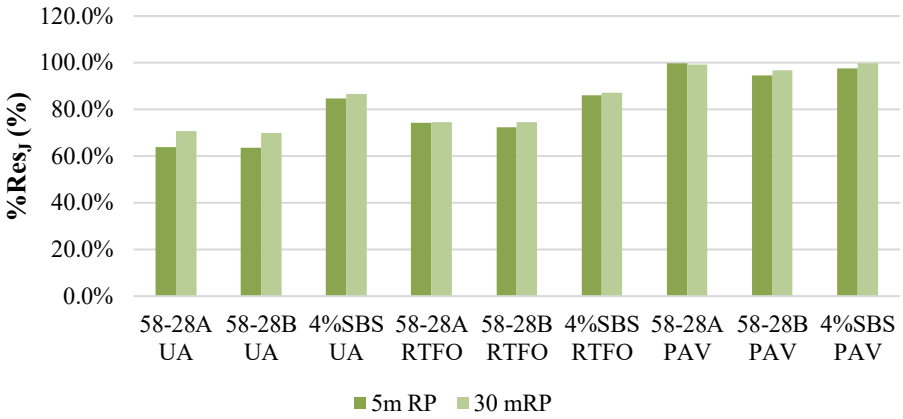

Figure 7-19 %Res$_J$ for tests with the γ_{peak} end condition with 5 and 30 minutes of rest (20°C).

7.4.4 The End Condition Dilemma

In the preceding sections, the results of each analysis method demonstrated that strain amplitude end condition played an important role in the perceived healing behaviour of the three binders. As was discussed, a greater difference in the healing ability was observed, especially in the unaged or RTFO-aged states, when loaded to the γ_{peak} value. To strengthen the validity of this claim, a statistical analysis was conducted.

A multivariate analysis of variance (MANOVA) was conducted to evaluate the main predictors of healing/ restoration: TH, %Ret, %Res, a_1/a_2, and c_1/c_2. Initially, the MANOVA was conducted on the entire data set to determine if there were any immediately significant differences between the independent variables: 1st loading phase end condition, rest period duration, aging level, and binder type. The initial MANOVA results can be viewed in Table 7-1; Table 7-1 displays the P-values for the Wilks' Lambda, Lawley-Hoteling Trace, and Pillai's Trace test statistics.

Table 7-1 Paired MANOVA results comparing the end condition, rest period duration, aging level and binder type.

		P-value/ Significance			
Dataset	**Criterion**	**End Condition**	**Rest Period Duration**	**Aging Level**	**Binder Type**
All three binders	Wilks' Lambda	1.95E-09	1.56E-04	1.10E-06	6.20E-02
	Lawley-Hoteling Trace	1.95E-09	1.56E-04	1.64E-07	5.00E-02
	Pillai's Trace	1.95E-09	1.56E-04	8.79E-06	8.00E-02
58-28A vs 58-28B	Wilks' Lambda	2.65E-06	2.90E-02	1.49E-05	8.78E-01
	Lawley-Hoteling Trace	2.65E-06	2.90E-02	6.17E-06	8.78E-01
	Pillai's Trace	2.65E-06	2.90E-02	4.64E-05	8.78E-01
58-28A vs 58-28A +4%SBS	Wilks' Lambda	4.28E-05	2.37E-03	4.24E-03	1.45E-01
	Lawley-Hoteling Trace	4.28E-05	2.37E-03	1.32E-03	1.45E-01
	Pillai's Trace	4.28E-05	2.37E-03	1.63E-02	1.45E-01
58-28B vs 58-28A +4%SBS	Wilks' Lambda	2.00E-05	3.21E-03	2.41E-04	1.20E-02
	Lawley-Hoteling Trace	2.00E-05	3.21E-03	8.93E-05	1.20E-02
	Pillai's Trace	2.00E-05	3.21E-03	8.18E-04	1.20E-02

For the MANOVA results, the null hypothesis set as equal means between dependant variables for each independent variable, *x*, ($\mu_{x,EC} = \mu_{x,RP} = \mu_{x,Age} = \mu_{x,Binder}$) and using a significance level of $\alpha = 0.05$. For any P-value in Table 7-1 lesser than or equal to α, the null hypothesis can be rejected. Thus, it is observed that the null hypothesis can be rejected for the binder-type variable when comparing the five healing indices used. It should be noted that this result does not determine which of the binders are similar/dissimilar, just whether there is a significant difference in the given dataset. Preparing a series pair-wise comparison of each binder at each aging level and each of the five healing indices would be

a relatively cumbersome endeavour, so three paired MANOVAs were prepared; the results of these MANOVAs are also displayed in Table 7-1. Based on the paired MANOVAs, the null hypothesis can be rejected for 58-28B and PG 58-28A + 4%SBS pairing. The null hypothesis for pairings of PG 58-28A and the other two binders cannot be rejected.

Returning to the MANOVA from the entire three binders datasets, the partial correlation error matrix can be constructed as shown in Table 7-2. The partial correlation matrix provides information about the correlation of two dependent variables when the remaining variables are omitted from the correlation analysis. Table 7-2 demonstrates that the full dataset has relatively strong correlations between all five indices, but correlations between %Ret and %Res and a_1/a_2, and c_1/c_2 are greater than 0.95, indicating an even stronger positive correlation. The very strong correlation pairings observed from the P-LASH and CL healing analysis methods are not unexpected, considering the similarities in their derivations.

Table 7-2 MANOVA partial correlation matrix between total healing (TH), %Ret (FREI), $\%Res_J$ (J-Integral), and cracking ratios ("a" and "c").

Index	TH	%Ret	$\%Res_J$	a_1/a_2	c_1/c_2
TH	1	0.87126	0.90044	0.89411	0.89788
%Ret	0.87126	1	0.9772	0.88221	0.8876
%Res	0.90044	0.9772	1	0.89128	0.90006
a_1/a_2	0.89411	0.88221	0.89128	1	0.99933
c_1/c_2	0.89788	0.8876	0.90006	0.99933	1

After determining the insignificance of the binder type, subsequent MANOVA studies were carried out on the individual binder data sets. Again, the end condition, rest period duration and aging level are used as independent variables, and the five healing indices as dependent variables. The null hypothesis was set as the equality of dependent variables means for each independent variable, *x*, ($\mu_{x,EC} = \mu_{x,RP} = \mu_{x,Age}$) and a significance level of $\alpha = 0.05$ was used. The results from the MANOVAs are found in Table 7-3. The highlighted values are P-values that are less than or equal to the selected significance level, in which case the null hypothesis can be rejected. Based on the binder-specific MANOVAs, it can be observed that in 14 out of 15 scenarios, the null hypothesis can be rejected for the end condition variable. Only two other scenarios report P-values below the selected significance level. This could be due to material variability leading to the presence of multivariate outliers, thus decreasing the robustness of the binder-individual MANOVAs. Finally, the dominance exhibited by the end condition variable confirms that the 1st phase amplitude sweep termination strain is the most crucial test condition from the proposed LASH V2 test protocol.

The previous chapter concluded that the peak shear stress corresponds to an observable change in the DSR geometry for the PG58-28 binder at all aging levels. Therefore, it may be sensible to hypothesize that the significant difference observed between the two end conditions is not likely caused by actual "fatigue damage" as evidenced by the results of $0.5\gamma_{peak}$ tests; but rather caused by changes in sample geometry leading to unreliable DSR-measured values as evidenced by the γ_{peak} test results. At the very least, this result shows that unaged and RTFO-aged binders are dominated by instability flow/ edge fracture failures at increasing strain amplitudes. Thus, the results of DSR-based amplitude sweep healing tests are completely unreliable for less-aged materials. This begs the question as to whether the healing tests should be conducted on long-term aged material only. Although it could be argued that the relatively intense standard PAV aging procedure (or other alternative non-standard accelerated binder aging processes) may irreparably alter different modifiers used to promote self-healing, thus, leading to potentially misleading conclusions and biasing "healing" characterization against more highly reactive modifiers.

Table 7-3 MANOVA comparison for all three binders featuring the total healing (TH), %Ret (FREI), $\%Res_J$ (J-Integral), and cracking ratios ("a" and "c").

		P-value/ Significance		
Index	**Source**	**58-28A**	**58-28B**	**58-28A+4%SBS**
TH	End Condition	0.003	0.006	0.003
	Rest Period Duration	0.382	0.336	0.023
	Aging Level	0.109	0.320	0.156
%Ret	End Condition	0.010	0.008	0.014
	Rest Period Duration	0.974	0.887	0.798
	Aging Level	0.079	0.043	0.098
%Res	End Condition	0.008	0.003	0.004
	Rest Period Duration	0.801	0.663	0.555
	Aging Level	0.099	0.062	0.092
a_1/a_2	End Condition	0.048	0.010	0.068
	Rest Period Duration	0.977	0.968	0.320
	Aging Level	0.137	0.136	0.214
c_1/c_2	End Condition	0.037	0.007	0.023
	Rest Period Duration	0.987	0.922	0.293
	Aging Level	0.154	0.161	0.259

7.4.5 RP:SH Analysis

Figures 7-20 and 7-21 below demonstrate that the observed ratio between the rest and pre-test conditioning periods ranges from 0.872 to 1.099; in most cases, the RP:SH ratio is near 1 or greater.

The RP:SH ratio generally tends to decrease with increased aging and, alternately, increases for longer rest periods. The original intention behind monitoring the conditioning and rest periods was to exclude the potential for material variability caused by small amounts of steric hardening that may occur during rest. Inadvertently, it may also have shown that: (1) only minor changes in geometry still occur when loading to the $0.5\gamma_{peak}$ value and more significant changes occur nearing γ_{peak}, and (2) very small strain amplitude loading ($\gamma_{applied} \approx 0.1\%$) is not as sensitive to changes in the sample geometry compared to larger strain amplitudes, and the DSR measurement is less accurate at these small strains.

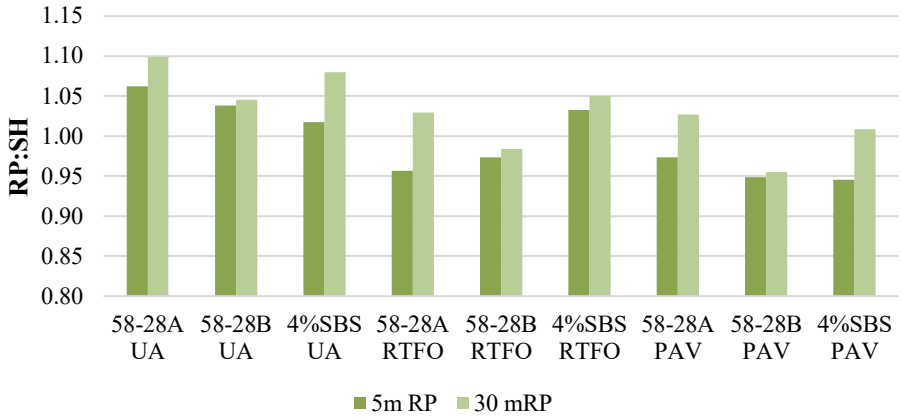

Figure 7-20 RP:SH ratios for tests at the $0.5\gamma_{peak}$ end condition (20°C).

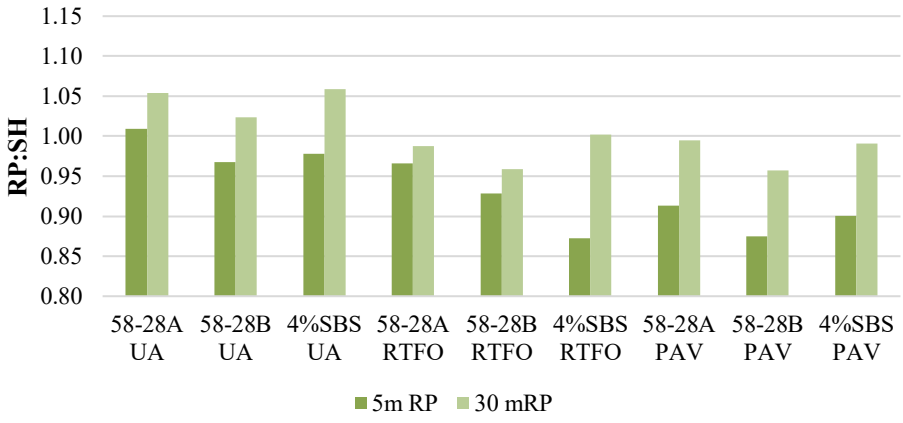

Figure 7-21 RP:SH ratios for tests at the γ_{peak} end condition (20°C).

7.4.6 Revisiting Electric Torque

In this section, it was prudent to use the knowledge gained in the previous studies to provide additional insight into the accuracy of the healing test results. The electric torque, M_{el}, from the DSR torque balance provides vital information to evaluate the total torque required to overcome the acceleration of

the measuring system and the sample. It was determined that M_{el} inflection point correlated strongly with a stress-strain post-peak behaviour and a complete "failure" of the DSR sample due to changes in sample geometry. From the statistical analysis of several failure criteria, the M_{el} inflection point was considered, along with the normal force, to be a reliable indicator of this occurrence. For example, the M_{el} inflection point was determined for the cLAS (i.e., the uninterrupted test) and the second loading phase for the PG 58-28A binder at all aging levels (Figures 7-22, 7-23 and 7-24).

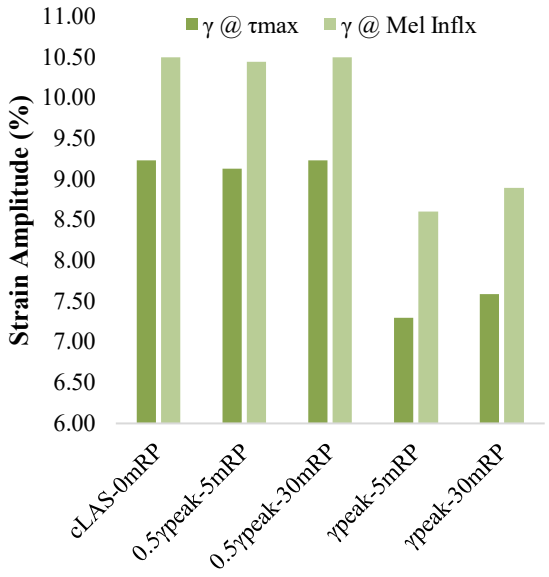

Figure 7-22 Peak shear (τ_{max}) and M_{el} inflection strain amplitude for unaged binders (20°C).

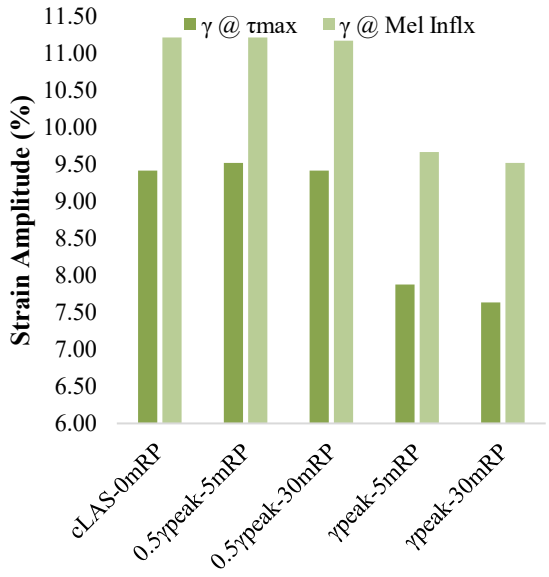

Figure 7-23 Peak shear (τ_{max}) and M_{el} inflection strain amplitude for RTFO-aged binders (20°C).

From Figures 7-22 and 7-23, it can be observed that loading the unaged and RTFO-aged binder to the $0.5\gamma_{peak}$ value produces nearly identical $S_{PeakStress}$ and S_{Mel} strain amplitudes. It is only when loading to γ_{peak} that a significant change is observed. When observing the results for the PAV-aged binder (Figure 7-24), only a marginal decrease in the S_{Mel} strain amplitudes is observed, while s similarly marginal increase in the $S_{PeakStress}$ can be seen. When comparing the corresponding strain amplitude lag (ΔS_f between $S_{PeakStress}$ and S_{Mel}) of all three binders at all aging levels, the ΔS_f appears consistent across all test treatments at a singular aging level regardless of the loading end condition and increases with increased aging. This result reinforces that the binder chemistry and changes due to accelerated laboratory oxidative aging plays a pivotal role in the thixotropic/flow behaviour (Coussot 2014) and the resultant measurement inaccuracy due to geometric changes. This result also reinforces the

conclusions of earlier studies (Canestrari et al. 2014), such that the current iteration of DSR tests for asphalt cements are not suitable to approximate trends/ draw conclusions about the fatigue or healing potential of a corresponding asphalt mixture.

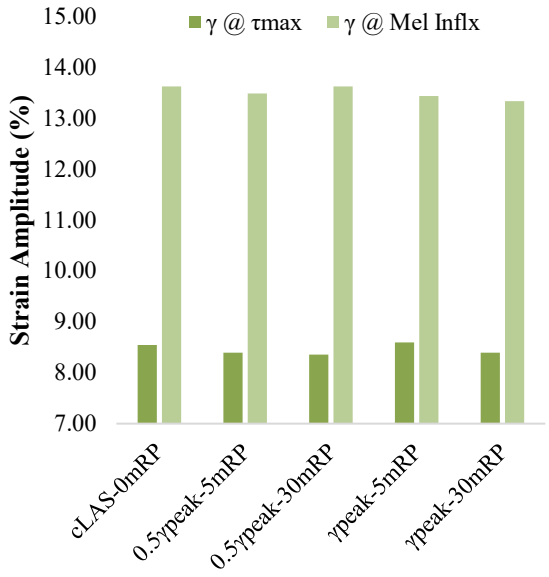

Figure 7-24 Peak shear (τ_{max}) and M_{el} inflection strain amplitude for PAV-aged binders (20°C).

7.5 Conclusions

In this chapter, modifications were proposed to the original linear amplitude sweep asphalt cement healing (LASH) test under the RILEM CHA-278 Task Group 2a interlaboratory testing and Task Group 3 (asphalt healing modelling). Several healing/ restoration indices were adapted from the literature and results were analyzed using either the fracture mechanics-based (i.e., crack length analysis, P-LASH) analysis or continuum damage mechanics (i.e., VECD). Based on the results of the modified healing test, the following conclusions can be drawn:

- For each of the five analysis methods, all three binders demonstrate complete restoration at all aging levels when loading to the $0.5\gamma_{peak}$ end condition; a decrease in healing or restoration is observed only when loading to the full γ_{peak} end condition for the unaged and RTFO aged binders. This observation was deemed statistically significant in the MANOVA analysis performed for all three binders.

- Any resultant decrease in the observed restoration of unaged and RTFO aged binder is attributed to DSR measurement artifacts due to instability flow occurring when the strain amplitude reaches the peak shear stress-strain amplitude.
- All PAV-aged binders exhibit essentially complete restoration with the results of all five analysis methods. PAV-aged binders would appear to have improved restoration/healing potential, in contrast with the conventional understanding of the detrimental effect of aging on fatigue/healing performance. This result is misleading as the PAV-aged binder is less affected by the described flow phenomenon.
- Examination of the RP:SH ratio at very low strains ($\gamma_{applied} \approx 0.1\%$) demonstrated that the DSR measurement is not accurate enough to detect changes to the sample geometry; these changes in sample geometry become more obvious when examining the direct effects of flow on the DSR electric torque.
- In general, the results of this study (and the previous chapters) indicate that the current iteration of DSR tests, either time or amplitude sweeps, have many challenges due to measurement artifacts common in viscoelastic materials. Thus, future DSR tests require significantly more study into the thixotropic, non-linear behaviour of asphalt cements before conclusions can be extrapolated to mixture fatigue/ healing performance.

Chapter 8
Asphalt Mixture Testing Experimental Test Setup

8.1 Introduction

Through the involvement of CPATT with RILEM TC CHA-278, some of the operating/procedural parameters may be influenced by working with colleagues in Europe while other parameters will follow the standards more commonly found in North America. The following chapter details the preparation of an 810 Material Testing Systems (MTS) multipurpose testing frame for fatigue-healing investigation of asphalt mixtures; more detailed information concerning the specimen installation, the custom conditioning chamber setup, and MTS software and data acquisition can be found in Appendix B Asphalt *Mixture Testing Setup and Data Acquisition*.

Both DIN 12697-26-2012 (including Annex D: Direct tension-compression test on cylindrical specimens), and AASHTO T 342 (Standard Method of Test for Determining Dynamic Modulus of Hot Mix Asphalt (HMA)) standards were considered in the creation of subsequent procedures for the analysis of cylindrical specimens in tension-compression. Correspondingly, fatigue analysis will be conducted following both North American and European methods, mainly the VECD modelling approaches found in AASHTO TP 107-18 (Standard Method of Test for Determining the Damage Characteristic Curve of Asphalt Mixtures from Direct Tension Cyclic Fatigue Tests) as well as the "Département Génie Civil et Bâtiment" also known as the "DGCB" or "Intrinsic Damage" method. As an addition to fatigue tests, loading frame extensions were constructed to allow transducers to be placed in line with the axis of loading to facilitate coupled ultrasonic measurements. Finally, the use of loading interruptions/ rest periods will be used to quantify restoration.

8.2 Scope

The procedures and equipment detailed hereafter are described to evaluate the fatigue resistance and restoration potential of lab-produced asphalt mixture samples. As an extension, the testing procedure is coupled with non-destructive/non-invasive characterization. This chapter will highlight the design decisions and lessons learned in the development of a new testing procedure. It is the intention that this chapter provides useful guidance to those who would work towards a test set-up and workflow for similar test procedures. The test procedures presented herein are recommended for mixture samples

with a nominal maximum aggregate size (NMAS) less than or equal to 12.5 mm due to the selected sample dimensions.

8.2.1 Apparatus

The following section highlights the apparatus and tools necessary to complete asphalt mixture testing for this study:

- *Loading Frame:* An MTS 810 testing frame is fitted with a top-mounted hydraulic actuator and a stationary 100 kN load cell located beneath the sample.
- *Axial Deformation Measurement System:* Axial deformations are measured with three on-specimen extensometers with a gauge length of 70 mm. Gauge points are glued to the specimen in the middle 70 mm of the cylindrical sample with Loctite® EA 608 two-part adhesive; gauge points are glued to the specimen after being affixed to the loading platens.
- *Loading Platens and End-Plate Gluing Apparatus:* Loading platens were constructed of 6061-T6 aluminum with a height of 25.4 mm and a diameter of 89 mm; 6061-T6 aluminum was chosen as it meets the minimum requirements and requires less tooling time compared to other platen materials. The loading/end plates are designed with 4 screw holes at approximately 30.6 mm from the center align with the mounting holes in the loading frame extensions. Samples are glued horizontally using a jig made from a wood-turning lathe with a V-shaped sample holder; the gluing procedure is detailed in the next section.
- *Loading Frame Extensions:* Custom loading extensions, made from 6061-T6 aluminum, were fabricated at the University of Waterloo Engineering Machine Shop. The loading extensions are dimensioned to accommodate ultrasonic transducers with a maximum diameter of 45 mm and height of 60 mm (additional space is necessary for the appropriate cabling and necessary mechanical fixtures). The extensions are fastened to the upper actuator and lower load cell using the appropriate bolts and locking washers.
- *External Conditioning Chamber:* A custom Burnsco environmental chamber is used to condition samples are the testing temperature within ±0.5°C. The chamber can control the internal air temperature in a range of -65 to 150°C using a series of compressors and heater fans. A “dummy” specimen containing a thermocouple with the same dimensions and NMAS as the test specimen is placed in the thermal chamber to monitor/ verify the test temperature. The control scheme for the conditioning chamber will be detailed in the subsequent sections.

- *Ultrasonic Pulse-Receiver System:* Any pulse-receiver system may be used provided it is capable of being triggered using a short-duration pulse or other circuitry (i.e., transistor-transistor logic/ TLL triggering). The OEM ultrasonic frontend, ACS-International A1560 Sonic-LF (Low Frequency), is used to provide UPV data acquisition and is synchronized with the testing frame using a TTL control scheme.
- *Frame Controller and Software:* The MTS 810 frame is accompanied by the frame controller; the frame controller is equipped with Digital Universal Conditioners (DUC) with the ability to customize several analog and digital inputs/outputs. The frame controller requires three interconnected software to function: (1) MTS Station Builder, (2) MTS Station Manager, and (3) MTS MPElite.

8.2.2 Test Specimen Preparation

This section details the specimen preparation parameters including aging, test specimen geometry, air voids, gluing procedure, gauge point gluing procedure and sample storage.

- *Aging*: Following common North American practices, lab specimens are oven aged for 4 hours according to AASHTO R30 before compaction.
- *Test Specimen Geometry*: Test specimens with a height of 120 mm (±2 mm) and a diameter of 75 mm are obtained through coring Superpave gyratory briquettes. Briquettes compacted to approximately 115 mm in height at a desired air void content. The cores are obtained by coring radially through the briquette and the ends are trimmed tangentially to the radius of the core to an initial height of approximately 130 mm. The core is then carefully ground on both ends to achieve the correct height using a cylinder end grinder (Figure 8-1).
- *Air Voids*: Samples are initially compacted using the 152.4 mm (6 in) Superpave gyratory mould to a height of approximately 115 mm. The desired air void content for pre-cored lab-prepared briquettes is 7.0% ±0.5%.

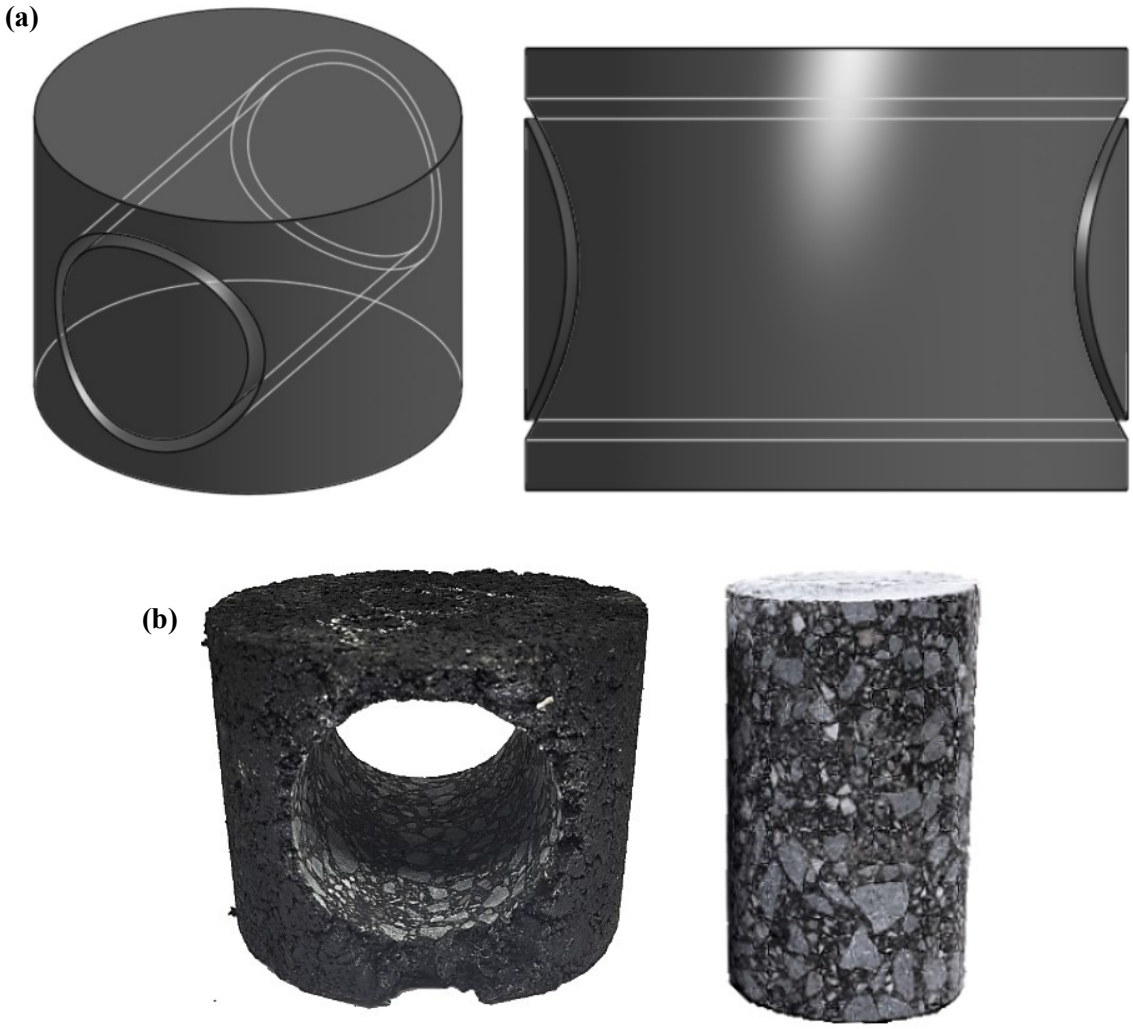

Figure 8-1 (a) Isometric and side view render of the proposed core before cutting (with hidden edges visible), (b) representative briquette after coring and complete specimen.

- *Gluing Procedure*: The end plates are affixed to the gluing jig chucks using a 6.35 mm spacer plate and at least 2 bolts. Approximately, 32 grams of Sikadur-30 epoxy are mixed (mix ratio A: B = 3:1 by weight) and divided between the upper and lower faces of the cylindrical sample; any surface defects or voids on the face or edge of the cylindrical specimens are filled with the epoxy at this point. The sample is placed on a height-adjustable V-shaped holder in the gluing apparatus, and the faces of the plates are mated to the sample surface by manually adjusting the chuck distance of the lathe (Figure 8-2). The chuck is adjusted such that the distance between the end plates is approximately 122 mm (±2 mm) and any adhesive "squeeze-out" is spread along the joint of the

sample and end plate using the appropriate tool. The sample is centred axially between the two plates and shims may be used if necessary to ensure proper alignment before the initial set of the epoxy. The epoxy is allowed to cure for at least 4 hours before it is removed from the gluing apparatus.

Figure 8-2 End-plate gluing jig constructed from a repurposed wood-turning lathe.

- *Gauge Point Gluing Procedure*: After removal from the gluing apparatus, the sample is placed horizontally on a separate jig and the gauge points are glued manually to the test specimen using Loctite EA E-00NS two-part epoxy. Gauge points are placed in the middle 70 mm of the specimen and each location is placed 120° apart when using a 3-extensometer configuration.
- *Sample Storage*: After evaluating the air voids of the post-cored specimens, the specimens are allowed to dry horizontally on a flat surface for at least 24 hours. After the specimens have reached a constant dry mass, the specimens are stored horizontally in a bed of fine aggregate/ sand at room temperature; samples are stored for a maximum of 21 days in this condition.

8.3 Complex Modulus Test Procedure

The complex modulus procedure presented hereafter is adapted from both AASHTO T 342 (Standard Method of Test for Determining Dynamic Modulus of Hot Mix Asphalt (HMA)) and DIN 12697-26-2012 (including Annex D: Direct tension-compression test on cylindrical specimens). This test is used to evaluate the stiffness of sinusoidally loaded asphalt mixtures at a combination of temperatures and frequencies at small strains in the Linear Viscoelastic (LVE) regime. This data can be used to construct

a master curve which is a practical tool for estimating, comparing, and ranking the mechanical behaviour of different asphalt materials under a wide variety of temperature/loading conditions. The constructed master curve will then be used in the VECD modelling approach described in AASHTO TP 107. Using the three-extensometer configuration, at least 2 specimens are required for this procedure with an approximate ±13.1% accuracy limit. The specimen installation procedure for the MTS 810 frame used in this study is described in Appendix B.1 Sample *Installation and Instrumentation*.

The test is conducted using "Force" control mode. One or several "dummy" specimens are used initially to estimate the force level required to reach the target on-specimen strain level for each temperature and frequency pairing. Strain level recommendations based on AASHTO T 342 range from 50 to 150 microstrain while DIN-12697-26 recommends an initial strain lower than or equal to 25 microstrain; for this research, a strain range of 40-60 microstrain was targeted. Based on DIN-12697-26, at least four temperatures must be used to generate a master curve and two isotherms are not separated by more than 10°C. The selected temperatures include: -5, 5, 10, 20 and 30°C. The procedure begins at the lowest selected temperature and a temperature limit of 30°C was imposed. Testing samples at temperatures above 30°C was limited as creep became a major concern as the asphalt cements used in Canada (and particularly the binder used in this study) tend to be softer compared to those used in other regions; the high-temperature limit can be increased for stiffer or modified binders as necessary. These selected temperatures differ from AASHTO T 342 which typically ranges from -10 to 54°C. Appendix B.2 *Environmental Testing Chamber Setup* details the custom conditioning chamber and the temperature control scheme.

The tested frequency range is selected from the recommendations of DIN-12697-26. A tapered sinusoidal waveform is applied at the selected frequencies including: 0.1, 0.2, 0.5, 1, 2, 10 and 0.1 Hz. The second 0.1 Hz measurement is intended to check that the sample has not been damaged during the frequency sweep; the sample is considered damaged if the difference between both 0.1 Hz measurements is greater than 3%. A minimum rest period of 2 minutes at 0 kN is applied after each frequency. The norm of the complex modulus, $|E^*|$, and phase angle, θ, for each temperature, T, and frequency, ω, are calculated at each temperature-frequency combination using the algorithm described in Section 12 of AASHTO T 342. The algorithm uses a sine fitting procedure to filter and center the raw force and displacement data; the generated sine waves can be used to conduct the stress and strain analysis of the asphalt mix under loading and is discussed in more detail in Appendix B.3 MTS *Data Acquisition*.

8.4 Fatigue/ Healing Test Procedures

The fatigue procedure described herein has influence from AASHTO TP 107-18 as well as several prior works (Baaj 2003; Baaj et al. 2003, 2005; Di Benedetto et al. 2011a; Perraton et al. 2010a; Underwood et al. 2012). This test is used to evaluate the fatigue performance of sinusoidally loaded asphalt mixtures at a single temperature and frequency at small strains. The description of the fatigue procedure used in this section will be generalized as the procedure could be modified to be conducted at a variety of temperatures, frequencies, and strain levels; procedure specifics will be elaborated on in the following chapter as necessary. At least three specimens are used at the given testing condition to produce 1 data point.

A tension-compression fatigue test can be conducted using three control modes: Force control (CS), Actuator Displacement control (CX), and On-Specimen Strain control (COS) modes. However, the On-Specimen Strain control was selected. Advantages of different control modes: FHWA report (2022), Underwood et al (2009 or 2012). Based on TP 107-18 Section 11.3, the testing temperature can be selected as 3°C below the average of the high and low LTPPBind PG temperatures of the chosen asphalt cement at a depth of 20 mm (e.g., a 58-28 binder could be tested at 12°C); however, a limit of 21°C is imposed even for binders with a calculated testing temperature greater than 21°C. For this research, a single temperature (10°C) will be selected regardless of the binder type or asphalt mixture used; this temperature will be consistent with the temperature selected by other research groups as a part of the RILEM TC CHA-278 interlaboratory testing. The norm of the complex modulus, $|E^*|$, and phase angle, θ, at the test temperature are calculated using the same algorithm described in Section 12 of AASHTO T 342 and in Appendix B.3 MTS *Data Acquisition*.

For uninterrupted fatigue tests conducted in this study, loading is terminated for three conditions: (1) after 1 million cycles, (2) when a macrocrack is observed at the surface of the sample, or (2) when the applied force declines toward 0 kN. Interrupted fatigue tests for evaluating healing and restoration will experience rest periods at 0 kN; at specified intervals during the rest period, a 300-cycle low strain loading period will be used to evaluate the change in stiffness of the resting sample. Rest periods can be programmed as short or long as desired, but longer rest periods ($\geq$8 hours) were preferred. Programming rest periods in the MTS MPElite software is also discussed in Appendix B.3.

8.5 Ultrasonic Signal Acquisition

Ultrasonic measurements are made using the ACS A1560 Sonic-LF Pulse-Receiver System using a pair of single-crystal 150 kHz P-wave transducers (although other transducers may also be used provided the maximum diameter is less than 45 mm and height less than 60 mm including the BNC connector). The 150 kHz Proceq transducers are rated to operate in a temperature range of -20 to 60°C by the manufacturer. As shown in Figure 8-3 (left), the pulse-receiver system is coupled to the sample through the two endplates and then activated using the external trigger port (referred to as the CTP port) on the A1560. Figure 8-3 (right) depicts the finalized T/C-UPV testing setup; more detail concerning coupled UPV measurements using the MTS with the designated pulse-receiver system can be found in Appendix B.4 Coupled *UPV Data Acquisition using the MTS.*

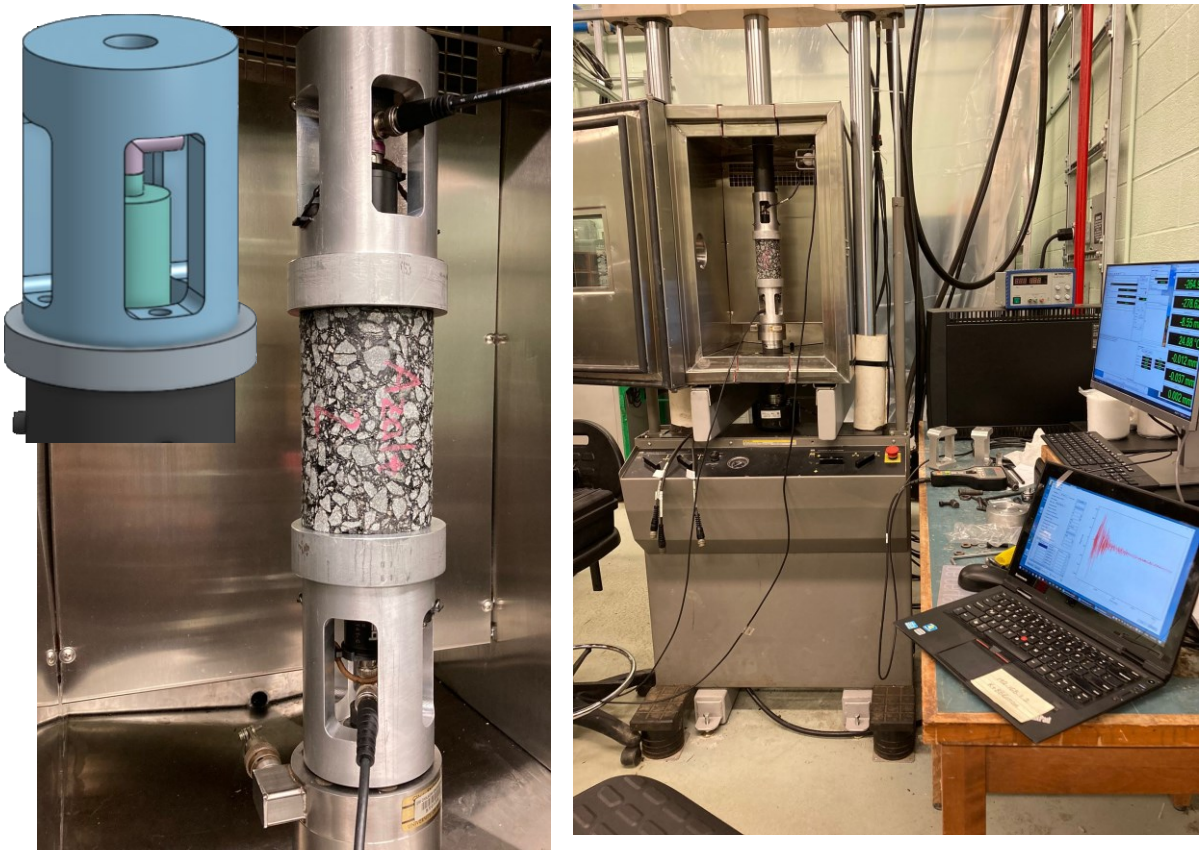

Figure 8-3 Render and a close-up photograph of the designed MTS extension with transducers installed (left), and completed test setup (right).

8.6 Additional Remarks for Specimen Preparation

This section briefly discusses the repeatability of the specimen mixing and compaction process as well as the typical specimen-platen glue thickness.

8.6.1 Specimen Air Voids

In typical fatigue studies, specimens have been cored transversally from asphalt slabs (pneumatic tyre/wheel compacted as completed by Baaj (2002), Mournier et al. (2016) and Boussabnia et al. (2019)) or through the top of Superpave gyratory specimens (Zeaida et al, 2014; Kim et al. 2022). In this study, test specimens with a height of 120 mm (±2 mm) and a diameter of 75 mm are obtained by coring horizontally through the side of Superpave gyratory briquettes.

Briquettes compacted to approximately 115 mm in height using a pre-determined mass of asphalt mix. The air void content was then determined using the procedure detailed in AASHTO T 166-21. Once a briquette was successfully determined to be in the target air void range (7.0% +/- 0.5%), specimens were cored, and the ends were trimmed and ground to its final height (as shown in Figure 8-1). Table 8-1 contains the before- and after-coring (as well as trimming/grinding) air voids for 22 specimens used in the calibration and testing of the fatigue-healing setup. Based on the 22 specimens, the before-coring air voids had an average of 7.2% with and standard deviation of 0.2%. After coring, the specimens had an average air void content of approximately 4.8% with an average loss of 2.4%. The coefficient of variation values found in Table 8-1 demonstrate that it was possible to produce specimens with a consistent air void content although the variability increases slightly after coring. When observing the plot in Figure 8-4, it is evident that there exists a linearly increasing relation between the before vs after coring air voids, but the overall linearity of the data is quite low (R^2 = 0.2131). As discussed in Section 8.2, this sample preparation technique is designated for specimens with an NMAS below 12.5 mm and may not be suitable for mixes with larger aggregate sizes. For larger stone mixes, the typical top-down coring method is recommended.

Table 8-1 Air voids before and after coring specimens to the final dimensions.

	Before Coring	**After Coring**
Average (%)	7.2	4.8
Standard Deviation (%)	0.2	0.3
Coefficient of Variation (%)	2.98	6.73

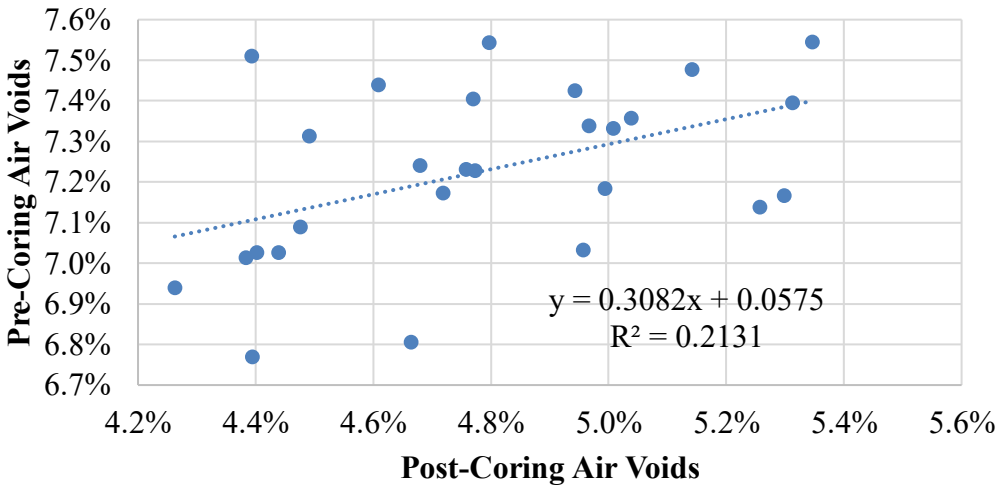

Figure 8-4 Pre-coring and post-coring air voids were obtained for 22 specimens using the same SP12.5 FC2 mix.

8.6.2 Gluing Thickness

As discussed in Section 8.2.2, the specimens are glued to two aluminum end plates using the custom gluing jig using a pre-determined mass of Sikadur-30 epoxy (halved between both ends). The chuck is adjusted such that the distance between the end plates is approximately 122 mm (±2 mm) and any adhesive "squeeze-out" is spread along the joint. A retrospective look at several specimens after testing revealed that typical glue thickness ranged from approximately 0.5 to 1.5 mm (Figure 8-5). This range was considered acceptable based on the recommendation (1 mm) provided in AASHTO TP107-18.

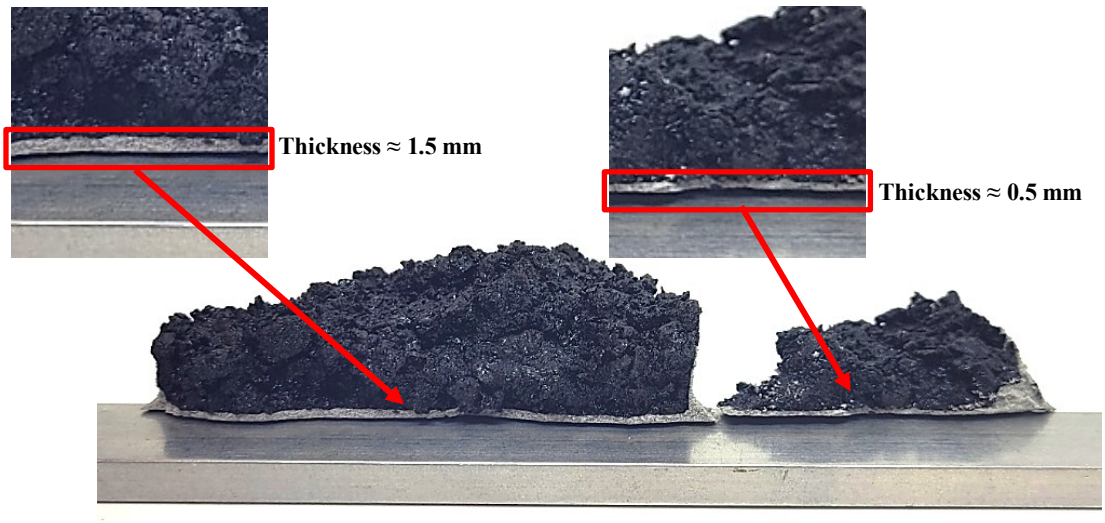

Figure 8-5 Representative glue thickness using the procedure described in Section 8.2.2; typical glue thickness = 0.5 to 1.5 mm.

8.7 Summary

In this chapter, the authour details the experimental test setup for the asphalt mixture testing required in the succeeding chapters. This chapter details the apparatus used, the data collection scheme, as well as the test procedures designed from both North American and European standards (e.g., DIN 12697-26-2012, AASHTO T 342, AASHTO TP 107-18) using a uniaxial tension-compression setup. The main contributions of this chapter include:

- The preparation of CPATT's Material Testing Systems (MTS) multipurpose testing frame and custom conditioning chamber/ control scheme. The test setup is capable of testing specimens over a wide array of frequencies and test temperatures. The design of test procedures use of loading interruptions/ rest periods is programmed into the MTS MPElite software to allow for the characterization of healing, recovery and restoration (Chapter 9).
- The design and implementation of custom MTS platen extensions to characterize cylindrical asphalt specimens using the complex modulus and fatigue tests coupled with ultrasonic pulse-receiver equipment. The coupled non-destructive/invasive measurements are capable of capturing UPV time signal measurements during loading/ rest periods to determine the viability of time-domain analysis methods for fatigue-healing characterization (Chapter 10).

Chapter 9
Preliminary Evaluation of Fatigue and Healing of Asphalt Mixtures using the "Intrinsic" VECD Method

9.1 Introduction

Fatigue cracking, as one of the primary failure modes in flexible pavements, is typically difficult to predict due to the intricate interactions between the asphalt mixture, environment/ climatic conditions and traffic/ loading level. At a micro level, recurring loading due to heavy vehicles and traffic at intermediate temperatures causes tensile stress to build up at the asphalt binder-aggregate interface/ film. As the stress reaches a critical threshold, microcracks initiate and eventually coalesce into macrocracks which propagate toward the surface, decreasing the useful service life of the pavement (Ozer 2018). Significant fatigue cracking can accelerate pavement deterioration affecting both the structural capacity and safety of highway users. Resistance to failure by fatigue is one of the most important elements in successfully designing a long-performing, safe pavement.

Di Benedetto et al. (2004) identified three primary stages of asphalt fatigue. The first and second stage of fatigue deal with the initiation of microcracks as the stress applied on the pavement exceeds the limit of the asphalt mixture. During Stage I, the asphalt experiences a sharp decrease in stiffness due to a combination of factors. Still, it is dominated by reversible bias effects such as thixotropy and local heating caused by heat dissipation generated by internal friction. Due to these effects, the first data point in a fatigue test can only be considered an artificial initial modulus, as the true initial modulus is much lower. Stage II is dominated by crack propagation and damage evolution, while bias effects play a much smaller role. Stage III relates to the propagation and development of macrocracks; the asphalt stiffness continues to decrease until the sample fails (Baaj 2018; Boussabnia 2019). Fatigue-damaged pavements become susceptible to moisture damage and intrusion by incompressible materials, which can further increase deterioration, weakening the pavement structure.

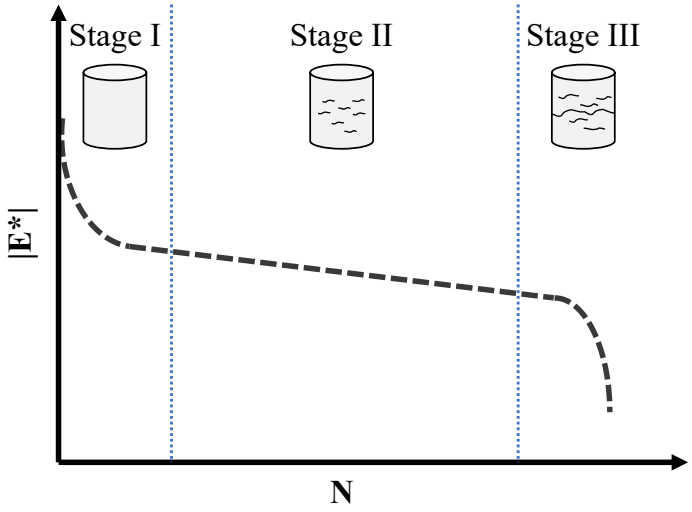

Figure 9-1 Three stages of fatigue in a typical accelerated fatigue test recreated from Baaj (2002).

Under cyclic loading, fatigue damage can be monitored as a decrease in stiffness from which characteristic damage curves/ plots can be generated, as shown in Figure 9-2a. Within the testing system, some hydraulic/ electrical energy is lost when loading the sample, and the sample itself dissipates some energy. As the sample is continuously cycled, the cyclic stress-strain behaviour can be visualized using a parametric Lissajous curve or hysteresis loop. In the stress-strain loop, the viscoelastic losses within the sample are a combination of bias effects and actual damage (Li et al. 2015).

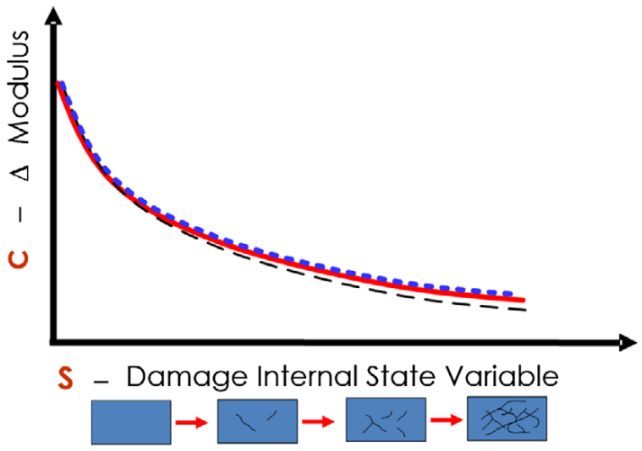

Figure 9-2 A typical stiffness/ pseudostiffness vs damage curve (Kutay and Lanotte 2018).

In a laboratory setting, fatigue is commonly characterized using 2-Point, 3-Point and 4-Point bending fatigue tests, indirect tensile (IDT), and tension-compression (T/C) tests. Bending tests are considered non-homogenous tests as the sample geometry and experimental setup produce a stress gradient in the material, causing part of the sample to be in tension and the opposite side to be in compression. Bending fatigue tests often demonstrate higher fatigue life estimates compared to diametral and uniaxial fatigue tests due to this difference in strain distribution throughout the specimen (Boussabnia et al. 2019). Homogenous tests such as uniaxial tension-compression (also referred to as push-pull or traction-compression) create a stress condition where the entire sample alternates between pure tension and pure compression; stiffness is then back-calculated as a material property. This type of test is recognized to be less influenced by specimen geometry (Li et al. 2015; Baaj 2002). Fatigue tests can be conducted using three primary control modes: stress control, displacement control and on-specimen strain control. Controlled stress modes are often employed using a tension-only haversine load to develop a permanent strain in the specimen. Due to machine compliance, actual on-specimen strain control modes are challenging to implement, and the resultant applied strain is considerably lower compared to the actuator displacement mode (Underwood et al. 2012).

As discussed previously, specimen geometry and loading type can play a significant role in the observed fatigue life of asphalt mixes (Underwood et al. 2012). As was discussed previously, specimen geometry and loading type can both play a major role in the observed fatigue life of asphalt mixes (Boussabnia et al. 2019). However, within the mixture itself, factors such as binder content, aggregate shape, angularity, gradation, and aggregate-binder adhesion also have significant influence on the local stress state experienced within the mixture and the fatigue behaviour (Hajj and Bhasin, 2017). The useful service life of asphalt mixtures is then difficult to accurately predict due to the inherent variability of mix characteristics, specimen preparation, specimen geometry and experimental set-up (Hajj and Bhasin, 2017). The useful service life of asphalt mixtures is then difficult to accurately predict due to the inherent variability of mix characteristics, specimen preparation, specimen geometry and experimental set-up (Boussabnia et al. 2019).

Furthermore, the presence of bias effects and damage healing during rest periods further complicate the matter. As such, characterizing fatigue resistance at the laboratory scale is often relegated to ranking due to the complexity of accurately modelling the fatigue behaviour while isolating bias effects such as thixotropy, heating, or non-linearity (Baaj 2002; Di Benedetto et al. 2012). Despite these obstacles,

accelerated fatigue test methods can be effectively used as simple ranking tools to help pavement designers compare the fatigue performance of different mixes.

9.1.1 Fatigue Modelling

In North America, fatigue modelling is widely conducted using the viscoelastic continuum damage model (VECD) as shaped through numerous works (Schapery 1975, 1984, 1990; Park et al. 1996; Park and Schapery 1997) according to AASHTO TP 107. In other locales, fatigue modelling may be achieved through less contrived means, such as damage mechanics or damage rate models, such as the DGCB "intrinsic" damage method (Baaj 2002) but are functionally very similar (Boussabnia et al. 2019; Mounier et al. 2015; Qian et al. 2013). In general, the fatigue characterization process requires several specimens to be tested at several microstrain levels, and after choosing a failure criterion they are plotted on a bi-logarithmic Wöhler plot as an [N_f, microstrain pair] as shown in Figure 9-2b.

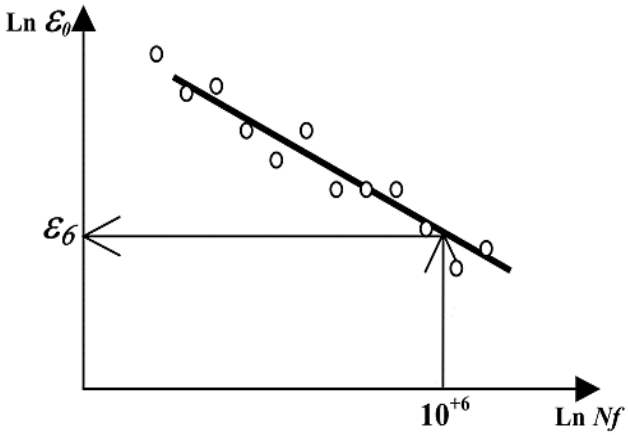

Figure 9-3 A typical Wöhler curve demonstrating the ε_6 concept (Baaj et al. 2005).

From the linear regression of the microstrain-failure pairs, the Wöhler curve is obtained to determine the fatigue life of the material. In European mix design, the ε_6 parameter is determined as the microstrain level at 10^6 cycles; the ε_6 values can be compared between different mixes or against a standard performance threshold with higher ε_6 values indicating better-predicted fatigue life (Baaj 2002). Notably, fatigue characterization has also been shown to follow the time-temperature superposition principle allowing for the estimation of the fatigue life of asphalt mixes over a variety of temperatures and testing conditions (Boussabnia et al. 2023; Underwood and Zeiada 2014; Wang et al. 2020).

9.1.2 Asphalt Mixture Healing

As a natural progression of the study of damage resistance (either directly as fatigue or indirectly by way of cracking resistance), characterizing the intrinsic healing ability of asphalt materials will be necessary to estimate the fatigue life of pavement materials more accurately. In literature, healing tests have often been adapted from both fracture and fatigue characterization tests with the addition of rest periods.

The 3-point bending (3PB) fatigue test coupled with dynamic measurements was used by Daniel and Kim (2001) to evaluate the role of temperature and rest period duration on the intrinsic healing ability of asphalt mixes. After loading, the 3PB beams were removed from the test chamber and allowed to rest for 4 hours at 20°C or 60°C. After the initial rest period, subsequent loading cycles and rest periods were alternated until a 50% reduction of the dynamic modulus was measured. It was observed that the life span of each beam increased, and the modulus recovered following the addition of rest periods (Daniel and Kim 2001). Similar 3PB fatigue-healing tests were conducted by Castro and Sanchez (2006) using an intermittent rest period scheme (0.1-second loading with 1 second of rest) at 20°C until a 50% drop in stiffness was observed (Castro and Sánchez 2006). Shirzad et al. (2019) also used a 3PB setup to test the influence of recycled asphalt materials and a UV-activated self-healing polymer. Temperature and exposure to UV light were varied for the rest period while the healing properties were evaluated from the strain energy recovery ratio. The researchers determined that the self-healing polymer improved healing and cracking resistance following exposure to UV light (Shirzad et al. 2019a).

In NCHRP Report 762, Witczak et al. (2013) carried out 4-point bending (4PB) fatigue tests in displacement control mode at 10 Hz allowing for a 0.1 sinusoidal load followed by a 1, 5 or 10-second rest period. The stiffness ratio (SR), which is defined as the ratio of stiffness at any cycle, N, compared to the initial stiffness, was initially used to quantify the effect of the added rest periods (Witczak et al., 2013). Xiang et al. (2020) tested asphalt mixtures modified with styrene-butadiene-styrene (SBS) using 4PB fatigue-healing tests. Fatigue tests were conducted at 15°C at five loading strains from 600 to 1400 microstrain. Xiang et al. also employed rest period temperatures ranging from 30 to 70°C and rest interval durations of up to 48 hours. Healing was characterized using two simple indices: the stiffness and the fatigue-life extension indices (Xiang et al. 2020). Other studies by Liu et al. (2012) and Khavandi Khiavi and Rasouli (2018) evaluated the use of different potential healing technologies

combined with the 4PB test using similar fatigue life extension indices (Khavandi Khiavi and Rasouli 2018; Liu et al. 2012).

Using uniaxial tension-compression, Little et al. (1998) developed a healing index based on the dissipated pseudostrain energy before and after rest periods. Cylindrical samples were tested using an intermittent loading pattern where they applied a 0.5-second rest period between haversine loads. The load was converted into a pseudo strain to eliminate time-dependent effects. They found that the pseudo strain energy consistently increased following a rest period. They noted that the recovery was mostly due to a change in stiffness and claimed that the healing index is not a fundamental material property due to the influence of molecular structuring and hysteresis (Little et al. 1998). Baaj (2002) used tension-compression to characterize the healing properties of several French mixtures, including one with SBS-modified asphalt cement. The test set-up used a sinusoidal loading frequency of 10 Hz and measured the strain with transducers placed triaxially around the cylindrical sample. The test consisted of alternating loading and rest periods. Each loading period consisted of either 300,000 or 150,000 cycles, followed by a 24-hour rest period. The temperature was held constant during loading but was varied during the rest periods (Baaj 2002). Underwood and Zeiada (2014) conducted a similar study to Little et al. (1998) with the addition of the simplified VECD model. The study proposed the newly derived "smeared damage model" for healing tests, and the healing was evaluated using an index obtained from the loss in pseudostiffness between uninterrupted fatigue tests and those with intermittent rest periods (Underwood and Zeiada 2014).

9.2 Objective

The numerous studies listed herein show that many past healing studies used relatively simple indices derived from the before-rest and after-rest changes in either stiffness or fatigue life. Bias effects (e.g., thixotropy, non-linearity, etc.) are known to significantly affect the initial stages of fatigue testing and are not typically accounted for in the second or subsequent rest periods. The primary objective of this chapter is to develop asphalt fatigue modelling methods to isolate bias effects from "true" fatigue; fatigue modelling methods can then be extended to healing characterization in fatigue tests with interruptions/ rest periods.

9.3 Fatigue Modelling Theoretical Background

9.3.1 The Simplified Viscoelastic Continuum Damage (S-VECD) Model for Mixtures

As discussed previously for asphalt cement, the VECD model, based on the works of Schapery (Schapery 1975, 1984, 1990) as well as Park, Kim and Schapery (Park et al. 1996; Park and Schapery 1997), provides a framework for the fatigue behaviour of viscoelastic materials under small strains. From these works, the Simplified-VECD model was adapted in the works of Hou (2009) and Underwood et al. (2012) to create an easily implemented algorithm to create the characteristic damage (C-S) curve, as shown in Figure 1 for the standardized Asphalt Material Performance Tester (AMPT). The AMPT is a standalone testing frame developed from several NCHRP projects (9-19, 9-29 and 2-5) with various accompanying AASHTO test standards for "fundamental" tests (e.g., Dynamic modulus/Flow number in AASHTO T 378, Cyclic Fatigue in AASHTO T 107 and "Stress Sweep" Rutting tests in AASHTO TP 134) to be used as inputs in the Pavement ME Design Guide (Kim et al. 2022).

The S-VECD modelling algorithm observed herein follows the work of Underwood et al. (2012) as well as the 2021 version of AASHTO TP 107 (Determining the Damage Characteristic Curve and Failure Criterion Using the Asphalt Mixture Performance Tester Cyclic Fatigue Test). The algorithm follows a piecewise approach to calculate the per cycle pseudostrain (ε^R), pseudostiffness (C) and damage parameter (S). Equations 9-1 to 9-3 below contain the functional form of the calculation when the reduced test time (ξ) is greater than the reduced time pulse (ξ_p):

$$\varepsilon^R = \left(\varepsilon^R_{0,ta}\right)_{cycle,i} = \frac{1}{E^R} \cdot \frac{\beta + 1}{2} \left(\left(\varepsilon_{0,pp}\right)_i \cdot |E^*|_{LVE}\right) \quad \text{Eqn. 9-1}$$

$$C^* = \frac{(\beta + 1)\sigma_{0,pp}}{2\varepsilon^R_{0,ta} \cdot DMR} \quad \text{Eqn. 9-2}$$

$$dS = \left(dS_{cyclic}\right)_{cycle,i} = \left(\frac{-DMR}{2} \cdot \left(\varepsilon^R_{0,ta}\right)^2 \Delta C_i\right)^{\alpha/(1+\alpha)} \cdot \left(\Delta t_R \cdot K_1\right)^{1/(1+\alpha)} \quad \text{Eqn. 9-3}$$

where $\varepsilon^R_{0,ta}$ is the pseudostrain tension amplitude, E^R is the reference modulus (taken as 1), β is the load form factor, $\varepsilon_{0,pp}$ is the peak-to-peak strain magnitude, $|E^*|_{LVE}$ is the LVE modulus obtained from a Prony series fitting of the dynamic modulus, C^* is the pseudo secant modulus, $\sigma_{0,pp}$ is the peak-to-peak stress magnitude, DMR is the dynamic modulus ratio = $|E^*|_{fingerprint}/|E^*|_{LVE}$ determined from an

exploratory per sample dynamic modulus test, dS is incremental damage parameter change, Δt_R is the reduced timestep, α is continuum damage power term/ evolution rate, and K_1 is the loading shape factor as is used in AASHTO TP 107 (Underwood et al. 2009, 2012).

The characteristic damage relationship can then be fitted using either an exponential or power law form:

$$C = e^{aS^b} \quad \text{Eqn. 9-4}$$

$$C = 1 - yS^z \quad \text{Eqn. 9-5}$$

where a and b are the exponential fitting coefficients, and y and z are the power model fitting coefficients. A closed-form solution for each model can then be used to predict the number of cycles to failure (N_f) at a given strain input and failure damage value (S_f) at a given test temperature using the reduced frequency (f_{red}) and the time-temperature superposition (TTSP) shift factor. The power law form is calculated as:

$$N_f = \frac{2^{3\alpha} f_{red} S_f^{\alpha - z\alpha + 1}}{(\alpha - z\alpha + 1)(yz)^{\alpha}\left[(\beta + 1)\varepsilon_{0,pp}|E^*_{LVE}|\right]^{2\alpha} K_1} \quad \text{Eqn. 9-6}$$

The exponential form can be solved using a trapezoidal integration approach with 200 discrete points between the integration limits of 0 to S_f:

$$N_f = \frac{(-1)^{\alpha} 2^{3\alpha} f_{red}}{\left[(\beta + 1)\varepsilon_{0,pp}|E^*_{LVE}|\right]^{2\alpha} K_1} \cdot \int_0^{S_f} \left(abS^{b-1}e^{aS^b}\right)^{-\alpha} dS \quad \text{Eqn. 9-7}$$

Failure for a single test specimen can be determined as a drop in the phase angle from the original linear portion of the δ x N curve, although the modulus multiplied by the number of cycles ($|E^*|$ x N) is a more reliable method to define failure (Kim et al. 2022). The failure damage value is calculated by inputting the failure pseudostiffness (C_f) into either the power law or exponential fitting equations. Both C_f and S_f can be obtained experimentally for a single mix over a range of temperatures and test frequencies or using different relationships found in the literature (Underwood et al., 2012, Hou et al., 2011). Further analysis of S-VECD for asphalt mixtures has led to several fatigue ranking parameters, including the average released pseudostrain per cycle (G^R), the D^R summation failure criterion as well as the S_{app} fatigue index (Wang et al. 2020; Kim et al. 2022; Kuchiishi et al. 2023; Wang and Kim 2017).

9.3.2 DGCB "Intrinsic" Damage Model

The DGCB fatigue model (named after the "Department Génie Civil et Bâtiment" at the École Nationale des Travaux Publics de l'État (ENTPE) in Lyon, France) is an alternative approach to fatigue analysis initially proposed by Di Benedetto et al. (1996, 1997) and further developed by Ashayer Soltani (1998) and (Baaj 2002). The DGCB model is an intrinsic damage model approach that can be used to correct the non-fatigue-related bias effects of asphalt mixtures. Through the DGCB method, three distinct stages of asphalt fatigue are identified, as shown in Figure 9-2a below. The first and second stage of fatigue deal with the initiation of microcracks as the stress applied to the specimen exceeds the allowable stress of the mixture.

During Stage I (called the adaptation stage), the asphalt experiences a sharp decrease in stiffness due to a combination of factors. However, it is dominated by reversible bias effects such as local heating (caused by viscous dissipation of heat generated by internal friction) and thixotropic effects (reversible time-dependent fluidization) caused by repeated loading. Due to these effects, the first data points in a fatigue test can only be considered an "artificial" initial modulus, as the true initial modulus is much lower. The fatigue stage, Stage II, is dominated by crack propagation and damage evolution, while bias effects play a much smaller role. During fatigue testing, samples in stages I and II experience an increase in the Poisson's ratio as cracks and air voids increase the sample's volume. The failure stage, Stage III, relates to the propagation and evolution of macrocracks; the asphalt stiffness and Poisson's ratio decrease until the sample fails (Baaj 2002; Baaj et al. 2003, 2018). An interval, i, of interest (in the first two stages) is defined for analysis. Generally, for the DGCB approach, two intervals are chosen where $i = 1$ is from N = 50,000 to 150,000 cycles, and $i = 2$ is from N = 150,000 to 300,000 cycles. In these intervals, the observed change in stiffness is quasilinear and the slope of linear regression of data points in these intervals is used to establish $E_{00i,}$ which represents the extrapolated initial modulus of the i^{th} interval. The value, a_{Ti}, is then defined as the slope of the linear regression normalized by E_{00i}; values for each interval are different due to the nonlinearity of damage (Baaj et al. 2003).

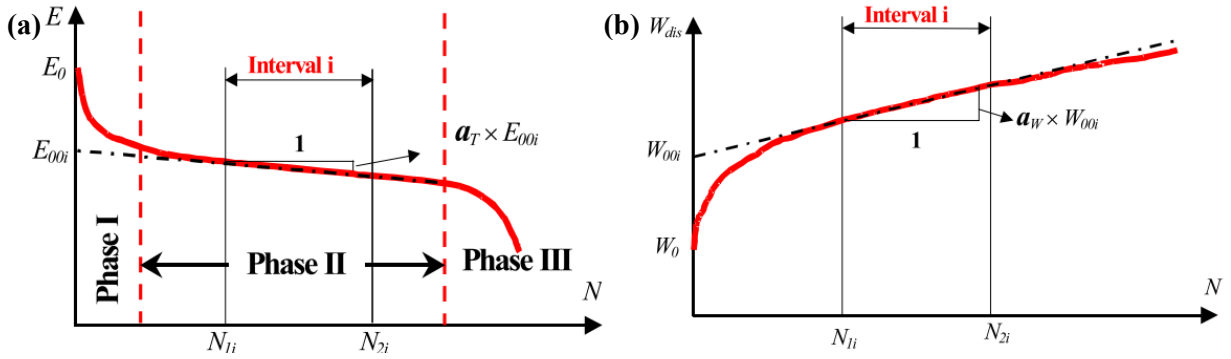

Figure 9-4 (a) Complex modulus evolution vs loading cycles and (b) dissipated energy evolution vs loading cycles during a fatigue test (Baaj 2002).

As the sample is loaded, an observed variation in the dissipated energy per cycle leads to a change in the sample stiffness. As dissipated energy per cycle increases due to non-linearity and internal heating, generally, stiffness decreases in the asphalt mixture. Consequently, the a_T is the sum of a_F and $a_{B,}$ which represents the contribution of damage evolution due to true fatigue and bias effects, respectively. The contribution of bias effects can be determined from the dissipated energy vs the number of cycles plotted for the desired interval. It was then proposed that the corrected fatigue slope can be calculated as follows:

$$a_{Fi} = a_{Ti} + a_{Wi}\frac{C_i(E_0 - E_{00i})}{E_{00i}} \qquad \text{Eqn. 9-8}$$

where a_{Wi} is the slope of the linear regression of the dissipated energy curve for the i^{th} interval as depicted in Figure 9-2b, C_i is a coefficient which accounts for the observable non-linearity in each interval (such that $C_1 = 3/4$ and for $C_2 = 2/3$), E_0 is the initial modulus performed for that specific sample treatment. Using the linear regression of the dissipated energy curve and the non-linearity coefficients as found in Eqn. 9-8, the corrected fatigue life can be estimated based on intervals 1 or 2. Furthermore, by correcting for bias effects due to fatigue loading, it has been demonstrated that this technique can be successfully used for either strain or stress-controlled tests proving that the damage rate is intrinsic to the material itself (Baaj 2002). The correction can then be extended to the modulus through the equation:

$$E_{cor} = E_{exp} + a_{Wi}C_i(E_0 - E_{00i})N \qquad \text{Eqn. 9-9}$$

where E_{cor} is the corrected modulus value, and E_{exp} is the experimentally obtained modulus value at the Nth cycle (Baaj 2002).

After completing the DGCB analysis, two (ε_i, a_{Fi})[1] pairs are generated. By testing the same mix at different microstrain amplitudes, it is possible to model the fatigue damage rate as a function of strain level:

$$a_{Fi} = A_i \varepsilon_i + B_i \quad \text{Eqn. 9-10}$$

where A_i and B_i are asphalt mixture and internal dependent linear regression coefficients. Using interval 1 parameters, the damage rate is generally higher, leading to a perceived shorter fatigue life. Conversely, using interval 2 parameters, asphalt mixtures demonstrate lower damage rates with improved fatigue life predictions for modified asphalt mixes compared to traditional failure criteria (Baaj et al. 2003, 2005). From the damage rate- microstrain curves, it is possible to estimate the fatigue life after 1 million cycles (also known as the ε_6) by computing the strain value at which the damage rate at 1 million cycles is $a_{Fi} = -0.5 \times 10^{-6}$ μm/m. This technique was initially applied to tension-compression fatigue testing, but similar interval-based analysis techniques have also been extended to 4-Point bending fatigue tests (Qabur 2018) and 2-Point bending tests (Boussabnia et al. 2019).

9.4 Materials and Methodology

9.4.1 Intrinsic-VECD Modelling

The proposed approach herein describes an "intrinsic damage"/interval-based method as an extension to the S-VECD proposed by Underwood et al. (2012). The Intrinsic-VECD or iVECD method is proposed to correct for the non-fatigue-related bias effects of asphalt mixtures that may still be present even after the conversion of stresses and strains to the equivalent pseudo-variables, which can have an increasing effect on the test specimen at increasing strain levels (Di Benedetto et al. 2011). Functionally, the iVECD method relies upon the same linearization methods as the DGCB with a few modifications. The proposed method changes the intervals of interest to the damage at the corresponding number of cycles (i.e., interval 1 ranges from S_{50k} to S_{150k}, and interval 2 ranges from S_{150k} to S_{300k}).

As was mentioned previously, changes in the dissipated energy per cycle lead to a change in the sample stiffness; however, the iVECD derivation requires the linearization of the change of dissipated energy to the damage parameter. Consequently, the VECD a_T is still the sum of a_F and a_B, representing

[1] ε_i is the strain amplitude experimentally obtained from the middle of the i^{th} interval.

the contribution of damage evolution due to true fatigue and bias effects, respectively. It is then proposed that the corrected fatigue slope can be calculated as follows:

$$a_{Fi\,VECD} = a_{Ti\,VECD} + a_{Wi\,VECD}\frac{(C_0^* - C_{00i}^*)}{C_{00i}^*} \cdot \frac{C_i}{a_{shift}} \quad \text{Eqn. 9-11}$$

where the TTSP shift factor, a_{shift},[2] is determined from the complex modulus master curve with a reference temperature of 21.1°C, C_i non-linearity coefficients can be appropriated from the DGCB method (i.e., C_1 = 3/4 and for C_2 = 2/3). The division of the C_i coefficient by the TTSP shift factor allows for the scaling from the number of cycles to the damage parameter, thus, producing a reduced non-linearity coefficient, $C_{i,red}$. This is a logical change to the original DGCB fatigue slope, as the iVECD method uses the dissipated energy vs damage parameter curve. Correspondingly, the use of the TTSP shift factor has been validated for fatigue and crack propagation in several studies (Di Benedetto et al. 2011b; Boussabnia et al. 2023; Hou 2009; Nguyen et al. 2013) and is already a fixture of the standard S-VECD algorithm in AASHTO TP 107. Similarly, the correction can be applied to the secant pseudostiffness through the equation:

$$C_{cor}^* = C_{exp}^* + a_{Wi}C_{i,red}(C_0^* - C_{00i}^*)S \quad \text{Eqn. 9-12}$$

where C^*_{cor} is the corrected secant pseudostiffness value, C^*_{exp} is the experimentally obtained secant pseudostiffness value at the Nth cycle. In line with the S-VECD method, a closed-form solution can also be derived for intervals 1 and 2:

$$N_{f\_00i} = \frac{f_{red}S_f}{\left(0.25a_{Fi\,VECD} \cdot \left[-0.5(\beta+1)\varepsilon_{0,pp}|E^*_{LVE}|\right]^2\right)^{\alpha} K_1} \quad \text{Eqn. 9-13}$$

Using the (ε_i, N_{f_00i}) pairs from tests completed at different strain levels, a Wöhler-style fatigue curve can be generated to estimate the fatigue life/ strain level at which the mix will fail after 1 million cycles (i.e., the iVECD ε_6).

9.4.2 Materials and Test Regime

The preliminary work for the iVECD model is conducted using a single Superpave 12.5 mix containing 5.2% PG 58-28 asphalt cement. Samples were initially compacted using the Superpave Gyratory compactor (SGC) to a height of 115 mm; air voids were measured to be an average of 7.2% from 18

[2] Typically, "a_T" is used to designate the TTSP shift factor, however, the shift factor will be denoted by a_{shift} to avoid confusion with the a_T from the DGCB derivation.

SGC briquettes used in this study. Compacted samples were cored horizontally through the SGC briquette using a coring bit with an internal diameter of 75 mm. After trimming samples using a wet saw, the samples were ground to their final height of approximately 120 (+/- 2.5) mm. After cutting and coring, the average air voids of the samples were measured to be 4.8%; thus, the reduction in air voids due to the coring procedure was approximately 2.4%. As is necessary for the calculation of the $|E^*|_{LVE}$ and DMR in the VECD analysis algorithm, the complex modulus test was conducted at several temperatures (-5, 5, 10, 20 and 30°C) and frequencies (0.1, 1, and 10 Hz). The complex modulus data were modelled using the Sigmoidal and 2S2P1D master curve models in the FHWA FlexMAT V2.1 Excel spreadsheet. The storage modulus master curve generated by the FlexMAT can be found in Figure 9-3; the master curve model parameters are also available in Table 9-1.

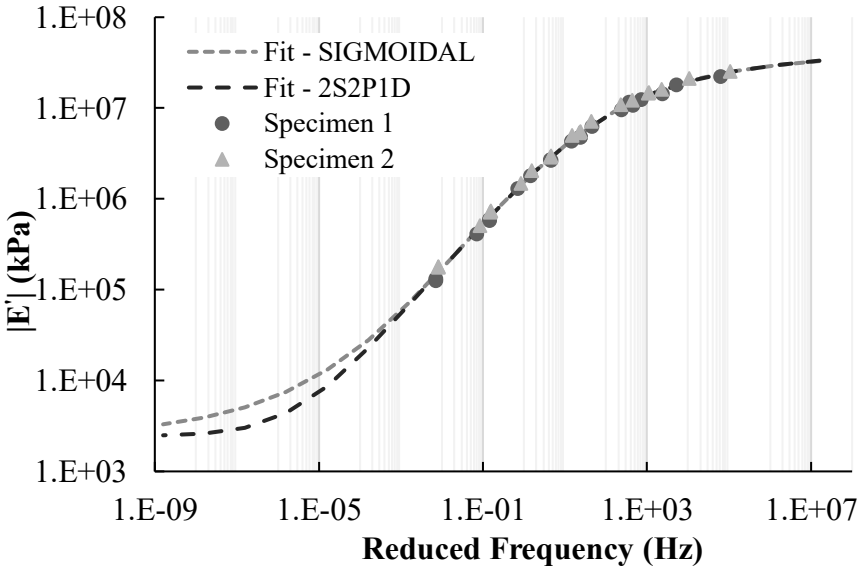

Figure 9-5 Storage modulus (|E'|) master curve generated by FHWA FlexMAT v2.1; T_{ref} = 21.1°C.

Table 9-1 Master curve fitting parameters for the Sigmoidal and 2S2P1D models generated by the FHWA FlexMAT v2.1 spreadsheet; T_{ref} = 21.1°C.

Model	E_0 (MPa)	E_∞ (MPa)	E_{00} (MPa)	b	d	g	δ	h	k	β	Sum of Error
Sigmoidal	-	2.44	-	3.39	-0.698	-0.471	-	-	-	-	0.0418
2S2P1D	2.44	-	4.00e4	-	-	-	2.17	0.206	0.517	1.0e12	0.0414

Figure 9-6 depicts the relaxation modulus, E(t), and the derivative of the log(E(t)) with respect to log(time). The maximum of the dlogE(t)/dlog(t) curve is used to determine the damage evolution rate, α; for the tested mix, the calculated α = 3.020. Based on the original work of Baaj (2002), tension-compression fatigue tests were conducted with a duration of either 150,000 or 300,000 cycles with a frequency of 10 Hz and test temperature of 10°C (+/-0.5°C).

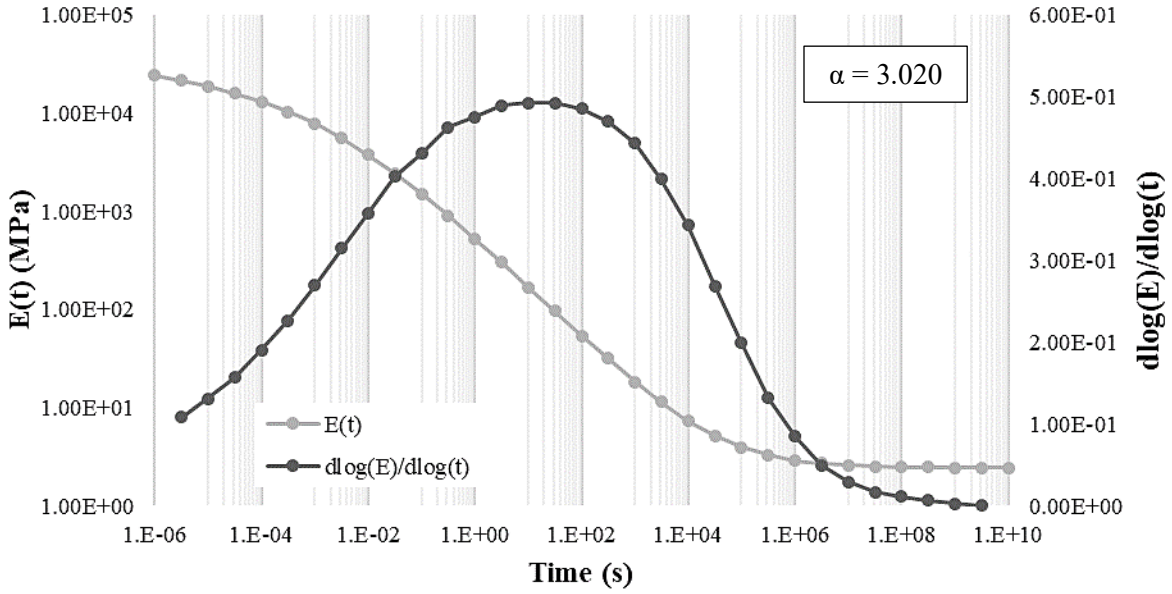

Figure 9-6 Relaxation modulus, E(t), and *d*logE(t)/*d*log(t) curves generated from FHWA FlexMAT v2.1; T_{ref} = 21.1°C. FlexMAT calculated damage evolution rate, α = 3.020.

In contrast to the standard AASHTO T 107 test procedure where specimens are tested at increasing strain levels (initially ranging from 300 to 800), only two strain levels were selected: 100 and 125 μm/m. The strain level was controlled using an on-specimen control scheme using three extensometers positioned at 180° around the radius of the sample. To evaluate the healing ability of the mix, fatigue tests terminating at 150,000 cycles were interrupted by a single rest period (duration: 4, 8 and 16 hours) before reloading the sample a subsequent 150,000 cycles. During each rest period, the sample is loaded for 300 cycles in 10-minute intervals to monitor the restoration of modulus during rest. The full experimental test matrix used for this study is summarized in Table 9-2. Three replicates were conducted for each treatment level and grouped; samples are designated by their group number corresponding to rest period duration, replicate letter designation, and strain level. For example, Gr1a-100 represents a sample with an uninterrupted fatigue test (i.e., 0-hour rest period) with an initial strain of 100 μm/m. In Figures 9-5 and 9-6, interval plots and Grubbs' outlier tests were prepared for samples

at both 100 and 125 μm/m, respectively. For the Grubbs' test, the null hypothesis is that all data values come from the same normal population, and the alternate hypothesis states that the smallest or largest value is an outlier; the values are tested at a significance level of 0.05. From the interval plots, it can be observed that there is no significant difference between the modulus value at 50 cycles from each group, and Grubbs' test demonstrates that no outliers exist at either strain level for the given significance level.

Table 9-2 Experimental test matrix for fatigue and healing tests.

Designation	Microstrain (μm/m)	Rest Period (hr)	LP1 Termination Cycle	RP Cycles	LP2 Termination Cycle
Gr1x-100	100	0	300,000	0	-
Gr2x-100	100	4	150,000	7,500	307,500
Gr3x-100	100	8	150,000	14,700	314,700
Gr4x-100	100	16	150,000	29,100	329,100
Gr1x-125	125	0	300,000	0	-
Gr2x-125	125	8	150,000	14,700	314,700

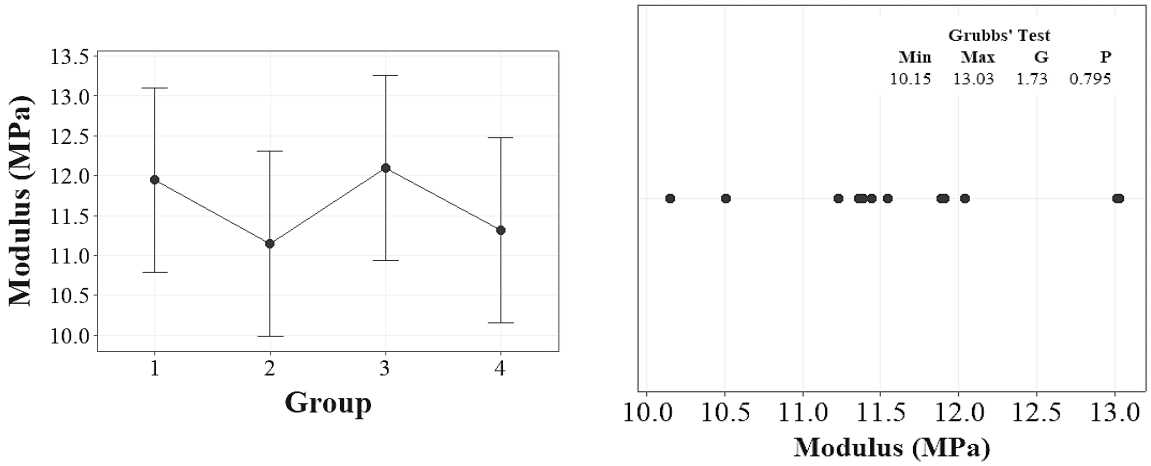

Figure 9-7 Modulus value at cycle 50, initial strain 100 μm/m: interval plot (left) and Grubbs' outlier test (right).

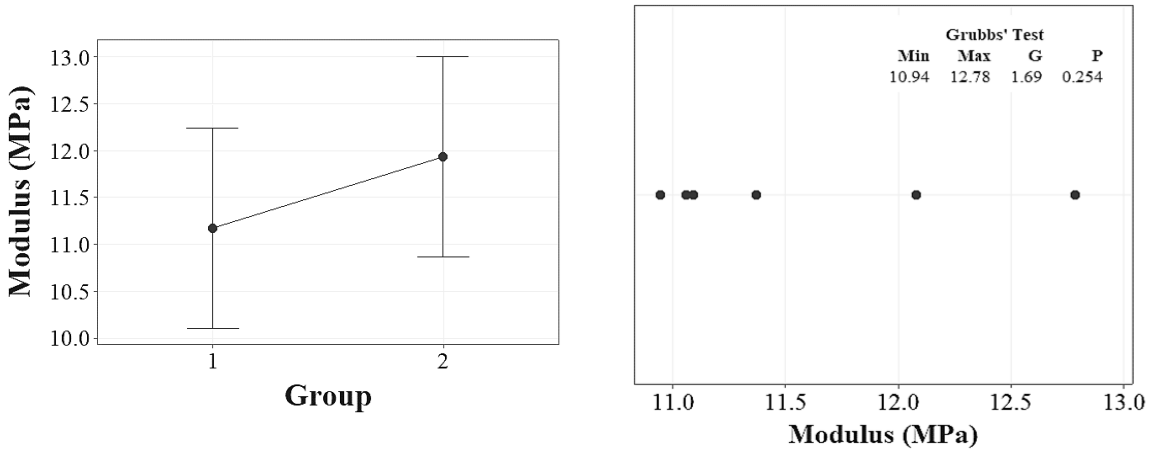

Figure 9-8 Modulus value at cycle 50, initial strain 125 μm/m: interval plot (left) and Grubbs' outlier test (right).

9.5 Results and Discussion

9.5.1 Fatigue Life Estimation Comparison: DGCB vs iVECD

For comparison purposes with the iVECD method, the DGCB fatigue curves are plotted as damage ($D = 1-(E_0-E_N)/E_0$) against the number of cycles, N; the damage curves for 100 and 125 μm/m are found in Figures 9-9 and 9-10, respectively. The resultant aFi values for each group are also displayed in Table 9-2. Based on the average a_{Fi} values reported for all groups in Table 9-2, rudimentary 2-point damage rate curves can be generated as seen in Figure 9-11; the resultant damage rate functions for intervals 1 and 2 are $a_{F1} = (-8.32e-9)\cdot\varepsilon + 5.12e-7$ and $a_{F2} = (-3.17e-9)\cdot\varepsilon + 1.29e-7$, respectively. As is consistent with the original literature for the DGCB method, the damage rate is greater for interval 1 compared to interval 2, presumably due to the combined effects of several bias effects, but primarily the effects of non-linearity (Baaj 2002).

In Figures 9-12 and 9-13, the C^*-S curves for 100 and 125 μm/m are shown; $a_{Fi\ VECD}$ values for each group are also shown in Table 9-4. It was observed that the calculated iVECD a_{Fi} values are significantly higher compared to the DGCB (by at least an order of magnitude). Also, when comparing the DGCB damage curves to the VECD C^*-S curves at the end of interval 1 (N = 150,000), it can be observed that there is greater variability with the unprocessed damage calculation of the DGCB method. This observation is similarly reflected through the calculation of the coefficient of variation (COV) for both the DGCB and iVECD a_{Fi} values found in Tables 9-3 and 9-4.

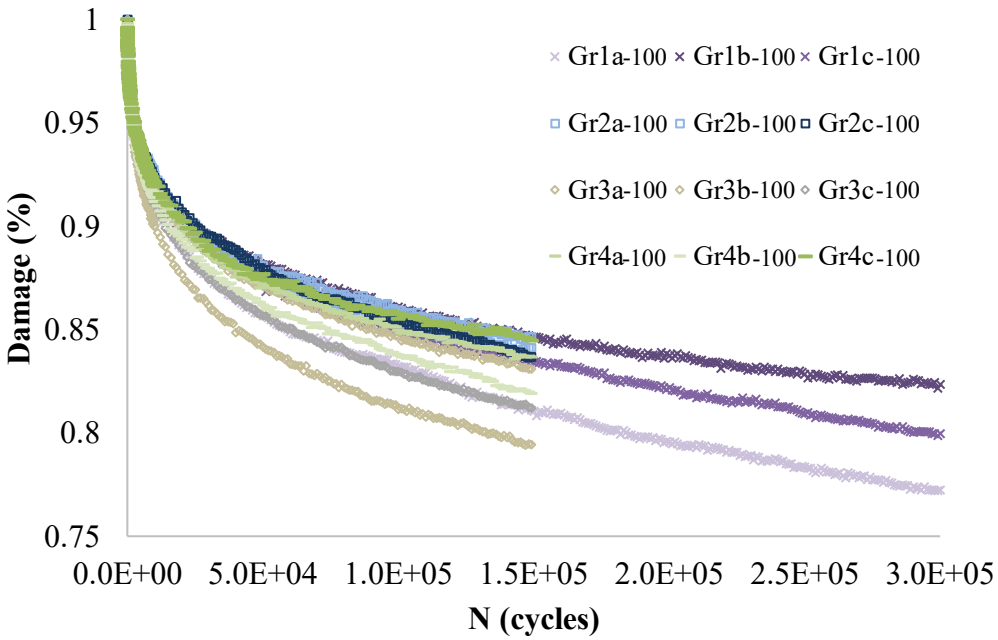

Figure 9-9 Damage vs Number of Cycles for samples tested using an initial strain of 100 μm/m.

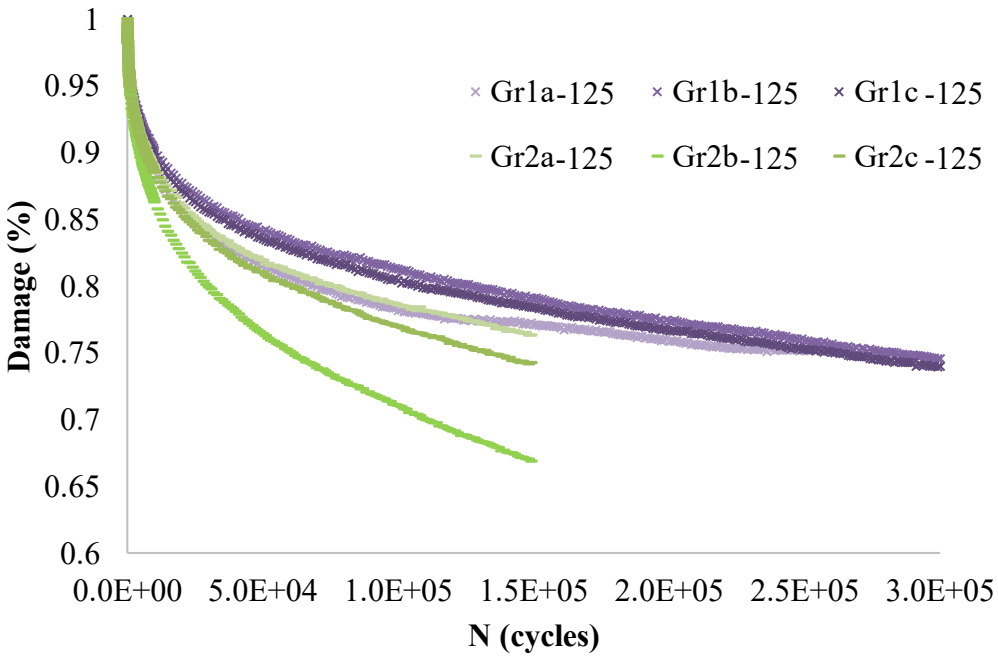

Figure 9-10 Damage vs Number of Cycles for samples tested using an initial strain of 125 μm/m.

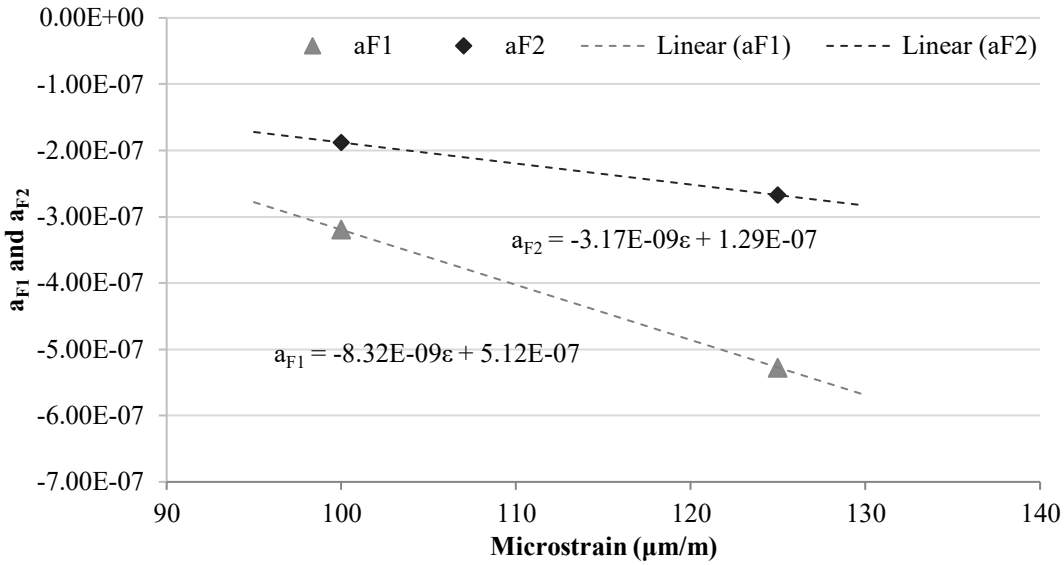

Figure 9-11 DGCB method damage rate and fatigue law for Interval 1 (a_{F1}) and Interval 2 (a_{F2}).

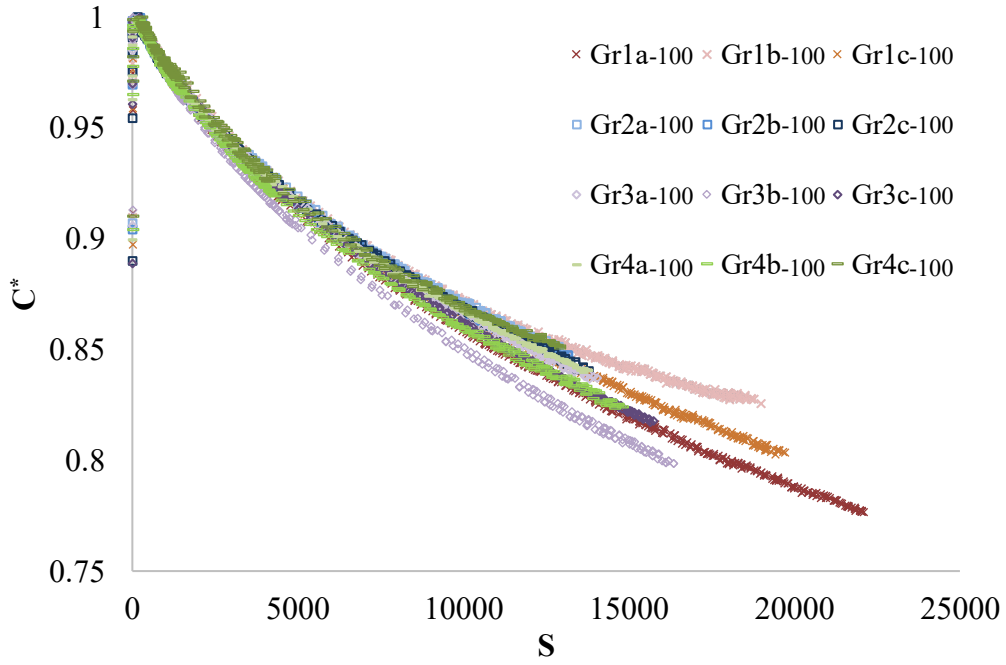

Figure 9-12 VECD C^*-S curves for samples tested using an initial strain of 100 µm/m.

It should be noted that specimen Gr2b-125 (circled in red in Figure 9-13) had the largest damage parameter (S_{150k}), even surpassing the S_{300k} from the Gr1x-125 specimens. This is a result of the calculation of the pseudostrain (Equation 9-1) and the peak-to-peak tensile strain parameter. By the end

of 150,000 cycles, the $\varepsilon_{0,pp}$ of Gr2b-125 was approximately 369.4 μm/m while the average for the other 5 samples (Gr1x-125, Gr2a-125 and Gr2c-125) was approximately 311.2 μm/m. Moreover, although this strain "drift" is not uncommon when using an on-specimen strain control scheme, specimen Gr2b-125 experiences almost 20% greater drift in its first loading phase compared to the other five specimens; despite this inconsistency, specimen Gr2b-125 was still included in the analysis as it seemed to have minimal effect on the calculation of the $a_{F1\ VECD}$ damage rate.

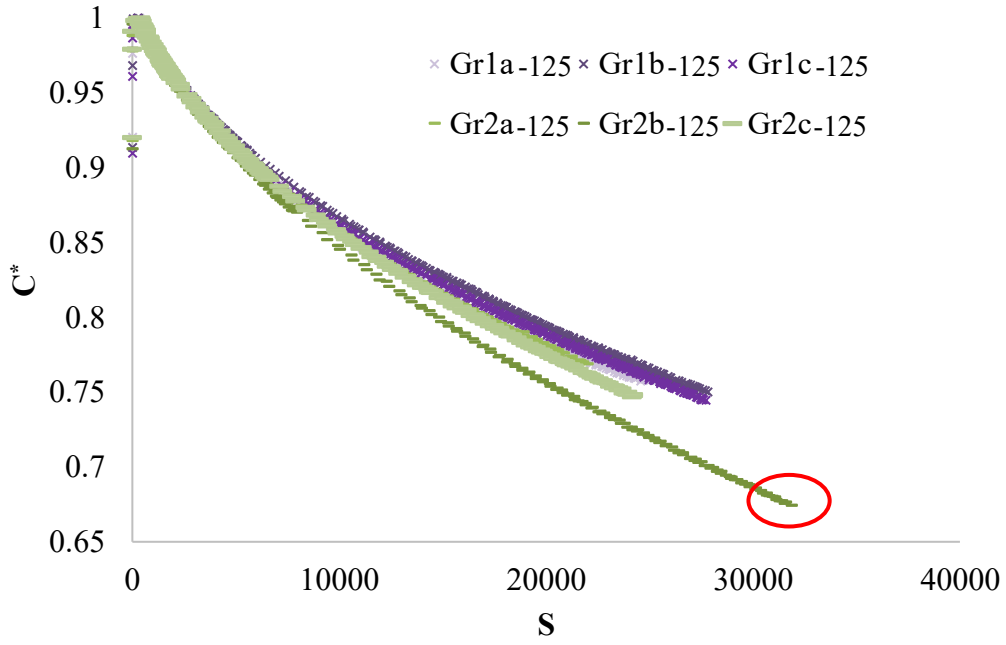

Figure 9-13 VECD C^*-S curves for samples tested using an initial strain of 125 μm/m.

The selection of a singular failure criterion has been one of the more contentious aspects of accelerated fatigue modelling. Some examples of basic failure criteria include: (1) failure occurs when at the number of cycles when the magnitude of the complex modulus is half of the mixture's initial complex modulus ($N_{f\,0.5|E^*|}$), (2) failure occurs at the number of cycles when the pseudostiffness of the material reaches half of the initial pseudostiffness ($N_{f\,50\%C}$), and/or (3) failure occurs at the number of cycles when the dissipated energy ratio (DER) deviates from the plateau on the DER vs Number of Cycles curve (Kutay and Lanotte 2018). Using the group-average a_{Fi} values from Table 9-4, the fatigue life was estimated using Equation 9-13 for two scenarios: (1) the traditional 50% drop from the initial pseudostiffness (i.e., $C^*_{fail} = 0.5C^*_{ini}$ corresponding to the $N_{f\,50\%}$), and (2) a 75% drop from the initial pseudostiffness (i.e., $C^*_{fail} = 0.25C^*_{ini}$ corresponding to the $N_{f\,25\%}$). This more conservative failure

definition alternative is more in line with the work of Hou (2011) indicated that failure for their specific non-RAP mixes occurred at approximately $0.26C^{*}_{ini}$. The results of these N_f estimates are provided in Table 9-5 using the power law form (Equation 9-6) as well as the iVECD forms for intervals 1 and 2.

Table 9-3 DGCB a_{Fi} values by group.

Designation	a_{F1} ($x10^{-7}$)	a_{F2} ($x10^{-7}$)
Gr1x-100	-3.57	-1.88
Gr2x-100	-2.87	-
Gr3x-100	-3.64	-
Gr4x-100	-2.70	-
Average	-3.20	-1.88
Standard Deviation	0.50	0.61
COV (%)	16.6	32.4
Gr1x-125	-4.59	-2.13
Gr2x-125	-5.96	-
Average	-5.27	-2.13
Standard Deviation	1.05	0.78
COV (%)	19.9	36.6

Table 9-4 iVECD a_{Fi} values by group.

Designation	$a_{F1\ VECD}$ ($x10^{-7}$)	$a_{F2\ VECD}$ ($x10^{-7}$)
Gr1x-100	-77.45	-59.49
Gr2x-100	-79.38	-
Gr3x-100	-81.89	-
Gr4x-100	-76.69	-
Average	-78.85	-59.49
Standard Deviation	3.55	3.64
COV (%)	4.5	6.1
Gr1x-125	-72.97	-58.00
Gr2x-125	-76.48	-
Average	-74.72	-58.00
Standard Deviation	2.75	6.53
COV (%)	3.7	11.3

Table 9-5 iVECD fatigue life estimates by group for a 50% and 75% drop in the initial pseudostiffness.

	$C^*_{fail} = 0.5C^*_{ini}$			$C^*_{fail} = 0.25C^*_{ini}$		
Designation	N_{f_PL}	N_{f_001}	N_{f_002}	N_{f_PL}	N_{f_001}	N_{f_002}
Gr1x-100	2.85E+06	5.13E+05	2.30E+06	1.06E+07	8.82E+05	3.16E+06
Gr2x-100	1.06E+06	5.02E+05	-	3.15E+06	7.85E+05	-
Gr3x-100	7.28E+05	4.43E+05	-	2.14E+06	6.97E+05	-
Gr4x-100	9.51E+05	5.85E+05	-	2.84E+06	9.19E+05	-
Gr1x-125	4.39E+05	1.78E+05	4.92E+05	1.49E+06	2.83E+05	8.13E+05
Gr2x-125	1.82E+05	1.46E+05	-	5.46E+05	2.36E+05	-

One notable difference in Table 9-5 is in the fatigue life estimate for Gr1x-100 when compared with the Gr2x-, Gr3x, and Gr4x-100 values for both scenarios. Average N_f values for Gr1x-100 specimens are almost three times greater compared to the other groups; this difference is primarily caused by the fitting of the power law function to only 150,000 cycles, as is done in Groups 2 to 4. Group 1 specimens are fitted to 300,000 cycles resulting in greater "y" and lower "z" power law fitting coefficients, thus, producing a "flatter" fitted curve and a larger calculated fatigue life. There is much less variation between all groups when comparing the fatigue life estimates for interval 1, demonstrating the benefit of the linearization procedure. Using an average value of all groups, the 2-point Wöhler curve curves are plotted for $N_{f\,50\%}$ and $N_{f\,25\%}$ scenarios in Figures 9-12 and 9-13, respectively. Overall, these curves demonstrate that there is a similar increase in fatigue life from interval 1 to interval 2 values, as seen in the DGCB method.

Using the rudimentary Wöhler curves in Figures 9-14 and 9-15, the estimated ε_6 values have been summarized for both scenarios in Table 9-6; the DGCB ε_6 values are also included for comparison. From Table 9-6, it can be observed that the DGCB ε_6 values are significantly higher when compared against the iVECD predictions for both scenarios, thus, demonstrating the efficacy of the original DGCB method to account for the bias effects during loading.

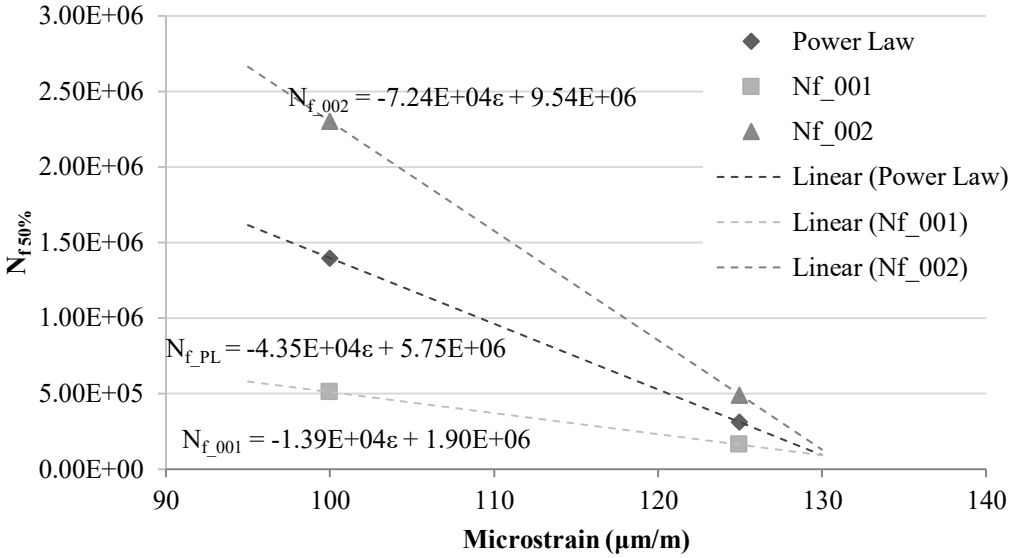

Figure 9-14 S-VECD power law, and iVECD Interval 1 and Interval 2 fatigue life predictions accounting for a 50% reduction in pseudostiffness ($N_{f50\%}$).

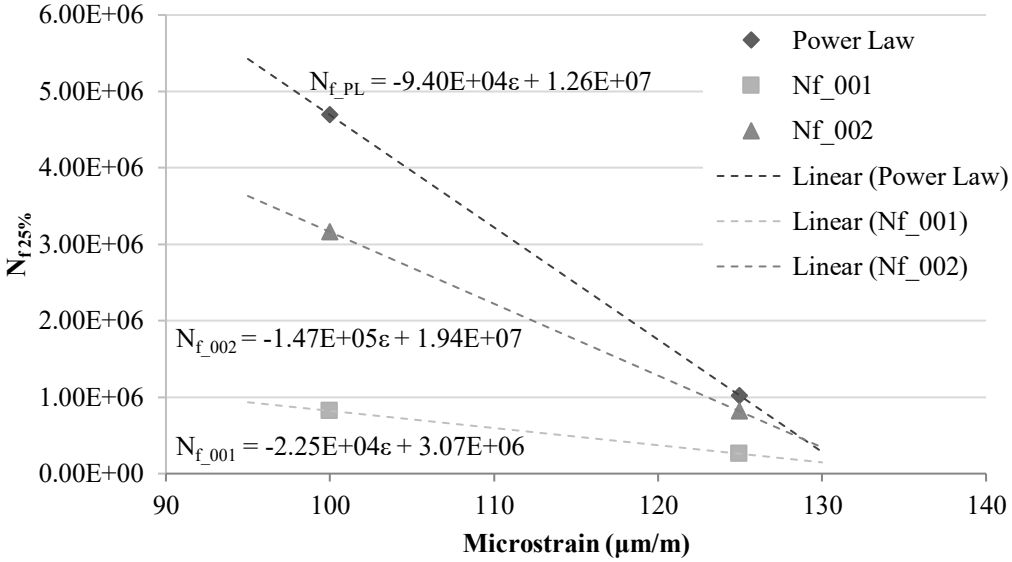

Figure 9-15 S-VECD power law, and iVECD Interval 1 and Interval 2 fatigue life predictions accounting for a 75% reduction in pseudostiffness ($N_{f25\%}$).

Table 9-6 Epsilon-6 (ε_6) predictions for the DGCB and iVECD methods.

			ε_6 (μm/m)				
Model	**Failure Condition**	**Fatigue/ Damage Predictor**	a_{F1}	a_{F2}	N_{f_PL}	N_{f_001}	N_{f_002}
DGCB	-	a_{Fi} = 0.5e-6 μm/m	121.7	198.4	-	-	-
i/S-VECD	$C^*_{fail} = 0.5C^*_{ini}$	N_{f_i} at 1e6 cycles	-	-	109.1	64.9	118.0
i/S-VECD	$C^*_{fail} = 0.25C^*_{ini}$	N_{f_i} at 1e6 cycles	-	-	125.1	92.0	123.0

When comparing the iVECD ε_6 values to the S-VECD power law, it is evident that the choice of C^*_{fail} significantly affects the fatigue life prediction of interval 1 while the change in fatigue life is not considerably different for interval 2 and the power law formulation. The fatigue life prediction using the interval 1 linearization process is significantly lower in both cases. Based on the fatigue characterization of this specific mix, interval 1 would not be recommended for ranking purposes in future studies. Due to the similarity of the power law and interval 2 fatigue life predictions, there is more confidence in the recommendation of interval 2 as a basis for future low-strain (below 150 μm/m) amplitude fatigue studies.

9.5.2 Healing Analysis

Although it was established that the first interval iVECD analysis may not be suitable for estimating the fatigue life, the linearization process is nevertheless valuable when determining the corrected C^* values in the C^*-S curve. Figure 9-14 below depicts an example healing curve with several suggested parameters presented:

- $C^*_{cor\_LP1}$: the C^*-intercept from the linearization of the corrected C^* values in Loading Phase 1 obtained using Equation 9-12; the corrected values are determined using the damage parameters corresponding to the interval 1 cycles.
- $C^*_{cor\_LP2}$: the C^*-intercept from the linearization of the corrected C^* values in Loading Phase 2 obtained using Equation 9-12; the corrected values are determined using the damage parameters corresponding to the interval 1 cycles.
- $C^*_{fin\_LP1}$: the final secant pseudostiffness value obtained at the end of the first loading phase.
- $C^*_{ini\_LP2}$: the initial secant pseudostiffness value obtained at the beginning of the second loading phase.
- S_0: the damage parameter corresponding to the end of the first loading phase.

- ΔS: the damage parameter in the second loading phase corresponding to the final secant pseudostiffness from the first loading phase, $C^*_{fin\_LP1}$.

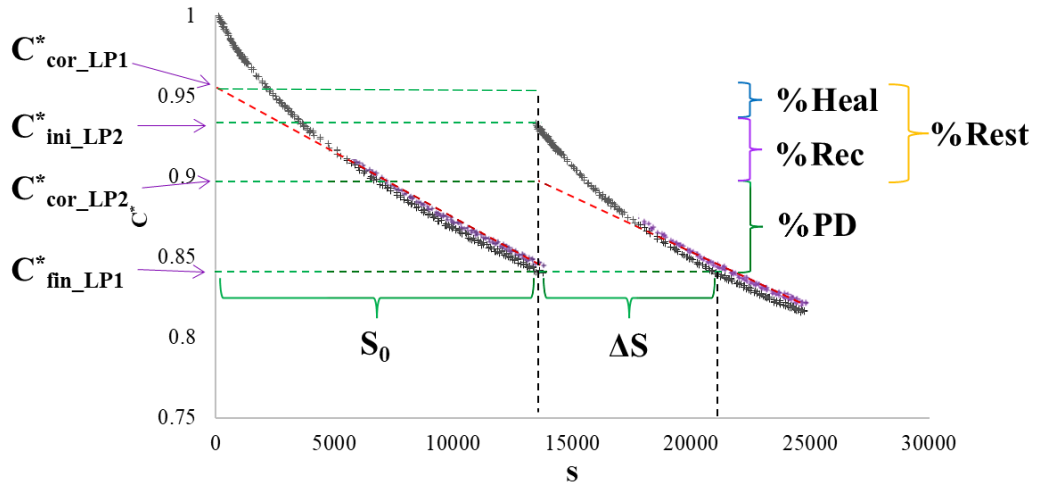

Figure 9-16 Example C^*-S healing curves with several designated parameters of interest: $C^*_{cor\_LP1}$, $C^*_{cor\_LP2}$, $C^*_{ini\_LP2}$, $C^*_{fin\_LP1}$, S_0 and ΔS.

From the above parameters, several simple indices from literature can be used, as shown in Equations 9-14 and 9-15 (Kim et al. 2022). The pseudostiffness healing index ($\%H_C$) and the damage parameter healing index ($\%H_S$) are calculated as follows:

$$\%H_C = \frac{C^*_{ini_{LP2}} - C^*_{fin_{LP1}}}{C^*_{ini_{LP2}}} \cdot 100\% \qquad \text{Eqn. 9-14}$$

$$\%H_S = \frac{\Delta S}{S_0} \cdot 100\% \qquad \text{Eqn. 9-15}$$

Taking advantage of the new iVECD analysis method, several new indices can be constructed based on the healing definitions proposed by RILEM TC CHA-278. In accelerated fatigue testing, the restoration is the total reversal of the deterioration of stiffness due to damage and other non-damage-related effects during the rest period. Restoration is composed of: (1) the recovery of biasing effects and (2) true "healing" due to microcrack closure (Leegwater et al. 2020). From these definitions, the following indices can be constructed:

$$\%Restoration = \frac{C^*_{cor_{LP1}} - C^*_{cor_{LP2}}}{\Delta C^*_{total}} \cdot 100\% = \frac{C^*_{cor_{LP1}} - C^*_{cor_{LP2}}}{C^*_{cor_{LP1}} - C^*_{fin_{LP1}}} \cdot 100\% \qquad \text{Eqn. 9-16}$$

$$\%PD = 1 - \%Rest = \frac{C^*_{cor_{LP2}} - C^*_{fin_{LP1}}}{C^*_{cor_{LP1}} - C^*_{fin_{LP1}}} \cdot 100\% \quad \text{Eqn. 9-17}$$

$$\%Recovery = \frac{C^*_{ini_{LP2}} - C^*_{cor_{LP2}}}{C^*_{cor_{LP1}} - C^*_{cor_{LP2}}} \cdot 100\% \quad \text{Eqn. 9-18}$$

$$\%Healing = \frac{C^*_{cor_{LP1}} - C^*_{ini_{LP2}}}{C^*_{cor_{LP1}} - C^*_{cor_{LP2}}} \cdot 100\% \quad \text{Eqn. 9-19}$$

From Equation 9-16, the restoration will be defined as the difference in the secant pseudostiffness from the linearized C^*_{cor} value from the first and second loading phases; these corrected values correspond to the initial secant pseudostiffness in each phase devoid of bias effects. The "permanent damage" or %PD index in Equation 9-17 is proposed here to account for the unhealed portion of the total change in C^* from the end of the first loading phase to the corrected C^* in the second loading phase. The %Recovery (Eqn. 9-18) and %Healing (Eqn. 9-19) are defined as the portion of the %Restoration corresponding to the ΔC^* less than and greater than $C^*_{ini\_LP2}$, respectively. Based on the experimental test matrix provided in Table 9-2, the indices described above will be used to evaluate the effects of different rest periods (4, 8 and 16 hours) and strain levels (100 vs 125 μm/m).

9.5.2.1 Effect of Rest Period

Figure 9-17 contains the damage vs number of cycles curves for all healing tests tested at 100 μm/m. C^*-S healing curves for the 4, 8 and 16-hour rest periods (i.e., Gr2x-, Gr3x- and Gr4x-100) specimens are plotted separately in Figures 9-18, 9-19 and 9-20 due to significant visual overlap. Note: Specimen Gr4c-100 (indicated by the red circle in Figure 9-20) was the only specimen in all healing tests (at both strain levels) such that $C^*_{ini\_LP2}$ was greater than $C^*_{cor\_LP1}$. Thus, it was discarded from the healing analysis using Equations 9-16 to 9-19.

From Figure 9-17, the initial damage calculated at the beginning of the second loading phase does not consistently increase after the rest period; Group 3 specimens have a lower D-value compared to both Group 2 and 4. However, it appears that the ΔD between the end of the first and the beginning of the second loading phase is relatively proportional. Using the DGCB and iVECD method linearization technique on the second loading phase allows for the calculation of the pre- and post-rest period a_{F1} ratio (Figure 9-21a). The DGCB a_{F1} ratio ranges from 90.8 to 107.5% while the iVECD a_{F1} ratio ranges from 87.9 to 91.2%; as was shown with the fatigue life estimates earlier, the DGCB linearization method produces much greater variability. The a_{F1} ratios using both techniques demonstrate that the

post-rest period fatigue damage rate is nearly indistinguishable from the damage rate in the first loading phase. Conversely, there does not appear to be a significant difference in the a_{F1} ratios for any of the three rest period durations. Rationally, this result should be expected as the damage rate should not change dramatically for the equivalent loading interval and mirrors the results in the original studies conducted by Baaj (2002).

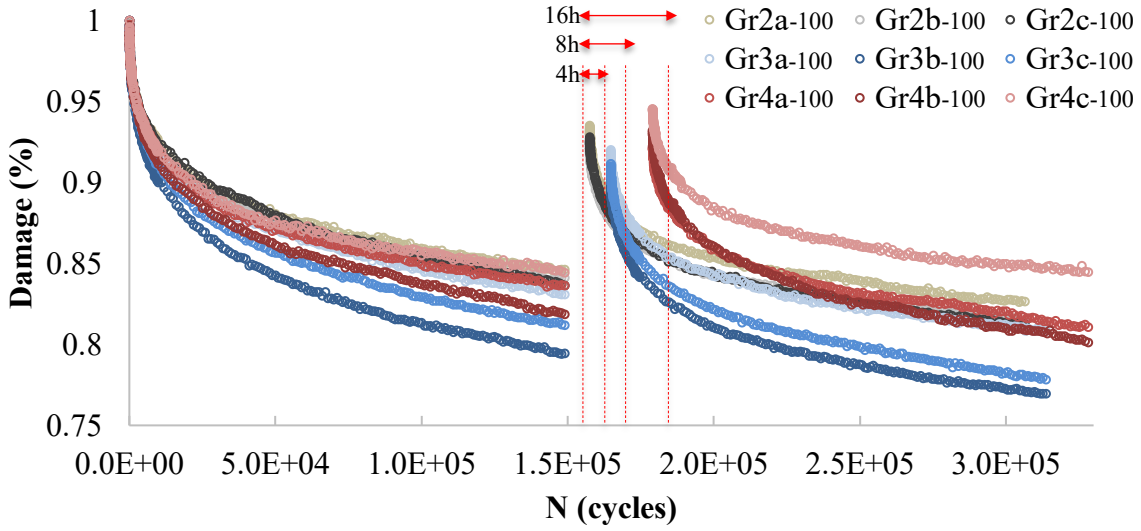

Figure 9-17 Damage vs number of cycles for the first and second loading phases using 4, 8 and 16-hour rest periods (initial strain: 100 μm/m).

To quantify the change in the total secant pseudostiffness change from before and after the rest period, the ΔC^*_{total} value is also calculated from the C^*-S curves in Figures 9-18 to 9-20; Figure 9-21b contains the resultant iVECD ΔC^*_{total} values for each group. ΔC^*_{total} values ranged from 0.114 to 0.144; statistically, no significant difference is observed between the rest period durations, but it can be noted that Group 3 (8-hour rest period), which had the greatest ΔC^*_{total} value also experienced the greatest decrease in C^* at the end of the first loading phase. A general trend can be observed that samples, when loaded at the same strain level, that have a greater damage rate also experience a greater observed ΔC^*_{total} after the rest period.

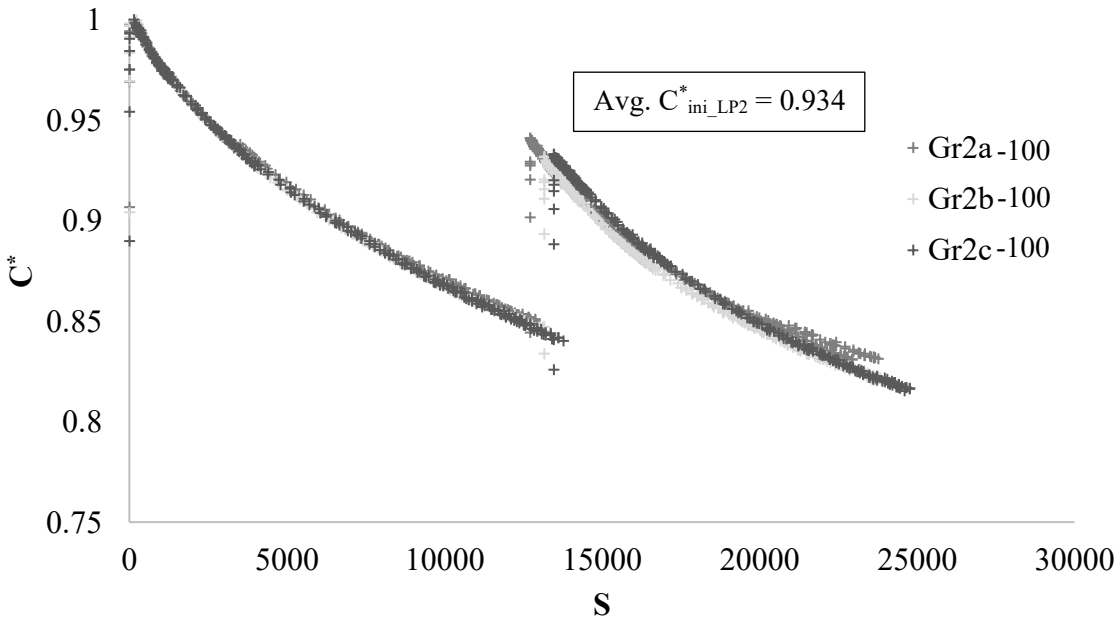

Figure 9-18 VECD C*-S curves healing curves using a 4-hour rest period (initial strain: 100 µm/m).

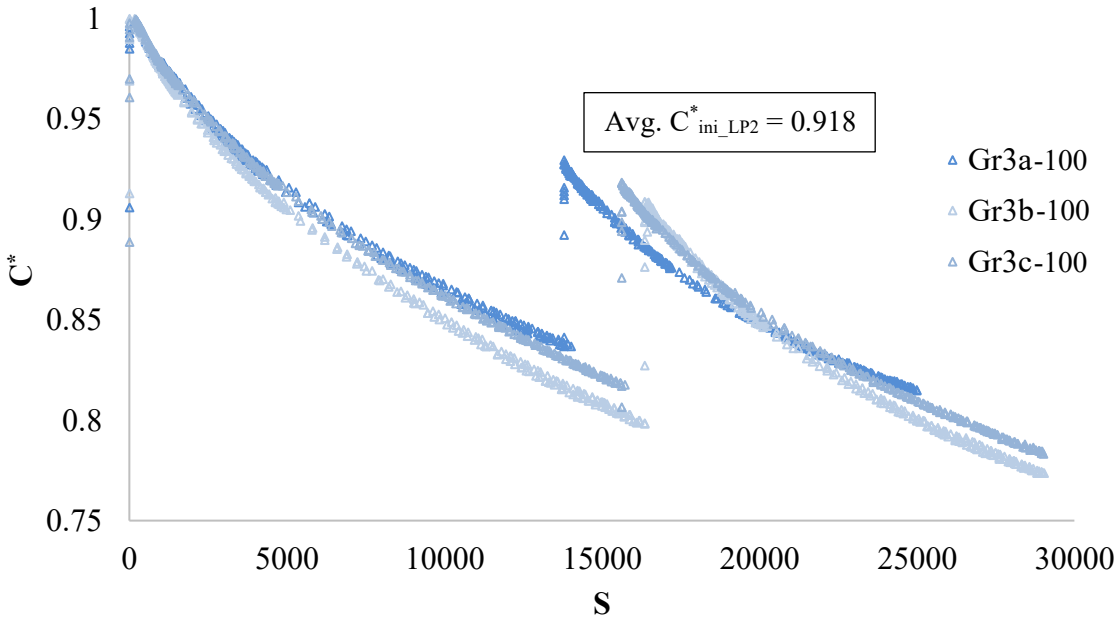

Figure 9-19 VECD C*-S curves healing curves using an 8-hour rest period (initial strain: 100 µm/m).

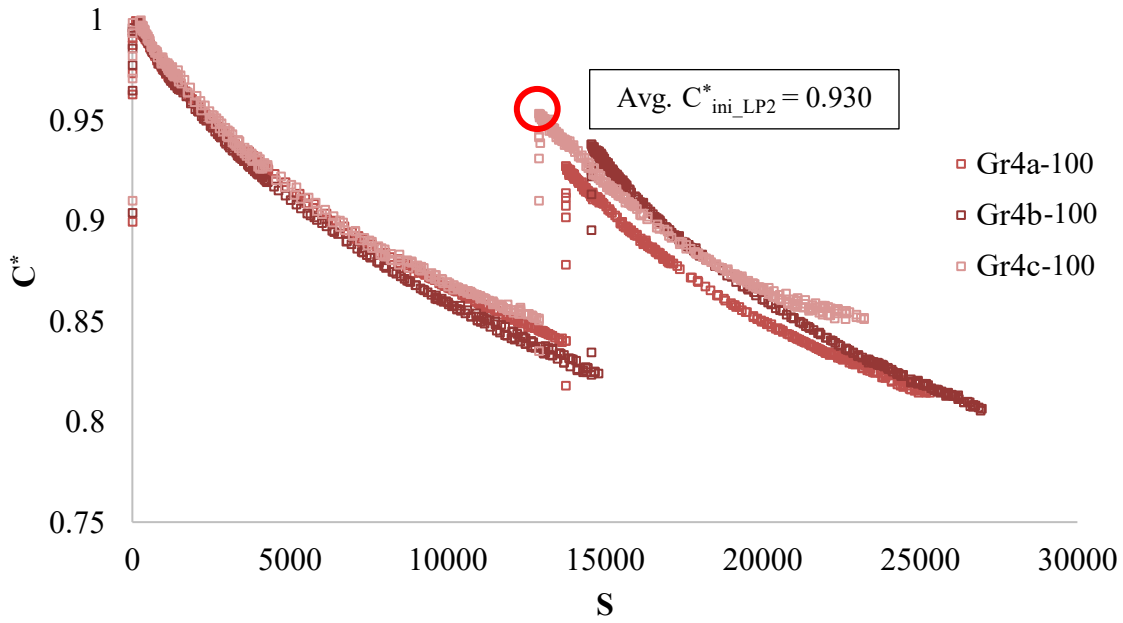

Figure 9-20 VECD C*-S curves healing curves using a 16-hour rest period (initial strain: 100 μm/m).

Figures 9-22a and 9-22b contain the results for the healing indices, $\%H_C$ and $\%H_S$, respectively. Based on the $\%H_C$ results at the same initial strain level, restoration of the secant pseudostiffness ranges from 11.9 to 13.8%; only a statistically significant difference can be observed between the 4 and 8-hour rest period specimens. The variability of Group 4 (16-hour) specimens is relatively larger. Thus, it is not distinguishable from either Group 2 or Group 3 specimens. When analyzing the data for the $\%H_S$ results, the $\%H_S$ ranges from 54.1 to 57.1%, and no meaningful difference is observed between the means of the three groups when testing at the same strain level.

Figure 9-23 contains the %PD, %Rest, %Rec and %Heal results obtained from Equations 9-16 to 9-19 for specimens tested at 100 μm/m (as was mentioned previously, specimen Gr4c-100 was discarded from the analysis. Consequently, error bars are omitted for Group 4/ 16-hour rest period results). From Figure 9-23a, it can be observed that there is a consistent ratio of permanent damage and restoration at both 4 and 8 hours. When comparing the 16-hour rest period specimens, there is an observed increase in the permanent damage and a decrease in restoration although it is expected that the %Rest should increase with increasing rest period duration. there is an observed increase in the permanent damage and a decrease in restoration, although it is expected that the %Rest should increase with increasing rest period duration. Congruently with the expected increase in restoration, it is expected that healing

should increase with rest period duration. However, Figure 9-23b results indicate that the portions of healing and recovery in the ΔC_{Rest} are also consistent across all test treatment levels when testing at the same strain level.

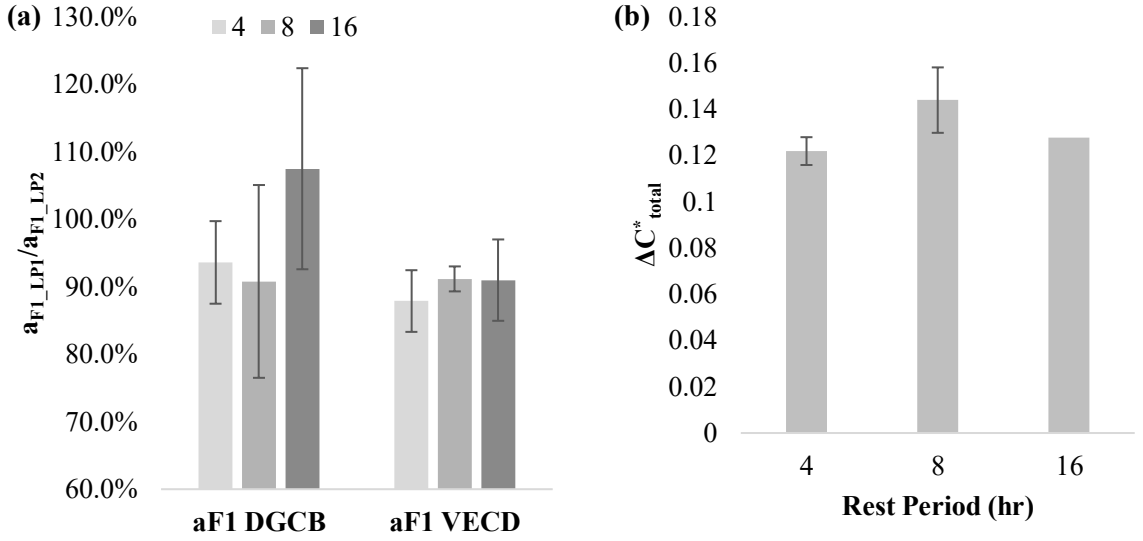

Figure 9-21 (a) DGCB and iVECD aF1 ratios, and (b) iVECD ΔC^*_{total} values for specimens tested using an initial strain of 100 μm/m with a 4, 8 or 16-hour rest period.

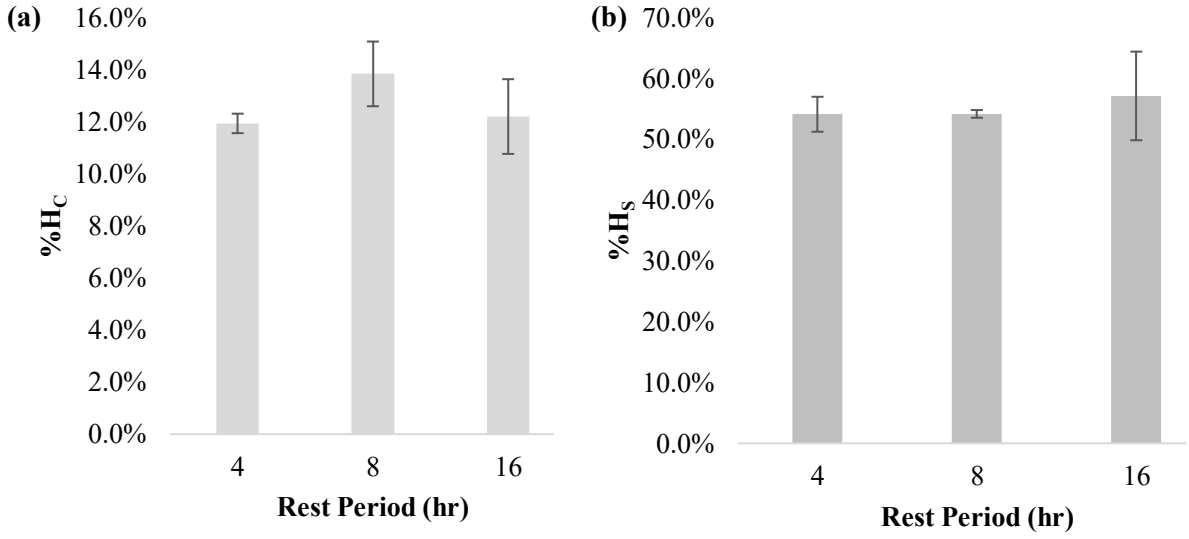

Figure 9-22 (a) $\%H_C$ and (b) $\%H_S$ values for specimens tested using an initial strain of 100 μm/m with a 4, 8 or 16-hour rest period.

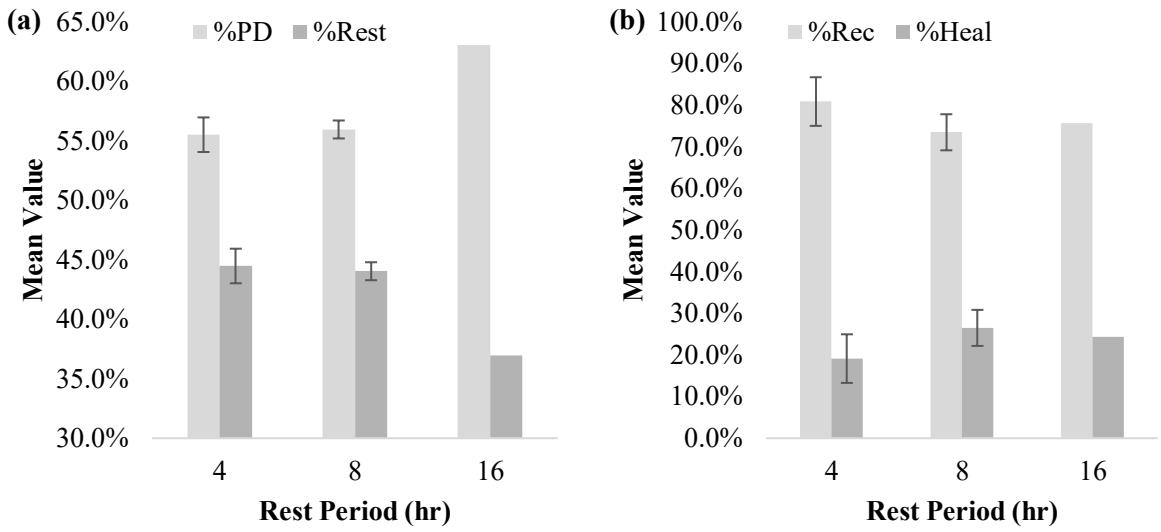

Figure 9-23 (a) %PD and %Restoration, and (b) %Recovery and % Healing values for specimens tested using an initial strain of 100 μm/m with a 4, 8 or 16-hour rest period.

9.5.2.2 Effect of Strain level

Figure 9-24 includes the damage vs the number of cycles curves while Figure 9-25 contains the C^*-S healing curves for specimens tested with an initial strain of 100 and 125 μm/m with the same 8-hour rest period. Damage curves in Figure 9-24 demonstrate a consistent decrease in the initial second loading phase damage level when increasing the strain from 100 to 125 μm/m; this result is also reflected in the increased damage parameter in the C^*-S from Figure 9-25.

Once again, the DGCB and iVECD linearization technique was used to evaluate the damage rate before and after the rest period through the pre- and post-rest period a_{F1} ratio; these results as shown in Figure 9-26a. From both methods, the a_{F1} ratio remains close to 100%. As an observation, the a_{F1} ratio is lower at 100 μm/m in both scenarios, but a significant difference is only observed when using the iVECD a_{F1} ratio due to its lower variability compared to the DGCB method. This trend mirrors the results from the rest-period analysis earlier as the second loading phase damage rate should not change significantly even after the sample has been damaged. The ΔC^*_{total} values for each strain level from the iVECD analysis can be found in Figure 9-26b. ΔC^*_{total} values indicate that there is a significant increase in the ΔC^*_{total} when increasing the strain as Gr3x-100 samples had a $\Delta C^*_{total} = 0.144$ while Gr2x-125 samples exhibited a $\Delta C^*_{total} = 0.224$. From these results, it is evident that the observable restoration

increases with the increase in damage as opposed to the negligible effect of increasing rest period duration.

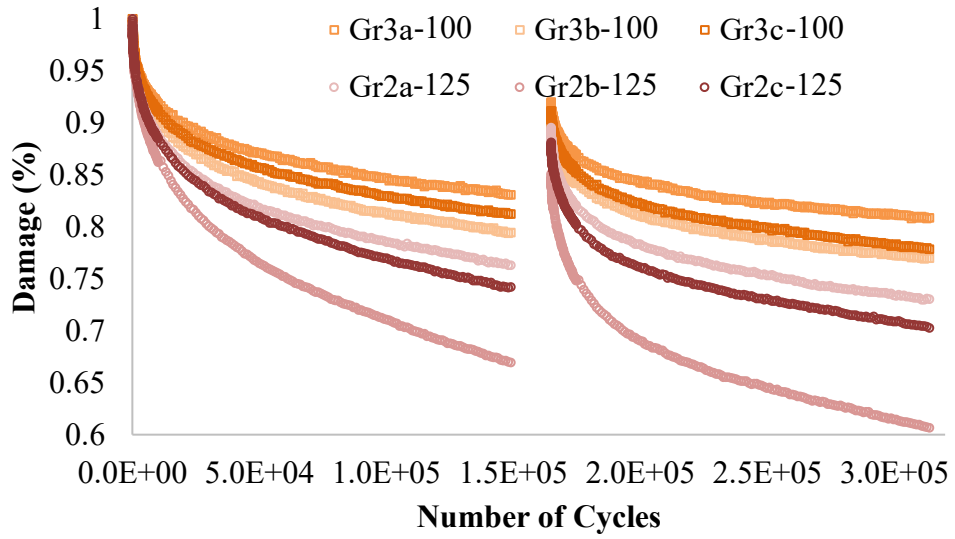

Figure 9-24 Damage vs the number of cycles for the first and second loading phases using an initial strain of 100 and 125 µm/m with a single 8-hour rest period.

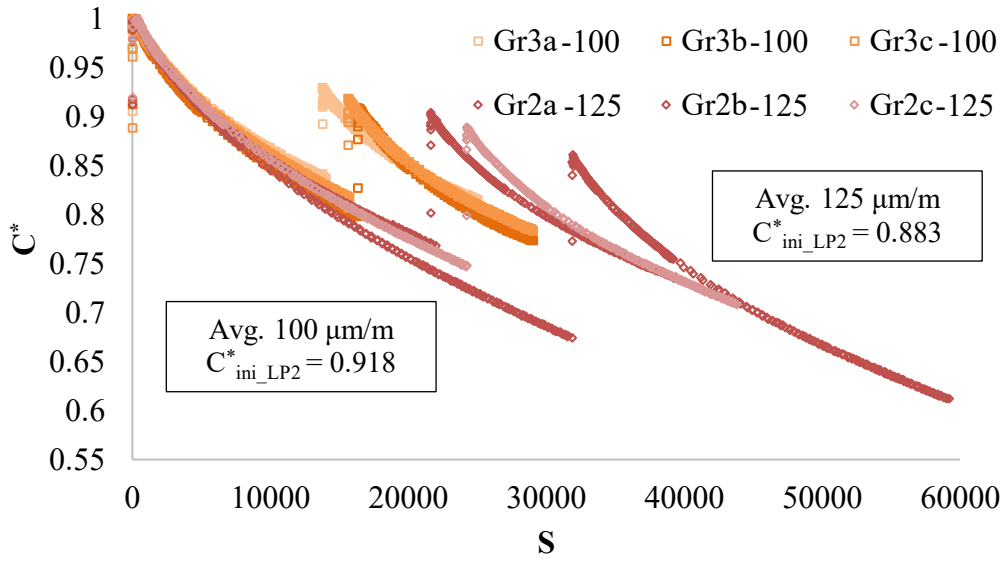

Figure 9-25 C*-S healing curves for specimens tested using an initial strain of 100 and 125 µm/m with a single 8-hour rest period.

Healing indices, $\%H_C$ and $\%H_S$, are displayed in Figures 9-27a and 9-27b, respectively. Based on the $\%H_C$ results, restoration of the secant pseudostiffness increases from 13.8 to 22.5% when increasing the strain level from 100 to 125 μm/m. Due to the variability of the S-damage parameter, there is no significant observable difference in the $\%H_S$ index when increasing the strain amplitude. This result is consistent with other literature (Kim et al. 2022), that demonstrated that increasing the damage level at the end of the first loading phase decreases the observed $\%H_S$ in short-time rest period tests; this effect appeared to plateau for rest periods greater than 90 seconds which would clarify as to why the longer rest periods (RP ≥ 4 hours) used in this study do not demonstrate any significant differences. It is then evident from the study of the $\%H_C$ and $\%H_S$ indices at both strain levels and all three rest period durations that these conventional healing indices are only appropriate to quantify some type of "restoration" based on the definitions of RILEM CHA-278. However, damage parameter S-based indices appear to drastically overpredict the total restoration in comparison to pseudostiffness C-based indices and are not recommended for future healing studies.

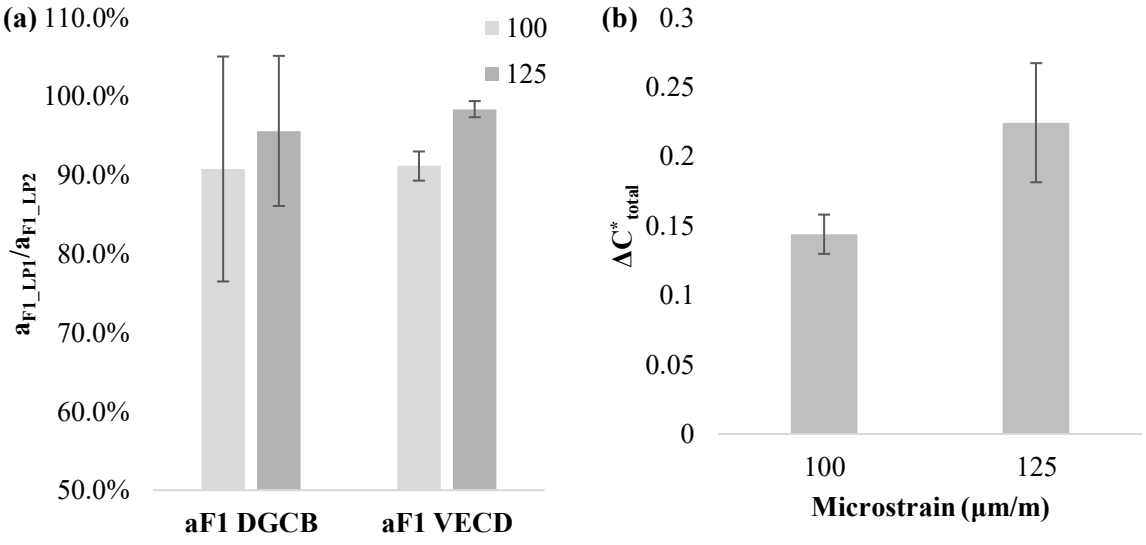

Figure 9-26 (a) DGCB and iVECD aF1 ratios, and (b) iVECD ΔC^*_{total} values for specimens tested using an initial strain of 100 and 125 μm/m with a single 8-hour rest period.

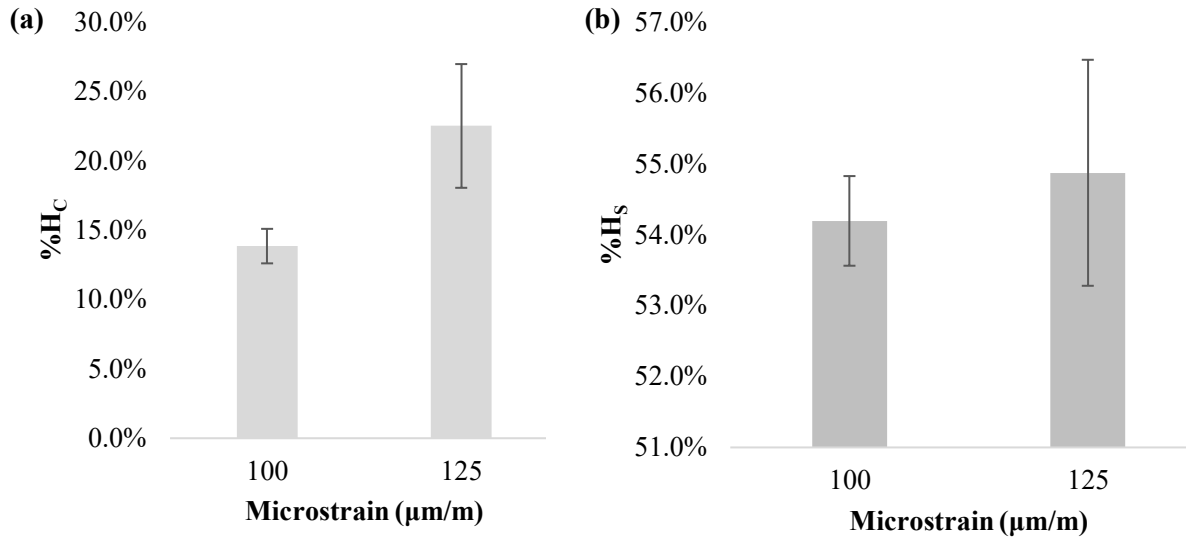

Figure 9-27 (a) $\%H_C$, and (b) $\%H_S$ values for specimens tested using an initial strain of 100 and 125 µm/m with a single 8-hour rest period.

Figure 9-28 contains the %PD, %Rest, %Rec and %Heal results obtained from Equations 9-16 to 9-19 for specimens tested at 100 and 125 µm/m. In contrast to the study of rest period duration, Figure 9-28a demonstrates a significant difference between the permanent damage and restoration observed when increasing the strain level. Although the ΔC^*total increases as shown in Figure 9-24b above, the observed %Rest decreases and a larger percentage of permanent damage remains after the rest period. When further examining the %Rec and %Heal within the restoration itself, it appears that there is no significant difference at the different strain levels; this result indicates that just as the damage rate is fixed for a single strain level that the corresponding healing rate is also fixed for a single test temperature-strain level pair. In general, these results appear to be consistent with the observation in other studies that demonstrate a decrease in recovery and an increase in damage with increasing strain levels (Ayar et al. 2016; Sun et al. 2018).

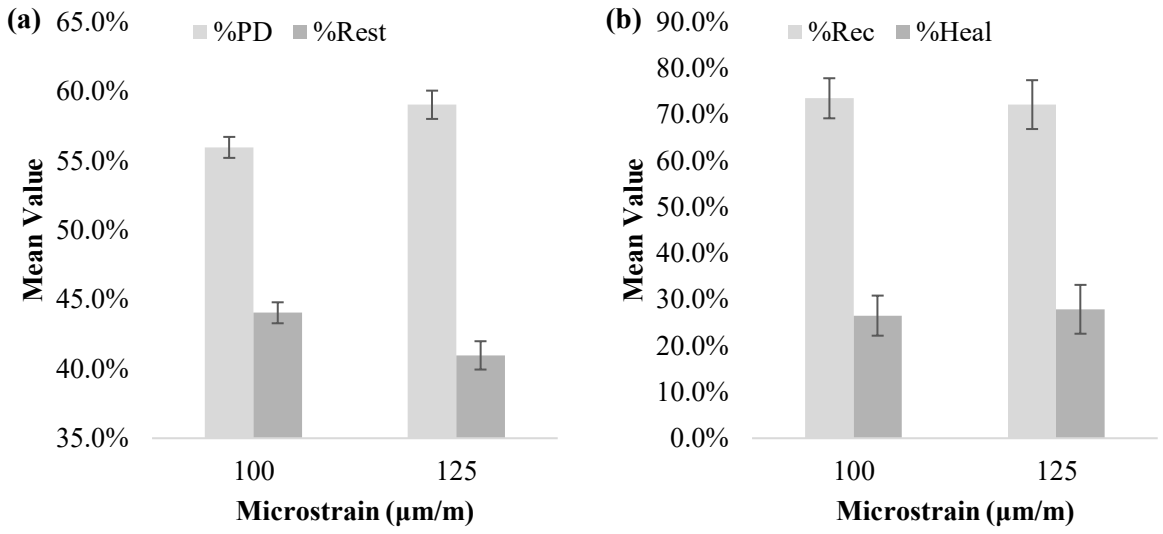

Figure 9-28 (a) %PD and %Restoration, and (b) %Recovery and % Healing values for specimens tested using an initial strain of 100 and 125 µm/m with a single 8-hour rest period.

Conclusions

The preliminary work presented herein proposed the use of a new fatigue modelling method called the Intrinsic-VECD or iVECD model. The iVECD fatigue model uses a "DGCB"-style global linearization of the common S-VECD model to remove bias effects (i.e., non-linearity, thixotropy, etc.) that may still be present through the conversion of the material properties to their pseudo-variable counterparts. This iVECD method was then used to complement interrupted fatigue tests to define healing indices under the RILEM CHA-278 healing definitions. These indices were compared against the more conventional healing indices, $\%H_C$ and $\%H_S$, to provide a clearer picture of restoration. From this work, the following conclusions can be drawn:

- Similar to the original DGCB method, the linearization process in different intervals leads to distinct iVECD damage rates. The iVECD damage rates calculated herein follow the same trend as the DGCB method, demonstrating that the interval 1 values are greater than interval 2.
- The ε_6 values obtained using the iVECD were significantly lower compared to the original DGCB method. However, the ε_6 values computed using interval 2 damage rates from the iVECD method provide good agreement with the power law fatigue life estimate from the original S-VECD analysis and may be suitable for mixture fatigue ranking. Interval 1 damage rates are too high and, thus, entirely underpredict the fatigue life of the mix even when considering a more conservative

failure condition (i.e., $N_{f\,25\%}$). It is recommended that all future tests using the iVECD method be conducted at strain levels appropriate to reach a minimum terminal cycle count equivalent to interval 2 (300,000 cycles).

- The simple linear C^* correction from the iVECD model was then used to provide additional detail when constructing new healing indices. The corrected values were integral in the derivations of the permanent damage (%PD) and restoration (%Rest). From the restoration, the portions related to the recovery (%Rec) and healing (%Heal) were also derived.
- From the healing tests, it was indicated that the majority of recovery and healing occurs with in the first 4 hours of rest; this demonstrates that the increased rest period duration was not a significant factor when testing at the lower strain level (100 μm/m). A marginal, but not statistically significant increase in healing was observed as the rest period increased from 4 to 8 hours and 8 to 16 hours.
- Healing tests also demonstrated that the amount of permanent damage observed is significantly affected by the strain level. Specimens tested at 125 μm/m demonstrated greater permanent damage and lower restoration. Despite the increase in damage, the ratios of recovery and healing were not considerably different from tests conducted at 100 μm/m, indicating that the healing rate may be greater when specimens experience greater damage in the same time period.

Although the work in this study was limited to a single asphalt mix at a single loading frequency and temperature, there are still several important opportunities for future studies. As was reported, the rest period did not significantly influence the change in healing observed. Although recovery continues after several hours (up to 24 hours in some studies), future healing tests may focus on the implementation of shorter rest periods (RP $\leq$ 4 hours) to evaluate healing. As restoration and healing are affected by the chemistry of the asphalt cement and the use of modifiers, the suggested 4-hour rest period threshold would need to be evaluated/ validated for other asphalt materials.

Chapter 10
Viability of Coda Wave Interferometry for Fatigue Monitoring of Asphalt Mixtures

10.1 Introduction

For asset management, an agency or contractor may employ various non-destructive techniques to assess the structural or functional integrity of the pavement structure. These assessments help determine the correct M&R treatment required to prolong the useful service life of a pavement, but also to ensure the road is adequately safe for motorists. Non-destructive testing for construction materials can be efficiently completed on-site, are non-hazardous and highly sensitive (Planes and Larose 2013). In the asphalt industry, techniques such as ground penetration radar (GPR), spectral analysis of surface waves (SASW) using the Portable Seismic Pavement Analyzer (PSPA), the hammer test, skid resistance testing and the many variations of deflection measurements (e.g., FWD- falling weight deflectometer, LWD- lightweight deflectometer, RWD- rolling weight deflectometer, the Benkelman Beam, etc.) are available (Hasheminejad et al. 2018; Pan et al. 2019; Partl et al. 2012). However, destructive sampling is often used to fill in the informational gaps and get a more accurate evaluation of the pavement structure or even just the asphalt material itself. Typically, cutting or coring of in-service asphalt pavements is conducted, and slabs/cores are taken to a lab to assess the microstructural and mechanical properties of the mix using destructive tests. Due to the inherent technical challenges of highly sensitive non-destructive tests combined with the thermomechanical sensitivity of asphalt cement, coupling non-destructive measurements with mechanical testing of asphalt materials in the laboratory is difficult.

10.2 Conventional Time Domain Analysis of Asphalt Materials

While non-destructive tests are used frequently in the field for pavement preservation, there exists no standard for these techniques in a laboratory setting. Over the past 15 to 20 years, however, there has been more interest in applying non-destructive or “non-invasive” techniques during mechanical and/or performance tests for asphalt mixtures (Arabani et al. 2009; Di Benedetto et al. 2009; Boz et al. 2017; Houel and Arnaud 2009; Mounier et al. 2012, 2016; Tavassoti-Kheiry et al. 2017). Ultrasonic wave propagation methods, having been used in many applications for other civil materials and structures, are currently the most developed lab characterization technique for asphalt mixes, although low ultrasound impact resonance, acoustic emissions and resonant column tests have also been

conducted (Boz et al. 2017; Daniel and Kim 2001; Mounier et al. 2012; Ragni et al. 2020). In contrast to cyclic fatigue tests where it is assumed that inertia effects up to certain frequencies (i.e., excitation frequencies below 10 kHz) are negligible, wave propagation techniques rely on high-frequency excitations to characterize the dynamic properties of the asphalt mixture (Di Benedetto et al. 2009). This section will briefly discuss the conventional time-domain analysis of wave propagation techniques.

In ultrasonic tests, three primary types of waves are transmitted through the media: compression (P-waves), shear/secondary (S-waves), and Rayleigh or surface waves. Transmission UPV test setups require a transducer-receiver system in either reflection (i.e., the signal is transmitted, and the same transducer detects the reflection of the signal) or transmission (i.e., there is a transduce-receiver pair separated by a known distance) mode. In typical ultrasonic acquisition (transducer-receiver) systems, the wave velocity of P-waves is easily measured (Planès and Larose 2013). As P-waves have the highest wave velocity, they are easily identifiable as the first arrival in the time trace, as depicted in Figure 10-1; the time from the first transmission to the first arrival is referred to as the time-of-flight (TOF). While the length between the transducer and receiver is known, TOF can be determined by using: (1) the time difference between the beginning of the initial signal and the first zero crossing and (2) the time difference between the maximum amplitudes of the signal envelopes using a Hilbert Transform, and (3) the time difference between the peaks with the largest amplitudes (Di Benedetto et al. 2009; Larcher et al. 2015). Thus, in the time-domain, the determination of the first arrival and TOF allows the observer to easily calculate the compression wave propagation speed as:

$$C_P = \frac{L}{t} \qquad \text{Eqn. 10-1}$$

where C_P is the P-wave velocity in m/s, L is the distance between the transducer-receiver pair in meters and t is the TOF of the waveform in seconds[3]. Indeed, the success of this measurement relies on the proper transducer, transducer location and frequency selection based on the geometry of the sample and material (Larcher et al. 2015).

[3] The time flight is also denoted as Δt in several sources; in this instance, the use of t relies on the simple assumption that t_0 is 0 seconds.

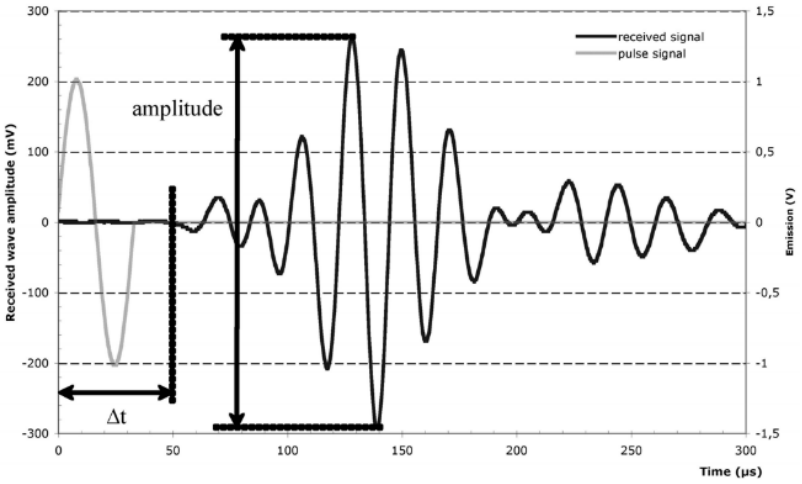

Figure 10-1 Example comparison of the original sine pulse (light grey) and the received signal (black) from (Houel and Arnaud 2009).

For a homogenous elastic solid in an infinite medium, wave velocity can be estimated in terms of the mechanical and physical properties of the material as:

$$C_P = \sqrt{\frac{M}{\rho}} = \sqrt{\frac{E(1-\upsilon)}{(1+\upsilon)(1-2\upsilon)\rho}} \qquad \text{Eqn. 10-2}$$

where M is the constrained modulus in $kg{\cdot}m^{-1}s^{-2}$, ρ is the density in kg/m^3, E is the elastic Young's Modulus in $kg{\cdot}m^{-1}s^{-2}$, and υ is the Poisson's ratio. However, to estimate the wave propagation in the viscoelastic asphalt, the contribution of the phase lag needs to be considered:

$$C_{P,VEL} = \frac{1}{\cos\left(\frac{\phi}{2}\right)} \sqrt{\frac{|E^*|(1-\upsilon)}{(1+\upsilon)(1-2\upsilon)\rho}} \qquad \text{Eqn. 10-3}$$

In Eqn. 10-3, the constrained modulus is converted to the norm of the elastic Young's modulus, and ϕ is the phase angle between the viscous and elastic response in the sample. For asphalt materials, $|E^*|$ and υ are both sensitive to temperature and loading frequency but are assumed to be constant, real values to simplify the calculation. Typically, a back-calculation approach is used to determine the modulus using the measured P-wave velocity (Arabani 2009; Di Benedetto et al. 2009; Houel and Arnaud 2009).

10.2.1 Non-Invasive Fatigue-Healing Characterization

Although few studies have been conducted, non-invasive damage-healing monitoring has been successful when applied to asphalt materials. In an early study by Daniel and Kim (2001), the impact resonance (IR) technique was employed during 3-Point Bending fatigue tests. Samples were loaded for 3000 cycles in the 3PB setup and allowed to rest for 4 hours at 20°C or 60°C. Following the rest period, the longitudinal impact resonance was measured before a subsequent 10,000 cycles were applied; this procedure was repeated until a 50% reduction of the modulus was observed. Daniel and Kim observed that the wave velocity of damaged samples was lower compared to undamaged samples and that it was there was a noticeable increase in wave velocity following rest periods. It was also observed that healing was greater for rest periods at higher temperatures but decreased as more loading-rest periods cycles were conducted (Daniel and Kim 2001). In a study by Abo-Qudais and Suleiman, UPV measurements were coupled with the Indirect Tensile test (IDT). The P-wave velocity was demonstrated to decrease as loading and damage increased. Healing was observable from changes in the UPV measurements, although there was greater variation in healing for longer rest periods (i.e., 7 to 14 days). As the IDT set-up induces permanent deformation during the test, IDT should be considered a cyclic compression test, not a fatigue test (Abo-Qudais and Suleiman 2005; Daniel and Kim 2001; Hofko and Blab 2014).

Houel and Arnaud (2009) used UPV measurements and tension-compression (T/C) tests at -10 and 10°C. Transducers (50 kHz) were placed axially at the two ends of the cylindrical T/C specimen to monitor the specimen during loading and rest periods. It was observed that ultrasonic wave propagation analysis using P-wave velocity could capture the resultant modulus decrease associated with microcrack fatigue damage with increasing cycles, but considerable variability was observed as damage increased. The change in energy observed during testing was also able to differentiate between loading and rest (Houel and Arnuad 2009). In a similar study by Mounier et al. (2015), a similar coupled T/C-UPV test was conducted. Using a higher frequency (137 kHz) transducer pair mounted radially along the curved surface of the cylinder, T/C tests were conducted at 10 Hz and 10°C. Mounier et al. (2016) determined a good correlation between the damage slope obtained from the on-specimen extensometers and the back-calculated modulus from ultrasonic measurements. However, the ultrasonic-based modulus could not capture the curvature observed due to bias effects (heating, non-linearity, etc.) typically observed in the first stage of fatigue tests (Mounier et al. 2016). In general, the slow adoption of these technologies is likely due to the prior technological limitations of ultrasonic testing equipment

and the inherent difficulties when testing a non-homogenous and highly attenuative medium such as asphalt (Di Benedetto et al. 2009; Houel and Arnaud 2009; Larcher et al. 2015).

10.2.2 Time-Domain Analysis of Wave Propagation using Coda

When a wave hits a boundary between two media, a portion is reflected while the remainder is transmitted. Within heterogeneous construction materials such as concrete and asphalt concrete, the transmittance is not only affected by the macroscale interfaces but also by mesoscale aggregates and microscale discontinuities (e.g., voids and cracks) (Deroo et al. 2010). The mode conversion effect associated with the reflection and refraction of the incident wave with these interfaces allows many different types of waves to propagate at different velocities and in different directions. As these waves propagate through the material, attenuation is observed due to geometry, but also as a result of the interaction with these scatterers. Thus, attenuation can be a good indicator of microstructural changes (Jiang 2007). As material attenuation can be as small as 1% compared to geometric attenuation, first arrival/ wave velocity methods are typically not sensitive enough to detect these scatterers (Jiang 2007; Wiciak 2020). Methods such as coda wave interferometry (CWI), non-linear elastic wave spectroscopy and non-linear impact resonance acoustic spectroscopy have been proposed to improve small-scale damage detection and overcome the limitations of conventional wave velocity analysis (Wiciak 2020).

In the 1980s, “coda” was initially proposed by researchers in the seismic community as a method to monitor velocity changes in scattered media by analyzing the tail end of the time signal. In heterogeneous media, the tail end of the time signal represents the culmination of reflection and the multiple scattering of the incident perturbing wave before being transmitted to the receiving sensor, as depicted in Figure 10-2. With successive measurements and repeated sampling, CWI can be used to measure small changes in velocity as time progresses (Liu et al. 2016a). As the media changes (presumably due to damage or other mechanisms), the wave paths also change inducing microscopic but measurable time shifts in the coda due to increased scattering. CWI is commonly conducted using a cross-correlation technique; the resultant correlation coefficient (CC) or decorrelation coefficient (1-CC) determines the similarity between successive signals of specimens in different states (Chen et al. 2021). The challenge of the CWI lies in the selection of the region of interest and/or window. By modelling the post-first arrival attenuation, the window location is often selected from the estimated mean free path using an Einsteinian diffusion model. Signals with greater diffusivity indicate weak scattering, while low diffusivity signal response indicates energy transfer through the media is slow

due to high scattering (Planès and Larose 2013). The window length is then optimized by determining the maximum relative velocity change using the doublet or cross-correlation coefficient "stretching" techniques (Hadziioannou et al. 2009; Sang et al. 2020). Despite their appearance as random noise, studies have shown that coda/ scattering is reproducible in various materials, leading to its prevalence in contemporary damage monitoring studies (Liu et al. 2016a; Planès and Larose 2013; Sang et al. 2020; Wiciak 2020).

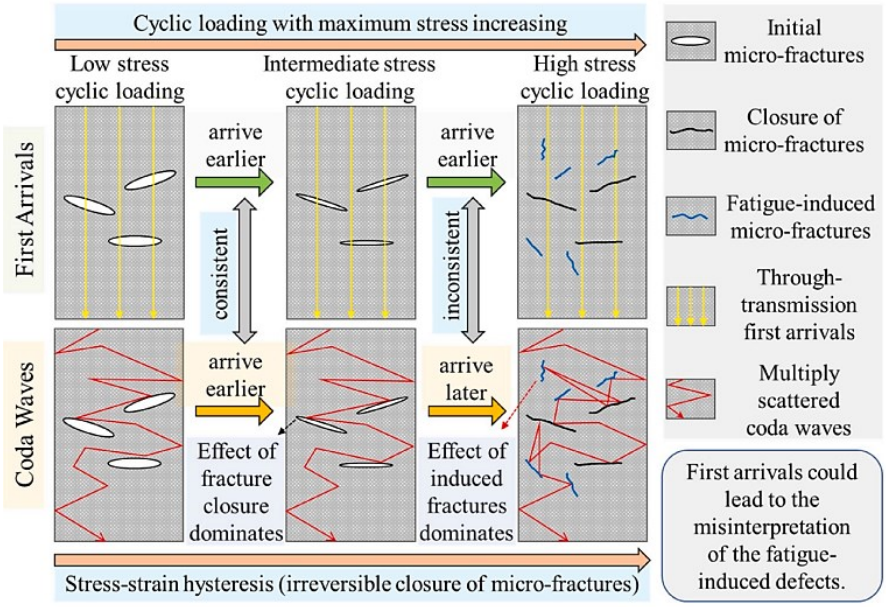

Figure 10-2 Transmission and scattering of ultrasonic waves through heterogeneous media (Sang et al. 2020).

In general, small microstructural changes due to both damage and healing occur gradually. Thus, a more sensitive technique such as CWI is ideal. This technique has been used in several studies evaluating damage evolution in concrete (He et al. 2022; Legland et al. 2015; Liu et al. 2016a) and woven fabric composites (Pomarède et al. 2019). In studies by Liu et al. (2016) and (Legland et al. 2015) the CWI analysis was even extended to concrete self-healing. As a continuation of the study conducted in Chapter 9, this study's main goal is to determine the viability of coda wave interferometry techniques for asphalt. CWI will be applied to asphalt materials under fatigue loading with and without rest periods to determine if it is feasible for future fatigue-healing studies.

10.3 Materials and Methodology

The materials used herein are the same Superpave 12.5 specimens containing 5.2% PG 58-28 asphalt cement as described in Chapter 9 Section 0. Samples were compacted using the Superpave Gyratory compactor (SGC), cored, and cut to cylinders with a final diameter of 75 mm and height of 120 (+/- 2.5) mm; the air voids were measured to be approximately 4.8% on average. Tension-compression testing was completed at 10°C (+/- 0.5°C) at 10 Hz, and three replicates were conducted for each treatment level; due to technical issues with some specimens, UPV measurements from at least two of the three replicates are used hereafter. Test specimens share the same designation corresponding to rest period duration, replicate letter designation, and strain level as used in Chapter 9. For example, Gr1a-100 represents a sample with an uninterrupted fatigue test (i.e., 0-hour rest period) with an initial strain of 100 μm/m. Table 10-1 below lists the specimen designations and the corresponding duration of each loading phase and/or rest period.

Table 10-1 Experimental test matrix for fatigue and healing tests.

Designation	Microstrain (μm/m)	LP1 Duration (hr)	Rest Period (hr)	LP2 Duration (hr)
Gr1x-100	100	8.33	0.0	-
Gr2x-100	100	4.16	4.0	4.16
Gr3x-100	100	4.16	8.0	4.16
Gr4x-100	100	4.16	16.0	4.16
Gr1x-125	125	8.33	0.0	-
Gr2x-125	125	4.16	8.0	4.16

10.3.1 Transducer Selection

Planès and Larose (2013) created the graphic featured in Figure 10-3 to demonstrate the limiting frequencies for different analysis regimes in concretes. At low ultrasound frequencies, the wavelength of the perturbing wave can be greater than the size of different scattering structures. Thus, there is limited sensitivity to microscopic changes. As the frequency increases (above 10 kHz), the wavelength becomes smaller than the associated structural components (e.g., larger aggregates and gravel) but may still be larger than heterogeneities such as cracks and smaller aggregates, leading to simple scattering.

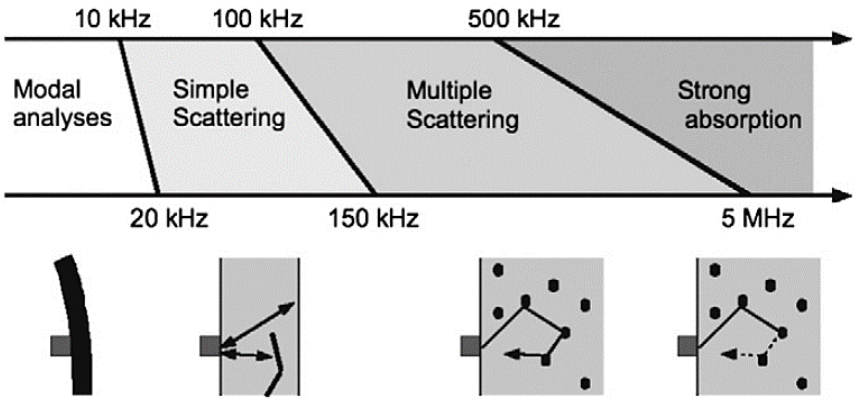

Figure 10-3 Scattering domains in concrete materials (Planès and Larose 2013).

At higher frequencies (150 kHz to 1 MHz), heterogeneities and cracks can lead to multiple scattering along the wave path; the resultant "random" data in the tail end of the ultrasonic signal has a reproducible coda providing valuable information about the scattering path. After 1 MHz, scattering and attenuation are significant enough that measurement may be impractical to observe on larger length scales but may still be possible in a laboratory setting with small-scale experiments. It should be noted that these proposed frequency ranges are not exact and can be influenced by the mix design of the concrete itself (Planès and Larose 2013). For asphalt materials, it has been shown that scattering becomes significant above 100 kHz (Jiang 2007). Based on the temperature sensitivity of asphalt, it is possible that this limit shifts with changes in temperature, further increasing the complexity of transducer selection.

As demonstrated in the studies by Houel and Arnaud (2009) and Mounier et al. (2016), the transducer selection is key to the back calculation of the modulus. Houel and Arnaud (2009) used a 50 kHz transducer and were able to observe changes in modulus, but there was considerable variability as damage increased. Mounier et al. (2016) were able to reduce variability using a considerably higher frequency transducer (137 kHz), but at the cost of sensitivity and were unable to observe the expected curvature found in the first stage of fatigue. As noted in Chapter 8 Section 8.5, an ultrasonic pulse-receiver frontend (i.e., the ACS A1560 Sonic-LF) was used with a pair of 150 kHz P-wave transducers to monitor sample integrity. Figure 10-4 below depicts representative time signals obtained at the beginning of the fatigue test (blue) and the final ultrasonic measurement (orange) after hundreds of thousands of loading cycles. The lefthand side of Figure 10-4 demonstrates that the arrival time of the p-wave is relatively unaffected by loading the sample using the 150 kHz transducers. However, the

low-energy coda highlighted in the window at the right of the figure is significantly shifted, presumably due to the increased presence of scattering media (e.g., voids, microcracks, etc.).

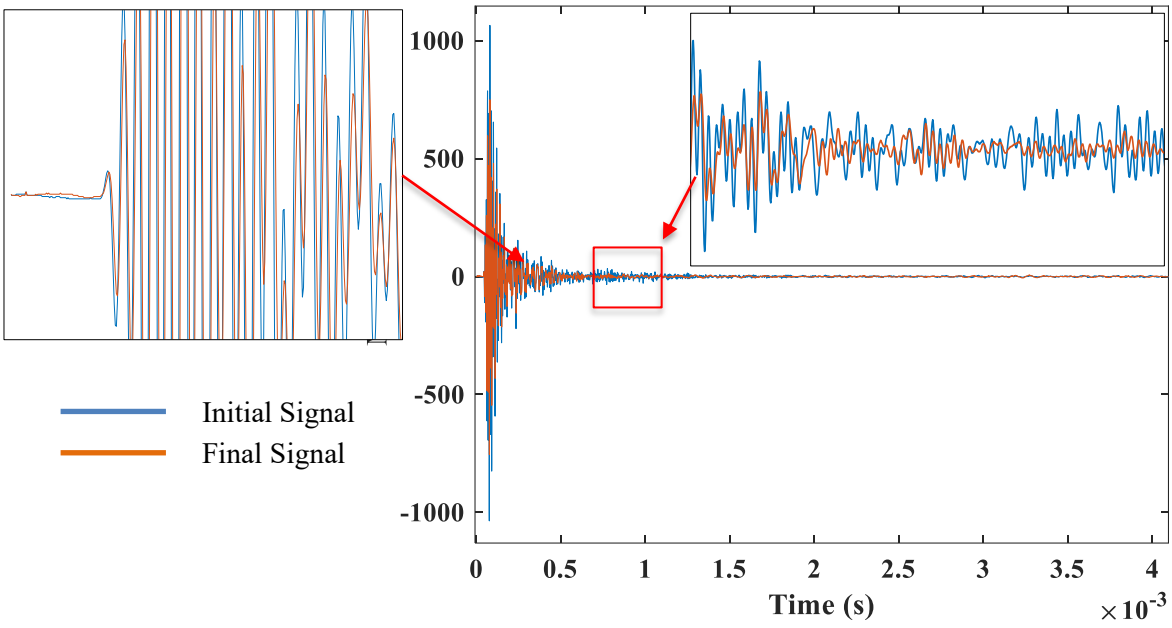

Figure 10-4 Initial and final time signals obtained during fatigue testing.

10.3.2 Ultrasonic Measurements

To complement the traditional tension-compression measurements conducted in Chapter 9, ultrasonic measurements are performed during both loading and rest periods during fatigue-healing tests. As shown in Figure 10-5, two transducers were aligned with the central axis of the sample and coupled to the aluminum upper/lower cap using Molykote® High Vacuum grease. With the two 25 mm aluminum end caps, the approximate receiver-receiver length was 170 mm. Using the custom-coded A1560 software and pulse-receiver system, a time signal was acquired at approximately 10-minute intervals using a TTL pulse triggered by the MTS test frame through the test frame controller. Based on several trial specimens, the A1560 software acquisition parameters were selected such that the acquired signal duration contained not only the P- and S-wave first arrivals but also the tail of the end of the time signal to fully capture the coda. In the case of this study, the typical signal was approximately 4096 microseconds using a sampling frequency of 2 MHz and a vector length of 8192 samples. A list of key DAQ parameters is summarized in Table 10-2.

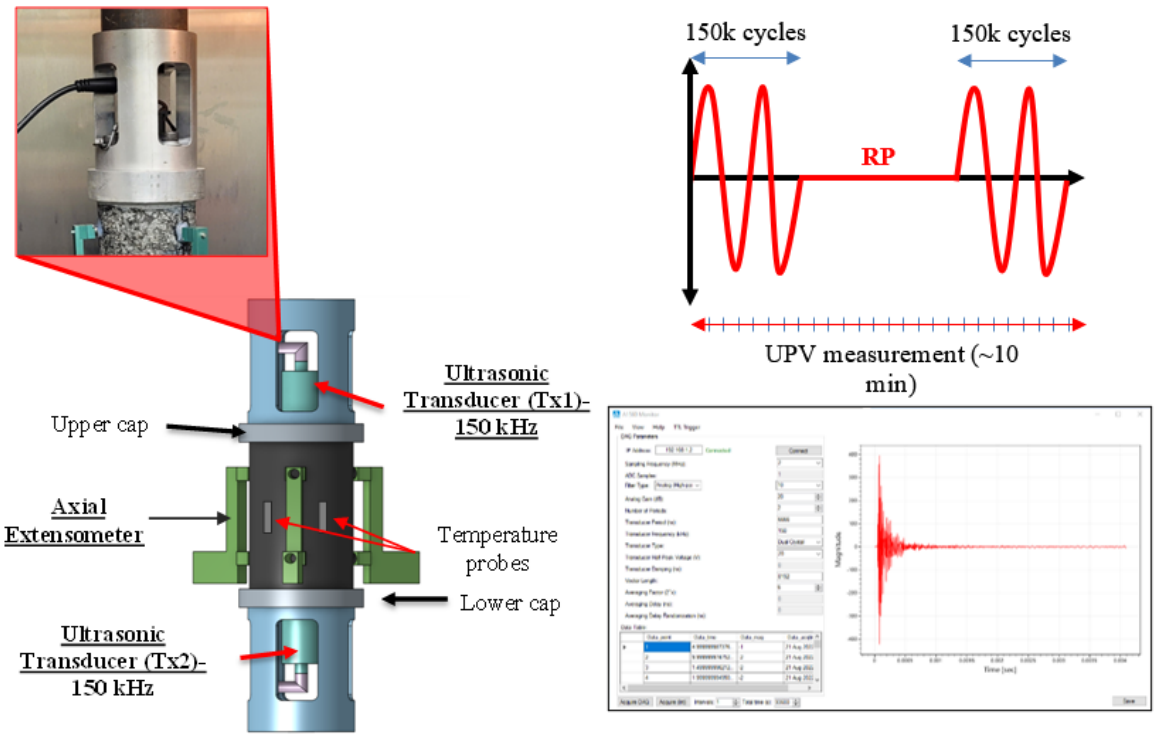

Figure 10-5 T/C-UPV test set-up schematic and example time-signal measurement.

Table 10-2 A1560 data acquisition parameters.

DAQ Parameter	Value	Unit
Sampling Frequency	2.0	MHz
Filter Type	Analog	-
Filter Cut-off Frequency	10	kHz
Analog Gain	0 to 40	dB
Transducer Frequency	150	kHz
Transducer Type	Dual Crystal	-
Transducer Half-Peak Voltage	20	V
Vector Length	8192	-
Averaging Factor (2^x)	6	-

As a final note, some assumptions are presented about the T/C-UPV procedure, including:

- *Aluminum end caps*: the four aluminum end caps used in this study were machined from the same slab of 6061-T6 aluminum. Although this material meets the hardness requirement for AASHTO T 342 mechanical testing, the end cap material is relatively soft and susceptible to dents/ scratches.

As the end caps are constantly reused throughout the study, there is the potential that end cap surfaces may be damaged while removing the asphalt specimen, even when extreme care is taken during specimen removal. For this study, it is assumed that the end caps are interchangeable, and any minor damage incurred on the end caps during the study is negligible.

- *Epoxy/ gluing procedure*: from Chapter 8, it was already demonstrated that the epoxy-layer thickness is variable between specimens ranging from approximately 0.5 to 1.5 mm; any variation in the epoxy thickness from specimen to specimen is assumed to be negligible. It is also assumed that the gluing procedure fills any significant surface void/defects between the specimen and the end plate. Thus, any transmission of the transducer signal is negligibly affected by either the upper or lower specimen-epoxy-end cap interfaces.
- *Transducer and test temperature*: in this study, the Pundit® Proceq 150 kHz transducers are used. Based on the specification provided by the manufacturer, the transducer is rated to have a normal operating range from -20 to 60°C (Proceq S.A. 2018). It is assumed that the transducers are then unaffected by testing at the selected test temperature (10°C). For this study, it is also assumed that any internal temperature changes within the asphalt specimen itself are inconsequential. Previous studies have shown that attenuation is much more significant as the testing temperature increases (Di Benedetto et al. 2009; Daniel and Kim 2001). Furthermore, considerable sample variation can be observed at higher temperatures and with higher frequency excitations (Di Benedetto et al. 2009).

10.3.3 Dynamic Time Warping Procedure

The dynamic time warping (DTW) procedure is employed in this study as it has been demonstrated to be better compared to cross-correlation or trace stretching methods, although at the cost of computational efficiency (Mikesell et al. 2015; Yuan et al. 2021). Unlike the traditional global trace stretching used in early seismological coda studies, DTW is a non-linear optimization method with a variable stretching factor. Phase shifts between each time lag are then determined by taking the shortest available "warping path" and be effective even when there is strong noise in the signal (Mikesell 2015). DTW algorithms are alignment-based such that the DTW procedure finds the optimal alignment between two-time signals, as shown in Figure 10-6.

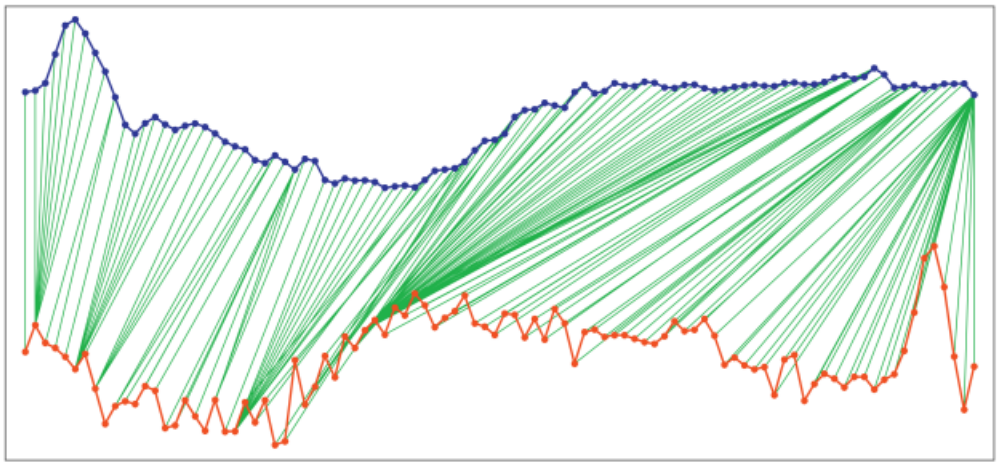

Figure 10-6 A typical example of a DTW alignment (from Zhang and Tavenard, 2017).

The overarching goal of the alignment process is to minimize the "global cost" between pairs of points or couples. The global cost is minimized through the selection of the warping path. A simple Euclidean warping path (as might be used in trace stretching procedures) has a rigid 1-to-1 alignment adding to the cumulative cost of the procedure. The DTW warping path does not follow this rigid path but is still bound by several rules related to monotonicity and continuity when using a step pattern between a sequence of couples (Zhang et al. 2017). The optimal warping path is determined using a recursive, back-tracking procedure at which the shortest path is found by looping through the time lags to recover the smallest shift in the sequence (Hale 2013). For this study, the Euclidean distance is minimized between the two signals, although other distance metrics such as the absolute/ Manhattan, squared Euclidean, and symmetric Kullback-Leibler can also be used (The MathWorks 2022).

10.3.4 Window Selection

It can be reasoned that the selection of the DTW window location and duration is critical to the success of CWI. In the following subsections, two window selection methods are presented.

10.3.4.1 Method 1: A Statistical Approach

In the first window selection method, a simple statistical changepoint detection algorithm is used. The algorithm is implemented through the MATLAB function named "findchangepts" included in the Signal Processing Toolbox (The MathWorks 2022) based on the works of Killick et al. (2012) as well as (Lavielle 2004). The changepoint detection algorithm employs a global parametric method to determine and divide a dataset into sections. An estimate of the section-to-section residual error is

determined at each point in the section; the changepoint is selected as the point that minimizes the residual error. The MATLAB findchangepts function can be used with several statistical parameters, including the mean value, the root-mean-square level, the standard deviation, and a linear best-fit parameter. The appropriate test statistic is extended to the contrast function and the penalty function is then computed. This process is completed for several sections until the penalty function is minimized (Lavielle 2004). For this study, the findchangepts function is used with the root-mean-square test statistic where the test stat with a maximum of two changepoints as shown in Figure 10-7. The first changepoint index corresponds to the window starting location, and the second index is used to determine the window duration. The window location and duration are determined from the initial, undamaged time signal obtained at the beginning of the test and applied to every successive time signal.

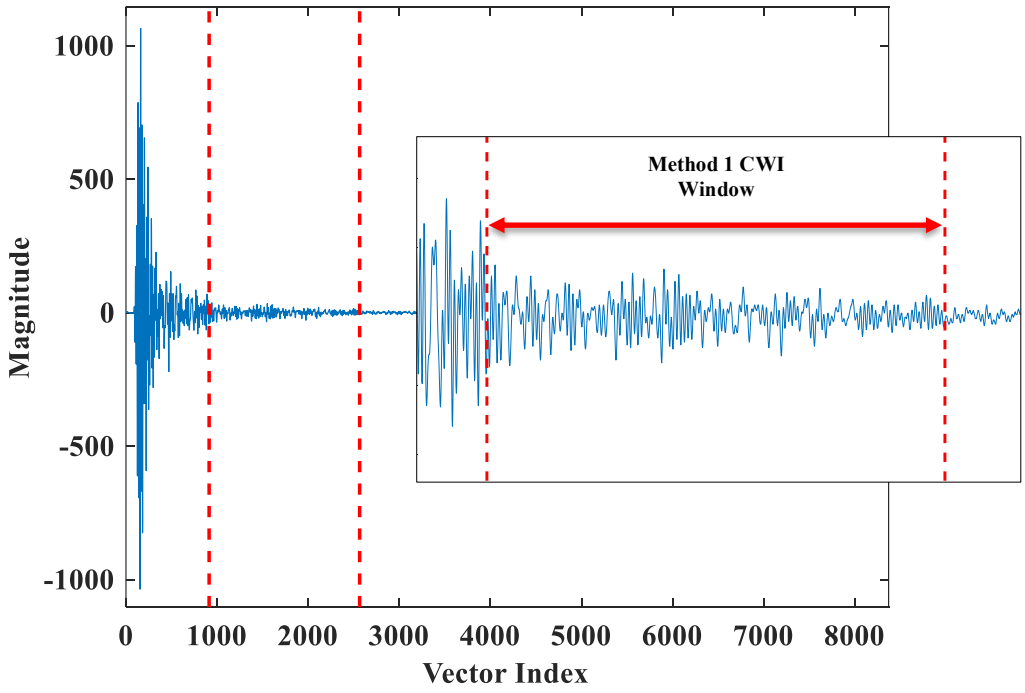

Figure 10-7 Method 1 window starting location and duration generated using the findchangepts function.

10.3.4.2 Method 2: An Analytical Approach

In the second window selection method, the coda window is determined analytically from the diffusivity of the time signal itself. The diffusivity or coda of a wave is a result of later arrivals caused by scattering media and is presented at the tail end of the time signal. Although these peaks appear to be random, they are often reproducible, and the intensity of the waveform can be modelled (Planès and

Larose 2013) In several seismic studies, the coda-Q or Q_c is modelled using the attenuation of the coda wave envelope, *e*(t):

$$e(t) = A_0 t^{-n} \exp\left(-\frac{\pi f}{Q_C} t\right) \quad \text{Eqn. 10-4}$$

where A_0 is the initial amplitude, t is the time selected from a certain reference point, and *f* is the frequency; the t^{-n} term represents geometric spreading, and the power *n* ranges from 1 to 2 depending on the dominant wave (Okamoto et al. 2013; Talebi et al. 2021).

In this study, the diffusivity is modelled using the diffusion equation:

$$E(r, t, f) = \frac{P_0}{(4D\pi t)^{d/2}} \exp\left(-\frac{r^2}{4Dt}\right) \exp\left(-\sigma t\right) \quad \text{Eqn. 10-5}$$

where E is the spectral energy density (SED) as a function of time, t, distance, r, and frequency, *f*. P_0 is the magnitude of the source pulse, D is the diffusivity, and σ is the dissipation rate. As presented by (Epple 2018) taking the logarithm of Eqn. 10-2, the resulting linear function can be used as:

$$f(A, B, C, t) = A + \frac{B}{t} + Ct \quad \text{Eqn. 10-6}$$

where $A = \ln\frac{P_0}{(4D\pi t)^{d/2}}$, $B = -\frac{r^2}{4D}$, and $C = -\sigma$. After solving for the coefficients, A, B and C by fitting the Log(SED) curve, P_0, D and σ can be back calculated to plot the diffuse envelope in the time domain (Deroo et al. 2010; Epple 2018; Planès and Larose 2013). Below in Figure 10-8, an example spectral energy density plot is prepared for the initial signal of an undamaged specimen before loading has begun. Based on the analysis of several specimens, the first 625 μs were selected (highlighted in red) for fitting. As this portion of the SED contains most of the energy in the time signal, the Eqn. 10-3 coefficients are fitted to the data in this time interval. After back calculating the diffusivity and dissipation rate, the diffuse envelope can be plotted as shown in Figure 10-9. Figure 10-9 also illustrates the time in the signal at which the area is 90, 95, 99 and 99.99% contained in the diffuse envelope. For this study, the $t_{99.99\%}$ was selected as the starting point of the window for Method 2.

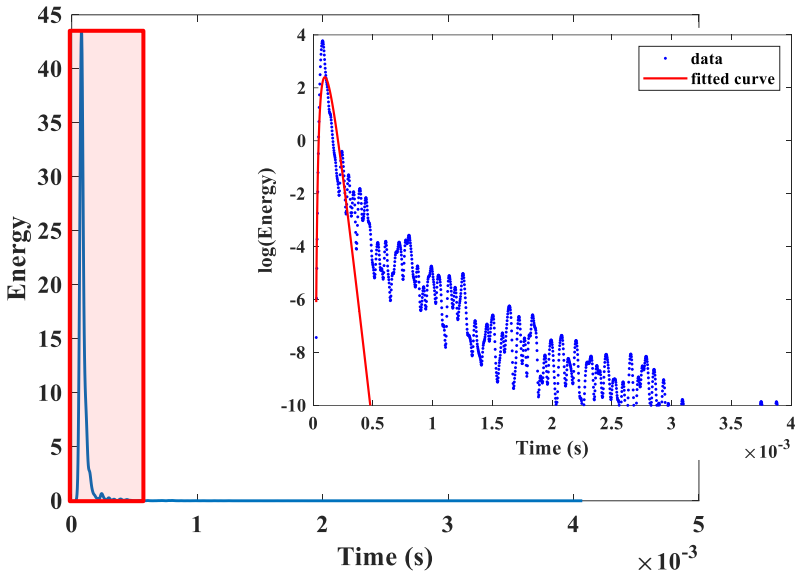

Figure 10-8 Energy spectral density and Log(SED) plots for the time signal obtained from an undamaged specimen.

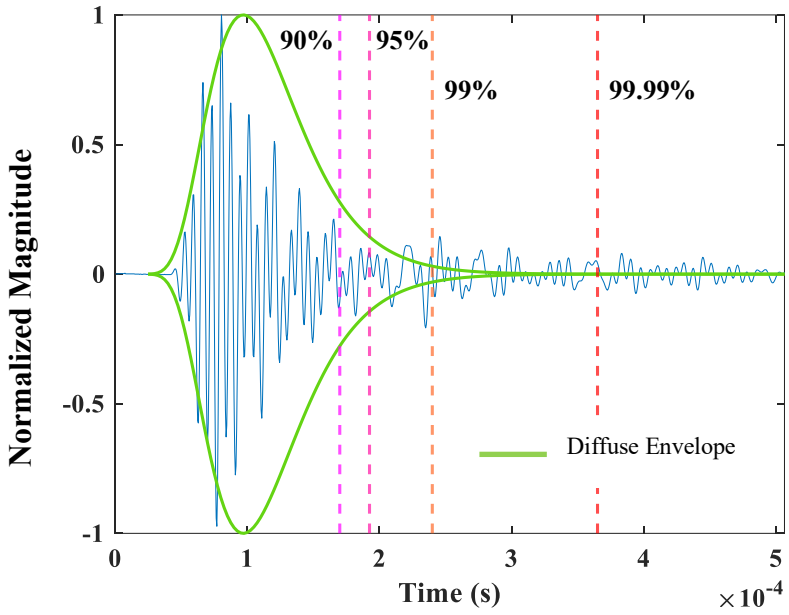

Figure 10-9 Diffuse envelope of the first signal of an undamaged specimen.

Typically, in studies using the cross-correlation technique, the doublet phase-shift technique or the stretching interpolation techniques can be used (Epple 2018; Hadziioannou et al. 2009). In the stretch interpolation method, the window length is determined using the coda velocity rate of change, dV/V. The dV/V is calculated for changing time durations using the stretching factor, ε_{st}. At the maximum dV/V, the cross-correlation coefficient is also maximized, providing the optimal window length.

However, this study uses a similar approach to determine the window length using the DTW algorithm. Starting at $t_{99.99\%}$, the rate of change of the DTW Euclidean distance between the initial time signal and the final time signal is calculated for increasing the window size. Plotting the rate of change (Figure 10-10), a bilinear curve can be identified with a transition point from a high to a low DTW rate of change. This transition point is selected as the end of the DTW window allowing a dynamic calculation of an appropriate window location and length on a per-sample basis, as shown in Figure 10-11.

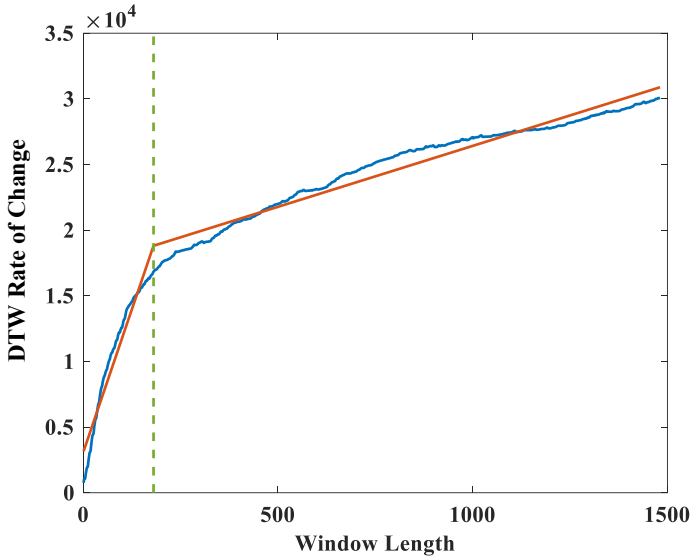

Figure 10-10 DTW rate of change.

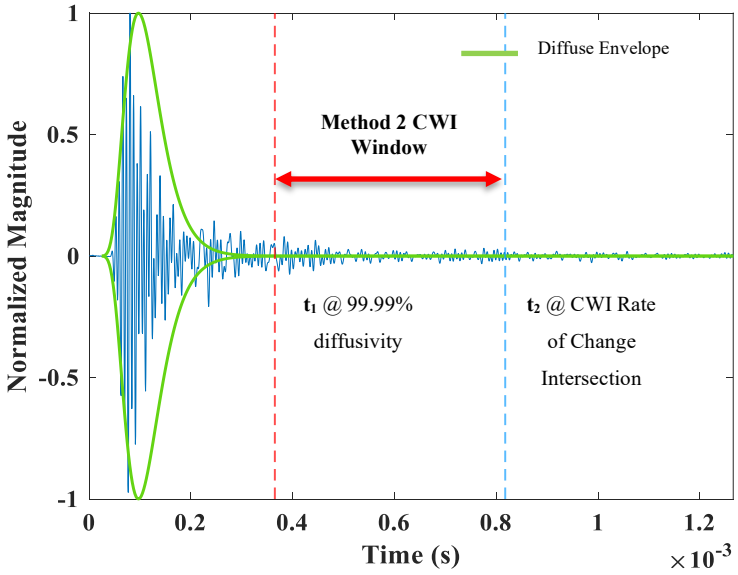

Figure 10-11 Method 2 CWI window determined from the diffuse envelope and DTW rate of change.

10.4 Results and Discussion

10.4.1 CWI for Uninterrupted Fatigue Tests

Using both Method 1 and Method 2 window selection (Figure 10-12 and 10-13, respectively), it can be observed that the CWI Euclidean distance increases with time as hypothesized, and there is a distinct difference between specimens tested at different strain levels. It should be noted that the CWI Euclidean distance will be shortened and referred to as the "CWI" in future discussions. Similar to the study by Legland et al. (2015), the decision was made to normalize distance values by the maximum CWI value as the scale of the CWI can fluctuate considerably on a specimen-to-specimen basis.

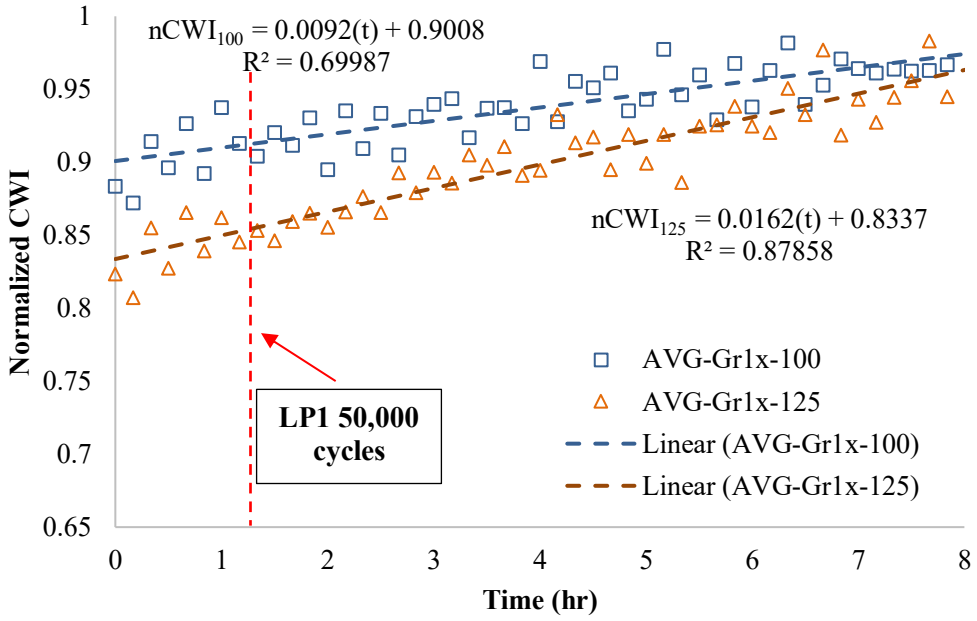

Figure 10-12 Averaged Normalized CWI at 100 and 125 μm/m for uninterrupted fatigue tests using window selection Method 1.

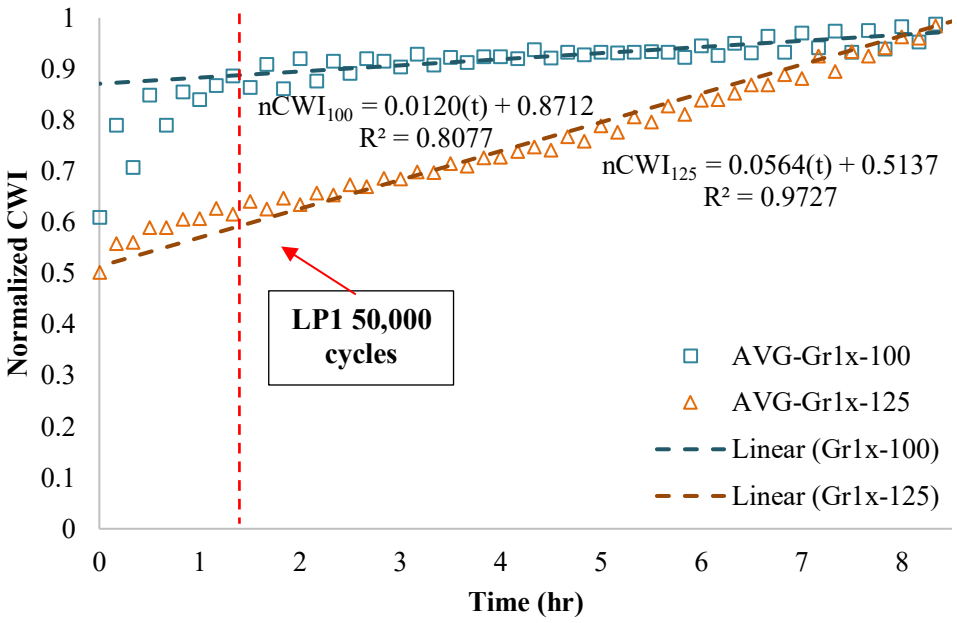

Figure 10-13 Averaged Normalized CWI at 100 and 125 μm/m for uninterrupted fatigue tests using window selection Method 2.

As a point of comparison with the damage rates observed in the DGCB and iVECD methods used in Chapter 9, a linear fitting is performed in the form:

$$nCWI_{strain} = a_{CWI}t + b_{CWI} \quad \text{Eqn. 10-7}$$

where $nCWI_{strain}$ is the normalized CWI Euclidean distance, a_{CWI} is the slope of the linear fit as related to the increase in scattering media caused by loading, and b_{CWI} is the nCWI intercept. The linearization is calculated from the time corresponding to 50,000 cycles until the end of the loading phase; for this feasibility study, the second interval (C_2) used the DGCB and iVECD fatigue analysis (i.e., corresponding to 150,000 to 300,000 cycles) is disregarded.

Consequently, looking at Figure 10-12 and 10-13 R-squared values (solely as a measure of data linearity), it can be observed that Method 2 provides a more linear dataset compared to Method 1 for the loading interval. When reviewing CWI results at times corresponding to 0 to 50,000 cycles (approximately the first 1.38 hours of the analysis), Method 2 can capture the non-linearity observed in the fatigue curves found in Chapter 9. Method 2 also generated higher a_{CWI} values compared to Method 1. Similarly to Chapter 9, the effect of rest period duration and strain level for interrupted fatigue-

healing tests will be further examined to evaluate the repeatability of the CWI method for fatigue monitoring.

10.4.1.1 Effect of Rest Period

Figures 10-14 and 10-15 below contain the normalized CWI fatigue curves at 100 μm/m for fatigue-healing tests with 4-, 8- and 16-hour rest using window selection Methods 1 and 2, respectively. In both figures, loading phases and rest periods are easily distinguishable. Gr2x-, Gr3x- and Gr4x-100 first loading phases appear to have relatively good agreement despite a variation of the nCWI intercepts using both Method 1 and 2; second loading phase a_{CWI} values, however, appear to have a greater deviation from Phase 1 values with increasing rest period duration. During rest periods specimens, a similar decrease in nCWI is observed in all three specimen groups. This decrease may be correlated to asphalt specimen restoration if using the RILEM CHA-278 definitions presented in previous chapters. For Gr3x- and Gr4x-100 (tests with greater than 4-hour rest periods), the decrease in nCWI begins to plateau after approximately 6 hours of rest, as denoted by the red circles in Figures 10-14 and 10-15. As seen in the uninterrupted fatigue tests, Method 2 retains the expected curvature/ non-linearity during loading and rest periods; Method 2 also provides less measurement variability during rest periods.

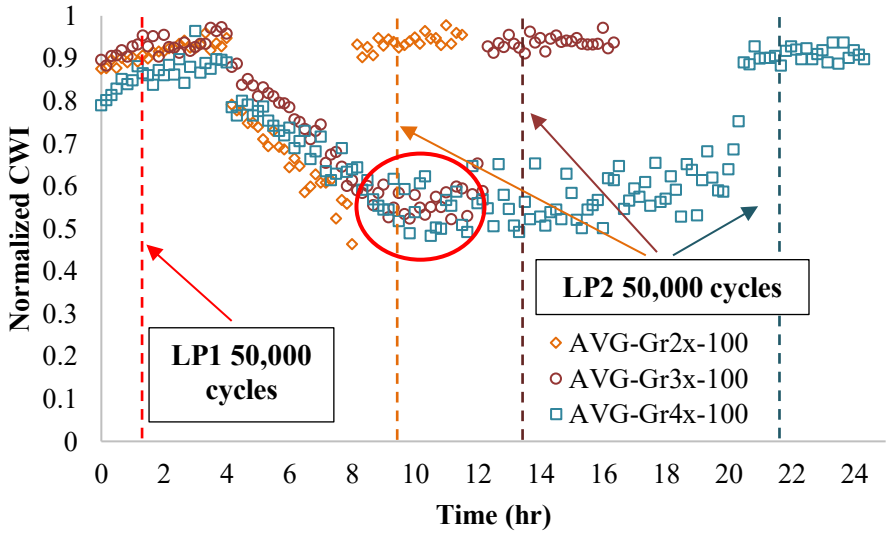

Figure 10-14 Averaged Normalized CWI for fatigue-healing tests (with 4-, 8- and 16-hour rest periods) using window selection Method 1.

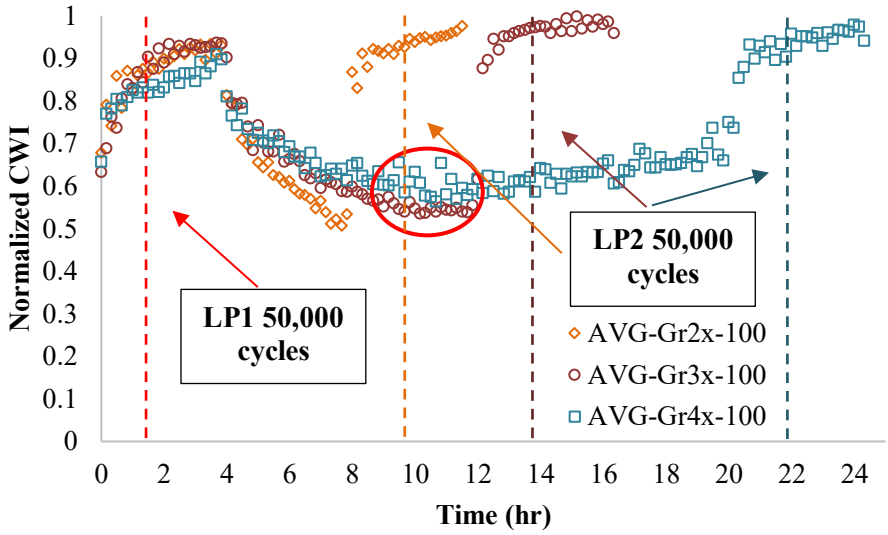

Figure 10-15 Averaged Normalized CWI for fatigue-healing tests (with 4-, 8- and 16-hour rest periods) using window selection Method 2.

10.4.1.2 Effect of Strain Level

To evaluate the effect of strain level on CWI measurements, Method 1 (Figure 10-16) and Method 2 (Figure 10-17) are presented for nCWI fatigue curves at 100 and 125 µm/m tests with an 8-hour rest period. The nCWI slope appears to be significantly greater when testing at the higher strain levels; this effect is even greater when using the Method 2 window selection. In contrast to specimens tested at 100 µm/m, Gr2x-125 specimens do not appear to retain the expected curvature observed during typical fatigue tests using Method 2. This could be a result of the normalization of CWI and the scaling of different features in the curve. Referring back to Figure 10-13, specimens tested at 125 µm/m similarly exhibited less curvature compared to 100 µm/m specimens. As a consequence of the lack of curvature observed in Method 2, only Method 1 demonstrates a defined plateau in the observed restoration for Gr2x-125 specimens. Notably, when testing at the higher strain level, the restoration continues past the 6-hour plateau observed for specimens tested at 100 µm/m; this result is consistent with the observation from Chapter 9 that increased damage (over the same loading duration) generates a proportionally greater ability to restore the mechanical properties of the asphalt specimen.

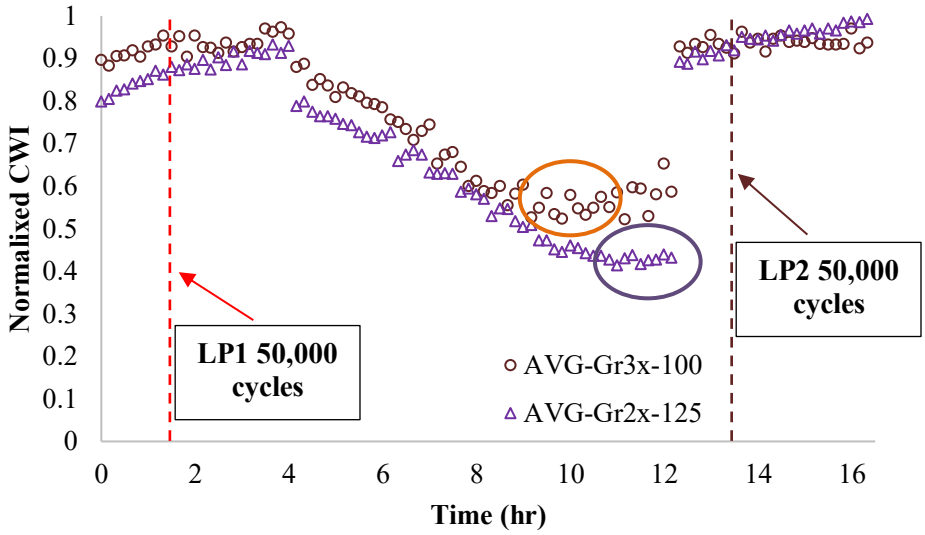

Figure 10-16 Averaged Normalized CWI for fatigue-healing tests at 100 and 125 μm/m (8-hour rest period) using window selection Method 1.

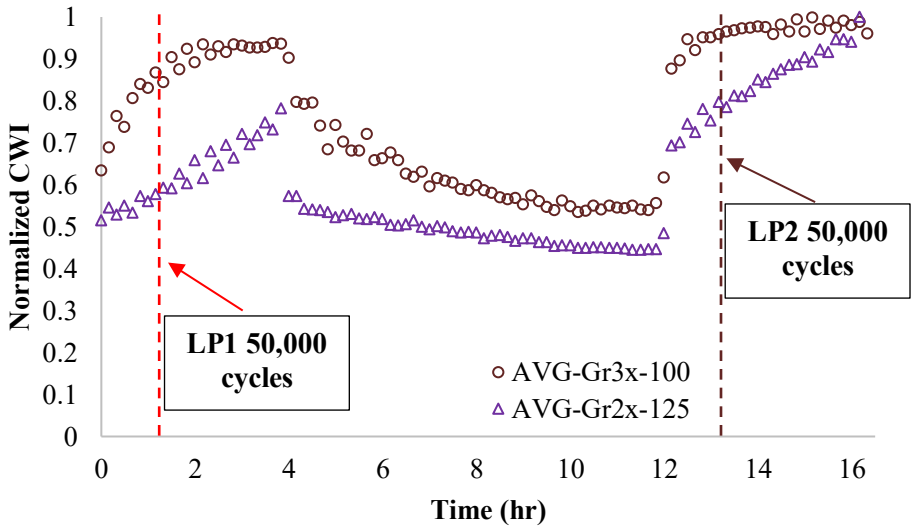

Figure 10-17 Averaged Normalized CWI for fatigue-healing tests at 100 and 125 μm/m (8-hour rest period) using window selection Method 2.

10.4.1.3 Variability Between Loading Phases

As mentioned in the rest-period section, there appears to be a much greater discrepancy between the nCWI slopes between the first and second loading phases compared to both the DGCB and iVECD methods in Chapter 9. Table 10-3 contains the a_{CWI} values for Loading Phases 1 and 2 for all test groups

using both Method 1 and 2 window selection. It is observed that uninterrupted a_{CWI} values are significantly lower compared to a_{CWI} values from fatigue-healing tests in Loading Phase 1; a similar trend was observed in the N_{f_PL} values obtained from the iVECD method and was attributed to the selection of the data interval for the fitting process producing a "flatter" fitted curve. Computing the $a_{LP1/LP2}$ ratios provides greater clarity about the discrepancy between the first and second loading phases. In contrast to DGCB and iVECD $a_{LP1/LP2}$ ratios, which showed relatively low variability across all test treatments, Gr3x- and Gr4x-100 have significantly lower Loading Phase 2 a_{CWI} values. Nevertheless, as this discrepancy occurs using both window selection methods but does not appear in either the Gr2x-100 or the Gr2x-125 specimens, this may be caused by material variability itself and less so by the window selection method, although this would need to be confirmed with additional testing.

Table 10-3 a_{CWI} and $a_{LP1/LP2}$ ratios using windowing Method 1 and Method 2.

	Method 1			**Method 2**		
Designation	$\mathbf{a_{CWI\_LP1}}$	$\mathbf{a_{CWI\_LP2}}$	$\mathbf{a_{LP1/LP2}}$ **(%)**	$\mathbf{a_{CWI\_LP1}}$	$\mathbf{a_{CWI\_LP2}}$	$\mathbf{a_{LP1/LP2}}$ **(%)**
Gr1x-100	0.0092	-	-	0.0120	-	-
Gr2x-100	0.0163	0.0126	129.4	0.0219	0.0228	96.1
Gr3x-100	0.0138	0.0029	475.9	0.0237	0.0031	764.5
Gr4x-100	0.0222	0.0030	740.0	0.0302	0.0113	267.3
Gr1x-125	0.0162	-	-	0.0564	-	-
Gr2x-125	0.0289	0.0238	121.4	0.0693	0.0617	112.3

10.4.2 Additional Comments on CWI Analysis

Dissipation of energy in fatigue tests is typically exhibited as a relative heating or cooling of the internal specimen temperature due to loading (Baaj 2002; Di Benedetto et al. 2011a). In literature, it is well documented that coda waves can be affected by variations in temperature (Chen et al. 2021; Pomarède et al. 2019; Sang et al. 2020) Although not highlighted in the previous analysis of the fatigue data, the specimen surface temperature was monitored throughout the test using three surface-mounted thermistors. Figure 10-18 contains the surface temperature plots of two representative specimens over 300,000 cycles (8.33 hours). In both cases, the external surface temperature increases by about 0.2 to 0.4°C throughout the test; the greatest increase in temperature occurs in the first 2 to 3 hours of loading before stabilizing. Additionally, the change in surface temperature appears to be higher when testing at 125 μm/m, but only by a marginal amount.

Another potential source of variability of the coda wave interferometry is the strain drift phenomenon discussed briefly in Chapter 9. As the test progresses, the on-specimen strain increases as the three extensometers begin to deviate from one another. Figure 10-19 demonstrates that the strain can drift upwards by approximately 19% and 28% over the course of 300,000 cycles for specimens with an initial target strain of 100 and 125 μm/m, respectively. This strain increase represents a minuscule increase in the transducer-to-transducer distance (less than approximately 6 microns over the 70 mm gauge length) and an increase in the axial displacement of less than 0.2 mm. Based on this understanding, it appears that the effect of internal heating and strain drift should have minimal effect on the computed CWI values during loading and rest periods. Despite the initial success of the CWI given the selected test conditions for this mix, the technique should be validated at higher temperatures. Attenuation may be more significant at other commons test temperatures (i.e., 15 and 20°C) thus decreasing the effectiveness of the technique.

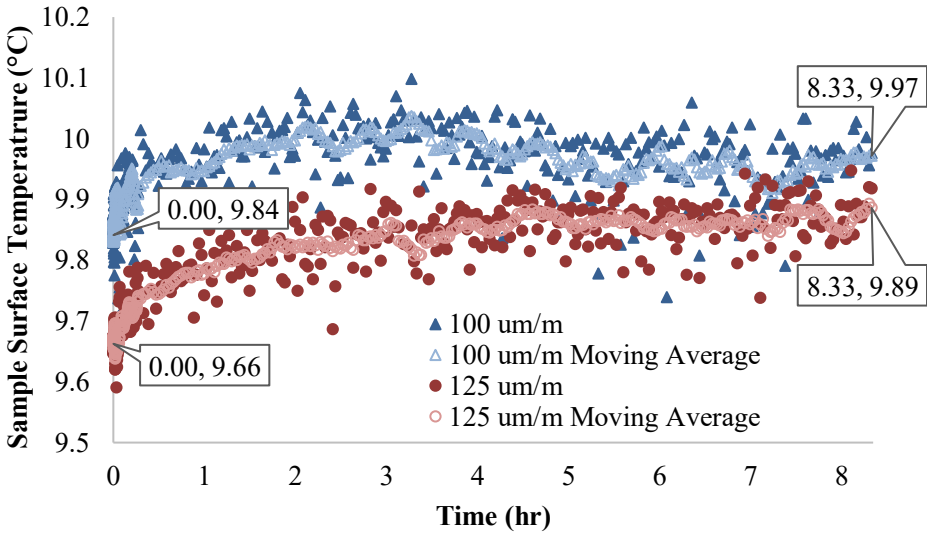

Figure 10-18 Representative specimen surface temperature for an uninterrupted fatigue test at 100 and 125 μm/m.

As an addition to this study, it was pertinent to discuss that (out of all specimens tested in this study) only one failed outside the gauge length as shown in Figure 10-20. The specimen shown in Figure 10-20 was intended to be included in the Gr2x-125 group (an initial strain of 125 μm/m with an 8-hour rest period). Figure 10-21 shows the evolution of the sample modulus over the test; the specimen appears to fail less than 30,000 cycles into the second loading phase. Whether the sample failed due to improper specimen preparation or a material defect, this specimen was not included in the fatigue analysis present in either this chapter or Chapter 9 as is recommended in AASHTO T 342.

Notwithstanding the purposeful omission from the fatigue analysis, the presence of a verifiable macrocrack can provide additional insight into the effect of a large void on UPV measurements. Several points of interest are labelled in Figure 10-21 relating to different intervals/ occurrences in the fatigue-healing test.

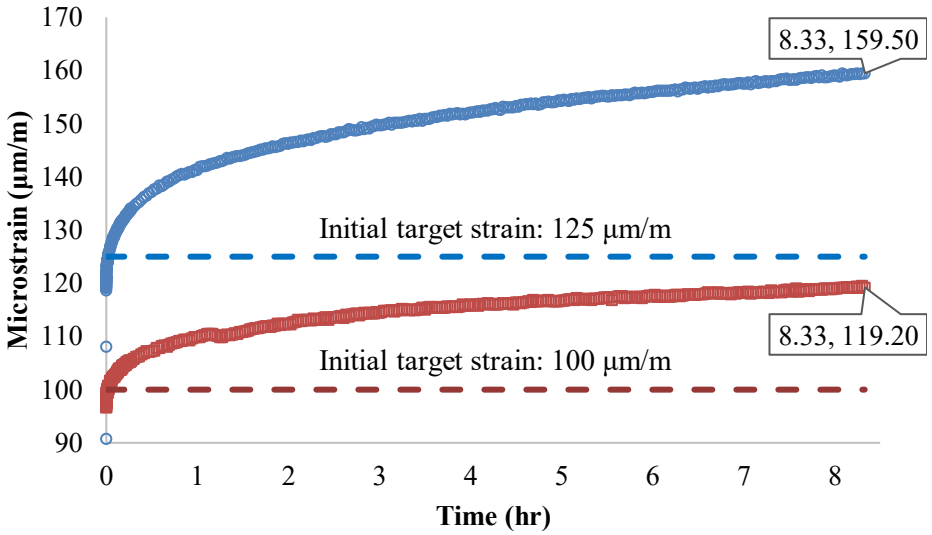

Figure 10-19 Representative strain drift for an uninterrupted fatigue test at 100 and 125 µm/m.

Figure 10-20 Left: Specimen with visible macrocrack on the surface of a Gr2x-125 replicate (using an initial strain of 125 µm/m with an 8-hour rest period). Right: Close-up image with the macrocrack highlighted in green.

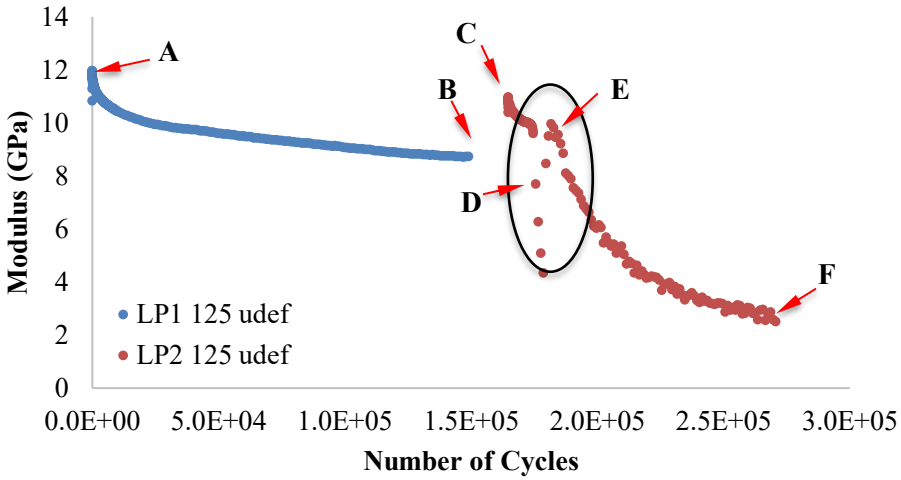

Figure 10-21 Modulus evolution for the failed Gr2x-125 replicate. Points of interest: (A) initial modulus at the beginning of the first loading phase, (B) modulus at the end of the first loading phase, (C) initial modulus at the beginning of the second loading phase, (D) modulus drop caused by specimen failure, (E) modulus recovery, (F) modulus at the end of the second loading phase.

Figure 10-22 displays the individual time signals corresponding to the points of interest labelled in Figure 10-21. A minor decrease in the signal magnitude from 600 to 390 is observed from points A to D. When observing the time signal at point E (where the modulus appears to recover after failure), the magnitude decreases by a factor of 10 and a new arrival is observed at approximately 2900 μs, but the signal is now dominated by noise. Finally, at the final time signal, a further decrease in the signal magnitude is observed. These final time signals demonstrate why the coda wave interferometry may not be suitable for fatigue monitoring. In general, these voids could lead to pathological singularities in the DTW algorithm leading to "incorrect" alignments and larger/smaller computed CWI Euclidean distances depending on the crack propagation speed (Zhang et al. 2017). Similarly, this reinforces the importance of choosing the correct window size and location; Mikesell et al. (2015) note that non-homogenous velocity pulses in the scattering media can make certain parts of the coda more sensitive to the perturbation itself. Using an approach such as that completed by Deroo et al. (2010), future damage studies could avoid the challenging window selection process and instead assess the damage on an energetic basis using the diffusion equation (Eqn 10-2) to determine changes in diffusivity and dissipation over the length of a fatigue test.

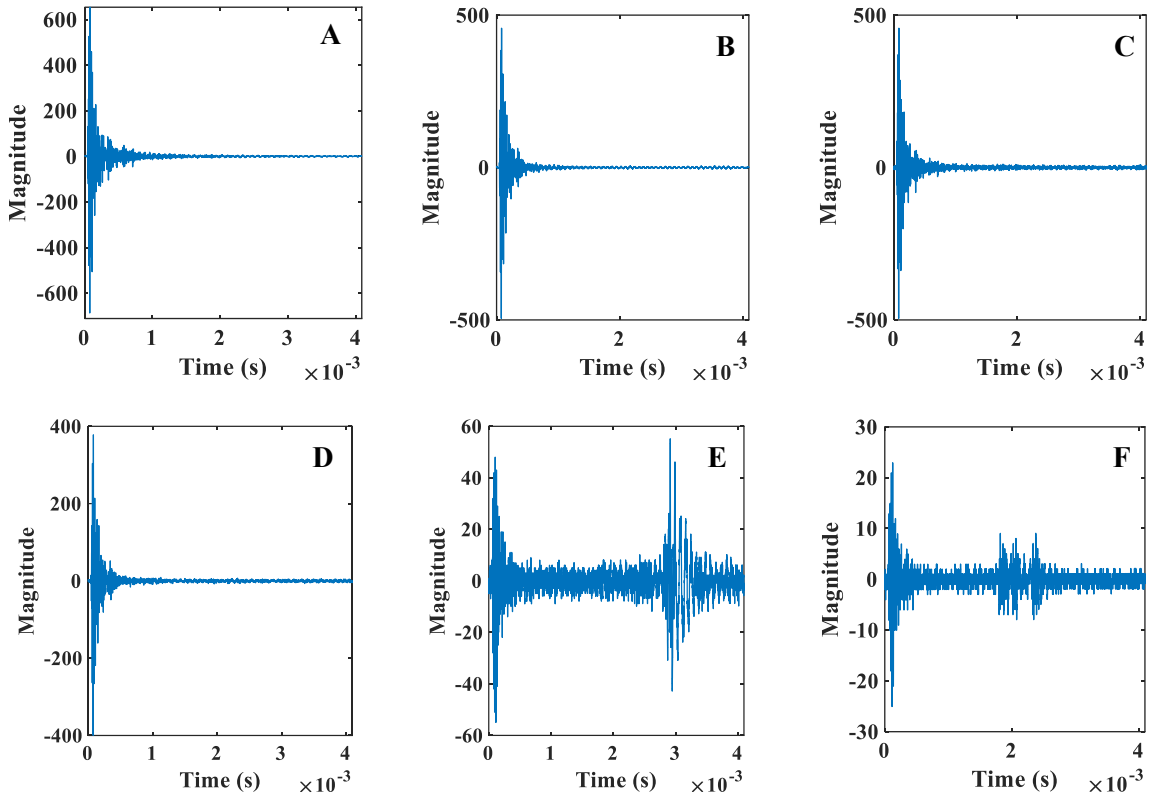

Figure 10-22 Time signals for the failed Gr2x-125 replicate (A) initial modulus at the beginning of the first loading phase, (B) modulus at the end of the first loading phase, (C) initial modulus at the beginning of the second loading phase, (D) modulus drop caused by specimen failure, (E) modulus recovery, (F) modulus at the end of the second loading phase.

Similarly, the time signals obtained from the ultrasonic measurements in this study can be further analyzed using the discrete Fourier transform. Using Fast Fourier transform (FFT) algorithms, modern computer programs can convert a discrete signal in the time domain to the frequency domain for analysis. Traditional Fourier analysis evaluates the magnitude of the frequency spectrum and the phase between the real and imaginary components of the FFT. While Fourier analysis is a powerful tool, the interpretation of these spectra can be quite difficult due to discretization effects such as aliasing. Similarly, the traditional FFT does not present a way to analyze the frequency content over time. However, more advanced techniques such as the short-time Fourier transform (STFT), wavelet transform (WT), and the wavelet synchrosqueezed transform (WSST) could also be used through special windowing/ filtering operations in the frequency domain to view frequency-time spectra to extract even more information from this data (Jiang 2007; du Tertre 2010).

10.5 Conclusions

In this chapter, the viability of the coda wave interferometry technique was successfully explored in ultrasonically coupled tension-compression tests of a single asphalt mixture. Repeated ultrasonic measurements were collected during fatigue-healing tests using a dedicated pulse-receiver front-end. The work proposed two windowing procedures for the time-domain analysis. The first is a simple statistical approach, and the second is an analytical method derived from the signal-diffusive energy envelope. The dynamic time warping algorithm was applied using these two windowing methods to measure microscopic time shifts in the coda of successive ultrasonic measurements as the asphalt mix was damaged under loading or as it healed during rest periods. From this work, the following conclusions can be drawn:

- The CWI technique, using both window procedures, is sensitive enough to distinguish between loading and unloading in fatigue-healing tests. As theorized, the CWI Euclidean distance is shown to increase under loading due to increased scatterers and decreased during rest periods as the specimen heals. The effect is significantly greater when increasing the strain level from 100 to 125 μm/m as the damage rate is greater at the higher strain level.
- Windowing Method 1 is demonstrated to be lower resolution compared to Windowing Method 2. Due to the greater resolution, Method 2 demonstrates the "curvature"/non-linearity observed during the fatigue due to bias effects; this effect is more noticeable in the CWI measurements at 100 μm/m, presumably due to the lower damage rate.
- Compared to the original DGCB and iVECD methods, normalized a_{CWI} slopes between the first and second loading phases had much greater variability. It was also observed that uninterrupted a_{CWI} values were also significantly lower compared to a_{CWI} values from fatigue-healing tests in Loading Phase 1, which may be attributed to the selection of the data interval for the fitting process.
- Computing the $a_{LP1/LP2}$ ratios demonstrated that the discrepancy between the first and second loading phases was greater in specimens with longer rest periods (Gr3x- and Gr4x-100). Specimens with 8 and 16-hour rest periods had significantly lower Loading Phase 2 a_{CWI} values compared to specimens with shorter rest periods. This discrepancy was observed using both window selection methods and may result from material variability or the test setup itself.

Chapter 11
Conclusions and Recommendations

11.1 Overall Summary

With increases in traffic loading and environmental stresses, asphalt pavements experience greater rates of deterioration. Fatigue cracking, produced by repeated heavy traffic loading at intermediate temperatures, is increasingly seen as the major weakness of modern pavement material design, increasing the economic, environmental and social cost of contemporary asphalt pavements. The use of high-performance self-healing pavement materials has been proposed as a strategy to combat this problem. These materials can potentially maintain higher levels of in-situ performance over the pavement service life, improve safety and reduce the need for costly maintenance/rehabilitation treatments.

As shown in the literature review, researchers first observed asphalt self-healing in the 1960s but had only been studied in a limited capacity. Recently, there has been an overwhelming interest in the study of the ability of asphalt materials to self-heal microcrack damage using a variety of accelerated fatigue and cracking tests. The intrinsic self-healing of asphalt is affected by factors such as rest period duration, rest period temperature, aging, moisture, additives, and asphalt cement chemistry. In literature, researchers have used a variety of testing procedures to evaluate self-healing in asphalt cement (e.g., amplitude sweeps and time sweeps with single or multiple rest periods) and asphalt mixtures (e.g., fatigue tests and cracking tests with rest periods), however, there exists no standardized healing tests. The lack of a standardized method to efficiently and accurately characterize the fatigue-damaged and healing for both asphalt cements and mixtures makes it increasingly challenging to compare the intrinsic healing ability of asphalt itself and the efficacy of new self-healing technologies.

The work presented in this thesis presented a multiscale approach to healing characterization. As a member of RILEM TC CHA-278, the author completed interlaboratory testing for Task Group (TG) 2a and 2b relating to self-healing and TG 3 relating to self-healing characterization analysis and modelling. The primary objective of this work was to then to evaluate existing characterization techniques found in the literature and develop asphalt healing test protocols for both asphalt cements and mixtures. Based on the initial healing studies conducted in Chapter 4, it was evident that current DSR-based fatigue characterization techniques were inaccurate due to measurement artifacts caused by geometry changes/ specimen flow under loading. As a result, the thesis shifted focus to the evaluation

of the linear amplitude (LAS) test and different failure criteria found in the literature. These failure criteria were then supplemented with the complementary parameters: the electric torque inflection point, the peak normal force and the DSR visual analysis FSA. Using a statistical significance test, it was determined that shear stress-strain peak behaviour in the LAS test correlated with the onset of specimen flow, indicating that the peak shear strain amplitude was the most appropriate first-phase terminal strain amplitude for subsequent healing tests. In cooperation with the RILEM CHA-278 TG 2a, a second version of the LASH test protocol was proposed and evaluated. Using the newly derived restoration indices from Chapter 7, a statistical analysis of several healing tests demonstrated that "damage" was only observed in healing tests when the first loading phase end condition was the peak shear stress-strain amplitude (γ_{peak}). Test parameters such as rest period duration and aging level were found to not be statistically significant factors in the analysis of LASH V2 data. The work completed in Chapter 4 to Chapter 7 highlighted the importance of the selection of the first loading phase terminal strain amplitude. The general conclusion of these works was that geometric changes of the DSR sample during loading produce increasingly inaccurate measurements of post-peak data in amplitude sweep tests. Thus, future work should take a greater emphasis on the characterization of pre-peak behaviour.

In the second phase of this work, asphalt mixture fatigue and healing were the primary focus. Beginning in Chapter 8, the author detailed the preparation of CPATT's MTS test frame for subsequent fatigue-healing tests in Chapter 9 and coupled non-invasive tests in Chapter 10. Chapter 9 featured the proposal of a new fatigue model called the Intrinsic-VECD or iVECD linearization model based on the previous works of Baaj (2002) and Underwood et al. (2012). The iVECD model was then extended to healing tests in an attempt to separate "true" fatigue damage from bias effects that may still be present in the AASHTO standard Simplified VECD model. From the iVECD model, the %Heal, %Recovery, %Restoration and Permanent Damage (%PD) parameters were derived for fatigue healing tests conducted at two strain levels (100 and 125 μm/m) and using three rest period durations (4, 8 and 16 hours). The non-invasive ultrasonic acquisition was also coupled to these destructive fatigue tests. Coda wave interferometry (CWI) was then used to analyze the effects of scattering due to damage and healing. Using the two window selection techniques, it was demonstrated that CWI could capture the effect of both loading/unloading and was sensitive enough to clearly distinguish between different strain levels over the same testing period.

11.2 Conclusions

This thesis consists of seven main chapters concerning the evaluation and development of both fatigue and healing characterization. The list below highlights their contents and contributions achieved during this study:

- The SLASH procedure used in Chapter 4 highlighted a major deficiency of amplitude sweep healing tests on the DSR. It was observed that more aged binders exhibit greater restoration, which contradicted the conventional understanding of asphalt self-healing. Upon further investigation using the DSR Visual Analysis, it was determined that a significant change in specimen stiffness was accompanied by a change in the specimen geometry for unaged and short-term aged asphalt cements. This result prompted the comprehensive evaluation of different amplitude sweep failure criteria in Chapter 5 and Chapter 6.
- The work in Chapter 5 demonstrated that strain amplitudes obtained from different failure criteria could be categorized as peak or post stress-strain peak phenomena. In general, aging plays a major role in post-peak failure criteria strain value. As a result of binder aging, the "peak broadening" effect led to an overestimation of fatigue resistance for more aged materials; this observation was consistent with other LAS studies. Notably, at every aging level, the peak shear stress-strain amplitude was observed to be the most conservative failure criterion. Ranking methods such as the P-LAS and ΔG procedure, which rely on the peak shear stress-strain amplitude, could capture the effect of aging from the LAS test.
- The DSR electric torque (M_{el}) inflection point and the peak normal force (F_N) are used in conjunction with the DSR Visual Analysis FSA used in Chapter 6 provides significant insight into the geometry change phenomenon during loading. The statistical analysis demonstrated that failure criteria with strain amplitudes near the peak shear-strain amplitude correlated significantly with the onset of edge fracture/ instability flow. Post-peak failure criteria shared a statistically significant relationship with the peak normal force and the electric torque inflection strain amplitudes.
- When investigating the effects of test temperature in Chapter 6, it was demonstrated that flow-based changes in geometry were still observable even at temperatures below the recommended "intermediate PG temperature minus 4°C" and with a measured stiffness surpassing 12 MPa. Flow phenomena and all associated failure strain amplitudes shifted to higher strain amplitudes with increasing temperature.

- Using the information gained in Chapter 5 and Chapter 6, Version 2 of the LASH protocol was proposed in cooperation with RILEM TC CHA-278 TG 2a. The peak shear stress-strain amplitude (γ_{peak}) was selected as the maximum first loading phase terminal strain amplitude based on the geometric flow phenomena.
- Three healing analysis methods were adapted from the literature (one being VECD-based and the other two crack-length-based) to evaluate LASHV2 testing. As a contribution to RILEM CHA-278 Task Group 3 (Self-Healing Modelling), the P-LASH analysis method was proposed based on the P-LAS method from Zhou et al. (2017). Two additional restoration indices were derived from the P-LAS on the fatigue resistance energy index (FREI) and released fracture energy, J-integral, parameters.
- From all five analysis methods used, "full" restoration was observed when loading to the $0.5\gamma_{peak}$ end condition. When loading to the peak-end condition, only unaged and short-term aged asphalt cements experienced losses due to "damage." It was also demonstrated that, along with an increase in stiffness, an elastomeric modification would delay flow compared to an unmodified binder but does not eliminate this phenomenon.
- "Damage" observed in amplitude sweep healing tests was concluded to be the result of loading to the γ_{peak} end condition. When comparing the electric torque inflection point for continuous amplitude sweep tests and the second loading phase in the LASH V2, the second loading phase had consistently lower M_{el} inflection point strain amplitudes indicating instability flow/ edge fracture has already occurred in specimens previously loading to the peak; this behaviour was not observed for $0.5\gamma_{peak}$ end condition specimens. Thus, large changes in stiffness observed after rest periods could be attributed to geometric changes due to flow and neither could it be attributed to cracking as theorized by Hintz (2012) and or "true" fatigue damage. This finding leads to the conclusion that the results of DSR-based fatigue-healing tests can easily be misleading based on the failure criteria chosen and the selection of the first phase termination strain amplitude. In conclusion, DSR-based fatigue and healing tests appear to be unsuitable for their intended purpose, and more emphasis should be taken to examine relatively low strain (i.e., less than $\gamma_{applied}$ = 10%) asphalt cement behaviour.
- Based upon the S-VECD and "DGCB"-style linearization method, the iVECD was proposed in Chapter 9. Using the DGCB-interval style analysis, the newly proposed iVECD method can successfully distinguish between different cycle intervals and obtain distinct damage rates.

- When compared to the traditional S-VECD power law fatigue life estimation, fatigue life estimates using Interval 2 (150,000 to 300,000 cycles) show good agreement. In contrast, Interval 1 (50,000 to 150,000 cycles) tend to underestimate the fatigue life due to a greater damage rate. Compared to the original DGCB method, iVECD fatigue life estimates are significantly lower.
- By incorporating rest periods (4-, 8-, and 16-hour rest periods), healing/restoration was evaluated using several indices found in the literature. The iVECD method was also extended to derive several key restoration and damage parameters, including the permanent damage (%PD) and %Restoration (%Rest), %Recovery (%Rec) and %Healing (%Heal).
- The results of the fatigue-healing tests demonstrated that the rest period duration was not a significant factor when testing at the lower strain level. As expected, the iVECD indices can capture the increase in permanent damage observed when increasing the strain level; specimens tested at 125 μm/m demonstrated greater permanent damage and, as a result, lower restoration compared to their counterparts tested at 100 μm/m.
- Ultrasonic measurements were coupled with the asphalt mixture fatigue-healing tests and were analyzed using coda wave interferometry (CWI). To facilitate the CWI technique, two time-domain window methods were proposed: (1) a simple, statistical procedure using the MATLAB "findchangepts" function and (2) an adaptive, analytical approach using the diffusive envelope of the time signal and the DTW rate of change parameter. CWI measurements using both windowing selection methods were demonstrated to be capable of distinguishing between different strain levels, loading and rest periods. Notably, Method 2 CWI was able to maintain lower signal-signal variability and capture the non-linearity/ curvature observed in traditional fatigue tests. Thus, the CWI technique appears to be viable for the fatigue-healing characterization of asphalt mixtures.

11.3 Contributions

Contributions to the study of asphalt cement fatigue and healing characterization include:

3. The comprehensive evaluation of the linear amplitude sweep (LAS) test parameters associated fatigue life estimations and failure criteria. From Chapter 5, the evaluation of LAS failure criteria from the literature demonstrated that the shear stress-strain amplitude was the most conservative failure criterion. Failure criteria related to post-peak behaviour can be rejected.
4. Creation of a workflow and analysis procedure (i.e., the DSR Visual Analysis MATLAB app) to evaluate the instability flow phenomenon occurring during loading using the DSR (Chapter 4 and

Chapter 6). This led to the formal derivation of the flow strain amplitude (FSA) parameter. FSA values were then correlated with the peak normal force and electric torque inflection point to demonstrate that DSR measurements become increasingly inaccurate as the strain amplitude increases past the peak shear stress-strain amplitude.

5. From the initial work in Chapter 4 and concluding Chapter 7, this work contributed to the development/modification of two healing test protocols: S-LASH and LASH V2 (in cooperation with RILEM CHA-278 TG 2a). From the LASH V2 protocol, the work of Zhou et al. (2017) was adapted to develop the P-LASH analysis (using both the FREI and J-integral) methods.
6. Analysis of several healing/restoration indices (e.g., VECD-based, crack-length-based, and P-LASH) highlighted that decreases in stiffness between the first and second loading phases in DSR healing tests is a by-product of loading to the peak shear stress-strain amplitude.

Contributions to the study of asphalt mixture fatigue and healing characterization include:

1. Creation of a framework and workflow for the preparation of an asphalt test frame with coupled non-destructive/non-invasive ultrasonic acquisition capabilities (Chapter 8). The workflow details the use of a unique ultrasonic frontend that could be employed during destructive fatigue and healing tests.
2. Development of the Intrinsic-VECD or iVECD model from the works of Baaj (2002) and Underwood et al. (2012) for asphalt mixtures. The iVECD model was then extended to healing tests, and the adoption of the permanent damage (%PD) and %Restoration (%Rest), %Recovery (%Rec) and %Healing (%Heal) parameters were used.
3. Evaluation of the coda wave interferometry (CWI) technique for fatigue and healing characterization of asphalt mixtures; based on the results of the coupled non-invasive measurements, this method was validated for asphalt mixture tests at 10°C. Two time-domain windowing selection methods were also successfully proposed for this analysis technique including the simplistic statistical approach and the diffusive envelope/ DTW rate of change method. Both windowing methods were able to distinguish between loading and rest periods as well as different strain levels.

11.4 Recommendations and Future Research

As stated in Chapter 6, the accurate measurement of complex materials using a rotational rheometer can be challenging due to the misunderstanding of potential artifacts occurring during loading. In

amplitude sweeps conducted by Qiu et al. (2020), a 10% decrease in the modulus was exhibited at 3.7, 3.0 and 2.2% strain amplitude for unaged, RTFO and PAV-aged binders, respectively. Comparable strain amplitudes were obtained in the determination of the time sweep strain amplitude in the original PoliTO procedure proposed in the early works of RILEM CHA-278 Task Group 2a interlaboratory testing. Based on the Visual Analysis in Chapter 6 and subsequent healing tests performed in Chapter 7, it is evident that post-peak amplitude sweep data is inaccurate due to changes in specimen geometry. Healing tests also demonstrated that some amount of flow occurs even when terminating the first loading phase at the shear stress peak amplitude. Thus, data analysis should be emphasized at lower strains (i.e., from 0.5 $\gamma_{peak\ to}\gamma_{peak}$). In this strain amplitude range, internally induced flow is considerable, and a non-homogenous flow state is achieved in the DSR specimen. Thus, the simplistic assumptions by the DSR used to generate shear moduli and phase angle values may already be violated in this regime. More advanced rheological characterization methods, such as the use of the LAOS test and Fourier Transform Rheology, may present a viable solution for "larger" strain, non-linear analysis of asphalt cement.

Since the DSR was introduced in the 1990s, parallel plate spindle geometry has become dominant in the asphalt industry and research. However, the DSR Visual Analysis conducted in Chapter 4 and Chapter 6 demonstrated that the same PAV-aged material could exhibit instability flow on one DSR and not another. Although not explored in this study, this is likely the result of the parallel plate spindle design itself. In Chapter 4, a low-inertia spindle was used, while a high-inertia spindle was used in the works related to Chapter 5 to Chapter 7. From a practical point of view then, it would be beneficial to evaluate different parallel plate spindles produced by different manufacturers to determine the effect of spindle inertia and compliance on artifacts in DSR tests. However, from this study and others, the parallel plate geometry may not be the most appropriate for advanced rheological testing of asphalt cement. It may be beneficial for future studies to explore different rheometer geometries such as cone and plate, annular rheometer, or even new experimental geometries such as the ring-type / PHP tests conducted by (Apostolidis et al. 2018). The characterization of fine aggregate matrix (FAM) or sand asphalt mortars (SAM) specimens using a torsional cylinder configuration may also be appropriate as these configurations are not subject to the same artifacts as the generic parallel plate geometry (Martono et al. 2007; Rezende et al. 2021).

Similarly, future asphalt cement fatigue and healing standard tests should discuss the use of Direct Strain Oscillation (DSO) modes. DSO was first implemented in the early 2000s to improve the position control of the rheometer spindle. When monitoring the real-time strain amplitude output of early rheometers, it was observed that most rheometers could not satisfactorily produce "true" sine loading paths when used in oscillatory shear experiments. DSO modes were then developed to allow the rheometer to make minute adjustments to the applied torque, thus minimizing the actual strain with the desired strain. In a practical sense, using this mode in modern DSRs yields an ideally linear amplitude sweep regardless of the geometry of the sample during the LAS test itself. Without the use of the direct strain oscillation mode, the amplitude sweep is demonstrated to be bi-linear, indicating before and after flow regions of the curve (Figure 11-1). As the DSR does not measure changes in specimen geometry during loading, the measurement accuracy of the DSR is severely diminished to a point where any data generated is dominated by the inertial effects of the measurement system itself. For this reason, the author recommends an evaluation of both time and amplitude sweep tests with and without the use of DSO.

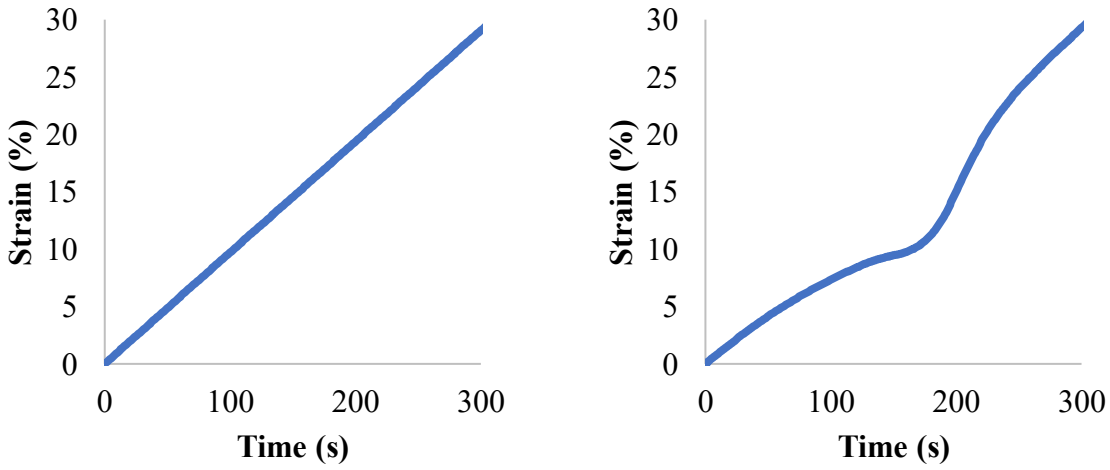

Figure 11-1 LAS test with DSO turned on (left) and DSO turned off (right).

Relating to asphalt mixture fatigue tests, a major limitation of this study was the lack of a variety of materials and testing parameters. The iVECD model proposed in Chapter 9 demonstrated that there is the DGCB interval linearization technique is relatively reproducible in the single asphalt mix tested at one loading frequency and temperature. Future studies should be conducted to determine if the iVECD model and test whether the assumptions made herein would be applicable at different frequencies and

temperatures, but could also be extended to explore binder content, air void content, compaction method, different binder modifiers, etc. As a consequence, the healing indices proposed in the same chapter should also be scrutinized further.

Finally, concerning the use of ultrasonic evaluation of asphalt materials, the CWI method was sensitive enough to successfully capture loading/ unloading as well as different strain levels. Due to the highly attenuative nature of asphalt and the temperature sensitivity of coda, any future work should first examine the effect of temperature (not just on a global/ macroscopic level, but also internally due to the heating/cooling effects generated during loading/ rest periods). As discussed in Chapter 10 Section 10.4.2, time signals obtained from these ultrasonic measurements could be further analyzed in the frequency domain using the Fast Fourier transform and other more powerful analytical tools such as the short-time Fourier transform, wavelet transform, and the wavelet synchro-squeezed transform to extract supplementary information about wave propagation of damaged and healed asphalt mixtures.

References

Abdewi, E. F. 2017. “Mechanical Properties of Reinforcing Steel Rods Produced by Zliten Steel Factory.” *Reference Module in Materials Science and Materials Engineering*. Elsevier. https://doi.org/10.1016/B978-0-12-803581-8.10362-5.

Abed, A., N. Thom, D. lo Presti, and G. Airey. 2020a. “Thermo-rheological analysis of WMA-additive modified binders.” *Materials and Structures/Materiaux et Constructions*, 53 (3): 1–13. Springer Netherlands. https://doi.org/10.1617/s11527-020-01480-1.

Abed, A., N. Thom, D. lo Presti, and G. Airey. 2020b. “Thermo-rheological analysis of WMA-additive modified binders.” *Materials and Structures/Materiaux et Constructions*, 53 (3): 1–13. Springer. https://doi.org/10.1617/S11527-020-01480-1/FIGURES/16.

Abo-Qudais, S., and A. Suleiman. 2005. “Monitoring fatigue damage and crack healing by ultrasound wave velocity.” *Nondestructive Testing and Evaluation*, 20 (2): 125–145. https://doi.org/10.1080/10589750500206774.

Alpizar-Reyes, E., J. L. Concha, F. J. Martín-Martínez, and J. Norambuena-Contreras. 2022. “Biobased Spore Microcapsules for Asphalt Self-Healing.” *ACS Appl Mater Interfaces*, 14 (27): 31296–31311. https://doi.org/10.1021/acsami.2c07301.

Amin, G. M., and A. Esmail. 2017. “Application of nano silica to improve self-healing of asphalt mixes.” *J. Cent. South Univ*, 24: 1019–1026. https://doi.org/10.1007/s11771-017-3504-y.

Anderson, D. A., Y. M. le Hir, M. O. Marasteanu, J. P. Planche, D. Martin, and G. Gauthier. 2001. “Evaluation of fatigue criteria for asphalt binders.” *Transp Res Rec*, 48–55.

Apostolidis, P., C. Kasbergen, A. Bhasin, A. Scarpas, and S. Erkens. 2018. “Study of asphalt binder fatigue with a new dynamic shear rheometer geometry.” *Transp Res Rec*, 2672 (28): 290–300. https://doi.org/10.1177/0361198118781378.

Arabani, M., P. Tavassoti-Kheiry, and B. Ferdosi. 2009. “Evaluation of the Effect of HMA Mixt Parameters on Ultrasonic Pulse Wave Velocities Laboratory.” https://doi.org/10.1080/14680629.2009.9690189.

Asadi, B., and N. Tabatabaee. 2020. “Alteration of initial and residual healing potential of asphalt binders due to aging, rejuvenation, and polymer modification.” *Road Materials and Pavement Design*, 0 (0): 1–21. Taylor & Francis. https://doi.org/10.1080/14680629.2020.1826345.

Ashayer Soltani, M. A. 1998. “Comportement en fatigue des enrobés bitumineux.” INSA de Lyon.

Aurilio, M. 2020. “Evaluation of the Effect of a Self-Healing Elastomer on the Self-Healing Properties of Asphalt Cement.” MASc Thesis. University of Waterloo.

Aurilio, M., A. Qabur, P. Mikhailenko, and H. Baaj. 2018. “Comparing the fatigue performance of HMA samples with PMA to their multiple stress creep recovery and double notched tension test properties.” *Proceedings, Canadian Technical Asphalt Association*, 63: 385–410.

Aurilio, M., P. Tavassoti, M. Elwardany, and H. Baaj. 2020a. “Comparing the Ability of Different Tests and Rheological Indices to Evaluate the Cracking Resistance of Polymer Modified Asphalt Binders.” *65th Annual Conference of the Canadian Technical Asphalt Association (CTAA)*, 5 (November).

Aurilio, R., M. Aurilio, and H. Baaj. 2020b. “High-Performance Pavements : A Focus on Self-healing Asphalt Technologies.” *65th Annual Conference of the Canadian Technical Asphalt Association (CTAA)*.

Aurilio, R., M. Aurilio, and H. Baaj. 2020c. “The Effect of a Chemical Warm Mix Additive on the Self-Healing Capability of Bitumen.” *RILEM International Symposium on Bituminous Materials*. Lyon.

Aurilio, R. M., M. Aurilio, and H. Baaj. 2021. “The effect of a chemical warm mix additive on the self-healing capability of bitumen.” *J Test Eval*, 50 (2). https://doi.org/10.1520/JTE20210207.

Aurilio, V., and D. Newcomb. 2018. “The Merits of Balanced Mix Design.” *Canadian Technical Asphalt Association*.

Ayar, P., F. Moreno-Navarro, and M. C. Rubio-Gámez. 2016. “The healing capability of asphalt pavements: a state of the art review.” *J Clean Prod*, 113: 28–40. https://doi.org/10.1016/j.jclepro.2015.12.034.

Azimi Alamdary, Y. 2019. “Investigation of Different Factors Affecting Asphalt Cement Ageing and Durability.” University of Waterloo.

Azimi Alamdary, Y., and H. Baaj. 2020. “Time-Temperature Superposition of Asphalt Materials and Temperature Sensitivity of Rheological Parameters (TSRP).” *Canadian Journal of Civil Engineering*.

Baaj, H. 2002. “Comportement à la fatigue des matériaux granulaires traités aux liants hydrocarbonés.”

Baaj, H. 2003. “Fatigue of mixes: an intrinsic damage approach.” *Sixth International RILEM Symposium on Performance Testing and Evaluation of Bituminous Materials*.

Baaj, H., H. Di Benedetto, and P. Chaverot. 2003. “Fatigue of Mixes: An Intrinsic Damage Approach.” *6th RILEM Symposium PTEBM’03*.

Baaj, H., H. Di Benedetto, and P. Chaverot. 2004. “Different Experimental Approaches and Criteria for Fatigue of Asphalt Mixes.” *49th Annual Canadian Technical Asphalt Association Conference*, 261–286. Montreal.

Baaj, H., H. Di Benedetto, and P. Chaverot. 2005. “Effect of binder characteristics on fatigue of asphalt pavement using an intrinsic damage approach.” *Road Materials and Pavement Design*, 6 (2): 147–174. https://doi.org/10.1080/14680629.2005.9690003.

Baaj, H., P. Mikhailenko, H. Almutairi, and H. Di Benedetto. 2018. “Recovery of asphalt mixture stiffness during fatigue loading rest periods.” *Constr Build Mater*, 158: 591–600. Elsevier. https://doi.org/10.1016/j.conbuildmat.2017.10.016.

Baglieri, O., H. Baaj, F. Canestrari, C. Wang, L. Tsantilis, and F. Cardone. 2020. “Testing methods to assess healing potential of bituminous binders.” *RILEM International Symposium on Bituminous Materials*, 6.

Baglieri, O., L. Tsantilis, and E. Santagata. 2018. “Evaluation of healing potential of bituminous binders using a viscoelastic continuum damage approach.” *Constr Build Mater*, 184: 344–350. Elsevier Ltd. https://doi.org/10.1016/j.conbuildmat.2018.05.228.

Bahia, H., D. I. Hanson, M. Zeng, H. Zhai, M. A. Khatri, and R. M. Anderson. 2001. *Characterization of Modified Asphalt Binders in Superpave Mix Design*.

Barman, M. 2019. *Cost/Benefit Analysis of the Effectiveness of Crack Sealing Techniques*.

Bazant, Z. P., and P. C. Prat. 1988. “Effect of Temperature and Humidity on Fracture Energy of Concrete.” *Journal of American Concrete Institute*, 85 (4).

Bekas, D. G., K. Tsirka, D. Baltzis, and A. S. Paipetis. 2016. “Self-healing materials: A review of advances in materials, evaluation, characterization and monitoring techniques.” *Compos B Eng*, 87: 92–119. Elsevier Ltd. https://doi.org/10.1016/j.compositesb.2015.09.057.

Di Benedetto, H., M. A. Ashayer Soltani, and P. Chaverot. 1996. “Fatigue damage for bituminous mixtures: a pertinent approach.” *Association of Asphalt Paving Technologists (AAPT)*. Baltimore.

Di Benedetto, H., M. A. Ashayer Soltani, and P. Chaverot. 1997. “Fatigue damage for bituminous mixtures.” *5th Annual RILEM Symposium: Mechanical tests for bituminous mixes*, 263–270. Lyon.

Di Benedetto, H., C. de La Roche, H. Baaj, A. Pronk, and R. Lundström. 2004. “Fatigue of bituminous mixtures.” *Mater Struct*, 37 (3): 202–216. RILEM Publications. https://doi.org/10.1007/bf02481620.

Di Benedetto, H., Q. T. Nguyen, and C. Sauzéat. 2011a. “Nonlinearity, Heating, Fatigue and Thixotropy during Cyclic Loading of Asphalt Mixtures.” https://doi.org/10.3166/RMPD.12.129-158.

Di Benedetto, H., C. Sauzeat, K. Bilodeau, M. Buannic, S. Mangiafico, Q. T. Nguyen, S. Pouget, N. Tapsoba, and J. van Rompu. 2011b. “General overview of the time-temperature superposition principle validity for materials containing bituminous binder.” *International Journal of Roads and Airports*, 1 (1). https://doi.org/10.5568/ijra.2011-01-03.3552.

Di Benedetto, H., C. Sauzéat, and J. Sohm. 2009. “Stiffness of bituminous mixtures using ultrasonic wave propagation.” *Road Materials and Pavement Design*, 10 (4): 789–814. https://doi.org/10.3166/rmpd.10.789-814.

Van den bergh, W. 2011. “The Effect of Ageing on the Fatigue and Healing Properties of Bituminous Mortars.”

Bhasin, A., D. N. Little, R. Bommavaram, and K. Vasconcelos. 2008. “A framework to quantify the effect of healing in bituminous materials using material properties.” *Road Materials and Pavement Design*, 9 (SPECIAL ISSUE): 219–242. https://doi.org/10.3166/RMPD.9HS.219-242.

Boussabnia, M. M., S. Lamothe, H. Di Benedetto, M. Proteau, and B. Proteau. 2019. “Comparison of Fatigue Law Parameters obtained from Two-Point Bending and Tension-Compression Tests.” *Canadian Technical Asphalt Association*.

Boussabnia, M. M., D. Perraton, H. Di Benedetto, S. Lamothe, and M. Proteau. 2023. “Validation of time temperature superposition principle for high modulus asphalt concrete in the linear viscoelastic and fatigue domains.” *Fatigue Fract Eng Mater Struct*, 46 (1): 80–95. John Wiley & Sons, Ltd. https://doi.org/10.1111/FFE.13849.

Boz, I., P. Tavassoti-Kheiry, and M. Solaimanian. 2017. “The advantages of using impact resonance test in dynamic modulus master curve construction through the abbreviated test protocol.” *Materials and Structures/Materiaux et Constructions*, 50 (3): 1–12. Kluwer Academic Publishers. https://doi.org/10.1617/S11527-017-1045-3/METRICS.

Canadian Technical Asphalt Association. 2018. *Hot Mix Asphalt Textbook*.

Canestrari, F., A. Virgili, A. Graziani, and A. Stimilli. 2015. “Modeling and assessment of self-healing and thixotropy properties for modified binders.” *Int J Fatigue*, 70: 351–360. Elsevier Ltd. https://doi.org/10.1016/j.ijfatigue.2014.08.004.

Cao, W., and C. Wang. 2018. “A new comprehensive analysis framework for fatigue characterization of asphalt binder using the Linear Amplitude Sweep test.” *Constr Build Mater*, 171: 1–12. Elsevier. https://doi.org/10.1016/J.CONBUILDMAT.2018.03.125.

Castro, M., and J. A. Sánchez. 2006. “Fatigue and healing of asphalt mixtures: Discriminate analysis of fatigue curves.” *J Transp Eng*, 132 (2): 168–174. https://doi.org/10.1061/(ASCE)0733-947X(2006)132:2(168).

Chen, B., M. Abdallah, P. Campistron, E. Moulin, D. Callens, S. O. Khelissa, P. Debreyne, N.-E. Chihib, and G. Delaplace. 2021. “Detection of biofilm formation by ultrasonic Coda Wave Interferometry.” *J Food Eng*, 290: 110219. https://doi.org/10.1016/j.jfoodeng.2020.110219.

Chen, H., and H. U. Bahia. 2021. “Modelling effects of aging on asphalt binder fatigue using complex modulus and the LAS test.” *Int J Fatigue*, 146. Elsevier Ltd. https://doi.org/10.1016/j.ijfatigue.2021.106150.

Chen, H., and H. U. Bahia. 2022. “Proposed asphalt binder fatigue criteria for various traffic conditions using the LAS or the G-R parameters.” *Mater Struct*, 55 (1). https://doi.org/10.1617/s11527-022-01883-2.

Chen, Y., and C. Wang. 2020. “Oxidative Aging Effects on Damage-Healing Performance of Unmodified and Polymer Modified Asphalt Binders.” *Proceedings of the 5th International*

Symposium on Asphalt Pavements & Environment (APE), M. Pasetto, M. N. Partl, and G. Tebaldi, eds., 395–403. Cham: Springer International Publishing.

Concha, J. L., and J. Norambuena-Contreras. 2020. "Thermophysical properties and heating performance of self-healing asphalt mixture with fibres and its application as a solar collector." *Appl Therm Eng*, 178: 115632. https://doi.org/10.1016/j.applthermaleng.2020.115632.

Coussot, P. 2014. *Soft and Biological Matter Rheophysics Matter in All Its States*.

Cuciniello, G., P. Leandri, M. Losa, and G. Airey. 2020. "Effects of ageing on the damage tolerance of polymer modified bitumens investigated through the LAS test and fluorescence microscopy." *https://doi.org/10.1080/10298436.2020.1788031*, 1–12. Taylor & Francis. https://doi.org/10.1080/10298436.2020.1788031.

Daniel, J. S., and Y. R. Kim. 2001. "Laboratory Evaluation of Fatigue Damage and Healing of Asphalt Mixtures." *Journal of Materials in Civil Engineering*, 13 (6): 434–440. American Society of Civil Engineers. https://doi.org/10.1061/(ASCE)0899-1561(2001)13:6(434).

Daniel, J. S., and Y. R. Kim. 2002. "Development of Simplified Fatigue Test And Analysis Procedure Using A Viscoelastic Continuum Damage Model." *Journal of the Association of Asphalt Paving Technologists*, 71.

Wang, Y., S. Underwood, and R. Kim. 2020. "Development of a fatigue index parameter, S app , for asphalt mixes using viscoelastic continuum damage theory." *International Journal of Pavement Engineering*, 23 (2): 438–452. https://doi.org/10.1080/10298436.2020.1751844.

De, D. K., and A. N. Gent. 1998. "Crack Growth in Twisted Rubber Disks. Part II: Experimental Results." *Rubber Chemistry and Technology*, 71 (1): 84–94. Allen Press. https://doi.org/10.5254/1.3538475.

Deroo, F., J.-Y. Kim, J. Qu, K. Sabra, and L. J. Jacobs. 2010. "Detection of damage in concrete using diffuse ultrasound." *J Acoust Soc Am*, 127 (6): 3315–3318. https://doi.org/10.1121/1.3409480.

Deshpande, A. P. 2010. *Oscillatory shear rheology for probing nonlinear viscoelasticity of complex fluids: Large amplitude oscillatory shear*. *Rheology of Complex Fluids*.

Epple, N. 2018. "From Seismology to Bridge Monitoring: Coda Wave Interferometry." Delft University of Technology.

Ewoldt, R. H., M. T. Johnston, and L. M. Caretta. 2015. *Experimental Challenges of Shear Rheology: How to Avoid Bad Data*.

Fakhri, M., B. B. Bahmai, S. Javadi, and M. Sharafi. 2020. "An evaluation of the mechanical and self-healing properties of warm mix asphalt containing scrap metal additives." *J Clean Prod*, 253: 119963. https://doi.org/10.1016/j.jclepro.2020.119963.

Federation of Canadian Municipalities. 2020. *The 2019 Canada Infrastructure Report Card*.

Ferrotti, G., H. Baaj, J. Besamusca, M. Bocci, A. Cannone Falchetto, J. Grenfell, B. Hofko, L. Porot, L. D. Poulikakos, and Z. You. 2019. "Comparison of Short Term Laboratory Ageing on Virgin and Recovered Binder from HMA/WMA Mixtures." *RILEM 252-CMB Symposium*, L. D. Poulikakos, A. Cannone Falchetto, M. P. Wistuba, B. Hofko, L. Porot, and H. Di Benedetto, eds., 21–26. Cham: Springer International Publishing.

Franck, A. 2005. *Instrument Inertia Correction during Dynamic Mechanical Testing*. *TA Instruments*.

Garcia, A., J. Jelfs, and C. J. Austin. 2015. "Internal asphalt mixture rejuvenation using capsules." *Constr Build Mater*, 101: 309–316. Elsevier Ltd. https://doi.org/10.1016/j.conbuildmat.2015.10.062.

Garcia Cucalon, L., F. Kaseer, E. Arámbula-Mercado, A. Epps Martin, N. Morian, S. Pournoman, and E. Hajj. 2019. "The crossover temperature: significance and application towards engineering balanced recycled binder blends." *Road Materials and Pavement Design*, 20 (6): 1391–1412. Taylor and Francis Ltd. https://doi.org/10.1080/14680629.2018.1447504.

Gaudenzi, E., F. Cardone, X. Lu, and F. Canestrari. 2020. "Analysis of fatigue and healing properties of conventional bitumen and bio-binder for road pavements." *Materials*. https://doi.org/10.3390/ma13020420.

Gent, A. N., and O. H. Yeoh. 2003. "Crack Growth in Twisted Rubber Disks. Part 3. Effects of Crack Depth and Location." *Rubber Chemistry and Technology*, 76 (5): 1276–1289. Allen Press. https://doi.org/10.5254/1.3547802.

Gonzalez-Torre, I., and J. Norambuena-Contreras. 2020. "Recent advances on self-healing of bituminous materials by the action of encapsulated rejuvenators." *Constr Build Mater*, 258: 119568. Elsevier Ltd. https://doi.org/10.1016/j.conbuildmat.2020.119568.

Grabowski, B., and C. C. Tasan. 2015. “Self-healing metals.” *Self-healing Materials*, 387–407.

Grosso, M., and P. Luca. 2011. “Fourier Transform Rheology: A New Tool to Characterize Material Properties.” *Fourier Transforms - New Analytical Approaches and FTIR Strategies*, (April). https://doi.org/10.5772/15725.

Hadziioannou, C., E. Larose, O. Coutant, P. Roux, and M. Campillo. 2009. “Stability of monitoring weak changes in multiply scattering media with ambient noise correlation: Laboratory experiments.” *J Acoust Soc Am*, 125 (6): 3688–3695. https://doi.org/10.1121/1.3125345.

Hajj, R., and A. Bhasin. 2017. “The search for a measure of fatigue cracking in asphalt binders – a review of different approaches.” *https://doi.org/10.1080/10298436.2017.1279490*, 19 (3): 205–219. Taylor & Francis. https://doi.org/10.1080/10298436.2017.1279490.

Hale, D. 2013. “Dynamic warping of seismic images.” *Geophysics*, 78 (2): S105–S115. https://doi.org/10.1190/geo2012-0327.1.

Hasheminejad, N., C. Vuye, W. Van den bergh, J. Dirckx, and S. Vanlanduit. 2018. “A Comparative Study of Laser Doppler Vibrometers for Vibration Measurements on Pavement Materials.” *Infrastructures (Basel)*, 3 (4): 47. MDPI Multidisciplinary Digital Publishing Institute. https://doi.org/10.3390/infrastructures3040047.

He, Y., L. Song, K. Xue, S. Liu, H. Li, W. Yang, and J. Huang. 2022. “Ultrasonic Coda Wave Experiment and Simulation of Concrete Damage Process under Uniaxial Compression.” *Buildings*, 12 (5): 514. https://doi.org/10.3390/buildings12050514.

Hemingway, E. J., and S. M. Fielding. 2019. “Edge fracture of entangled polymeric fluids: onset criterion and possible mitigation strategy.” 11–15.

Hintz, C. 2012. “Understanding Mechanisms Leading to Asphalt Binder Fatigue.” University of Wisconsin-Madison.

Hintz, C., and H. Bahia. 2013. “Understanding mechanisms leading to asphalt binder fatigue in the dynamic shear rheometer.” *Road Materials and Pavement Design*, 14: 231–251. https://doi.org/10.1080/14680629.2013.818818.

Hintz, C., R. Velasquez, Z. Li, H. U. Bahia, R. Velasquex, Z. Li, H. U. Bahia, R. Velasquez, Z. Li, H. U. Bahia, R. Velasquex, Z. Li, and H. U. Bahia. 2011. "Effect of Oxidative Aging on Binder Fatigue Performance." *Journal of the Association of Asphalt Paving Technologists*, 80: 527–547.

Hofko, B., and R. Blab. 2014. *Performance-based hot mix asphalt and flexible pavement design-the European Perspective*.

Hou, T. 2009. "Fatigue Performance Prediction of North Carolina Mixtures Using Simplified Viscoelastic Continuum Damage Model." North Carolina State University .

Houel, A., and L. Arnaud. 2009. "Damage characterization of asphalt in laboratory by ultrasonic wave propagation." pp 823-828.

Huang, W., Q. Lv, and F. Xiao. 2016. "Investigation of using binder bond strength test to evaluate adhesion and self-healing properties of modified asphalt binders." *Constr Build Mater*, 113: 49–56. Elsevier. https://doi.org/10.1016/J.CONBUILDMAT.2016.03.047.

Inozemtcev, S., and E. Korolev. 2018. "Technological Features of Production Calcium-Alginate Microcapsules for Self-Healing Asphalt." *MATEC Web of Conferences*, 01008. https://doi.org/10.1051/matecconf/201825101008.

Jahanbakhsh, H., M. M. Karimi, B. Jahangiri, and F. M. Nejad. 2018. "Induction heating and healing of carbon black modified asphalt concrete under microwave radiation." *Constr Build Mater*, 174: 656–666. Elsevier Ltd. https://doi.org/10.1016/j.conbuildmat.2018.04.002.

Jiang, Z. 2007. "Innovative Non-Destructive Testing (NDT) For Condition Assessment of Longitudinal Joints in Asphalt Pavements." University of Waterloo.

Johnson, C. M. 2010. "Estimating Asphalt Binder Fatigue Resistance Using an Accelerated Test Method." University of Wisconsin-Madison.

Khan, N. I., S. Halder, S. B. Gunjan, and T. Prasad. 2018. "A review on Diels-Alder based self-healing polymer composites." *IOP Conf Ser Mater Sci Eng*, 377 (1). https://doi.org/10.1088/1757-899X/377/1/012007.

Khavandi Khiavi, A., and M. Asadi. 2022. "Effect of specific heat capacity of aggregates and nano-graphite on self-healing of hot mix asphalt under microwave radiation." *Constr Build Mater*, 328: 127091. https://doi.org/10.1016/j.conbuildmat.2022.127091.

Khavandi Khiavi, A., and R. Rasouli. 2018. “Laboratory evaluation of loading frequency effects on HMA self-healing.” *Constr Build Mater*, 162: 1–8. https://doi.org/10.1016/j.conbuildmat.2017.11.169.

Kie Badroodi, S., M. Reza Keymanesh, and G. Shafabakhsh. 2020. “Experimental investigation of the fatigue phenomenon in nano silica-modified warm mix asphalt containing recycled asphalt considering self-healing behavior.” *Constr Build Mater*, 246: 117558. https://doi.org/10.1016/j.conbuildmat.2019.117558.

Killick, R., P. Fearnhead, and I. A. Eckley. 2012. “Optimal Detection of Changepoints With a Linear Computational Cost.” *J Am Stat Assoc*, 107 (500): 1590–1598. https://doi.org/10.1080/01621459.2012.737745.

Kim, Y. R. 1999. “An analysis of the mechanism of microdamage healing based on the application of micromechanics first principles of fracture and healing.” *Proceedings of the Association of Asphalt Paving Technologists*, 68: 501–542.

Kim, Y. R., M. N. Guddati, Y.-T. Choi, D. Kim, D. Wang, B. Keshavarzi, M. Ashouri, A. Ghanbari, A. D. Wargo, and S. B. Underwood. 2022. *Hot-Mix Asphalt Performance-Related Specification Based on Viscoelastoplastic Continuum Damage (VEPCD) Models*.

Kim, Y. R., H.-J. Lee, and D. N. Little. 1997. “Fatigue Characterization of Asphalt Concrete Using Viscoelasticity and Continuum Damage Theory.” *Journal of the Association of Asphalt Paving Technologists*, 66.

Kim, Y. R., D. N. Little, and F. C. Benson. 1990. “Chemical and mechanical evaluation of healing mechanism of asphalt concrete.” *Journal of Associated Asphalt Paving Technologists*, 59: 240–275.

Kuchiishi, A. K., K. “Caleb” Lee, and B. S. Underwood. 2023. “Simplified protocol for fatigue cracking characterization of asphalt mixtures using the direct tension cyclic fatigue test.” *Constr Build Mater*, 363. Elsevier. https://doi.org/10.1016/J.CONBUILDMAT.2022.129828.

Kutay, M. E., and M. Lanotte. 2017. “Viscoelastic continuum damage (VECD) models for cracking problems in asphalt mixtures.” *https://doi.org/10.1080/10298436.2017.1279492*, 19 (3): 231–242. Taylor & Francis. https://doi.org/10.1080/10298436.2017.1279492.

Kutay, M. E., and M. Lanotte. 2018. “Viscoelastic continuum damage (VECD) models for cracking problems in asphalt mixtures.” *International Journal of Pavement Engineering*, 19 (3): 231–242. Taylor & Francis. https://doi.org/10.1080/10298436.2017.1279492.

Kutay, M., N. Gibson, and J. Youtcheff. 2008. “Conventional and Viscoelastic Continuum Damage (VECD)-Based Fatigue Analysis of Polymer Modified Asphalt Pavements (With Discussion).”

Larcher, N., M. Takarli, N. Angellier, C. Petit, and H. Sebbah. 2015. “Towards a viscoelastic mechanical characterization of asphalt materials by ultrasonic measurements.” *Materials and Structures/Materiaux et Constructions*, 48 (5): 1377–1388. https://doi.org/10.1617/s11527-013-0240-0.

Läuger, J., and H. Stettin. 2016. “Effects of instrument and fluid inertia in oscillatory shear in rotational rheometers.” *J Rheol (N Y N Y)*, 60 (3): 393–406. https://doi.org/10.1122/1.4944512.

Läuger, J., K. Wollny, and S. Huck. 2002. “Direct Strain Oscillation: A new oscillatory method enabling measurements at very small shear stresses and strains.” *Rheol Acta*, 41 (4): 356–361. https://doi.org/10.1007/s00397-002-0231-5.

Lavielle, M. 2004. *Using penalized contrasts for the change-point problem*.

Leegwater, G. A., A. Scarpas, and S. M. J. G. Erkens. 2018. “The influence of boundary conditions on the healing of bitumen.” *Road Materials and Pavement Design*, 19 (3): 571–580. Taylor and Francis Ltd. https://doi.org/10.1080/14680629.2018.1418720.

Leegwater, G., A. Tabokovic, O. Baglieri, F. Hammoum, and H. Baaj. 2020. “Terms and definitions on crack-healing and restoration of mechanical properties in bituminous materials.” *RILEM International Symposium on Bituminous Materials*, 1–6.

Legland, J.-B., B. Hilloulin, O. Abraham, A. Loukili, F. Grondin, O. Durand, and V. Tournat. 2015. “Monitoring of the Healing in Cementitious Materials Using Nonlinear Coda Wave Modulation.” Berlin, Germany.

Lesueur, D. 2009. “The colloidal structure of bitumen: Consequences on the rheology and on the mechanisms of bitumen modification.” *Adv Colloid Interface Sci*, 145 (1–2): 42–82. https://doi.org/10.1016/j.cis.2008.08.011.

Li, L., Y. Gao, and Y. Zhang. 2020. “Crack length based healing characterisation of bitumen at different levels of cracking damage.” *J Clean Prod*, 258: 120709. Elsevier Ltd. https://doi.org/10.1016/j.jclepro.2020.120709.

Li, N., A. A. A. Molenaar, A. C. Pronk, M. F. C. van de Ven, and S. Wu. 2015. “Application of the partial healing model on laboratory fatigue results of asphalt mixture.” *Constr Build Mater*, 95: 842–850. Elsevier B.V. https://doi.org/10.1016/J.CONBUILDMAT.2015.07.127.

Liao, H. 2023. “Optimizing the Performance of Asphalt Mixes with High Reclaimed Asphalt Pavement Content Using Rejuvenators.” Ph.D. University of Waterloo.

Little, D. N., R. L. Lytton, D. Williams, and Y. R. Kim. 1998. “An Analysis of the Mechanism of Microdamage Healing Based on the Applciation of Micromechanics First Principles of Fracture and Healing.” *Association of Asphalt Paving Technologies*, 2–41.

Liu, Q., E. Schlangen, M. F. C. van de Ven, G. van Bochove, and J. van Montfort. 2012. “Evaluation of the induction healing effect of porous asphalt concrete through four point bending fatigue test.” *Constr Build Mater*, 29 (1): 403–409. Elsevier B.V. https://doi.org/10.1016/j.conbuildmat.2011.10.058.

Liu, S., Z. B. Bundur, J. Zhu, and R. D. Ferron. 2016a. “Evaluation of self-healing of internal cracks in biomimetic mortar using coda wave interferometry.” *Cem Concr Res*, 83: 70–78. https://doi.org/10.1016/j.cemconres.2016.01.006.

Liu, S., Z. B. Bundur, J. Zhu, and R. D. Ferron. 2016b. “Evaluation of self-healing of internal cracks in biomimetic mortar using coda wave interferometry.” *Cem Concr Res*, 83: 70–78. Elsevier Ltd. https://doi.org/10.1016/j.cemconres.2016.01.006.

Liu, X., D. Choy, Q. Cui, and C. W. Schwartz. 2017. “Capitalizing Green Pavement: A Method and Valuation.” *Pavement Life-Cycle Assessment: Proceedings of the Symposium on Life-Cycle Assessment of Pavements*, I. Al-Qadi, H. Ozer, and J. Harvey, eds. Champaign, Illinois, USA.

Liu, Z., S. Li, and Y. Wang. 2022. “Waste engine oil and polyphosphoric acid enhanced the sustainable self-healing of asphalt binder and its fatigue behavior.” *J Clean Prod*, 339: 130767. https://doi.org/10.1016/j.jclepro.2022.130767.

Lv, Q., W. Huang, X. Zhu, and F. Xiao. 2017. “On the investigation of self-healing behavior of bitumen and its influencing factors.” *Mater Des*, 117: 7–17. Elsevier. https://doi.org/10.1016/J.MATDES.2016.12.072.

Lyngdal, E. T. 2015. “Critical Analysis of PH and PG+ Asphalt Binder Test Methods.”

Lyu, L., D. Li, Y. Chen, Y. Tian, and J. Pei. 2021. “Dynamic chemistry based self-healing of asphalt modified by diselenide-crosslinked polyurethane elastomer.” *Constr Build Mater*, 293: 123480. https://doi.org/10.1016/j.conbuildmat.2021.123480.

Mainieri, J. J. G., P. Singhvi, H. Ozer, B. K. Sharma, and I. L. Al-Qadi. 2021. “Fatigue Tolerance of Aged Asphalt Binders Modified with Softeners.” *https://doi.org/10.1177/03611981211025510*, 2675 (11): 1229–1244. SAGE PublicationsSage CA: Los Angeles, CA. https://doi.org/10.1177/03611981211025510.

Martono, W., H. U. Bahia, and J. D’Angelo. 2007. “Effect of Testing Geometry on Measuring Fatigue of Asphalt Binders and Mastics.” *Journal of Materials in Civil Engineering*, 19 (9): 746–752. American Society of Civil Engineers. https://doi.org/10.1061/(ASCE)0899-1561(2007)19:9(746).

Mauldin, T. C., and M. R. Kessler. 2010. “Self-healing polymers and composites.” *International Materials Reviews*, 55 (6): 317–346. https://doi.org/10.1179/095066010X12646898728408.

Mikesell, T. D., A. E. Malcolm, D. Yang, and M. M. Haney. 2015. “A comparison of methods to estimate seismic phase delays: numerical examples for coda wave interferometry.” *Geophys J Int*, 202 (1): 347–360. https://doi.org/10.1093/gji/ggv138.

Mirwald, J., D. Maschauer, B. Hofko, and H. Grothe. 2020. “Impact of reactive oxygen species on bitumen aging – The Viennese binder aging method.” *Constr Build Mater*, 257: 119495. Elsevier Ltd. https://doi.org/10.1016/j.conbuildmat.2020.119495.

Mneina, A., and J. Smith. 2019. “Promoting Sustainability in Infrastructure Through Quantifying Reclaimed Asphalt Pavement-An Ontario Municipal Case Study.” *2019 Conference of the Transportation Association of Canada*. Manager Member /Technical Services.

Mneina, A., and J. Smith. 2022. “Towards Harmonization of Pavement Condition Evaluation for Enhanced Pavement Management: An Ontario Case Study.” *2022 Transportation Association of Canada (TAC) Conference*. Edmonton, Alberta.

Modified Asphalt Research Center. 2022. *Clarification about different versions of analysis tools for the Linear Amplitude Sweep (LAS)* .

Motamed, A., and H. U. Bahia. 2011. "Influence of Test Geometry, Temperature, Stress Level, and Loading Duration on Binder Properties Measured Using DSR." *Journal of Materials in Civil Engineering*, 23 (10): 1422–1432. https://doi.org/10.1061/(asce)mt.1943-5533.0000321.

Mounier, D., ; H Di Benedetto, ; C Sauzéat, and K. Bilodeau. 2015. "Observation of Fatigue of Bituminous Mixtures Using Wave Propagation." https://doi.org/10.1061/(ASCE)MT.1943-5533.0001353.

Mounier, D., H. Di Benedetto, and C. Sauzéat. 2012. "Determination of bituminous mixtures linear properties using ultrasonic wave propagation." *Constr Build Mater*, 36: 638–647. https://doi.org/10.1016/j.conbuildmat.2012.04.136.

Mounier, D., H. Di Benedetto, C. Sauzéat, and K. Bilodeau. 2016. "Observation of Fatigue of Bituminous Mixtures Using Wave Propagation." *Journal of Materials in Civil Engineering*, 28 (1). https://doi.org/10.1061/(ASCE)MT.1943-5533.0001353.

Nguyen, M. L., C. Sauzéat, H. Di Benedetto, and N. Tapsoba. 2013. "Validation of the time–temperature superposition principle for crack propagation in bituminous mixtures." *Mater Struct*, 45: 1075–1087.

O'Connell, J., G. A. J. Mturi, J. Komba, and L. du Plessis. 2017. "Analysis of the binder yield energy test as an indicator of fatigue behaviour of asphalt mixes." *IOP Conf Ser Mater Sci Eng*, 236 (1): 012012. IOP Publishing. https://doi.org/10.1088/1757-899X/236/1/012012.

Okamoto, K., H. Mikada, T. Goto, and J. Takekawa. 2013. "Numerical analysis of the relationship between time-variant coda-Q and the variation in crustal stress." *Geophys J Int*, 195 (1): 575–581. https://doi.org/10.1093/gji/ggt243.

Ontario Hot Mix Producers Association. 1999. *The Use of Performance Graded Asphalt Cements in Ontario The ABCs of PGAC*.

Pan, C., P. Tang, M. Riara, L. Mo, M. Li, and M. Guo. 2018. "Effect of healing agents on crack healing of asphalt and asphalt mortar." *Materials*, 11 (8): 1373. MDPI AG. https://doi.org/10.3390/ma11081373.

Pan, W. H., X. D. Sun, L. M. Wu, K. K. Yang, and N. Tang. 2019. “Damage detection of asphalt concrete using piezo-ultrasonicwave technology.” *Materials*, 12: 1–10. https://doi.org/10.3390/ma12030443.

Park, S. W., Y. R. Kim, and R. A. Schapery. 1996. “A viscoelastic continuum damage model and its application to uniaxial behavior of asphalt concrete.” *Mechanics of Materials*, 24 (4): 241–255. https://doi.org/10.1016/S0167-6636(96)00042-7.

Park, S. W., and R. A. Schapery. 1997. “A viscoelastic constitutive model for particulate composites with growing damage.” *Int J Solids Struct*, 34 (8): 931–947. https://doi.org/10.1016/S0020-7683(96)00066-2.

Partl, M., H. Bahia, F. Canestrari, C. De la Roche, H. Di Benedetto, H. Piber, and D. Sybilski. 2012. *Advances in Interlaboratory Testing and Evaluation of Bituminous Materials*. *Rilem STAR*.

Partl, M. N. 2019. “High Performance – What Does that Mean?” *RILEM High Performance Asphalt Materials Symposium*.

Pérez-Jiménez, F. E., R. Botella, and R. Miró. 2012. “Differentiating between damage and thixotropy in asphalt binder’s fatigue tests.” *Constr Build Mater*, (31): 212–219. https://doi.org/10.1016/j.conbuildmat.2011.12.098.

Perraton, D., H. Baaj, and A. Carter. 2010a. “Comparison of some pavement design methods from a fatigue point of view: Effect of fatigue properties of asphalt materials.” *Road Materials and Pavement Design*, 11 (4): 833–861. https://doi.org/10.3166/RMPD.11.833-861.

Perraton, D., H. Baaj, and A. Carter. 2010b. “Comparison of Some Pavement Design Methods from a Fatigue Point of View: Effect of Fatigue Properties of Asphalt Materials.” *Road Materials and Pavement Design*, 11 (3): 833–861. Taylor & Francis Group. https://doi.org/10.1080/14680629.2010.9690309.

Planès, T., and E. Larose. 2013. “A review of ultrasonic Coda Wave Interferometry in concrete.” *Cem Concr Res*, 53: 248–255. https://doi.org/10.1016/j.cemconres.2013.07.009.

Pomarède, P., L. Chehami, N. F. Declercq, F. Meraghni, J. Dong, A. Locquet, and D. S. Citrin. 2019. “Application of Ultrasonic Coda Wave Interferometry for Micro-cracks Monitoring in Woven Fabric Composites.” *J Nondestr Eval*, 38 (1): 26. https://doi.org/10.1007/s10921-019-0563-z.

Proceq S.A. 2018. *Pundit Transducers Data Sheet*.

Qabur, A. 2018. "Fatigue Characterization of Asphalt Mixes with Polymer Modified Asphalt Cement." University of Waterloo.

Qian, G., H. Liu, J.-I. Zheng, and L. Jiang. 2013. "Experiment of Tension-compression Fatigue and Damage for Asphalt Mixtures." *Journal of Highway and Transportation Research and Development (English Edition)*, 7 (2): 15–21. American Society of Civil Engineers (ASCE). https://doi.org/10.1061/JHTRCQ.0000308.

Qiu, J. 2012. "Self Healing of Asphalt Mixtures: Towards a Better Understanding of the Mechanism." *Delft University of Technology*, 242.

Qiu, J., A. A. A. Molenaar, M. F. C. van de Ven, and S. Wu. 2012. "Development of Autonomous Setup for Evaluating Self-Healing Capability of Asphalt Mixtures." *Transportation Research Record: Journal of the Transportation Research*, 2296: 15–23. https://doi.org/10.3141/2296-02.

Qiu, J., M. F. C. van de Ven, A. A. A. Molenaar, S. P. Wu, and J. Yu. 2009. "Investigating the self healing capability of bituminous binders." *Road Materials and Pavement Design*. Elsevier. https://doi.org/10.1080/14680629.2009.9690237.

Qiu, X., W. Cheng, W. Xu, S. Xiao, and Q. Yang. 2020. "Fatigue evolution characteristic and self-healing behaviour of asphalt binders." *https://doi.org/10.1080/10298436.2020.1806277*, 23 (5): 1459–1470. Taylor & Francis. https://doi.org/10.1080/10298436.2020.1806277.

Ragni, D., G. Ferrotti, X. Lu, and F. Canestrari. 2019. "Influence of chemical additives for warm mix asphalts on the short-term ageing of a plain bitumen." *Road Materials and Pavement Design*, 20: S34–S48. Taylor & Francis. https://doi.org/10.1080/14680629.2019.1588772.

Ragni, D., M. Takarli, C. Petit, A. Graziani, and F. Canestrari. 2020. "Use of acoustic techniques to analyse interlayer shear-torque fatigue test in asphalt mixtures." *Int J Fatigue*, 131: 105356. Elsevier. https://doi.org/10.1016/J.IJFATIGUE.2019.105356.

Rezende, L. R. de, S. R. Kommidi, Y. R. Kim, and M. Khedmati. 2021. "Strain Sweep Fatigue Testing of Sand Asphalt Mortar to Investigate the Effects of Sample Geometry, Binder Film Thickness, and Testing Temperature." *https://doi.org/10.1177/03611981211011646*, 2675 (10): 516–529. SAGE PublicationsSage CA: Los Angeles, CA. https://doi.org/10.1177/03611981211011646.

Riara, M., P. Tang, L. Mo, B. Javilla, and S. Wu. 2017. “Investigation into crack healing of asphalt mixtures using healing agents.” https://doi.org/10.1016/j.conbuildmat.2017.11.074.

Sabouri, M., D. Mirzaeian, and A. Moniri. 2018. “Effectiveness of Linear Amplitude Sweep (LAS) asphalt binder test in predicting asphalt mixtures fatigue performance.” *Constr Build Mater*, 171: 281–290. https://doi.org/10.1016/j.conbuildmat.2018.03.146.

Safaei, F., and C. Castorena. 2016. “Temperature Effects of Linear Amplitude Sweep Testing and Analysis.” *Transportation Research Record: Journal of the Transportation Research*, 2574: 92–100. https://doi.org/10.3141/2574-10.

Safaei, F., J. Lee, L. A. H. do Nascimento, C. Hintz, and Y. R. Kim. 2014. “Implications of warm-mix asphalt on long-term oxidative ageing and fatigue performance of asphalt binders and mixtures.” *https://doi.org/10.1080/14680629.2014.927050*, 83 (January): 143–169. Taylor & Francis. https://doi.org/10.1080/14680629.2014.927050.

Sang, G., S. Liu, and D. Elsworth. 2020. “Quantifying fatigue-damage and failure-precursors using ultrasonic coda wave interferometry.” *International Journal of Rock Mechanics and Mining Sciences*, 131: 104366. https://doi.org/10.1016/j.ijrmms.2020.104366.

Santagata, E., O. Baglieri, D. Dalmazzo, and L. Tsantilis. 2017. “Investigating cohesive healing of asphalt binders by means of a dissipated energy approach.” *International Journal of Pavement Research and Technology*, 10 (5): 403–409. No longer published by Elsevier. https://doi.org/10.1016/J.IJPRT.2017.06.004.

Santagata, E., O. Baglieri, L. Tsantilis, and G. Chiappinelli. 2015. “Fatigue and healing properties of nano-reinforced bituminous binders.” *Int J Fatigue*, 80: 30–39. Elsevier. https://doi.org/10.1016/j.ijfatigue.2015.05.008.

Santagata, E., O. Baglieri, L. Tsantilis, and D. Dalmazzo. 2013. “Evaluation of self healing properties of bituminous binders taking into account steric hardening effects.” *Constr Build Mater*, 41: 60–67. https://doi.org/10.1016/j.conbuildmat.2012.11.118.

Schapery, R. A. 1975. “A theory of crack initiation and growth in viscoelastic media - III. Analysis of continuous growth.” *Int J Fract*, 11 (4): 549–562. Kluwer Academic Publishers. https://doi.org/10.1007/BF00116363/METRICS.

Schapery, R. A. 1984. “Correspondence principles and a generalized J integral for large deformation and fracture analysis of viscoelastic media.” *Int J Fract*, 25 (3): 195–223. Martinus Nijhoff, The Hague/Kluwer Academic Publishers. https://doi.org/10.1007/BF01140837/METRICS.

Schapery, R. A. A. 1990. “A theory of mechanical behavior of elastic media with growing damage and other changes in structure.” *J Mech Phys Solids*, 38 (2): 215–253. Pergamon. https://doi.org/10.1016/0022-5096(90)90035-3.

Seif, M., and M. Molayem. 2022. “Estimation of Fatigue Life of Asphalt Mixtures in Terms of Fatigue Life of Asphalt Binders Using the Rate of Dissipated Energy Change Approach.” *Journal of Materials in Civil Engineering*, 34 (8): 04022185. American Society of Civil Engineers. https://doi.org/10.1061/(ASCE)MT.1943-5533.0004334.

Shi, C., X. Cai, T. Wang, X. Yi, S. Liu, J. Yang, and Z. Leng. 2021. “Energy-based characterization of the fatigue crack density evolution of asphalt binders through controlled-stress fatigue testing.” *Constr Build Mater*, 300: 124275. Elsevier. https://doi.org/10.1016/J.CONBUILDMAT.2021.124275.

Shirzad, S., M. M. Hassan, M. A. Aguirre, S. Cooper, L. N. Mohammad, I. I. Negulescu, S. Cooper, and I. I. Negulescu. 2019a. “Laboratory Testing of Self-Healing Polymer Modified Asphalt Mixtures Containing Recycled Asphalt Materials (RAP/RAS).” *MATEC Web of Conferences*, 271: 3003. EDP Sciences. https://doi.org/10.1051/matecconf/201927103003.

Shirzad, S., M. M. Hassan, M. A. Aguirre, L. N. Mohammad, S. Cooper, and I. I. Negulescu. 2019b. “Rheological properties of asphalt binder modified with recycled asphalt materials and light-activated self-healing polymers.” *Constr Build Mater*, 220. https://doi.org/10.1016/j.conbuildmat.2019.05.189.

Shu, B., S. Wu, L. Dong, J. Norambuena-Contreras, Y. Li, C. Li, X. Yang, Q. Liu, Q. Wang, F. Wang, D. M. Barbieri, M. Yuan, S. Bao, M. Zhou, and G. Zeng. 2020. “Self-healing capability of asphalt mixture containing polymeric composite fibers under acid and saline-alkali water solutions.” *J Clean Prod*, 268: 122387. https://doi.org/10.1016/j.jclepro.2020.122387.

Shu, B., L. Zhang, S. Wu, L. Dong, Q. Liu, and Q. Wang. 2018. “Synthesis and characterization of compartmented Ca-alginate/silica self-healing fibers containing bituminous rejuvenator.” https://doi.org/10.1016/j.conbuildmat.2018.09.121.

Steineder, M., M. J. Peyer, B. Hofko, M. Chaudhary, N. Saboo, and A. Gupta. 2022. “Comparing different fatigue test methods at asphalt mastic level.” *Materials and Structures/Materiaux et Constructions*, 55 (5): 1–16. Springer Science and Business Media B.V. https://doi.org/10.1617/S11527-022-01970-4/TABLES/7.

Sun, D., T. Lin, X. Zhu, Y. Tian, and F. Liu. 2016. “Indices for self-healing performance assessments based on molecular dynamics simulation of asphalt binders.” *Comput Mater Sci*, 114: 86–93. Elsevier. https://doi.org/10.1016/J.COMMATSCI.2015.12.017.

Sun, D., G. Sun, X. Zhu, A. Guarin, B. Li, Z. Dai, and J. Ling. 2018. “A comprehensive review on self-healing of asphalt materials: Mechanism, model, characterization and enhancement.” *Adv Colloid Interface Sci*, 256: 65–93. https://doi.org/10.1016/j.cis.2018.05.003.

Sun, D., F. Yu, L. Li, T. Lin, and X. Y. Y. Zhu. 2017. “Effect of chemical composition and structure of asphalt binders on self-healing.” *Constr Build Mater*, 133: 495–501. Elsevier. https://doi.org/10.1016/J.CONBUILDMAT.2016.12.082.

Sun, G., D. Sun, A. Guarin, J. Ma, F. Chen, and E. Ghafooriroozbahany. 2019. “Low temperature self-healing character of asphalt mixtures under different fatigue damage degrees.” *Constr Build Mater*, 223: 870–882. Elsevier Ltd. https://doi.org/10.1016/j.conbuildmat.2019.07.040.

Tabaković, A., and E. Schlangen. 2015. “Self-Healing Technology for Asphalt Pavements.” 285–306. Springer, Cham.

Talebi, A., H. Rahimi, A. Moradi, M. Mirzaei, and I. Koulakov. 2021. “Qp, Qs, Qc, Qi, and Qsc Attenuation Parameters in the Zagros Region, Iran.” *Pure Appl Geophys*, 178 (11): 4487–4505. https://doi.org/10.1007/s00024-021-02879-9.

Tan, Y., L. Shan, Y. Richard Kim, and B. S. Underwood. 2012. “Healing characteristics of asphalt binder.” *Constr Build Mater*, 27 (1): 570–577. Elsevier. https://doi.org/10.1016/J.CONBUILDMAT.2011.07.006.

Tariq Morshed, M. M., Z. Hossain, D.-H. Chen, and G. Baumgardner. 2020. “Exploration of alternatives of elastic recovery and conventional fatigue tests of modified binders.” *International Journal of Pavement Research and Technology*, 13: 630–636. https://doi.org/10.1007/s42947-020-6009-2.

Tavassoti-Kheiry, P., I. Boz, X. Chen, and M. Solaimanian. 2017. "Application of Ultrasonic Pulse Velocity Testing of Asphalt Concrete Mixtures to Improve the Prediction Accuracy of Dynamic Modulus Master Curve." *Airfield and Highway Pavements 2017: Testing and Characterization of Bound and Unbound Pavement Materials*, 2017-Augus (August): 152–164. https://doi.org/10.1061/9780784480939.014.

du Tertre, A. 2010. *Nondestructive Evaluation of Asphalt Pavement Joints Using LWD and MASW Tests*.

The Mathworks. 2022. *Signal Processing Toolbox Reference (R2022b)*.

Transport Canada. 2019. *Transportation in Canada 2018: Overview report*.

Underwood, B. S., Y. R. Kim, and M. N. Guddati. 2009. "Improved calculation method of damage parameter in viscoelastic continuum damage model." *International Journal of Pavement Engineering*, 11 (6): 459–476. https://doi.org/10.1080/10298430903398088.

Underwood, B. S., Y. R. Kim, B. S. Underwood, C. Baek, and Y. R. Kim. 2012. "Simplified Viscoelastic Continuum Damage Model as Platform for Asphalt Concrete Fatigue Analysis." *Transportation Research Record: Journal of the Transportation Research*, 2296: 36–45. https://doi.org/10.3141/2296-04.

Underwood, B. S., and W. A. Zeiada. 2014. "Characterization of Microdamage Healing in Asphalt Concrete with a Smeared Continuum Damage Approach." *Transportation Research Record: Journal of the Transportation Research Board*, 2447 (1): 126–135. https://doi.org/10.3141/2447-14.

Varma, R., R. Balieu, and N. Kringos. 2021. "A state-of-the-art review on self-healing in asphalt materials: Mechanical testing and analysis approaches." *Constr Build Mater*, 310: 125197. https://doi.org/10.1016/j.conbuildmat.2021.125197.

Wang, C., C. Castorena, J. Zhang, and Y. R. Kim. 2015. "Unified failure criterion for asphalt binder under cyclic fatigue loading." *Asphalt Paving Technology: Association of Asphalt Paving Technologists-Proceedings of the Technical Sessions*, 84: 269–300. https://doi.org/10.1080/14680629.2015.1077010.

Wang, C., Y. Chen, and W. Xie. 2020. “A comparative study for fatigue characterization of asphalt binder using the linear amplitude sweep test.” *Materials and Structures/Materiaux et Constructions*, 53 (4): 1–12. Springer. https://doi.org/10.1617/S11527-020-01530-8/METRICS.

Wang, C., W. Xie, and B. S. Underwood. 2018. “Fatigue and healing performance assessment of asphalt binder from rheological and chemical characteristics.” *Materials and Structures/Materiaux et Constructions*, 51 (6): 171. Springer Netherlands. https://doi.org/10.1617/s11527-018-1300-2.

Wang, Y., and Y. R. Kim. 2017. “Development of a pseudo strain energy-based fatigue failure criterion for asphalt mixtures Development of a pseudo strain energy-based fatigue failure criterion for asphalt mixtures.” *International Journal of Pavement Engineering* , 20 (10): 1182–1192. https://doi.org/10.1080/10298436.2017.1394100.

Wiciak, P. 2020. “Quality Assessment of Composite Materials using Ultrasonic Non-Destructive Testing Methods.” University of Waterloo.

Williams, B., J. R. R. Willis, and T. C. C. Ross. 2019. *Annual Asphalt Pavement Industry Survey on Recycled Materials and Warm-Mix Asphalt Usage 2018*.

Witczak, M., M. Mamlouk, M. Souliman, and W. Zeiada. 2013. *Laboratory Validation of an Endurance Limit for Asphalt Pavements*. *Laboratory Validation of an Endurance Limit for Asphalt Pavements*.

Wool, R. P., and K. M. O′Connor. 1981. “A theory crack healing in polymers.” *J. Appl. Phys*, 52 (June 1998): 5953.

Wu, S., Y. Ye, Y. Li, C. C. Li, W. Song, H. Li, C. C. Li, B. Shu, and S. Nie. 2019. “The effect of UV irradiation on the chemical structure, mechanical and self-healing properties of asphalt mixture.” *Materials*, 12 (15). MDPI AG. https://doi.org/10.3390/ma12152424.

Xiang, H., W. Zhang, P. Liu, and Z. He. 2020. “Fatigue–healing performance evaluation of asphalt mixture using four-point bending test.” *Mater Struct*, 53 (3): 47. https://doi.org/10.1617/s11527-020-01482-z.

Xie, W., C. Castorena, C. Wang, and Y. Richard Kim. 2017. “A framework to characterize the healing potential of asphalt binder using the linear amplitude sweep test.” *Constr Build Mater*, 154: 771–779. Elsevier Ltd. https://doi.org/10.1016/j.conbuildmat.2017.08.021.

Xu, S., Á. García, J. J. J. Su, Q. Liu, A. Tabaković, E. Schlangen, A. García, J. J. J. Su, Q. Liu, A. Tabaković, E. Schlangen, Á. García, J. J. J. Su, Q. Liu, A. Tabaković, and E. Schlangen. 2018a. "Self-Healing Asphalt Review: From Idea to Practice." *Adv Mater Interfaces*, 1800536 (17): 1–21. https://doi.org/10.1002/admi.201800536.

Xu, S., Á. García, J. Su, Q. Liu, A. Tabaković, and E. Schlangen. 2018b. "Self-Healing Asphalt Review: From Idea to Practice." *Adv Mater Interfaces*, 1800536: 1–21. https://doi.org/10.1002/admi.201800536.

Xu, S., A. Tabaković, X. Liu, D. Palin, and E. Schlangen. 2019. "Optimization of the calcium alginate capsules for self-healing asphalt." *Applied Sciences (Switzerland)*, 9 (3). https://doi.org/10.3390/app9030468.

Yan, Y., D. Hernando, B. Park, C. Allen, and R. Roque. 2021. "Understanding asphalt binder cracking characterization at intermediate temperatures: Review and evaluation of two approaches." *Constr Build Mater*, 312: 125163. Elsevier. https://doi.org/10.1016/J.CONBUILDMAT.2021.125163.

Yang, S., J. Ji, H. Tao, Y. Muhammad, J. Huang, S. Wang, Y. Wei, and J. Li. 2021. "Fabrication of urea formaldehyde–epoxy resin microcapsules for the preparation of high self-healing ability containing <scp>SBS</scp> modified asphalt." *Polym Compos*, 42 (8): 4128–4137. https://doi.org/10.1002/pc.26135.

Yildirim, Y. 2007. "Polymer modified asphalt binders." *Constr Build Mater*, 21 (1): 66–72. Elsevier. https://doi.org/10.1016/J.CONBUILDMAT.2005.07.007.

Yuan, C., J. Bryan, and M. Denolle. 2021. "Numerical comparison of time-, frequency- and wavelet-domain methods for coda wave interferometry." *Geophys J Int*, 226 (2): 828–846. https://doi.org/10.1093/gji/ggab140.

Zhang, Y., and Y. Gao. 2019. "Predicting crack growth in viscoelastic bitumen under a rotational shear fatigue load." *https://doi.org/10.1080/14680629.2019.1635516*, 22 (3): 603–622. Taylor & Francis. https://doi.org/10.1080/14680629.2019.1635516.

Zhang, Z., R. Tavenard, A. Bailly, X. Tang, P. Tang, and T. Corpetti. 2017. "Dynamic Time Warping under limited warping path length." *Inf Sci (N Y)*, 393: 91–107. https://doi.org/10.1016/j.ins.2017.02.018.

Zhou, F., P. Karki, and S. Im. 2017. “Development of a Simple Fatigue Cracking Test for Asphalt Binders.” *Transportation Research Record: Journal of the Transportation Research Board*, 2632 (1): 79–87. SAGE PublicationsSage CA: Los Angeles, CA. https://doi.org/10.3141/2632-09.

Zhou, F., W. Mogawer, H. Li, A. Andriescu, A. Copeland, Z. Fujie, M. Walaa, L. Hongsheng, A. Adrian, and C. Audrey. 2013. “Evaluation of fatigue tests for characterizing asphalt binders.” *Journal of Materials in Civil Engineering*, 25 (5): 610–617. American Society of Civil Engineers. https://doi.org/10.1061/(ASCE)MT.1943-5533.0000625.

Zhu, J., B. Birgisson, and N. Kringos. 2014. “Polymer modification of bitumen: Advances and challenges.” *Eur Polym J*, 54: 18–38. Pergamon. https://doi.org/10.1016/J.EURPOLYMJ.2014.02.005.

Appendix A

Healing Test Supplementary Results (Chapter 7)

A.1 VECD Healing Analysis

Table A-1: VECD analysis for unaged asphalt cements (C_1, S_1, S_2, S_3).

Binder	1st Phase ends at:	Rest Period (min)	C_1	S_1	S_2	S_3
58-28A	$0.5\gamma_{peak}$	5	0.853	11.3	10.5	21.6
	$0.5\gamma_{peak}$	30	0.853	11.3	9.5	20.9
	γ_{peak}	5	0.597	54.2	52.1	93.7
	γ_{peak}	30	0.593	54.7	51.7	94.9
58-28B	$0.5\gamma_{peak}$	5	0.766	5.5	5.1	10.6
	$0.5\gamma_{peak}$	30	0.772	5.5	4.7	10.5
	γ_{peak}	5	0.600	49.4	48.1	83.1
	γ_{peak}	30	0.596	49.8	46.4	84.8
58-28A +4%SBS	$0.5\gamma_{peak}$	5	0.687	28.3	27.6	54.6
	$0.5\gamma_{peak}$	30	0.699	27.8	26.3	54.3
	γ_{peak}	5	0.421	109.6	108.6	204.6
	γ_{peak}	30	0.431	108.7	106.5	210

Table A-2: VECD analysis for unaged asphalt cements (Initial Healing, Residual Healing, Total Healing).

Binder	1st Phase ends at:	Rest Period (min)	IH (%)	RH (%)	TH (%)
58-28A	$0.5\gamma_{peak}$	5	6.7	91.6	98.3
	$0.5\gamma_{peak}$	30	15.5	85.6	101.1
	γ_{peak}	5	3.8	72.8	76.7
	γ_{peak}	30	5.3	73.6	78.9
58-28B	$0.5\gamma_{peak}$	5	6.7	92.3	99.0
	$0.5\gamma_{peak}$	30	13.4	93.0	106.5
	γ_{peak}	5	2.8	68.0	70.8
	γ_{peak}	30	6.7	70.2	77.0
	$0.5\gamma_{peak}$	5	2.5	93.3	95.8

58-28A +4%SBS	$0.5\gamma_{peak}$	30	5.5	95.0	100.6
	γ_{peak}	5	0.9	86.6	87.5
	γ_{peak}	30	2.1	93.1	95.2

Table A-3: VECD analysis for RTFO aged asphalt cements (C_1, S_1, S_2, S_3).

Binder	1st Phase ends at:	Rest Period (min)	C_1	S_1	S_2	S_3
58-28A	$0.5\gamma_{peak}$	5	0.767	14	13.3	27
	$0.5\gamma_{peak}$	30	0.767	14	12.4	26.5
	γ_{peak}	5	0.486	58.8	57.8	107.5
	γ_{peak}	30	0.483	59.5	57.2	107.7
58-28B	$0.5\gamma_{peak}$	5	0.765	12.9	12.1	24.7
	$0.5\gamma_{peak}$	30	0.765	12.8	11.2	24.1
	γ_{peak}	5	0.479	54.8	53.7	99.6
	γ_{peak}	30	0.476	55.1	52.6	99.6
58-28A +4%SBS	$0.5\gamma_{peak}$	5	0.650	27.0	26.3	52.5
	$0.5\gamma_{peak}$	30	0.650	27.0	25.6	52.8
	γ_{peak}	5	0.363	102.5	101.6	190.2
	γ_{peak}	30	0.379	102.7	100.7	190.9

Table A-4: VECD analysis for RTFO aged asphalt cements (Initial Healing, Residual Healing, Total Healing).

Binder	1st Phase ends at:	Rest Period (min)	IH (%)	RH (%)	TH (%)
58-28A	$0.5\gamma_{peak}$	5	5.0	92.9	97.9
	$0.5\gamma_{peak}$	30	11.0	90.0	101.0
	γ_{peak}	5	1.8	82.7	84.5
	γ_{peak}	30	3.9	80.9	84.9
58-28B	$0.5\gamma_{peak}$	5	5.8	92.4	98.2
	$0.5\gamma_{peak}$	30	12.7	87.4	100.1
	γ_{peak}	5	2.1	81.7	83.8
	γ_{peak}	30	4.6	80.8	85.3
	$0.5\gamma_{peak}$	5	2.5	94.5	96.9

58-28A +4%SBS	$0.5\gamma_{peak}$	30	5.2	95.5	100.8
	γ_{peak}	5	0.9	85.5	86.4
	γ_{peak}	30	1.9	85.9	87.9

Table A-5: VECD analysis for PAV-aged asphalt cements (C_1, S_1, S_2, S_3).

Binder	1st Phase ends at:	Rest Period (min)	C_1	S_1	S_2	S_3
58-28A	$0.5\gamma_{peak}$	5	0.698	12.5	12	24.2
	$0.5\gamma_{peak}$	30	0.698	12.5	11.6	24.2
	γ_{peak}	5	0.403	51.3	50.6	98.8
	γ_{peak}	30	0.403	51.3	49.9	100.4
58-28B	$0.5\gamma_{peak}$	5	0.718	10.4	10	20.2
	$0.5\gamma_{peak}$	30	0.715	10.5	10	20.3
	γ_{peak}	5	0.408	44.4	43.8	84.3
	γ_{peak}	30	0.413	44.2	42.8	86.1
58-28A +4%SBS	$0.5\gamma_{peak}$	5	0.636	19.3	18.9	37.5
	$0.5\gamma_{peak}$	30	0.635	19.4	18.4	37.9
	γ_{peak}	5	0.359	71.6	71.0	137.8
	γ_{peak}	30	0.360	71.5	70.1	140.5

Table A-6: VECD analysis for PAV-aged asphalt cements (Initial Healing, Residual Healing, Total Healing).

Binder	1st Phase ends at:	Rest Period (min)	IH (%)	RH (%)	TH (%)
58-28A	$0.5\gamma_{peak}$	5	3.6	93.8	97.4
	$0.5\gamma_{peak}$	30	7.2	93.9	101.1
	γ_{peak}	5	1.3	92.7	94.0
	γ_{peak}	30	2.6	95.8	98.5
58-28B	$0.5\gamma_{peak}$	5	4.3	93.3	97.6
	$0.5\gamma_{peak}$	30	4.8	94.0	98.8
	γ_{peak}	5	1.5	89.8	91.3
	γ_{peak}	30	3.1	94.9	98.1
	$0.5\gamma_{peak}$	5	2.5	94.0	96.5

58-28A +4%SBS	$0.5\gamma_{peak}$	30	4.9	95.6	100.6
	γ_{peak}	5	0.9	92.4	93.3
	γ_{peak}	30	1.9	96.5	98.4

A.2 Crack Length Healing Analysis

Table A-7: Crack length healing analysis for unaged asphalt cements

Binder	1st Phase ends at:	Rest Period (min)	a_1/a_2 (%)	c_1/c_2 (%)
58-28A	$0.5\gamma_{peak}$	5	101.6	102.8
	$0.5\gamma_{peak}$	30	101.0	102.4
	γ_{peak}	5	65.2	63.2
	γ_{peak}	30	70.6	68.8
58-28B	$0.5\gamma_{peak}$	5	102.1	103.2
	$0.5\gamma_{peak}$	30	100.3	101.4
	γ_{peak}	5	65.3	63.4
	γ_{peak}	30	70.6	69.1
58-28A +4%SBS	$0.5\gamma_{peak}$	5	101.7	102.2
	$0.5\gamma_{peak}$	30	100.5	101.2
	γ_{peak}	5	97.4	96.5
	γ_{peak}	30	95.9	95.6

Table A-8: Crack length healing analysis for RTFO aged asphalt cements.

Binder	1st Phase ends at:	Rest Period (min)	a_1/a_2 (%)	c_1/c_2 (%)
58-28A	$0.5\gamma_{peak}$	5	94.0	94.1
	$0.5\gamma_{peak}$	30	93.4	93.8
	γ_{peak}	5	87.1	85.2
	γ_{peak}	30	84.8	83.0
58-28B	$0.5\gamma_{peak}$	5	100.3	100.8
	$0.5\gamma_{peak}$	30	99.7	100.3
	γ_{peak}	5	84.2	82.0
	γ_{peak}	30	84.4	82.5
58-28A +4%SBS	$0.5\gamma_{peak}$	5	101.3	101.6
	$0.5\gamma_{peak}$	30	99.8	100.3
	γ_{peak}	5	98.1	96.9
	γ_{peak}	30	95.9	95.5

Table A-9: Crack length healing analysis for PAV-aged asphalt cements.

Binder	1st Phase ends at:	Rest Period (min)	a_1/a_2 (%)	c_1/c_2 (%)
58-28A	$0.5\gamma_{peak}$	5	100.1	100.2
	$0.5\gamma_{peak}$	30	99.3	99.7
	γ_{peak}	5	101.7	101.1
	γ_{peak}	30	99.6	99.6
58-28B	$0.5\gamma_{peak}$	5	100.0	99.9
	$0.5\gamma_{peak}$	30	99.1	99.5
	γ_{peak}	5	97.9	96.4
	γ_{peak}	30	96.8	96.2
58-28A +4%SBS	$0.5\gamma_{peak}$	5	100.7	100.8
	$0.5\gamma_{peak}$	30	99.6	100.0
	γ_{peak}	5	103.0	102.3
	γ_{peak}	30	100.3	100.2

A.3 P-LASH Healing Analysis

Table A-10: P-LASH healing analysis for unaged asphalt cements: FREI method (%Ret, %Loss).

Binder	1st Phase ends at:	Conditioning Period (min)	Rest Period (min)	$FREI_1$	$FREI_2$	%Ret (%)	%Loss (%)
58-28A	30	0	0	3.694	-	-	-
	30	30	0	3.567	-	-	-
	$0.5\gamma_{peak}$	0	5	0.445	0.447	100.6	-0.6
	$0.5\gamma_{peak}$	0	30	0.445	0.447	100.6	-0.6
	γ_{peak}	0	5	3.414	1.649	48.3	51.7
	γ_{peak}	0	30	3.348	1.849	55.2	44.8
58-28B	30	0	0	2.870	-	-	-
	30	30	0	2.872	-	-	-
	$0.5\gamma_{peak}$	0	5	0.316	0.316	100.0	0.0
	$0.5\gamma_{peak}$	0	30	0.317	0.316	99.7	0.3
	γ_{peak}	0	5	2.729	1.2345	45.2	54.8
	γ_{peak}	0	30	2.564	1.434	55.9	44.1
58-28A +4%SBS	30	0	0	10.297	-	-	-
	30	30	0	8.677	-	-	-
	$0.5\gamma_{peak}$	0	5	1.507	1.506	99.9	0.1
	$0.5\gamma_{peak}$	0	30	1.502	1.505	100.2	-0.2
	γ_{peak}	0	5	8.038	6.301	78.4	21.6
	γ_{peak}	0	30	8.6395	6.751	78.1	21.9

Table A-11: P-LASH healing analysis for unaged asphalt cements: J-Integral method (%J_{Ret}, %J_{Loss}, J_{RP}/J_{SH}) (*Extrapolated using 30-minute conditioning period)

Binder	1st Phase ends at:	Cond. Period (min)	Rest Period (min)	J_{SH} (kPa)	J_1 (kPa)	J_{RP} (kPa)	J_2 (kPa)	%Res_J (%)	%$Loss_J$ (%)	J_{RP}/J_{SH}
58-28A	30	0	0	-	8.91	-	-	-	-	-
	30	30	0	4.73	8.72	-	-	-	-	-
	30	5	0	0.78*	-	-	-	-	-	-
	$0.5\gamma_{peak}$	0	5	-	2.77	0.83	2.76	99.6	0.4	1.062
	$0.5\gamma_{peak}$	0	30	-	2.78	5.20	2.79	100.4	-0.4	1.099
	γ_{peak}	0	5	-	9.44	0.79	6.03	63.9	36.1	1.010
	γ_{peak}	0	30	-	9.25	4.98	6.53	70.6	29.4	1.054
58-28B	30	0	0	-	8.96	-	-	-	-	-
	30	30	0	5.35	8.76	-	-	-	-	-
	30	5	0	0.89*	-	-	-	-	-	-
	$0.5\gamma_{peak}$	0	5	-	2.71	0.92	2.70	99.8	0.2	1.038
	$0.5\gamma_{peak}$	0	30	-	2.64	5.60	2.65	100.2	-0.2	1.046
	γ_{peak}	0	5	-	9.14	0.86	5.81	63.6	36.4	0.967
	γ_{peak}	0	30	-	9.04	5.48	6.32	69.9	30.1	1.023
58-28A +4%SBS	30	0	0	-	16.54	-	-	-	-	-
	30	30	0	4.59	14.20	-	-	-	-	-
	30	5	0	0.76*	-	-	-	-	-	-
	$0.5\gamma_{peak}$	0	5	-	5.19	0.77	5.14	99.1	0.9	1.018
	$0.5\gamma_{peak}$	0	30	-	5.31	4.96	5.32	100.2	-0.2	1.080
	γ_{peak}	0	5	-	15.49	0.74	13.13	84.8	15.2	0.978
	γ_{peak}	0	30	-	15.98	4.86	13.84	86.6	13.4	1.059

Table A-12: P-LASH healing analysis for RTFO aged asphalt cements: FREI method (%Ret, %Loss).

Binder	1st Phase ends at:	Conditioning Period (min)	Rest Period (min)	$FREI_1$	$FREI_2$	%Ret (%)	%Loss (%)
58-28A	30	0	0	2.388	-	-	-
	30	30	0	2.130	-	-	-
	$0.5\gamma_{peak}$	0	5	0.374	0.375	100.3	-0.3
	$0.5\gamma_{peak}$	0	30	0.374	0.372	99.5	0.5
	γ_{peak}	0	5	2.231	1.49	66.8	33.2
	γ_{peak}	0	30	2.128	1.338	62.9	37.1
58-28B	30	0	0	1.871	-	-	-
	30	30	0	1.887	-	-	-
	$0.5\gamma_{peak}$	0	5	0.299	0.288	96.3	3.7
	$0.5\gamma_{peak}$	0	30	0.299	0.288	96.3	3.7
	γ_{peak}	0	5	1.835	1.115	60.7	39.3
	γ_{peak}	0	30	1.694	1.048	61.9	38.1
58-28A +4%SBS	30	0	0	5.309	-	-	-
	30	30	0	4.693	-	-	-
	$0.5\gamma_{peak}$	0	5	1.026	1.027	100.1	-0.1
	$0.5\gamma_{peak}$	0	30	1.026	1.028	100.2	-0.2
	γ_{peak}	0	5	3.892	3.385	87.0	13.0
	γ_{peak}	0	30	4.059	3.3105	81.6	18.4

Table A-13: P-LASH healing analysis for RTFO aged asphalt cements: J-Integral method (%J_{Ret}, %J_{Loss}, J_{RP}/J_{SH}) (*Extrapolated using 30-minute conditioning period)

Binder	1st Phase ends at:	Cond. Period (min)	Rest Period (min)	J_{SH} (kPa)	J_1 (kPa)	J_{RP} (kPa)	J_2 (kPa)	$\%Res_J$ (%)	$\%Loss_J$ (%)	J_{RP}/J_{SH}
58-28A	30	0	0	-	15.03	-	-	-	-	-
	30	30	0	8.72	13.57	-	-	-	-	-
	30	5	0	1.45*	-	-	-	-	-	-
	$0.5\gamma_{peak}$	0	5	-	4.56	1.39	4.56	100.0	0.0	0.957
	$0.5\gamma_{peak}$	0	30	-	4.74	8.98	4.76	100.4	-0.4	1.030
	γ_{peak}	0	5	-	14.96	1.40	11.12	74.4	25.6	0.966
	γ_{peak}	0	30	-	13.87	8.61	10.35	74.6	25.4	0.987
58-28B	30	0	0	-	15.50	-	-	-	-	-
	30	30	0	10.60	15.73	-	-	-	-	-
	30	5	0	1.74*	-	-	-	-	-	-
	$0.5\gamma_{peak}$	0	5	-	4.89	1.69	4.70	96.1	3.9	0.974
	$0.5\gamma_{peak}$	0	30	-	4.85	10.43	4.68	96.5	3.5	0.984
	γ_{peak}	0	5	-	15.36	1.62	11.11	72.3	27.7	0.929
	γ_{peak}	0	30	-	14.65	10.16	10.92	74.5	25.5	0.959
58-28A +4%SBS	30	0	0	-	21.34	-	-	-	-	-
	30	30	0	7.44	19.04	-	-	-	-	-
	30	5	0	1.24*	-	-	-	-	-	-
	$0.5\gamma_{peak}$	0	5	-	7.35	1.28	7.30	99.4	0.6	1.033
	$0.5\gamma_{peak}$	0	30	-	7.14	7.82	7.15	100.2	-0.2	1.051
	γ_{peak}	0	5	-	17.11	1.08	14.71	86.0	14.0	0.872
	γ_{peak}	0	30	-	17.87	7.46	15.6	87.3	12.7	1.002

Table A-14: P-LASH healing analysis for PAV-aged asphalt cements: FREI method (%Ret, %Loss).

Binder	1st Phase ends at:	Conditioning Period (min)	Rest Period (min)	$FREI_1$	$FREI_2$	%Ret (%)	%Loss (%)
58-28A	30	0	0	0.960	-	-	-
	30	30	0	0.960	-	-	-
	$0.5\gamma_{peak}$	0	5	0.211	0.214	101.4	-1.4
	$0.5\gamma_{peak}$	0	30	0.211	0.214	101.4	-1.4
	γ_{peak}	0	5	0.943	0.978	103.7	-3.7
	γ_{peak}	0	30	0.944	0.943	99.9	0.1
58-28B	30	0	0	0.583	-	-	-
	30	30	0	0.682	-	-	-
	$0.5\gamma_{peak}$	0	5	0.132	0.144	109.1	-9.1
	$0.5\gamma_{peak}$	0	30	0.132	0.132	100.0	0.0
	γ_{peak}	0	5	0.571	0.610	106.7	-6.7
	γ_{peak}	0	30	0.599	0.5835	97.4	2.6
58-28A +4%SBS	30	0	0	1.692	-	-	-
	30	30	0	1.713	-	-	-
	$0.5\gamma_{peak}$	0	5	0.414	0.414	100.0	0.0
	$0.5\gamma_{peak}$	0	30	0.414	0.414	100.0	0.0
	γ_{peak}	0	5	1.677	1.703	101.6	-1.6
	γ_{peak}	0	30	1.692	1.707	100.9	-0.9

Table A-15: P-LASH healing analysis for PAV-aged asphalt cements: J-Integral method (%J_{Ret}, %J_{Loss}, J_{RP}/J_{SH})
(*Extrapolated using 30-minute conditioning period)

Binder	1st Phase ends at:	Cond. Period (min)	Rest Period (min)	J_{SH} (kPa)	J_1 (kPa)	J_{RP} (kPa)	J_2 (kPa)	%Res_J (%)	%$Loss_J$ (%)	J_{RP}/J_{SH}
58-28A	30	0	0	-	22.25	-	-	-	-	-
	30	30	0	18.91	22.70	-	-	-	-	-
	30	5	0	3.16*	-	-	-	-	-	-
	$0.5\gamma_{peak}$	0	5	-	7.78	3.08	7.73	99.4	0.6	0.973
	$0.5\gamma_{peak}$	0	30	-	7.83	19.42	7.85	100.3	-0.3	1.027
	γ_{peak}	0	5	-	22.74	2.89	22.68	99.8	0.2	0.914
	γ_{peak}	0	30	-	22.76	18.82	22.56	99.1	0.9	0.995
58-28B	30	0	0	-	21.32	-	-	-	-	-
	30	30	0	22.34	22.68	-	-	-	-	-
	30	5	0	3.71*	-	-	-	-	-	-
	$0.5\gamma_{peak}$	0	5	-	7.41	3.52	7.41	100.0	0.0	0.949
	$0.5\gamma_{peak}$	0	30	-	7.17	21.34	7.23	100.8	-0.8	0.955
	γ_{peak}	0	5	-	19.91	3.25	18.82	94.5	5.5	0.875
	γ_{peak}	0	30	-	21.02	21.38	20.34	96.8	3.2	0.957
58-28A +4%SBS	30	0	0	-	25.55	-	-	-	-	-
	30	30	0	15.13	25.38	-	-	-	-	-
	30	5	0	2.51*	-	-	-	-	-	-
	$0.5\gamma_{peak}$	0	5	-	9.03	2.37	8.96	99.2	0.8	0.945
	$0.5\gamma_{peak}$	0	30	-	9.21	15.27	9.22	100.2	-0.2	1.009
	γ_{peak}	0	5	-	25.46	2.26	24.82	97.5	2.5	0.900
	γ_{peak}	0	30	-	25.76	14.99	25.725	99.9	0.1	0.991

Appendix B
Asphalt Mixture Testing Setup and Data Acquisition

B.1 Sample Installation and Instrumentation

This section details the specimen installation and instrumentation used with CPATT's MTS 810 test frame. For either complex modulus or T/C fatigue testing, the test frame and hydraulic lines are initially inspected. The hydraulics are then turned on and the appropriate interlocks are set in the MTS software to ensure the safety of the operator during loading. The actuator can then be raised to an appropriate height (approximately 10 to 20 mm above the top-end plate of the specimen). The specimen can then be carefully inserted between the loading frame extensions and fastened securely to the bottom extension using four M8 bolts; bolts are tightened using an alternating/ "crisscross" tightening sequence to ensure a roughly even load distribution through the four fasteners. Two fasteners are fitted with locking washers and the remaining two fasteners are fitted with a custom washer for securing the elastics accompanying the UPV transducers.

After fastening the bottom four bolts, the actuator is lowered using the "Displacement" control mode until the top extension is approximately 0.5 to 1 mm from the top endplate and the appropriate interlocks are adjusted. Once in position, the control mode is set to "Force" mode and a maximum seating load of approximately 0.1 kN is applied. Four M8 bolts are used to fasten the top end plate and top extension using the same tightening sequence as previously described and the load is reduced to 0 kN. At this time, the three thermocouples can be fixed to the surface of the sample. Each thermocouple is positioned in the middle of the sample and roughly 60° apart from the adjacent gauge points and 120° apart from the other thermocouples. The extensometers can then be installed at the gauge points and the setting pins can be removed (Figure B-1). The ultrasonic transducers are installed on the top and bottom endplates using the appropriate couplant (e.g., Molykote® High Vacuum Grease) and custom 3D-printed transducer holders (Figure B-2). In combination with the couplant, the transducer holders hold the transducer in constant contact with the endplate surface using elastic bands secured to the two custom washers fastened to the frame extension. A "trial" scan is performed to confirm that there is an adequate coupling between the transceiver and receivers. Finally, the door to the environmental chamber can be closed and the cooling/heating system can be turned on to allow the specimen to reach the test temperature. The temperature is ramped and then maintained until the dummy specimen is saturated to within ±0.5°C of the testing temperature.

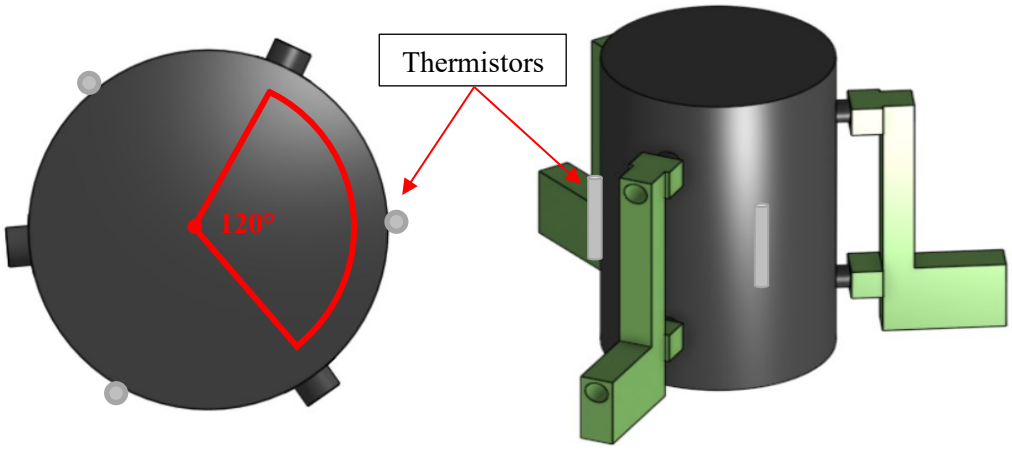

Figure B-1 Specimen gauge point position schematic (left) and CAD render of the specimen with the 3 extensometers attached (right).

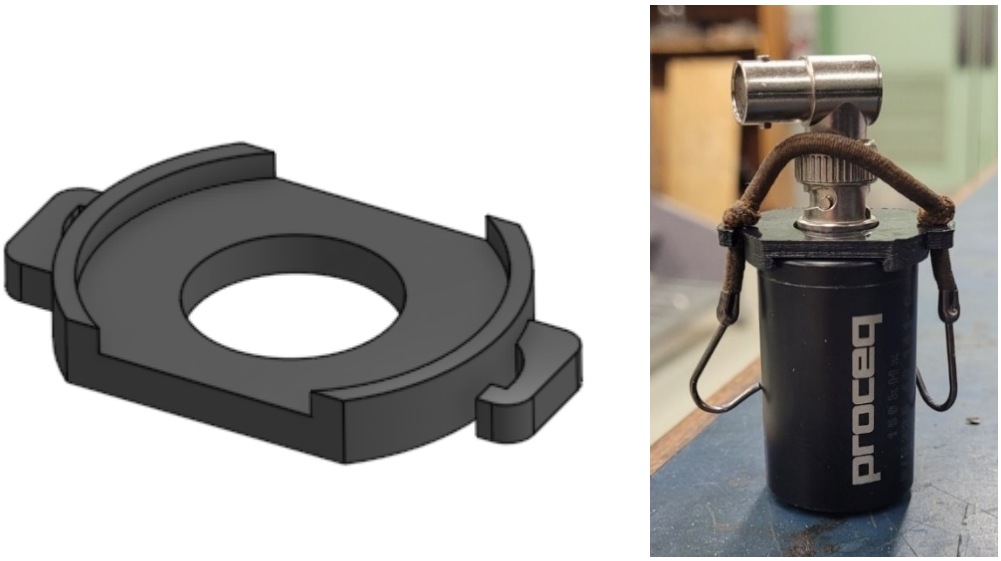

Figure B-2 CAD render of the 3D-printed transducer holders (left) and final transducer setup (right).

B.2 Environmental Testing Chamber Setup

A custom Burnsco environmental chamber was acquired to condition specimens at the testing temperature with a tolerance of ±0.5 °C. The environmental chamber is controlled using a combination of the MTS 810 controller and the existing Watlow F4T® process controller. The F4T controller was fitted with two additional Watlow Mixed I/O Flex modules. The temperature control scheme for the conditioning chamber requires several thermocouples placed at different locations in the thermal chamber: (1) the built-in thermocouple located at the top of the chamber, (2) a thermocouple embedded

within a dummy sample placed behind at the same height as the test specimen, and (3) an array of three thermocouples that will be placed on the surface of the sample during the test. For this control scheme to function, the controller must be interfaced with a computer through the included RJ45 port and the Watlow Composer software on a compatible Windows computer. The Composer software also gives access to the internal Functional Block Diagram (FBD) as shown in Figure B-3.

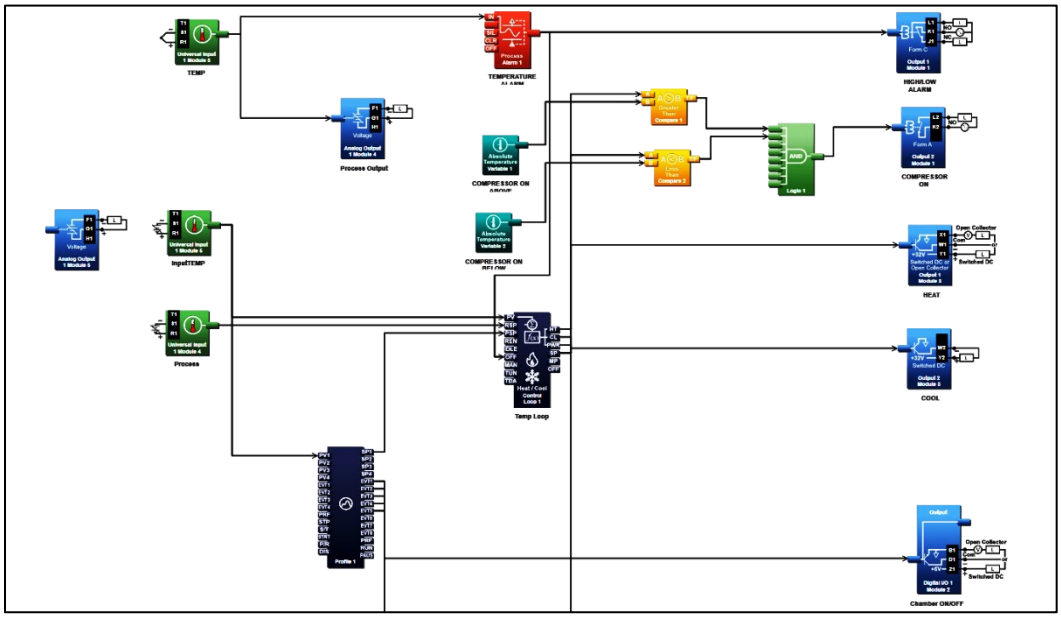

Figure B-3 Watlow Composer functional block diagram (FBD).

The FBD allows for the connection of different process variables (i.e., inputs and outputs) that facilitate the control of the chamber heating and cooling system as well as the tuning of specific PID settings for those processes. Using the Composer software, the Flex modules are initialized and added to the FBD. The Flex modules provide one additional input and output, however, using only one of the available outputs was necessary for this control scheme; the wiring schematic featured in Figure B-4 below demonstrates the connections required. Each input and output signal ranges from -10 to 10V and the signal scale is adjusted to the corresponding temperature range of each thermocouple and is powered by a BK Precision 1621A variable power supply.

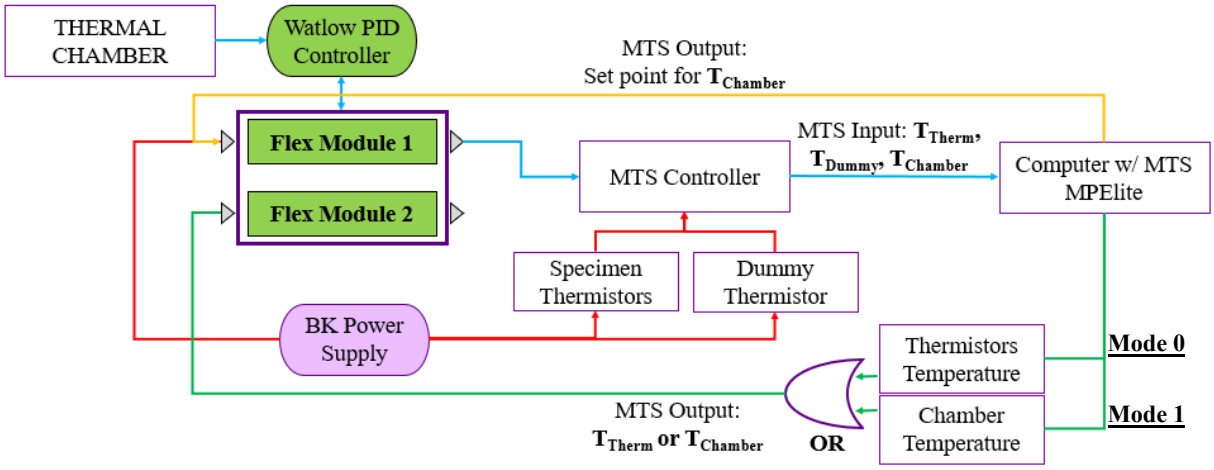

Figure B-4 Simplified wiring schematic for test temperature control.

The purpose of each input/output of the Flex modules is summarized in the list below:

Flex Module 1

- *Process Output 1*: this signal provides a voltage between 0 and 10V to the MTS controller and is converted to the Chamber Temperature.
- *Process Input 1*: this signal receives a voltage between 0 and 10V from the MTS controller and is used to provide the Temperature Control command/ set point to the Process Variable.

Flex Module 2

- *Process Output 2*: this signal is unused.
- *Process Input 2*: this input receives a voltage signal between 0 and 10V to from the MTS controller and is used to provide the Temperature Control value to the Process Variable.

To facilitate temperature control, a single temperature signal is output from the MTS controller as is configured in the MTS Station Builder. After the output signal is created, the built-in MTS Station Manager and Calculator Editor are used to create a "dummy" calculation variable capable of receiving inputs from several sources using logical comparison (i.e., if statements). Using the wiring scheme as depicted in Figure B-4, the chamber temperature can then be controlled using the Watlow controller using two modes: Mode 0 (using the three surface-mounted thermocouples) and Mode 1 (using the already installed chamber thermocouple).

These modes are activated using the MTS MPElite software and the "Set Calculation Parameter" activity. The reasoning behind the described temperature control scheme is as follows: (1) using the surface mounted thermocouples allows for shorter ramp times; as the surface temperature of the specimen changes at a lower rate compared to the air temperature in the chamber, the chamber can provide larger, short-term temperature inputs to decrease the time necessary to reach the conditioning temperature, (2) during testing, the chamber is controlled using the built-in thermocouple while the surface mounted thermocouples can be used to monitor any temperature evolution caused by loading/ unloading, (3) the internal PID of the F4T controller can be easily incorporated and adjusted with the Watlow Composer software independently of the MTS controller and (4) temperature control using the internal "dummy" temperature is disregarded as it would require impractically large temperature inputs to affect small temperature changes in the sample thus generating large amplitude temperature oscillations with a very long period. The dummy sample and surface-mounted thermocouples are calibrated for temperatures ranging from -10 and 30°C.

B.3 MTS Data Acquisition

The frame controller requires three interconnected software to function: (1) MTS Station Builder, (2) MTS Station Manager, and (3) MTS MPElite. MTS Station Builder is used to program a "station;" the station is a digital collection of the channels, inputs, and outputs necessary for the operation of sensors and hydraulic cs during testing. The Station Manager loads a station during operation and provides immediate control of the hydraulics and interlocks; the Station Manager also allows for the creation of variables, calculations, and tuning parameters. The MPElite software is used to design testing "activities"/procedures, monitor test progress and download completed test data. For both complex modulus and T/C fatigue testing, data is collected using the MTS frame controller from 3 channels and their accompanying 16 signals as designated in the MPElite Software. The signals can be collected into four primary groups:

- *Group 1 (Timing)*: Cycle count, Time (seconds) and Time of Day (seconds).
- *Group 2 (Axial Channel Measurement)*: Force (kN), Displacement (mm), Average Tri-Epsilon (mm), Extensometer 1 (mm), Extensometer 2 (mm), Extensometer 3 (mm).
- *Group 3 (Axial Channel Command)*: Force Command (kN), Displacement Command (mm) or Average Tri-Epsilon Command (mm).

- *Group 4 (Temperature)*: Thermistor 1 (°C), Thermistor 2 (°C), Thermistor 3 (°C), Dummy Temperature (°C), Chamber Temperature (°C).

Group 1 signals are used to determine the timing of the measurements, while Groups 2 to 4 are used to capture the specimen axial measurements, the axial command, and the temperature of the system. For both complex modulus and T/C fatigue tests, each signal is acquired at a rate of 1024 Hz.

B.3.1 Modulus and Phase Angle Calculation

The norm of the complex modulus, $|E^*|$, and phase angle, θ, for each temperature, T, and frequency, ω, are calculated using the algorithm described in Section 12 of AASHTO T 342. The algorithm uses a sine fitting procedure to filter and center the raw force and displacement data; the generated sine waves can be used to conduct the stress and strain analysis of the asphalt mix under loading. Typically, a subset of data is filtered from each individual temperature-frequency pairings, and a minimum of 5 cycles containing a total of at least 250 points is used for the calculation as recommended in AASHTO T 342. For brevity, the calculation algorithm will only be described for an unspecified signal variable, denoted as X, but the process is relatively similar for all axial components. The initial step in the analysis is to determine the average, X_{avg}:

$$X_{avg} = \frac{\sum_{i=1}^{n} X_i}{n} \quad \text{Eqn. B-1}$$

where X_i is the signal value at the *i*th data point and n is the number of points in the dataset. Using the average signal, the centred signal, X′, at the *i*th data point is calculated:

$$X_i' = X_i - X_{avg} \quad \text{Eqn. B-2}$$

The centred force is then used to calculate the offset, A_{X0}, the in-phase magnitude, A_{X1}, and the out-of-phase magnitude, B_{X1}.

$$A_{X1} = \frac{\sum_{i=1}^{n} X_i'}{n} \quad \text{Eqn. B-3}$$

$$A_{X1} = \frac{2}{n}\sum_{i=1}^{n} X_i' \cos(\omega_0 t_i) \quad \text{Eqn. B-4}$$

$$B_{X1} = \frac{2}{n}\sum_{i=1}^{n} X_i' sin\ (\omega_0 t_i) \qquad \text{Eqn. B-5}$$

where ω_0 is the angular frequency (rad/s) of the applied force and t_i is the time (seconds) at the *i*th data point. The signal magnitude, $|X^*|$, is computed from the in-phase and out-of-phase contributions as follows:

$$|X^*| = \sqrt{A_{X1}^2 + B_{X1}^2} \qquad \text{Eqn. B-6}$$

Finally, the signal phase angle, θ_X, is computed as:

$$\theta_X = \arctan(-\frac{B_{X1}}{A_{X1}}) \qquad \text{Eqn. B-7}$$

Using the coefficients, A_{X0}, A_{X1}, and B_{X1}, the predicted signal values can be computed. In the case of the stress analysis, the central force signal can be converted to the centred stress by dividing the force coefficients by the cross-sectional area. The remaining axial channels (i.e., the three extensometers) can be analyzed by using the same algorithm with the addition of the drift rate correction parameter, D_j, for the *j*th extensometer in the centred strain calculation. The complex modulus, $|E^*(\omega,T)|$, at a specific frequency-temperature pairing is calculated as the ratio of the stress magnitude, $|\sigma^*|$, and the average strain magnitude, $|\varepsilon^*|$, as:

$$|E^*(\omega,T)| = \frac{|\sigma^*|}{|\varepsilon^*_{avg}|} \qquad \text{Eqn. B-8}$$

The phase angle, $\theta(\omega,T)$, at a specific frequency-temperature pairing is then calculated as the difference between the average phase angle of the three extensometers, $\theta_{\varepsilon Avg}$, and the stress phase angle, θ_σ, as:

$$\theta(\omega,T) = \theta_{\varepsilon_{Avg}} - \theta_\sigma \qquad \text{Eqn. B-9}$$

Based on DIN-12697-26, at least four temperatures must be used to generate a master curve and two isotherms are not separated by more than 10°C. The selected temperatures include: -5, 5, 10, 20 and 30°C. The procedure begins at the lowest selected temperature and a temperature limit of 30°C was imposed. Testing samples at temperatures above 30°C was limited as creep became a major concern as the asphalt cements used in this study was relatively soft compared to those used in other regions; the high-temperature limit can be increased for stiffer or modified binders as necessary. These selected temperatures differ from AASHTO T 342 which typically ranges from -10 to 54°C. The conditioning

times are presented in Table B-1 below; conditioning times were selected based on experimentation using the calibrated "dummy" sample of the same dimensions and NMAS. Using the selected conditioning times, the complex modulus procedure is completed in approximately 12 to 13 hours for a single specimen. Table B-2 contains the data acquisition scheme for all complex modulus tests conducted in this work.

Table B-1 Test Temperature Conditioning Times (*Conditioning times do not include the time necessary to ramp to the desired temperature; the ramp period varies based on the initial temperature of the ramp.)

Testing Temperature (°C)	Conditioning Time (h)*
-5	3
5	2.5
10	2
20	1
30	1

Table B-2 Complex modulus data acquisition scheme

Frequency (Hz)	Cycles Acquired	Acquisition Rate (Hz)
0.1	40	5
0.2	60	5
0.5	100	25
1	200	51.2
2	200	256
10	400	1024

For fatigue and fatigue-healing tests, the specimen is installed in the testing chamber and allowed to reach the testing temperature ±0.5°C as discussed Appendix B.1; this process takes approximately 1.5 hours if starting at room temperature. Once the specimen has reached the testing temperature, the Strain Level Analysis (SLA) procedure is used to determine the force level required to produce the target on-specimen strain level. Using the COS mode, the specimen is initially loaded for 100 cycles at two strain levels using the testing frequency; a minimum 2-minute rest period is allowed between each loading period. The last 20 cycles (approximately 1100 data points) at each loading level are analyzed using the same algorithm described earlier from AASHTO T 342.

After analyzing the on-sample strain level of the preliminary test, the target strain can be attained using linear regression and then verified using a secondary SLA test as necessary. The results of the SLA will also be used to acquire the fingerprint complex modulus value for subsequent VECD modelling. It is the recommendation of AASHTO TP 107-18 that any sample experiencing peak-to-peak microstrain values greater than 150 microstrain should be discarded. However, this recommendation was disregarded as the selected strain levels are considerably lower than those

recommended in AASHTO TP 107-18 which ranges from 200 to 2000 peak-to-peak microstrain and, depending on the fingerprint modulus obtained, will typically begin at 300 to 800 microstrain. Using AASHTO TP 107-18, two to three additional specimens are tests. For these specimens, the strain level is increased and recommendations for this increase are detailed in AASHTO TP 107-18 Appendix X1. In this study, the peak-to-peak microstrain of 3 replicates was not increased after each specimen and all tests were conducted at strain levels below 250 microstrain. For uninterrupted fatigue tests, the data acquisition scheme employed can be found in Table B-3 below.

Table B-3 Fatigue test data acquisition scheme

Cycles	Acquisition Interval
3 – 120	3
121 – 999	15
1000 – 9999	150
10000 – 300000	1000
300001+	5000

In this study, a single rest period was used, however, the procedure can be altered using a "Loop" activity to employ as many loading and rest periods as the user desires in MTS MPElite software. Interrupted fatigue tests for evaluating healing and restoration will experience rest periods at 0 kN. At specified intervals during the rest period, a 300-cycle low strain loading period will be used to evaluate the change in stiffness of the resting sample; for this study, this was conducted at 10-minute intervals during the rest period. Rest periods can be programmed as short or long as desired, but longer rest periods (≥8 hours) were preferred.

B.4 Coupled UPV Data Acquisition using the MTS

The A1560 is connected to a Windows computer using a wired connection through the included RJ45 port located at the back of the unit (although wireless data transfer is also possible if desired) and linked over TCP/IP (Transmission Control Protocol/Internet Protocol) through the provided IP address. To access the signals from the acquired data signal, a custom software application was coded using Visual Studio and the A1560 application programming interface (API) provided by the manufacturer. Version 1.0 of the software allowed the user to input parameters such as: sampling frequency, filter type, filter frequency, analog gain, transducer type, transducer frequency, and averaging factor. Version 1.0 also featured the ability to view/ plot the acquired time-domain signal and save the acquired data to a .CSV file. In Version 2.0 of the A1560 software, the functionality was updated to include the ability to: (1) view/ plot the acquired signal in the frequency domain, (2) acquire and save signal data on a timed

interval basis, and (3) acquire and save signal data using a user-defined schedule. Currently, the software used for this work exists as Version 2.1 (Figure B-5); updates to the Version 2.1 of the software include the ability to: (1) automatically save a Log file (in .txt file format) detailing the selected parameters at the time of acquisition, and (2) acquire and save signal data using the TTL triggering function of the API.

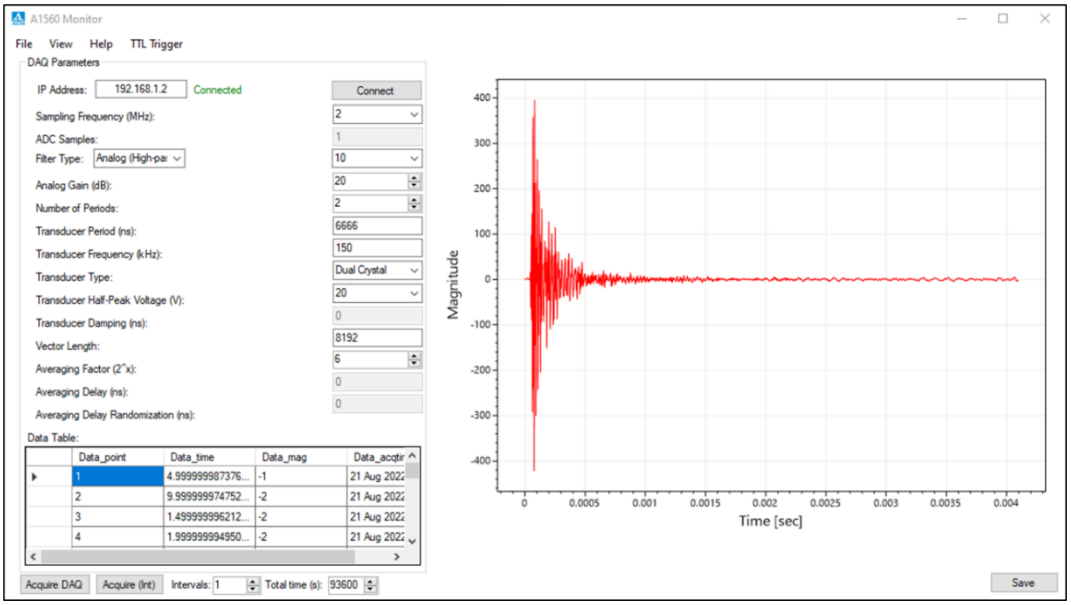

Figure B-5 Custom A1560 software featuring a representative time signal obtained from the completed experimental test setup.

Primarily, the TTL triggering function will be utilized to synchronize data acquisition between the pulse-receiver system and the MTS controller. The "TTL Trigger" mode in the software sets the A1560 system in a "waiting" state for a time duration specified by the user. In the waiting state, the TTL port on the A1560 can be triggered using a low-voltage, short-time pulse from the MTS controller. In the MTS Station Builder, an output channel is created and set to an operating range of 0 to 3.1V. This output channel can be set to produce a 0.02-second 1.0V pulse when a UPV measurement is desired using the "Custom Waveform" activity in the MPElite software (Figure B-6). The A1560 control software automatically saves the individual .CSV file from each pulse in a folder on the computer's desktop with the filename convention "A1560-*Date_Time*.csv", where Date_Time is formatted as "YYYYMMDD_HHMMSS" for the convenience of the operator.

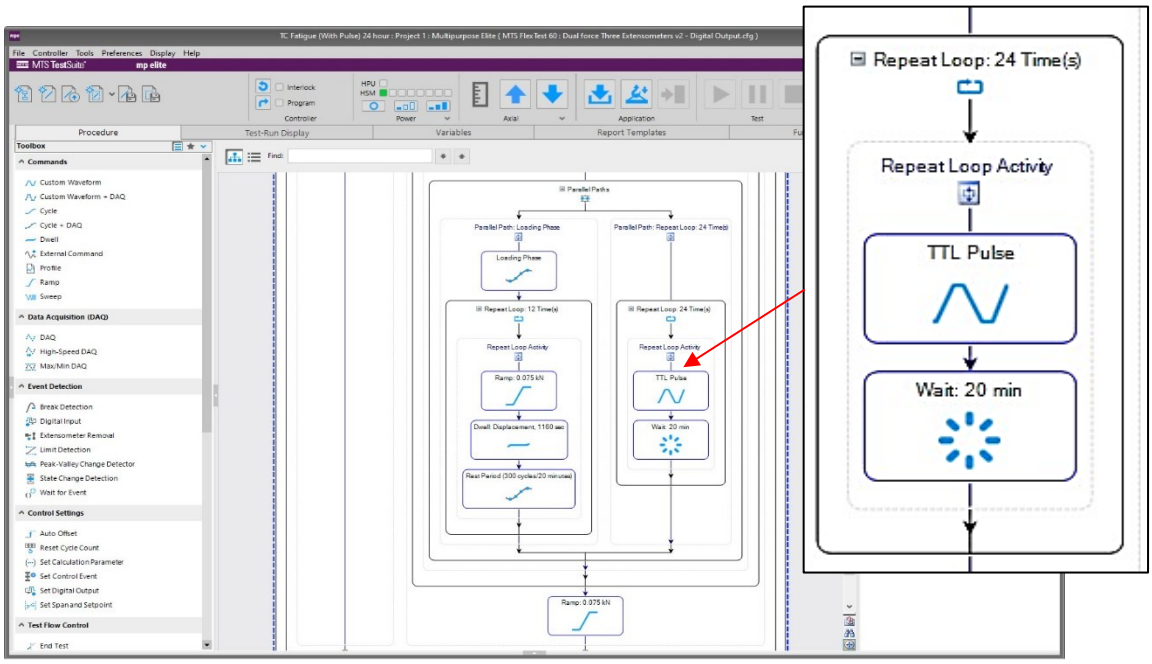

Figure B-6 MTS MPElite software with TTL pulse triggering included in the test procedure.

Each data file contains four columns: (1) the data point number, (2) the data point time in seconds (determined from the sampling frequency), (3) the signal magnitude, and (4) a Date_Time identifier corresponding to the user-initiated or triggered acquisition time. The in-file Date_Time identifier is formatted as "YYYYMMDD_HHMMSSSSSS" to increase the precision of the acquisition time using the internal clock of the computer. The data files can then be sorted by the Date_Time and processed using a MATLAB script to prepare a 3-dimensional (k *x* m *x* n) array, where k is the number of data files in a folder, m is the row vector length of the acquired signal and n is the number of columns acquired for each signal. Once imported into the MATLAB array, each signal can be post-processed individually or as a group using the appropriate signal-processing techniques.